Vortex Shedding-Induced Noise Reduction Using (DBD) Plasma Actuator

Laith Ayad AL-Sadawi

Brunel University London
College of Engineering Design and Physical Sciences
Department of Mechanical Aerospace and Civil Engineering

A dissertation submitted for the Doctor of Philosophy degree

January 2018

Abstract

The Dielectric Barrier Discharge (DBD) plasma actuators have received a significant attention of many researchers in the last few decades. The main focus of these studies has been on the flow control areas such as turbulent boundary layer separation and turbulent skin friction reduction. Little attention has been paid on the effect of the DBD plasma actuators on the aerodynamic noise reduction. In this regard, the aim of the current work is to investigate the effect of the DBD plasma actuator driven at relatively low voltages on vortex-induced noise.

The first part of the current work includes an extensive assessment of the effect of the DBD plasma actuator on the narrowband tonal noise radiated from a flat plate with blunt trailing edge and an airfoil (NACA 0012) with blunt and cut-in type serrated trailing edge. The measurements were carried out at Reynolds numbers between 0.75 x 10^5 and 4 x 10^5. It is found that the DBD plasma actuator effectiveness depends on the direction of the generated electric wind. For example, a high reduction in the narrowband tonal noise level is achieved when a direct streamwise electric wind is injected into the wake region. However, using a plasma actuator, which can induce streamwise vortices into the wake region, shows more superior noise reduction capability at lower voltages.

Flow measurement results revealed that the mechanism responsible for the narrowband tonal noise reduction when the electric wind is directly injected into the wake is not due the momentum injection into the wake deficit. Rather, the streamwise jet isolates the two separated shear layers and prevents the interaction between them. On the other hand, it is found that the break-up of the spanwise coherence of the vortex shedding is responsible for the significant reduction in the tonal noise level when the spanwise actuation is used.

The second part of the current work comprises the effect of the DBD plasma actuator on both the narrowband tonal noise and interaction broadband noise radiated from both single and tandem cylinder, respectively. The experiments were conducted at subcritical Reynolds number Re_D = 1.1 x 10^4. The actuators were positioned at different azimuthal angles $27^o \leq \theta_j \leq 153^o$. For the single cylinder case, the acoustic results show the DBD plasma actuator that is positioned at $\theta_j = 133^o$ leads to a more reduction in the narrowband tonal noise level when compared to the other angles. It is found that the streamwise jet produced by the plasma actuators plays an

important role in prevention of the interaction between the shear layers that separates from the cylinder.

For the tandem cylinders case, the acoustic results show that the simultaneous actuation of both the upstream and the downstream cylinders leads to more reduction in both the narrowband tonal noise and the interaction broadband noise level compared with the case where only the upstream or the downstream cylinder is actuated. The mechanism responsible for this noise reduction is found to be mainly due to the streamwise jet induced by the upstream cylinder activation, which delays the vortex shedding formation and reduces the turbulence intensity in the near wake region. On the other hand, the plasma induced jet against the main-flow direction works as a virtual fluidic barrier which displaces the wake produced by the upstream cylinder away from the downstream cylinder.

Acknowledgment

I would like to express my sincere thanks to my supervisor Dr. Tze Pei Chong for his guidance, and for making this project such a great experience. I am so grateful for his continuous support, encouragement, and for being available at any time I needed his valuable advice. I could not have hoped for a better research team for my PhD study.

I would like to express my gratitude to the EPSRC in the UK for their support through research grant No. EP/K002309/1.

I would like to express my deep thanks to Mr. Till Biedermann and Professor Frank Kameier from the Düsseldorf University of Applied Sciences for their generosity to loan the PIV system to Brunel University London.

I would also like to extend my thanks to my sponsor the Iraqi Ministry of Higher Education and Scientific Research and the Iraqi Cultural attaché in London for making this opportunity possible and for their continuous support.

Special thanks to Dr. Kim Jung Hoon for spending those endless hours in the lab with me during the first year in my PhD study.

I would like to thank the technical staff, Kevin Robinson, Chris Allan, Paul Yates, William, Michael, Clive Barret, and Peter Wilson for their help and support in the laboratories and workshops during the last four years.

I am so grateful to my fellow students and friends Alexandros, Chioma, Oliver, Jonne, Auris, Philip, Vivian, Magna, Salam, Ommar, Ann, Shireen, Raad, Yousif, and Bilal for their support and for making my time at Brunel University such a nice time.

Special thanks to Till and his girlfriend Katharina for their hospitality and care during my stay in Germany.

Finally, I would like to thank my parents and my brother Muhammad for their tremendous support and encouragement during the course of my PhD study.

Table of Contents

List of Symbols

A^i	=	eigenvector
AR	=	aspect ratio
a_n	=	expansion factor
B	=	width of the flat plate mm
C	=	the chord of the flat plate and the airfoil mm
C_D	=	drag coefficient which equals to the sum of the mean $C_{D(mean)}$ and fluctuating $C_{D(rms)}$ components
c_∞	=	speed of sound, ms^{-1}
D	=	cylinder diameter, mm
E	=	hot wire probe acquired voltage, V
f	=	frequency, Hz
$f_{(input)}$	=	the input frequency to the plasma actuator, Hz
F	=	focal point of the recirculation region
G	=	Green function
g	=	gravity ms^{-2}
H	=	the thickness of the flat plate, mm
H_s	=	Heaviside step function
I	=	particles intensity in the first frame
I'	=	particles intensity in the second frame
IA	=	interrogation area, pixles

M	=	position of the velocity vectors, Mach number Eq. (2.5)
N	=	the number of the snapshots
n_i	=	surface unite normal vector
P	=	static pressure, Pa
p'	=	pressure fluctuations, Pa
p_o	=	total pressure, pa
$\overline{p'^2}$	=	mean square pressure fluctuation, Pa
P_{xx}	=	power spectral density, dB/Hz
R_e	=	Reynolds number
$R_{ii'}$	=	particle displacement
R_{pp}	=	pressure fluctuation correlation function
R	=	distance from the source of sound, m
S	=	Saddle point
St	=	Strouhal number
T	=	time, s
Ta	=	hot wire acquisition temperature, c^o
Tc	=	hot wire calibration temperature, c^o
Tw	=	hot wire probe temperature, c^o
T_{ij}	=	Lighthill's stress tensor, Nm^{-2}
$T_{u,v}$	=	turbulence intensity in the x and y direction
T	=	observer time, s

U	=	mean flow velocity, ms^{-1}
U	=	velocity component in the x direction, ms^{-1}
u	=	plasma induced jet velocity in the x direction, ms^{-1}
$V_{(input)}$	=	the input voltage to the plasma actuator, kV
V	=	velocity component in the y direction, ms^{-1}
$\tilde{v}$	=	plasma induced jet velocity in the y direction, ms^{-1}
X	=	streamwise direction, mm
Y	=	wall-normal direction, mm
y_{+}	=	normalized wall-normal distance (yu_{τ}/v), where u_{τ} is the friction velocity and v is the kinematic viscosity
Z	=	spanwise direction, mm
Δ	=	boundary layer thickness, mm
δ^{*}	=	boundary layer displacement thickness
δ_{99}	=	boundary layer thickness at vertical position where $u = 0.99\ U_{\infty}$, mm
E	=	bluntness of the saw tooth at the root of the serration ,mm
Λ	=	serration period from peak to peak, sinusoidal exposed electrode period peak to peak, mm
M	=	Absolute viscosity, $N.s.m^{-2}$
Θ	=	momentum thickness, mm
θ_{j}	=	the angle of the plasma actuator position on the cylinder measured from the front stagnation point (Single cylinder case), deg.
θ_{DCj}	=	the angle of the plasma actuator position on the downstream cylinder

(tandem cylinder case), deg.

θ_{UCj}	=	*the angle of the plasma actuator position on the upstream cylinder (tandem cylinder case), deg.*
Φ	=	*serration angle, deg.*
Ω_x	=	*streamwise vorticity, s^{-1}*
Ω_z	=	*spanwise vorticity, s^{-1}*

Abbreviations

DBD	=	*Dielectric Barrier Discharge plasma actuator*
EPN	=	*Effective Perceived Noise,dB*
OASPL	=	*Overall Sound Pressure Level, dB*
PIV	=	*Particle Image Velocimetry*
POD	=	*Proper Orthogonal Decomposition*
PSJ	=	*Plasma Synthetic Jet*
SPL	=	*Sound Pressure Level, dB*
T-S	=	*Tolmien- Schlichting instability wave*

List of Figures

List of Tables

Publications

L. Al-sadawi, T.P Chong,and J.H. Kim (2017). Aerodynamic noise reduction by plasma actuators for a flat plate with blunt trailing edge (submitted to JSV).

L.AL-Sadawi & T.P.Chong (2017). Active Noise Control of Single and Tandem Cylinders Using Plasma Actuator. European Drag Reduction and Flow Control Meeting, Italy

Al-Sadawi, L. A., & Chong, T. P. (2016). Vortex shedding noise reduction by single dielectric barrier discharge plasma actuators. In *22nd AIAA/CEAS Aeroacoustics Conference* (p. 2759).

Flat Plate Vortex Shedding Noise Suppression with Surface Dielectric Barrier Discharge Plasma Actuators. European Drag Reduction and Flow Control Meeting, Italy (2015)

Kim, J.H., Al-Sadawi, L., Vathylakis, A. and Chong, T.P., (2014). Trailing Edge Noise Reduction by Passive and Active Flow Controls. In 20th AIAA/CEAS Aeroacoustics Conference (p. 3300).

Chapter 1

Introduction

Aerodynamic sound can be defined as the sound that is generated as a result of the interaction between a solid body and the surrounding airflow rather than being a by-product of body vibration. The first formulation of aerodynamically generated noise was given by Lighthill in 1952, which led to the prediction of jet noise for the first time and set the base for a wide range of aeroacoustic problems. The current research will contribute in the study of the vortex shedding noise reduction and the explanation of the mechanism behind it, which will be relevant in the aircraft landing gear and wind turbines.

1.1 Aircraft Noise

Air traffic has seen a dramatic growth in many regions around the world in the last few decades. The advancement in civil aviation along with the higher living standards has played a vital rule in the increased popularity of air transport. With the ongoing increase in popularity of air travel, aircraft noise has been considered a major issue especially for near airport communities.

People awareness of aircraft noise has started in the middle of the 20th century, when jet transports were introduced for the first time. Aircraft noise has been linked to several health issues especially for people who live in the vicinity of airports or under the flight path. For instance, in 1993 the World Health Organisation (WHO) summarised several health problems that aviation noise may cause to human. These include: hearing impairment, pain, annoyance, Interference with communication and speech perception, sleep disturbance, deficits in reading acquisition among children, effects on social behavior, and effects on physical health [Whitelegg, (2000)]. Some of the aforementioned problems could happen in everyday life, such as the interference with communication and speech and sleep disturbance, while other problems like hearing damage may happen after long term exposure to aircraft noise. In order to ensure good human health, the World Health Organization proposed a range of noise threshold that the aircraft may not exceed [Whitelegg, (2000), Grimwood et al. (2002)]. For example the noise threshold for indoor, school and Hospitals should not exceed 30 dB.

The problems associated with aircraft noise have resulted in community objection to the operation and expansion of airports, and aircraft noise has been considered as one of the greatest pollution problems. In an attempt to control aircraft noise and reduce the number of people affected by aircraft noise, several regulations called "chapters" have been developed by the International Civil Aviation Organization (ICAO) and other committees such as the Community of Aviation Environmental Protection (CAEP).The first noise standards was enforced by (ICAO) in 1972 for the new subsonic jets (Annex 16, Volume 1 Chapter 2). As a result of the initiation of the new noise standards, engines with higher by-pass ratio entered the service. The introduction of this new technology resulted not only in engine noise reduction but also encouraged ICAO to increase the stringency of noise regulations. Following the meeting of the Community of Aviation Environmental Protection (CAEP) in 2001, ICAO has published more stringent standards. Annex 16 Volume 1 Chapter 4 for jet and heavy propeller driven airplanes. In 2014, new standards, chapter 14, were recommended by (CAEP) which will be applicable to new airplanes submitted for certification before the end of 2017 and on or after 31st of December 2020 for aircrafts less than 55 tones [Dickson, (2013]. The progression of ICAO effective perceived noise (EPNdB), which represents the subjective effect of aircraft noise on human beings, with respect to the maximum take-off weight is illustrated in Fig.1.1.
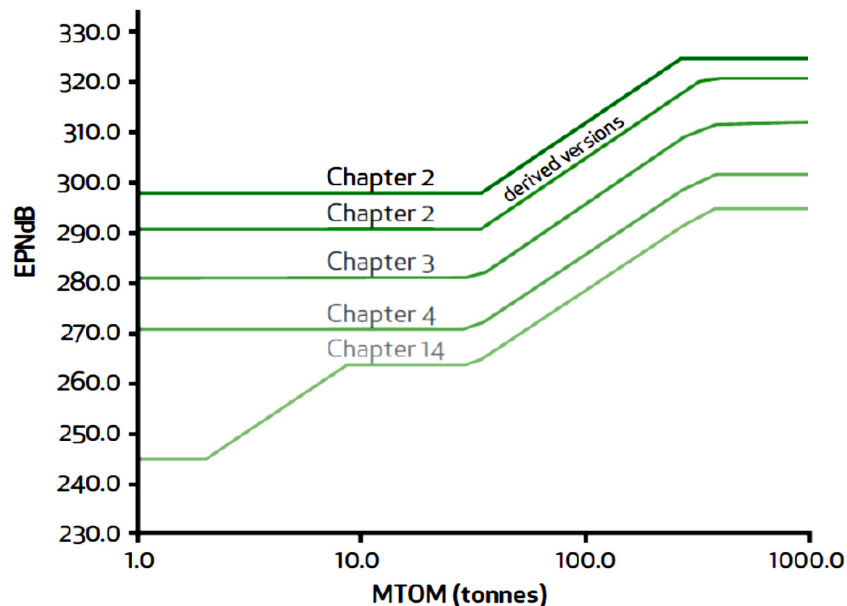
Figure 1.1 ICAO noise regulation standards. [Dickson, (2013)]

These stringent regulations have forced aircraft and aero-engines manufacturers and their research centers to put more effort to design quieter aircrafts. In this regards, the Advisory Council for Aeronautical Research in Europe (ACARE) set a number targets in order to reduce the perceived noise by a 10 dB for each civil plane and each operation between 2000 and 2020 [Argüelles et al. (2001)]. As a result, the European Commission and national agencies supported several technological projects. For instance, the European commission encouraged a large number of projects through its subsequent Framework Research Programs (FRP) [Leylekian et al. (2014)]. Several technological projects were granted in order to address different problems such as the jet noise, fan broadband noise, landing gear noise, and high lift devices noise. These technologies are divided into two groups: first and second generation noise reduction technologies (NRT1) and (NRT2), respectively, as shown in Fig. 1.2 [Leylekian et al. (2014)]. In 2011, the 2020 targets was replaced by a new highly ambitious set of targets "Flightpath 2050", which requires a reduction of 65% in the aircraft effective perceived noise level relative to the new aircrafts which are introduced in 2000, [Dareck et al. (2014)].
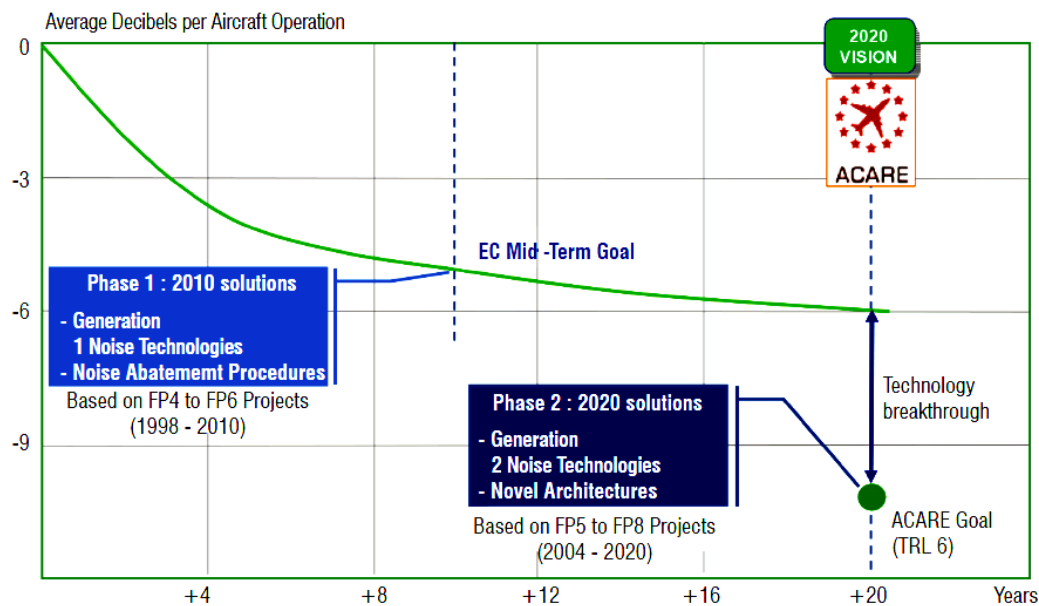
Figure 1.2 Advances on noise reduction (NRT1) and (NRT2). [Leylekian et al. (2014)]

In order to achieve the desired noise reduction target, novel approaches are needed to improve noise performance of the current airplanes and to design quieter future airplanes. Aviation

industry, aero-engines, and aircraft manufacturers have been working on developing novel technologies to fulfill the growing demand for low noise aircrafts.

University research community also plays a major role in supporting the above initiatives to achieve the stated noise targets. In this thesis, the focus is to implement a state of the art technology. Dielectric Barrier Discharge (DBD) plasma actuators to reduce the bluntness induced vortex shedding noise, as well as the wake interaction noise in the configuration of tandem cylinders. The work is expected to have significant impact on the landing gear noise on airplanes.

1.2 Aircraft Noise Sources

The main contributors to aircraft noise can be divided into two groups: engine noise and airframe noise. Fig. 1.3 illustrates the main noise sources of civil aircrafts. The first dominated source of aircraft noise is the engine noise, which includes the noise produced by fan, compressor, turbine, and jet exhaust. The second contributor to aircraft noise is the airframe noise sources, which can be identified as the noise that comes from the aircraft parts such as the wing leading edge slats, trailing edge flaps, and landing gears. The domination of each of the aforementioned noise sources depends on two factors; engine operation condition and airframe design. For instance, jet noise is considered to be the dominant noise source during take-off, because engines are at full thrust. On the other hand, in the landing phase, when engine power is low, the airframe noise becomes the main contributor to the aircraft overall noise. Fig. 1.4 demonstrates the difference between the engine and airframe contribution to the aircraft noise during the take-off and landing.

Jet noise is considered as the most dominant highest noise source compared with the other aircraft noise sources. Since the introduction of high by-pass turbofans and effective nacelle's acoustic treatment in the 1970's, jet noise has remarkably been reduced by about 20 EPNdBs. Unlike the aircraft engines back in the 1970's, today's aircraft engines have had a dramatic increase in the bypass ratio up to 10-12. Higher bypass ratio means that the thrust is mostly generated by slower exhaust jet moderately compressed air. The reduction in jet noise has made other engine noise sources such the fan noise to be comparable and may be even the most

convenient especially when larger fans are used. Fan noise has the tonal and broadband characteristics and the mechanism responsible behind the fan noise can be described as follows:

- The interaction between fan blade tip and turbulent boundary layer on the inlet duct.
- Fan trailing edge noise.
- Interaction between the rotor and the downstream guide vanes.
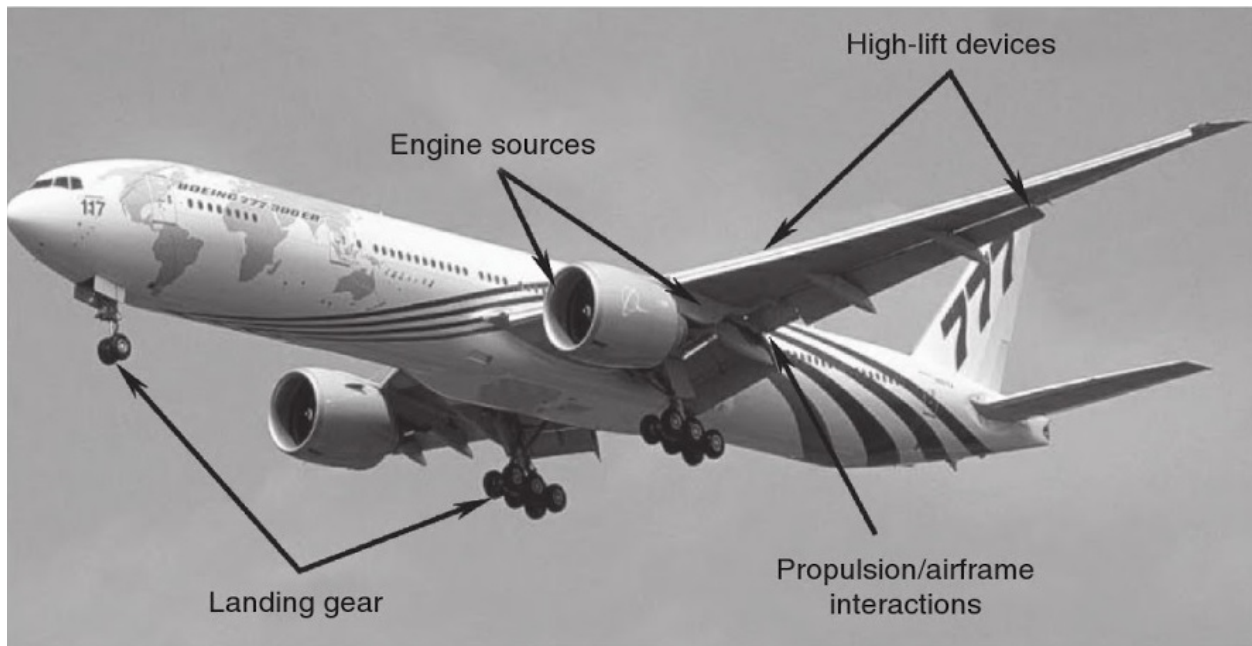
Figure 1.3 Major sources of aircraft noise. [Zaporozhets, (2011)]

a)   b)
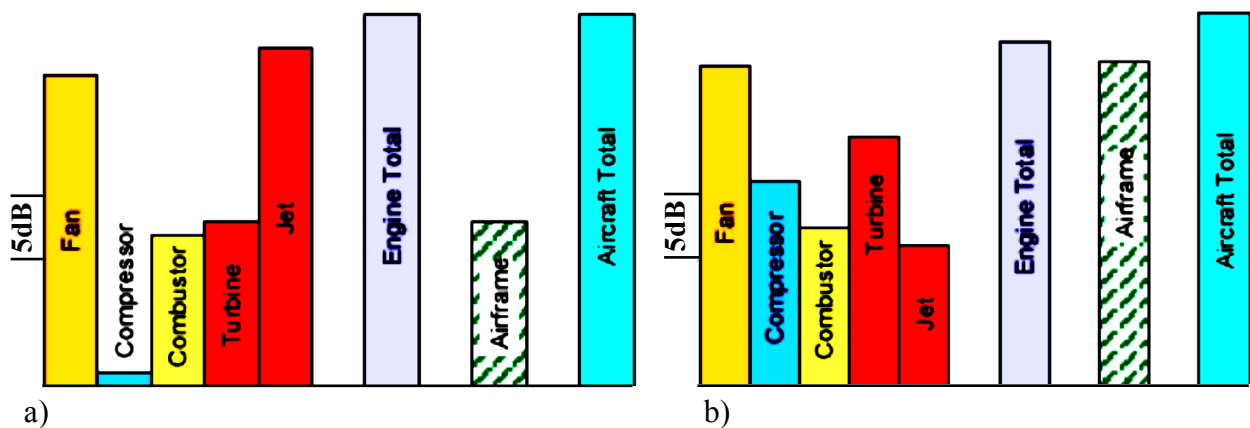
Figure 1.4 Difference between engine and airframe noise level during a) Take off and b) Landing.
[Leylekian, (2014)]

This dramatic reduction in jet noise has led to the present situation where the airframe noise is considered the dominant noise source during landing phase; though jet noise is still important in take-off and cruise. Airframe noise can be subdivided into four noise sources; the order is placed according to the level of importance as follows: landing gears, slats, flap and slat side edges, and interaction noise between gears and the downstream components [Dobrzynski, (2010)]. The contribution of each of the aforementioned noise sources may differ for different aircraft designs. For instance, landing gear noise is the dominant source for wide body aircrafts, while for regional aircrafts, the noise produced by the high lift devices is found to be comparable to the landing gear noise. Other airframe noise sources such as the wing tip, free wake turbulence, surface roughness and vibration are of secondary importance, but still contribute to the aircraft over all noise which needs to comply with the ACARE 2020 and Flightpath 2050 targets.

One of the important sources of the airframe noise is generated by the high lift devices, such as the slats, trailing edge flaps, and spoilers when deployed in steep approach. Choudhari and Khorrami, (2006) showed that a number of mechanisms are responsible for the leading edge slat noise as summarised in Fig. 1.5. These are: the unsteady vortex structure in the slat cove, the interaction between the vertical flow and the downstream cove, and the turbulent flow shedding from the trailing edge. In addition, it has been shown that the side edge vortices and their impingement with the flap surface are responsible for the trailing edge flap noise. Furthermore, airfoil self-noise or airfoil trailing edge noise is considered as a prominent noise source, which is resulted from the turbulent eddies scattering from the airfoil trailing edge. Brooks et al. (1989) summarized the airfoil self-noise mechanisms as follows: trailing edge noise, vortex shedding noise, laminar boundary layer noise, separation noise, and wing tip vortex noise. These mechanisms will be reviewed in Section 2.3.1.

Landing gear is considered one of the major noise sources of airframe noise. The landing gears noise has both a broadband and tonal noise nature. For the conventional landing gears, a number of noise sources have been identified. For instance, it has been found that both the wheels and struts are linked to the low frequency noise, while the high frequency noise can be produced by the small details such as the hoses and dressings [Li et al. (2013)]. Some studies showed that tonal noise can be generated from the vortex shedding behind the struts.

The intensity of the tonal noise depends on a number of factors such as, the turbulence, velocity, and flow direction. On the other hand, the mechanism of landing gear broadband noise is associated with the impingements between the large scale coherent structures in the turbulent flow wake from the bluff body components and the downstream components. Several experimental and CFD studied have been conducted to measure and predict landing gear noise sources. Figure 1.6 demonstrates both the flow filed and near field surface pressure fluctuations spectra of a simplified two wheel landing gear. From fig. 1.6a it can be seen that the instantaneous flow field can be distinguished by a turbulent separation, intensive interaction, and unsteady vortex shedding. From surface pressure fluctuation, it can be seen that the main noise source is spherical and located near the wheel. On the other hand, the near field surface pressure spectra (Fig. 1.6b) shows that the landing gear noise has a broadband nature with two narrowband tonal peaks, which are probably due to the vortex shedding and the acoustic resonance of wheel cavity [Deck et al. (2014)].
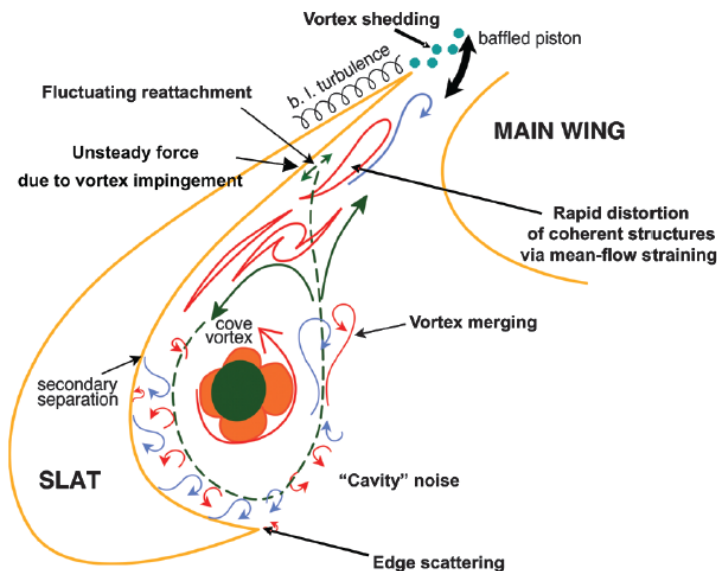
Figure 1.5 Slat noise source mechanisms. [Choudhari and Khorrami, (2006)]
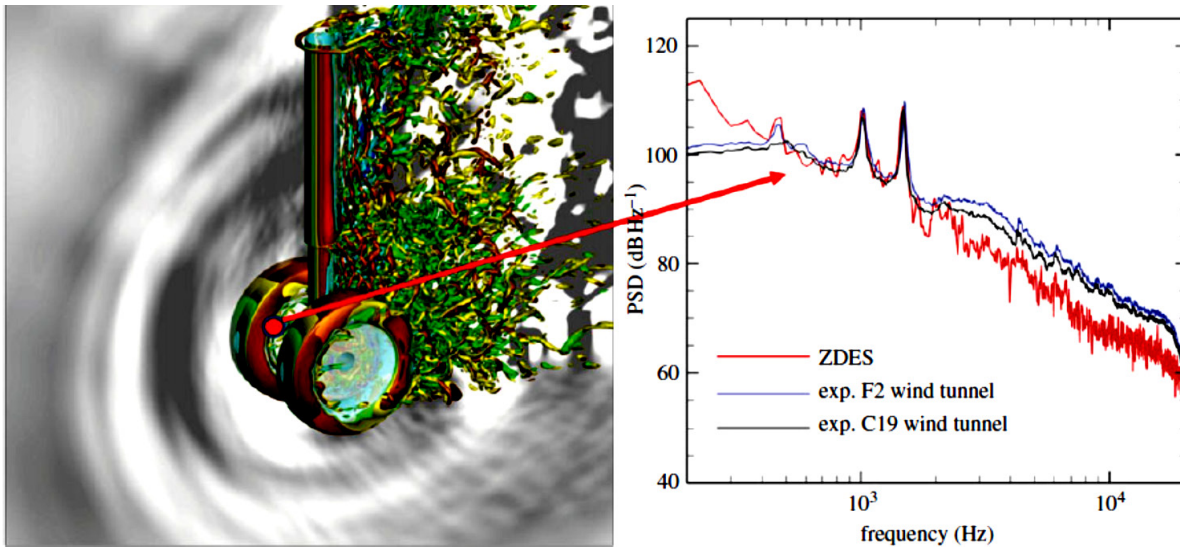
a) Instantaneous flow field   b) Surface pressure fluctuations

Figure 1.6 Prediction of landing gear a) instantaneous flow field and b) near field surface pressure fluctuation. [Deck et al. (2014)]

1.3 Engine and Airframe Noise Existing Treatments

Engine jet noise has been dramatically reduced through increasing the by-pass ratio (BPR). This increase in BPR results in an increase in the size of nacelle which is considers an important part for turbo-machinery noise reduction through its acoustic treatment. This in turn will result in an increase in the nacelle's weight and drag. Shortening the nacelle is a possible solution that the aerospace industry is trying to achieve without reducing the benefits of the previous design through the use advanced technologies such as, fine liners.

Fan noise is another important noise source after the jet noise. Several treatments have been investigated to reduce fan noise. Fan noise reduction could be achieved through two strategies: blade shape modification and reduction of air flow velocity. The modification of blade geometry cannot be achieved using acoustic treatments (liners), due to the degradation of the blade structural strength. Rather, focusing on the optimizing of the 3D shape of the blade could represent a better strategy to increase in the engine's efficiency [Leylekian, (2014)]. On the other hand, reducing the airflow velocity at the blade tip, which could reach transonic speed, can be achieved by decoupling the fan from the main shaft using gear box. To further reduce engine

noise, a number of new engine architectures have been investigated. These include the ultra-high by-pass engines. These new designs are intended to reduce both the fuel consumption and engine noise

Because of the rapid advances in the aircraft engine technology, airframe noise currently represents the major source of aircraft noise during landing phase. In order to reduce the overall noise of aircrafts, many noise control studies have been focusing on the airframe noise since the last decade.

Different noise control techniques have been implemented to reduce the airframe noise (high lift devices and landing gear). Several passive techniques has been used for reducing the high lift devices noise, such as the slat cove cover, slat cove filler, and slat hook extensions as shown in Fig 1.7 [Dobrzynski et al. (2001)]. It has been reported that a promising noise reduction could be achieved using slat cove cover. Furthermore, acoustic liners are used to attenuate the sound wave. It has been reported that by applying the acoustic liners at the pressure side of the airfoil leading edge can significantly reduce both the far-field noise and near-field unsteady pressure fluctuations [Chen et al. (2011)].

A number of passive flow control techniques have been used in an attempt to reduce the landing gear noise such as the solid and perforated fairing, meshes, and splitter plates. Although, a total noise reduction of up to 10 dB was achieved by shielding the landing gear components, it has been reported that this technique is impractical as it slows down the inspection process and it may reflect flow towards the uncovered components which may increase the overall noise. Another passive control technique has been used for the landing gear noise reduction is known as the splitter plate. It has been reported that using splitter plate behind landing gear components can reduce landing gear noise by up to 2 dB [Pott-Pollenske, (2010)]. In addition, new modification on both the nose landing gears (NLG) and the main landing gear (MLG) was investigated through the European SILINCER project. The modification for (NLG) was achieved by keeping the complicated upper leg part inside the body in order to prevent the interaction with the incoming flow, whereas for the (MLG), a telescoping side stay is used instead of the folding one. The implementation of the aforementioned technique resulted in (NLG) noise reduction of up to 7dB and 5 dB for the (MLG). Recently, a number of successful landing gear noise reduction techniques have been developed. Most of these techniques are passive control methods

such as fairing and splitter plate. Dobrzynski et al. (2002) reported that a reduction of about -3 and -3.5 dB in the landing gear overall noise level can be achieved when bogie beam and under-tray fairing are used , as shown in Fig. 1.8. Recently, a number of successful landing gear noise reduction techniques have been developed. Most of these techniques are passive control methods such as fairing and splitter plate.
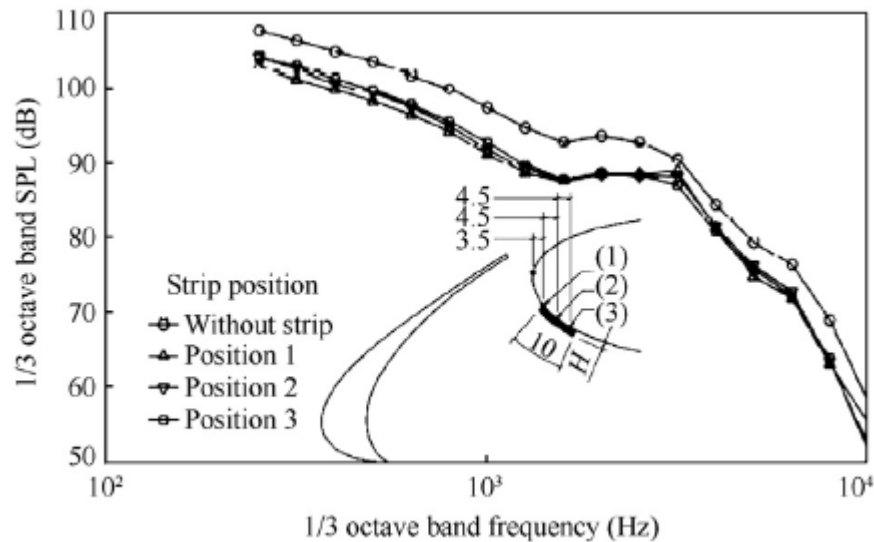
Figure 1.7 Slat noise control using acoustic liners. [Dobrzynski et al. (2001)]
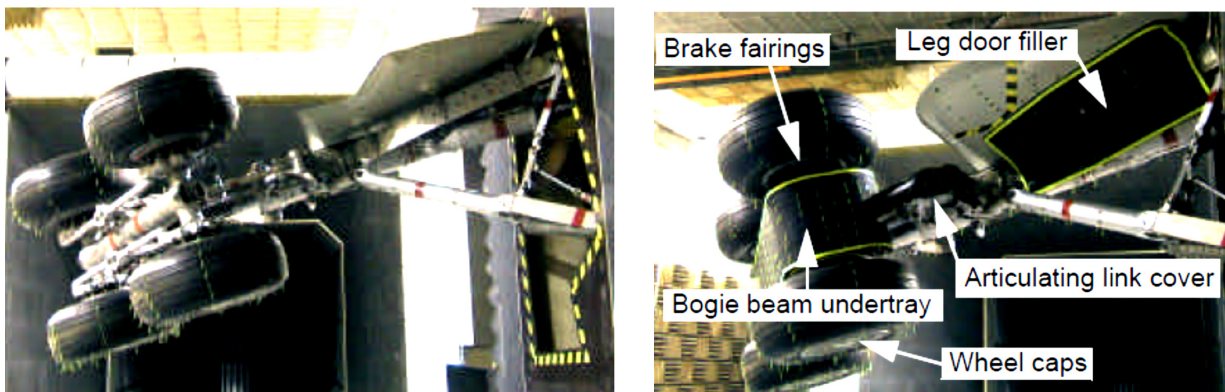
a) Uncontrolled landing gear   b) Passively controlled landing gear

Figure 1.8 Landing gear passive noise reduction techniques. [Dobrzynski et al. (2002)]

A number of active flow control techniques have been used to control both landing gear and high lift devices noise. Air suction and blowing has been used as an active fairing for reducing the

landing gear noise. The mechanism of the noise reduction using blowing is based on deflecting the flow from gear components and reducing the local speed. In the case of the high lift devices, blowing is used to reduce flaps side edge noise. The air was applied on both upper and lower surface of the flap sides and resulted in vorticity size reduction in the flap side shear layer of the vorticity [Oerlemans and Bruin (2009)]. Moreover, the downside of the blowing technique is the requirement of heavy air-supply system, which can outweigh the benefit of this particular active flow control technique.

Despite the intense research on airframe noise reduction techniques, it seems that the current techniques for the airframe noise control is still a long way to achieve the ambitious targets noise reduction set by the ACARE 2020 and the Flight path 2050. Alternative approaches need to be adopted by the aviation industry in order to achieve the desired noise reduction level. In this regards, the current research focuses on using a promising control technique, aerodynamic plasma actuator, which is also known as Dielectric Barrier Discharge (DBD) plasma actuator to suppress the vortex shedding from bluff bodies and reduce the associated aerodynamic noise.

1.4 Wind Turbine Noise

Wind power is considered as one of the most promising renewable energies. The worldwide annual growth rate of wind power has been about 17.96% since 1994. In the United States alone by the end of 2001 the electricity produced by the wind energy was 20% of that of the world. This fast growth of demand on wind power comes as result of the wide range of advantages that wind power can offer, like being cost effective, clean source of energy, and providing jobs [Oerlemans and Fuglsang, (2012)].

In order to compete with the other existing energy generating technologies, wind power industry should increase the output power while maintain or reduce the power cost per kilowatt hour. The output power of wind turbines depends on the rotor diameter. The relation between the output power and rotor diameter is presented in Fig. 1.9. It can be seen that in order to increase the output power that wind turbine can provide larger rotor diameter is needed. The drawbacks of using larger rotor diameter are the increase in blade aerodynamic loading, and noise radiation.
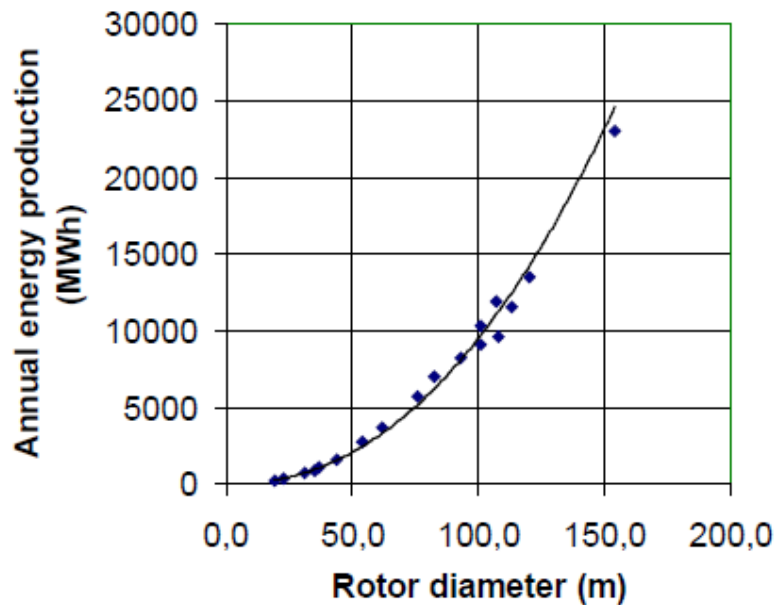
Figure 1.9 The relation between rotor diameter and the annul energy production of wind turbines. [Oerlemans and Fuglsang, (2012)]

The noise emitted from wind turbines can be divided into two categories: mechanical and aerodynamic noise. The former one is generated as a result of the gearbox and the generator, which may generate tones and low frequency noise. The solution to the mechanical noise is using a gearless wind turbine. On the other hand, aerodynamic noise of the blade is considered as the dominant noise source. The aerodynamic noise sources are: blade tip noise, leading edge interaction noise, and trailing edge self-noise.

Another type of the airfoil self-noise mechanisms is related to the bluntness-induced tonal noise, which is generated as a result of the bluntness at trailing edge. This type of blunt trailing edge can also be found in the wind turbine industry commonly known as "Flat-back" airfoil [Van Dam et al. (2010)]. The tonal noise is generated because of the vortex shedding from a blunt trailing edge and it can be eliminated by designing blades with sharp trailing edge. The difficulty and the high cost of making sharp trailing edge have encouraged the wind turbine designers to modify the blade shape. As a result new blade design that has a blunt trailing edge has been tried out. The advantages are: structural improvement and increase the moment of inertia, improve sectional lift coefficient, and reduces sensitivity to leading edge contamination. However, it has several drawbacks such as, the increase of base drag, high abrupt stall due to the

high sectional lift, and increased noise level due to the vortex shedding. In this thesis, results on the investigation of the vortex shedding control using the DBD plasma actuators can also have a positive impact on the wind turbine not only in terms of the aerodynamic performance, but also the elimination of the tonal noise component produced by the wind turbine blades with blunt trailing edge.

1.5 Thesis Structure

The aim of the current study is to control vortex shedding noise using aerodynamic plasma actuator, also known as Dielectric Barrier Discharge Plasma actuators (DBD). In this thesis, the vortex shedding tonal noise from blunt trailing edge flat plate, an airfoil (NACA 0012) with serrated trailing edge, and wake interaction broadband noise of two cylinders in tandem configuration will be investigated. The thesis is composed of six chapters including this introductory chapter. The second chapter looks at the definition of vortex shedding problem, the aerodynamic bodies that this physical phenomenon associated with, and a review on the recent passive and active control techniques used to tackle this problem. The experimental setup, test models, plasma actuator configurations, measurement techniques are presented in **Chapter 3**. **Chapter 4** is devoted to the acoustic and flow measurement findings of the effect of different plasma actuator configurations on the bluntness induced vortex shedding tonal noise radiation from flat plate with blunt trailing edge and NACA 0012 airfoil with cut-in serrated trailing edge. In this chapter, the flow structure in the near wake region is investigated in details using three different measurement means; hot-wire anemometry, Pitot tube, and 2D PIV system. Both noise and hydrodynamic filed measurement results of single cylinder and two cylinders in tandem configuration are presented in **Chapter 5**. Finally, a summary and discussion of this study's findings and conclusions will be provided in **Chapter 6**. Areas of further research and future work will also be given.

1.6 Research Contribution

The main points of research contribution are as follow:

- Extensive study on bluntness-induced vortex shedding tonal noise for a flat plate with blunt trailing edge using three different plasma actuator configurations. Study the effect of a sinusoidal DBD plasma actuator on the bluntness-Induced vortex shedding noise for NACA0012 airfoil with cut-in type serration and blunt trailing edges. Investigate the flow mechanism related to vortex shedding using both hot wire and PIV system for the blunt trailing edge flat plate at $U = 7.5\text{ms}^{-1}$ which corresponds to a Reynolds number of $Re_C = 0.75 \times 10^5$. (Chapter 4)

- Extensive noise measurement for vortex shedding-induced narrowband tonal noise of single circular cylinder. Study the flow mechanism of the tonal noise reduction using both hot wire and PIV system. (Chapter 5)

- Noise measurement of turbulent broadband noise by the fluid-structure interaction between tandem cylinders at $Re_D = 1.1 \times 10^4$ using three different plasma actuator combinations. Investigate the flow mechanism related to the interaction broadband noise radiation from the tandem cylinder using hot wire and PIV system. (Chapter 5)

Chapter 2

Literature Review

2.1 Introduction

Because of the sustainable growth of the aviation industry, and the sharp increase in the number of passengers flying by air in the last few decades, people's awareness of noise, especially those who live in close proximity to the airports, has propelled the need to reduce aircraft noise. Aircraft noise sources can be mainly divided in to two prominent noise sources, namely the jet and airframe noise. Since the introduction of the turbofan engines in the 1970's and the use of the high bypass ducts and serrated nozzle, airframe noise has become the main noise source, especially during landing phase when both high lift devices and the landing gears are deployed and the engines operate at low power.

2.2 Lighthill Analogy

Due to the growing growth in air traffic in the recent years, noise level has become an important issue for urban communities. It was Lighthill (1952, 1954) who developed the theory of aerodynamic sound in which he successfully identified the source of the sound wave for the first time. In his theory, the turbulent region in a fluid motion is considered as an acoustic source that drives the surrounding fluid. Lighthill analogy is unique because it correctly couples the acoustic wave motion outside and inside the turbulent region. His analogy is based on Navier-Stockes and continuity equations, from which an inhomogeneous wave equation can be derived and has the following form:

$$\frac{\partial^2 \rho'}{\partial t^2} - c_\infty^2 \frac{\partial^2 \rho'}{\partial x_i^2} = \frac{\partial^2}{\partial x_i \partial x_i} T_{ij} \tag{2.1}$$

Where ρ' is the density perturbation relative to the surrounding medium, c_∞ is the speed of sound of free stream flow, and T_{ij} is Lighthill's stress tensor which can be expressed as:

$$T_{ij} = \rho v_i v_j + (p - p_\infty) - \rho' c_\infty^2 \delta_{ij} - \sigma_{ij} \tag{2.2}$$

Where v_i, v_j are velocity components, $\rho v_i v_j$ is the Reynolds stress, which describes the turbulence in the source region, δ_{ij} is the kronecker delta, and σ_{ij} is the viscous stress tensor. The left hand side of the equation represents the propagation of an acoustic wave, while the right side is the source term, which contains the effects that generate acoustic waves. For fluid flow outside the turbulent region, the Lighthill's stress tensor $T_{ij} = 0$, thus Eq. (2.2) is reduces to the linear acoustic wave equation.

When the acoustic wave propagates through the non-uniform flow to the far field acoustic region, the acoustic waves bend as they propagate. Therefore, for a sound wave propagating in a uniform flow, the Lighthill equation can be re-written as follows:

$$\frac{\partial \rho'}{\partial t} + U_j^\infty \frac{\partial \rho'}{\partial x_j} - c_\infty^2 \frac{\partial^2 \rho'}{\partial x_i^2} = \frac{\partial^2}{\partial x_i \partial x_j} \left(\rho\, w_i w_j + p_{ij} - \rho'\, c_\infty^2\, \delta_{ij} \right) \tag{2.3}$$

The solution to the exact equation in terms of the density perturbation ρ' can be described by the following equation:

$$\rho'(x,t)c_\infty^2 = \int_{-T}^{T} \int \left(\rho'(y,\tau)c_\infty^2 \frac{\partial G}{\partial y_i} - G \frac{\partial(\rho'(y,\tau)c_\infty^2)}{\partial y_i} \right) n_i\; dS(y)d\tau$$

$$+ \int_{-T}^{T} \int G\left(\frac{\partial^2 T_{ij}(y,\tau)}{\partial y_i \partial y_j} \right) dV(y)d\tau \tag{2.4}$$

where G is the green function. From the above equation it can be concluded that in a non-uniform region in a free space the generated sound is quadrupole sound. Therefore for a known flow, it is possible to evaluate the sound using Eq. (2.4).

Lighthill found that if cold subsonic jet is dimensionally analyzed, the mean squared value of the radiated sound is proportional to the eighth power of the jet velocity and can be described by the following equation:

$$\overline{\rho'^2} \sim \rho_o^2\, M^8\, \frac{D^2}{|x|^2} \qquad \text{for } M < 1 \tag{2.5}$$

The above analysis describes the sound radiated from a free jet introduced into still region or for a region where, the effect of solid boundaries is neglected. However, the importance of the solid boundaries role in sound generation is pointed out by Lighthill. Lighthill's concept was extended

by Curle and Doak to include the effect of the presence of solid surfaces in a turbulent flow. Curle (1955) showed that when a solid surface is present in the flow with low Mach number (*M*), the sound field is generated by a single dipole, which represents the fluctuating forces exerted by the solid surface on the flow. This dipole sound can be estimated as follows:

$$\overline{\rho'^2} \sim \rho_o^2\, M^6\, \frac{D^2}{r^2} \qquad\qquad \text{for } M < 1, \tag{2.6}$$

Where *D,* is the characteristic length of the solid surface.

Up to now, a description to the Lighthill's inhomogeneous wave equation that describes sound generation in high turbulent flow region in the absence of solid surfaces and Curle's general effect of stationary surfaces were given. Williams and Hawkings (1969) extended Lighthill's inhomogeneous wave equation to include the effect of moving surfaces that appears on the right hand side of following equation:

$$\frac{\partial^2(\rho' H_s)}{\partial t^2} - c_\infty^2 \frac{\partial^2(\rho' H_s)}{\partial x_i^2} = \frac{\partial^2\left(T_{ij} H_s\right)}{\partial x_i \partial x_j} - \frac{\partial}{\partial x_i}\left(\left(\rho v_i(v_j - V_j) + p_{ij}\right)n_i \delta(f)|\nabla f|\right)$$

$$+ \frac{\partial}{\partial t}\left(\left(\rho v_j - \rho' V_j\right)n_j \delta(f)|\nabla f|\right) \tag{2.7}$$

The above equation is the general form of Ffowcs Williams and Hawkings equation which can be solved using the Green's function method.

2.3 Airframe Noise

As jet noise has been significantly reduced, airframe noise has received a lot of attention in the last few decades. Airframe noise was firstly identified in the 1970s'. The early airframe noise studies focused on the noise level and sources through aircraft flyover noise measurements, [Gibson (1972)]. Airframe noise sources generally include wing trailing edge, flaps and slats edge, landing gear, cavities and spoilers. Early studies showed that aircraft's airframe noise level in landing approach phase was about 10 dB higher than that during cruise phase [Dobrzynski and Buchholz (1997)]. Wing trailing edge, landing gear has been considered as the major source of airframe noise among the other noise sources. Airfoil self-noise (bluntness-induced noise) and landing gear noise are the focus of the current study.

2.3.1 Airfoil Self-Noise

Airfoil self-noise (trailing edge noise) can be defined as the noise that is generated due to the interaction between the solid surface of the airfoil and the turbulence generated within its boundary layer and the near wake [Brooks et al. (1989)]. Through an extensive experimental study on airfoil self-noise, Brook et al. (1989) proposed five different mechanisms of airfoil-self noise:

a) **Laminar boundary layer –vortex shedding noise** (Fig. 2.1a). This noise mechanism occurs as a result of the convection of the turbulent boundary layer past the airfoil trailing edge at high Reynolds numbers. As the turbulent boundary layer has turbulent eddies of different sizes and intensity, the interaction of these turbulent eddies with the sharp trailing edge of the airfoil will cause the generation of trailing edge noise of broadband nature.

b) **Turbulent boundary layer - trailing edge noise** (Fig. 2.1b) takes place as a result of the vortex shedding that is generated due to the instabilities, Tolmien-Schlichting (T-S waves), within the laminar boundary layer at low Reynolds numbers. This type of noise has a narrowband tonal nature and it is been believed that the T-S waves may not be the only mechanism behind the noise. The existence of a laminar separation bubble which amplifies the T-S waves near the trailing edge.

c) **Blunt trailing edges-vortex shedding noise** (Fig. 2.1c) occurs as a result of flow separation at the sharp corners of blunt trailing edges of bluff body. The roll up of the separated shear layer will cause vortex shedding. The generated noise has a nature of distinct narrowband tonal peak noise. Tonal noise intensity depends on the bluntness factor, which can be defined as the ratio between the thickness of the blunt edge to boundary layer displacement thickness (δ^*) at the trailing edge. It is found that bluntness trailing edge noise occurs for bluntness factors, higher than 0.3, which is considered a typical value that distinguishes between the flow of sharp and blunt trailing edges, Blake (1986). The frequency of the vortex shedding was measured for the first time by Roshko (1955). The shedding frequency can be represented by a dimensionless number, Strouhal Number as follows:

$$St = fH/U \hspace{8cm} (2.8)$$

Where f is vortex shedding frequency, H is the thickness of the blunt edge, and U is the free stream velocity. The control of bluntness tonal noise associated with vortex shedding from profiled bluff body (Blunt trailing edge flat plate) will be investigated in the present study using active control techniques. Vortex shedding Principle will be further investigated in section 2.4.

d) **Flow separation – Stall noise** (Fig. 2.1d2) takes place due to the large scale separation near the airfoil trailing edge at high angles of attack. This results in radiation of low frequency noise that is similar to that of bluff body. Peterson et al. (1975) identified to noise sources for light and deep stall. For light stall a tonal noise would generate from the trailing edge, whereas for deep tall a broadband noise would originate from the chord as whole.

e) **Tip vortex noise** (Fig. 2.1e) is generated due to the local separation which results in vortex formation with thick viscous and highly turbulent core. The mechanism of the generated noise is believed to be the turbulence convection in the vicinity of the trailing edge of the airfoil tip region.

2.3.2 Landing Gear Noise

Landing gear noise has been considered as one of the major airframe noise sources for large commercial aircrafts and has the same importance as high lift devices for single aisle and regional aircrafts [Dobrzynski (2010)]. In order to quantify the characteristics of landing gear noise, general scaled landing gear models were experimentally tested. Due to the lack of details in the design of the landing gears, these wind tunnel tests provided inaccurate results that showed that landing gear noise is a low frequency phenomenon. It was until 1990's; these misleading results were realized due to the existence of large high quality acoustic wind tunnels. Full scale landing gears were tested and the results confirmed the importance of landing gear noise which has levels occurs between 0.3 to 3 kHz, which represents the most sensitive range of human noise perception. It has been shown that the aerodynamic noise radiated from landing gears is of broadband nature. As landing gears are composed of different bluff body structures, the broadband noise source is generated as a result of the turbulent flow separation off these structures and the interaction of the generated turbulent wake with downstream elements.

Because of the interaction of the highly turbulent wake with solid surface, part of the turbulence energy will be converted in to propagating sound pressure waves. In addition to the broadband noise, narrow band components are seen as a result of the periodic coherent vortex shedding from the smooth circular cross sections struts at low Reynolds numbers.

Since landing gears has broadband noise nature, circular cylinders (single and tandem) can be considered a generic bluff body geometry that resembles landing gear strut in many of the essential aspects of noise generation process. Therefore, both single and tandem cylinder configuration noise control will be examined in the present study.
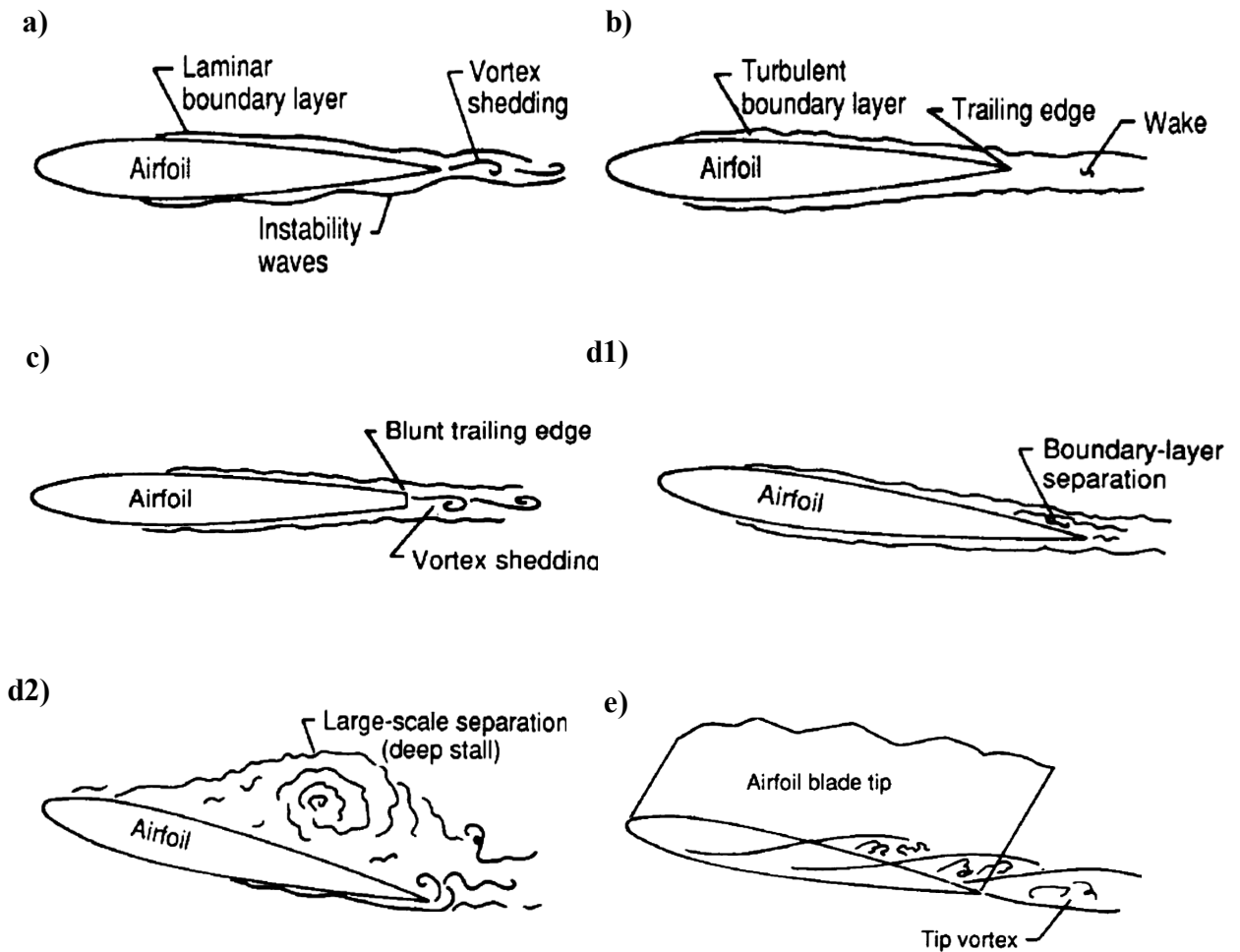
Figure 2.1 Airfoil self-noise mechanisms identified by Brooks et al.(1989), a) Laminar boundary layer noise, b) Turbulent Boundary layer-Trailing edge noise, c) Trailing edge-Bluntness noise vortex shedding noise, d 1-2) Separation-stall noise, e) Tip vortex noise.

2.4 Vortex Shedding Phenomenon

Vortex shedding is a physical phenomenon which can be observed in the wake of bluff bodies such as, circular cylinders, airfoil with blunt trailing edge, and a sphere, Fig. 2.2. It is known as Karman Vortex Street because it was Von Karman, who described this phenomenon for the first time [Von Karman, (2004)].
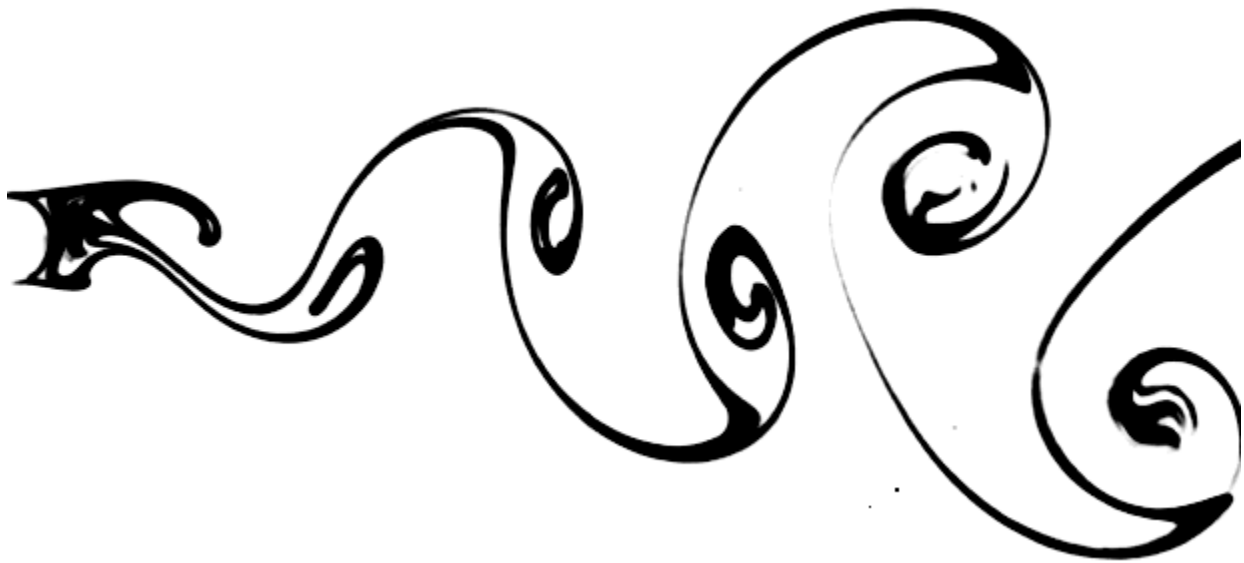
Figure 2.2 Vortex shedding from cylinder. [Von, (2004)]

Vortex shedding occurs in the wake region behind a bluff body, when the flow is unable to follow the shape of the body. As a result flow separates from the body and two regions of high shear, free shear layers, will be developed from both the upper and the lower sides. When kelvin-Helmholtz instabilities are big enough, the elongated shear layer will roll up into vortex of negative vorticity for the upper shear layer and positive vorticity for the lower shear layer. Then, pressure gradient will lead to the deflection of the developed vortex towards the wake centerline. Due to the exchange of energy between the upper and lower high shear regions, one forming structure will be separated and grow in size but decrease in strength as it convects further in the wake [Benard and Moreau, (2012)]. The process repeats itself and eventually evolves into Vortex Street.

The shedding of large coherent vortex structures within the wake region results in pressure fluctuations in the wake. These pressure fluctuations are the cause of several engineering problems. For instance, structural failure may occur when the shedding frequency is close to the natural frequency of the body. A second consequence associated with the shedding is acoustics noise emissions. This noise occurs as a result of pressure fluctuations and has two components tonal and broadband noise. The narrow band tonal noise is related to the shedding of large scale coherent vortices that shed in the wake of blunt trailing edge body/cylinder. On the other hand, the broadband noise is due the interaction of the unsteady wake with solid surfaces such as, flow between two cylinders in tandem configuration, which is generic geometry that resembles aircraft landing gear noise.

2.5 Vortex Shedding Regimes of Circular Cylinder

Fluid flow over cylinder can be characterized using a non-dimensional number called Reynolds number, which can be defined as follows:

$$Re_D = \frac{\rho U_\infty D}{\mu}$$

(2.9)

Where ρ is the fluid density, $U\infty$ is the free stream velocity, D is the cylinder diameter, and μ is the dynamic viscosity. An extensive overview of circular cylinder's vortex shedding regimes was given by Williamson (1996). Vortex shedding regimes can be described as follows:

- **Laminar steady regime, *Re* < 49**

  This regime is characterized by a pair of symmetrical vortices placed on each side of the wake. The separated shear layers meet behind the cylinder and forms free stagnation point. As Reynolds number increases, wake length behind the cylinder increases as well.

- **Vortex shedding, 49 < *Re* < 194**

  The flow behind the cylinder in this region is composed of alternating vortices that shed periodically. A critical Reynolds number of 49 at which the vortex shedding starts was defined by Roshko (1954). The wake over this region is completely periodic and the vortex shedding parallel to cylinder center.

- **Wake interaction regime, *Re* (190 to 260)**

  In the flow regime a transition to turbulence occurs in the wake. This region has two types of discontinuities which start as a Strouhal number when Reynolds number increases. In the first discontinuity, the beginning of vortex loop and the formation of streamwise vortex pairs were observed at *Re* = 194 due to the deformation of the primary vortices. On the other hand, shedding of small scale streamwise vortices and large intermittent low frequency wake velocity fluctuation were reported at *Re* = 250. At Reynolds numbers higher than 260, the Reynolds stresses get to it highest value in the near wake region.

- **Shear layer transition region, *Re* (10^3 to $2\text{x}10^5$)**

  Due to the growth of the separated shear layers from the sides of the cylinder as Reynolds number increases, a decrease in Strouhal number, increase in the shear stresses, and a decrease in the formation length observed.

2.6 Aerodynamic Bodies Subjected to Vortex Shedding

Many researchers have been investigating vortex shedding phenomenon since the middle of the 20th century, because of its relation to large number of aerodynamic applications, and the associated issues. Several bluff body geometries have been investigated. These can be divided into two groups; fixed separation point bodies (bodies with blunt trailing edge) and bodies with natural separation point such as, cylinders.

An example of aerodynamic bodies that is related to vortex shedding problem is wind turbine blade with blunt/truncated trailing edge. Wind turbine industry has witnessed great growth as it represents the future of green energy. Power output of wind turbines can be increased using larger wind turbine blade as they help increasing the disk area swept by the blade [Standish and van Dam, (2003)]. The problem associated with large blades is the increase in aerodynamic loading. In order to enhance the aerodynamic characteristics and structural strength of wind turbine blades which have thick airfoil sections, blunt trailing edge airfoils have been investigated by many researchers. Blunt trailing edge can be formed either by cutting a certain

amount of the rear part of the airfoil or by symmetrically adding the thickness to either side of the camber line as can be seen in Fig. 2.3 [Standish and van Dam, (2003)]. The second modification method is preferred as it allows a consistent comparison of the aerodynamic characteristics of the resulted airfoils. Although both designs show a huge increase in lift coefficient, flow separation from the blunt edge leads to vortex shedding, which in turn increases the base drag and scatters noise. In the current work, the first modification is used because the current investigation focuses on studying the effect of the DBD plasma actuator on the vortex shedding generated from the blunt trailing edge. It is worth noting that the effect of the bluntness on the aerodynamic characteristics of the airfoil is beyond the scope of the current work.
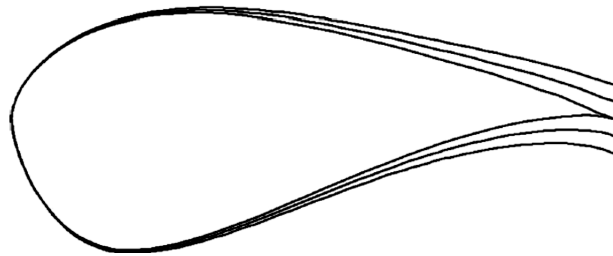
Figure 2.3 Blunt trailing edge airfoil. [Standish and van Dam, (2003)]

In the late 1980's, Ver (1987) used trailing edge serration for the first time on the exhaust of a jet engine to reduce jet noise. The results showed that the serration can reduce jet noise by 5 dB. It was Howe (1991), who derived an analytical model for the first time to predict the effect of serration on trailing edge noise of a flat plate. The results showed that optimal noise attenuation of 8 dB can be achieved using serrations with edges inclined at less than 45° to the mean flow. In many cases serrations are cut into flat plate, which are then inserted into the trailing edge of the main airfoil body. Although serrated flat plate inserts can be easily manufactured, they do not have strength or integrity especially when operated under high loading condition [Vathylakis and Chong, (2015)].

Another type of serration that is resulted from direct cut into the trailing edge of the airfoil main body has been investigated. Chong et al. (2013) investigated different trailing edge cut-in serration geometries, as shown in Fig. 2.4 a. They reported that the cut-in serration can

successfully reduce the trailing edge broadband noise but at the same time it produces tonal noise, which is due to the vortex shedding generation form the bluntness that is resulted from the cut-in serration. Fig. 2.4 b shows a comparison between the sound power level spectra of the airfoil with sharp trailing edge (S0) and different serrated trailing edge geometries (S1, S2, S3 and S2*). The solid black line represents the airfoil with sharp trailing edge. In the current work, the effect of a new DBD plasma actuator design on the bluntness-induced noise from cut-in type serration will be investigated.

a)   b)
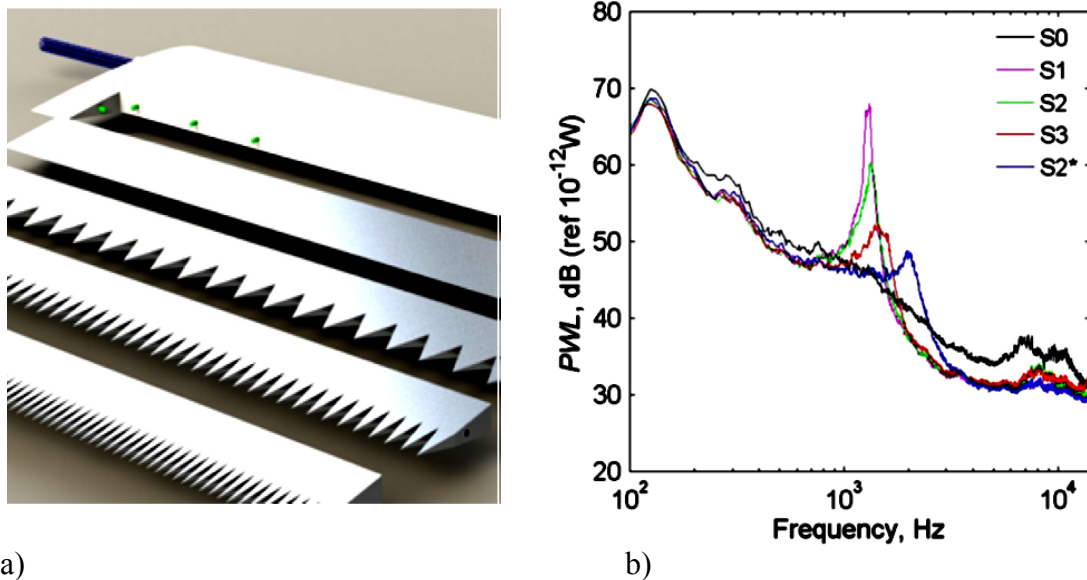
Figure 2.4 a) Trailing edge serration and b) Comparison between sound power level spectra of sharp and serrated Trailing edge airfoil at U=54ms^{-1}. [Chong et al. (2013)]

Aircraft landing gear represents one of the main airframe noise sources during approach. As the landing gears have the characteristics of bluff body, the generated noise is mainly due to the unsteady wake separation and the associated large scale periodic vortex shedding, which interacts with other downstream elements. In spite of the fact the landing gear noise is found to be broadband in nature, a clear tonal noise can be observed as a result of the vortex shedding from landing gear struts of circular cross sections. Circular cylinders have been used as a simplified aerodynamic body, which shares some of the flow characteristics in landing gear case. The flow structure over circular cylinder has been studied extensively due to its importance in many of the engineering applications. Different passive and active flow control techniques have

implemented to control flow separation, vortex shedding, and vibration over circular cylinders. The classification of flow separation control techniques will be given in the next section.

2.7 Classification of Flow Separation Control

Flow control can be defined as a way to alter flow characteristics by either modifying geometry or by direct deposition of energy into the flow. For aerodynamic applications, flow control is of immense importance as it can enhance the aerodynamic performance. Flow control methods are usually used to manipulate different physical phenomena such as separation delay, increase lift, drag reduction, mixing enhancement, turbulence reduction and aerodynamic noise reduction. For aerospace industry flow control is of great importance as it results in modifying aircraft design to be able to land and take-off with lower velocities, produce less noise, and reduce fuel consumption.

It was Prandtl (1904), who found boundary layer theory, defined the separation and implemented active flow control for the first time using suction to delay separation from the surface of circular cylinder and diffuser [Schlichting et al. (1955)].

Flow control techniques can be divided into two categories: Passive flow control (PFC) and active flow control (AFC). In general, PFC techniques require no input energy and can be achieved by modification of already existing geometries. On the other hand, AFC techniques require external power source, such as blowing, suction, flaps and slats.

2.7.1 Passive Flow Control (PFC)

PFC can be defined as a way to modify flow characteristics by changing /adding parts to the already existing body geometry. Unlike AFC techniques, PFC methods require no external source of energy, more effective, and are less expensive than AFC methods. One major drawback of the PFC methods is that they could increase drag due to their existence at different flight conditions [Nati et al. (2013)]. Different flow phenomena has been treated by PFC techniques such as, drag reduction, lift augmentation, separation control, bluff body vortex shedding. Several vortex shedding PFC techniques have been investigated. An extensive review on bluff body vortex shedding PFC techniques was provided by Choi et al. (2008). In this study, the control techniques were classified into two categories; a) two dimensional versus the three

dimensional forcing, which can be further divided into boundary layer versus wake control techniques. Zdravkovich (1981) reported that helical strake can successfully reduce fluctuations in the wake region. A significant drag reduction from blunt trailing edge body using slotted trailing edge was achieved by Petrusma and Gai (1994). Tombazis & Bearman (1997) studied the effect of the wavy base on the wake of blunt trailing edge D-shape body. In this study, waviness leads to recovery of base pressure due to vortex dislocation in the wake. Many other PFC techniques have been tested such as, Splitter plate, wavy cylinder, surface protrusions, and small control cylinders. Fig. 2.5 demonstrates some of the PFC techniques that are used for flow control over two dimensional bluff bodies.
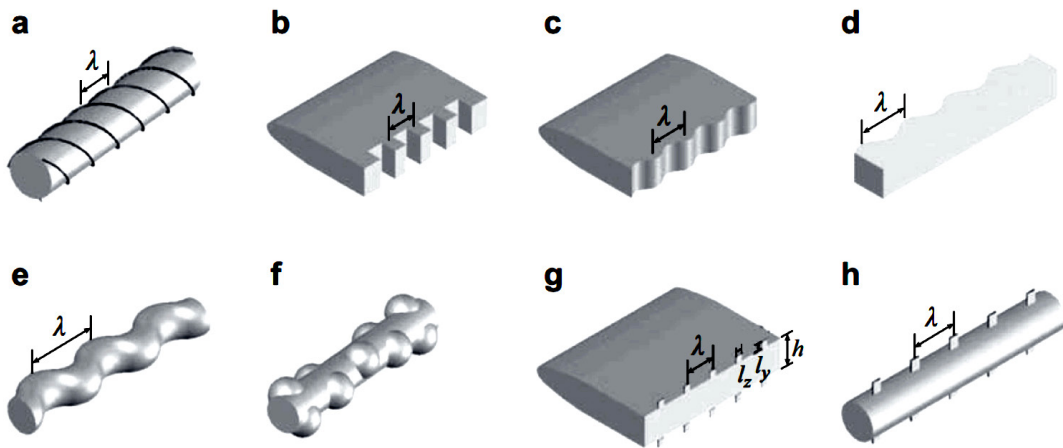
Figure 2.5 Passive Techniques foe vortex shedding control, a) circular cylinder with helical element and b) D-Profile with slotted Trailing edge, c) D-Profile with Wavy Trailing edge, d) square cylinder with wavy leading edge, e) sinusoidal circular cylinder, f)Bumps, g) and h) small surface protrusions. [Choi et al. (2008)]

Flow separation and vortex shedding control can be successfully achieved by using a splitter plates downstream the wake region of bluff body. Several studies have been utilized the splitter plates to suppress the interaction between the separated shear layers from the upper and lower sides of both flat plate and circular cylinder.

 Roshko (1954) used a splitter plate in the wake region of a circular cylinder in order to prevent the interaction between the separated shear layers. The experiments were conducted at Reynolds number of $Re = 14500$. The results showed that using a splitter plate with 5 diameters length attached to the cylinder can decrease the mean drag by 37%. For a plate length of 1.14D and

various gap lengths between the cylinder and the plate the results showed that base pressure coefficient increases as the gap length increases.

Bearman (1965) study the effect of different plate lengths on the wake region of profiled body at Re = 2.56 x 10^5. Based on the length of the splitter plate, he identified various flow regimes in the wake region behind the blunt base. For the baseline case, the results showed that a peak of the unsteady velocity occurs at a distance equal to one base eight from the blunt trailing edge of the plate. The position of the maximum value of the unsteady velocity is referred to as the position where the vortices are fully formed. When the splitter plate is attached to the base of the plate, the position of the peak is proportional to the splitter plate length. When no splitter plate is attached, the vortex forms just after the base of the flat plate. However, the introduction of the splitter plate leads to growth of the recirculating region in the downstream direction as the splitter plate extends downstream.

Apelt et al. (1973) conducted an experiment to understand the effect of different splitter plate lengths on the wake region of a circular cylinder. The tests were conducted at Reynolds numbers $10^4 < Re < 5$ x 10^4. The results showed that short splitter plates reduce the drag coefficient by stabilizing the separation point and reduces the wake width compared to baseline case, while long plates lead to inhibition of the interaction between the separated shear layers. In addition, they reported that as the plate length increases the vortex forms further downstream the back of the cylinder.

Extending their previous work in 1973, Apelt and West (1975) investigated the effect of long splitter plates on the wake region of circular cylinder and vertical flat plate. The tests were conducted at subcritical Reynolds numbers between 10^4 and 5 x 10^4. The results showed that short splitter plates significantly modify the flow over both the flat plate and circular cylinder. Splitter plates with 5D length modifies both drag coefficient and vortex shedding of the circular cylinder. In addition, the results showed that increasing the length of the splitter plates leads to a reduction in the drag coefficient and vortex shedding frequency. Further increase in the splitter plate length results in no further increase in the drag reduction and elimination of the vortex shedding.

In an attempt to reproduce the effect of a splitter plate on vortex shedding in the wake region of a profiled body, Nakayama and Noda (2000) applied the LES technique to predict the separation and the reattachment of the flow over a flat plate with blunt trailing edge at Reynold number $Re = 2.56$ x 10^5. The results showed that LES model can successfully predict the separation and the reattachment of the vortices due to the existence of the splitter pate. The instantaneous vorticity of the flow without and with splitter plate is shown in Fig.2.6.

Hwang et al. (2003) numerically investigated the effect of detached splitter plate on the wake region of circular cylinder at low Reynolds numbers. The splitter plate has a length equal to the cylinder diameter. The results showed that when the splitter plate is positioned at an optimum position the vortex shedding is eliminated and the drag is significantly reduced. Placing the plate at a streamwise location greater than the optimum location leads to a sharp increase in the drag coefficient and the flow behind the cylinder looks similar to the no splitter plate case. Fig. 2.6 shows the time averaged stream lines for the unsteady flow at $Re = 100$.
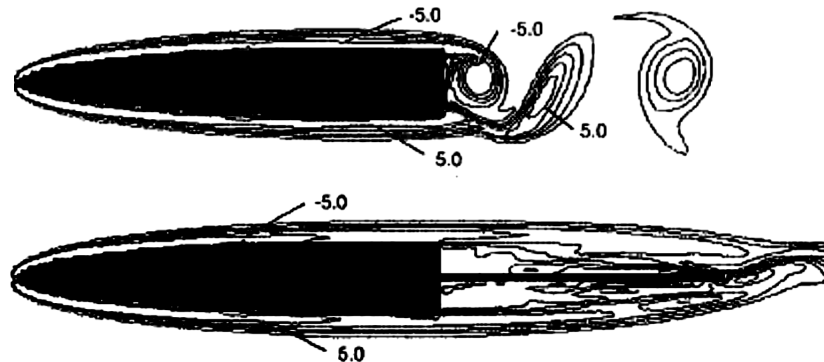
Figure 2.6 Instantaneous vorticity for a flat plate without splitter plate (top) and with a splitter at Re = 2.56 x 10^5. [Nakayama and Noda (2000)]

2.7.2 Active Flow Control (AFC)

Active flow control (AFC) techniques have received a lot of attention in the last few decades. The importance of these actuators comes as result of their effectiveness, flexibility and adaptiveness. Due to the difficulties associated with the design of AFC actuators, small number of AFC systems has been successfully transformed from laboratory scales to real world applications. An actuator can be defined as a device that produces steady or oscillatory

disturbances with or without imposing mass flux in to the flow. Good actuator can be defined as an actuator that is small in size to be integrated within the existing system, robust, and has wide working bandwidth [Cattafesta et al. (2011)]. There are many types of AFC actuators whose main design features depends on the system to be controlled. AFC actuators can be classified in to two main categories; the mechanical and fluidic actuators, as shown in Fig 2.7. On the one hand mechanical actuators involve moving internal or external parts that are able enhance the performance of the system by inducing local fluid motion. Kim et al. 2003 used surface mounted diaphragm to control separation on an airfoil, and Thill et al. (2008) review the use of morphing skins for flight performance enhancement. On the other hand, fluidic actuators main function is to inject or draw fluid in to the flow, such as zero net mass flux (ZNMF) synthetic jets, and steady or pulsed blowing/suction actuator. AFC Actuators can be further classified in to open loop (no feedback) sensors and closed loop and the application (high/low speed flows).
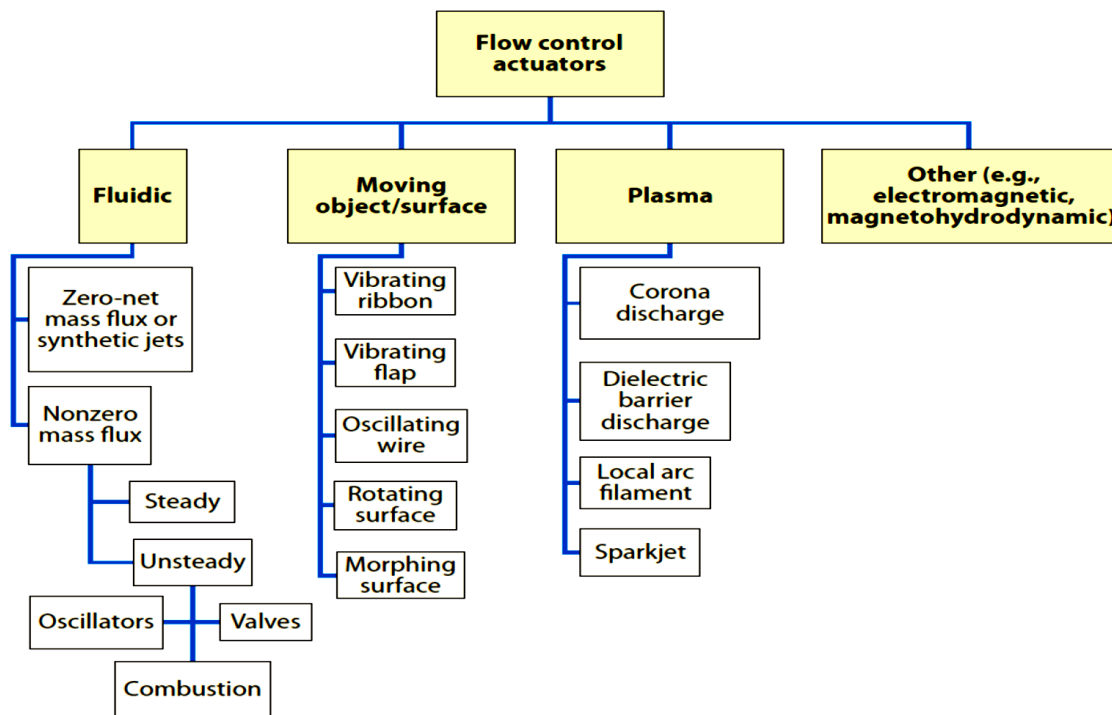
Figure 2.7 Classification of active flow control actuators. [Cattafesta et al. (2011)]

A relatively new type of AFC actuators that has recently gained a great amount of attention is plasma actuators because of their light weight, adaptability, and their fast response. The most popular form of plasma actuator designs is Dielectric Barrier Discharge plasma actuators (DBD).

Few other types of plasma actuators have been investigated such as plasma corona discharge, local arc filament, plasma spark jet actuators. The present study will focus on using the DBD plasma actuator as an active control technique.

2.8 Plasma Actuators

Plasma can be defined as the forth state of matter. In 1920's the term "Plasma" was firstly introduced by Irving Langmuir who initiated the study of ionized gasses [Chen, (2012)]. Plasma is formed because of atoms collision with each other, which results in electron release from the atomic nuclei, when enough energy is added to the gas. In the ionized gasses, it is the charge that separate between the ions and the electrons that cause the generation of an electric field, thus current and magnetic field is given rise by the flow of charged particles. Plasma has been used in different application such as, x-rays, etching and deposition in semi-conductor technology, and production of power from thermos nuclear fusion.

Plasma can be divided in to two different categories; thermal and non-thermal plasma. Thermal Plasma is normally associated with Joule heating and arc plasma discharge, which can be used in metal cutting, and welding spraying. On the other hand, non-thermal plasma or the so-called cold plasma the added energy is mainly heats up the electrons instead of the whole gas, therefore they can work at low pressure and temperature. Cold plasma can be used in many applications such as, etching and semi-conductor film deposition, surface cleaning, and recently used in active flow control [Guo et al. (2010)].

The implementation of plasma for flow control was firstly embarked in the 1950's, when a few number of patents were received in both Europe and the United States of America [Moreau (2007)]. It was until 1968 when Ketchman and Velkoff published the first paper on this subject. In their study, an electrical field was applied to manipulate the transition point on a flat plate. In 1978, Yabe et al. investigated the electro hydrodynamic force (EHD) wind generated between a wire and flat plate both theoretically and experimentally. The growth of this topic was really started in 1990's when two groups started working on using a dc corona discharge in both France and America. American group led by Roth successfully made plasma actuator that can work at atmospheric pressure and generates surface electric wind of several ms^{-1} [Moreau, (2007)]. This

actuator was the first (DBD), which is firstly called One Atmosphere Uniform Glow Discharge Plasma (OAUGDP).

2.9 Types of Plasma Actuators

Simplicity of Plasma actuator is one among few other factors that considerably encouraged the research on active flow control by plasma. Since the birth of plasma flow control, several types of plasma actuators were investigated. For example, cold plasma actuators, which include corona surface discharge and Surface dielectric barrier, discharge DBD. In addition, thermal plasma actuators like Plasma spark/Synthetic jet actuators have gained the interest of researchers in recent years because of its high speed jet that could be useful for both subsonic and supersonic flow applications.

2.9.1 DC Corona Discharge Plasma Actuators

Direct Current corona discharge plasma is the early form of cold plasma that has been investigated since the middle of the 20th century. This type of discharge appears at atmospheric pressure as weakly luminous discharge normally concentrates near sharp points when high voltage DC is applied between two electrodes apart from each other by few millimeters. The generated discharge polarity depends on the location of the electric field. For instance, if the generated electric field localizes near the anode, then the generated discharge is a positive corona discharge otherwise it is a negative corona discharge [Schutze et al. (1998)]. Fig. 2.8 demonstrates an example of point to surface corona discharge plasma.

The electric wind was firstly reported by Hauksbee 1709 and then explained by Faraday in 1838. The generated electric wind of corona discharge is due to two different phenomena. The first one states that the collisions between the ions, which are produced as result of the breakdown of gas molecule and the neutral particles in the electrodes gap is responsible for the electric wind generation [Schutze et al. (1998)] . The second one states that the wind is generated as result of streamer propagation not because of the ion drifting. Recently, Parks et al. (2018) reported that the electric wind is mainly due to the drift of the space charges, while the propagation of the plasma streamers has a negligible effect to the averaged Electro-Hydrodynamic Force (EHF).
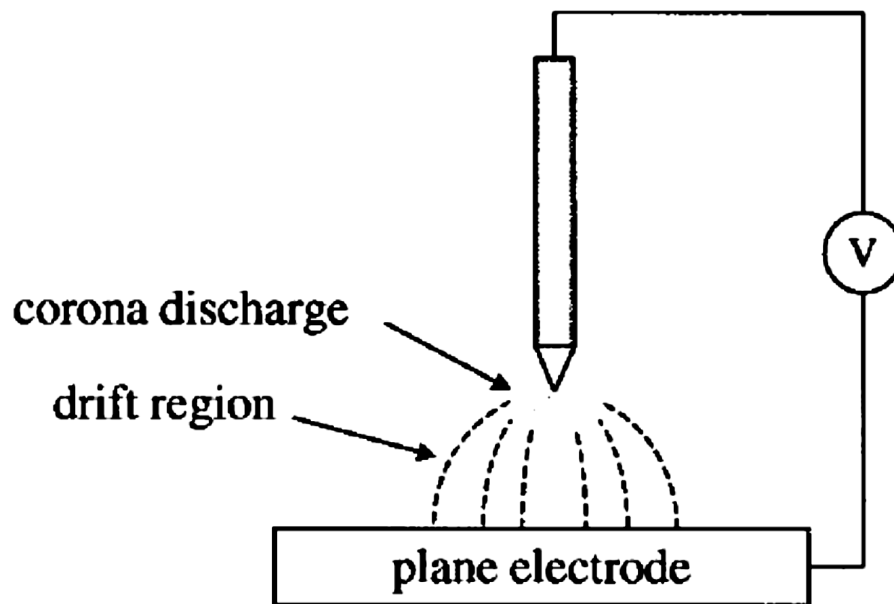
Figure 2.8 Schematic of point to plane corona discharge. [Schutze et al. (1998)]

The studies on the surface corona discharge can be classified in to two categories: Firstly, studies focus on the design of the actuator and its mechanical and electrical characteristics; secondly, works deal with the effect of the actuator discharge in airflow application. Several studies, which focus on the corona discharge electrical and mechanical characteristics, have been published since 1998 [Artana et al. (2002), Léger et al. (2002), Labergue et al. (2005), Louste et al. (2005), and Moreau et al. (2006)]. The characterization of these actuators is based on different geometrical and atmospheric parameters. Malik et al. (1983) first used DC corona discharge to manipulate the boundary layer over a flat plate. They reported that a 20% drag reduction can be achieved at free stream velocities up to 30 ms^{-1}. Leger et al. (2002) studied the effect of plasma corona discharge on the boundary layer over flat plate using two different electrode configurations, wire to wire and wire to plate electrodes. Their study revealed that both electrode geometry and air humidity play an important role in discharge characteristics. They found that the discharge becomes less stable when air relative humidity increases. Boundary layer control using DC corona discharge over a flat plate for low airflow velocities up to 25ms^{-1} was investigated by Moreau et al. (2006) and Moreau et al. (2005). Two wire configuration electrodes were mounted on the surface of flat plate made of PMMA. Their main observations were as follows: the generated electric wind near the wall depends highly on the discharge current and more stable discharge, no glow to arc transition, was obtained in the presence of

cross flow. Louste et al. (2005) tested the effect of using an insulated flat plate on the corona discharge stability. Their test proved the crucial role that the insulating plate played in the stability of the generated corona discharge.

In addition to DC high voltage, the effect of an AC corona discharge has been investigated by several researchers. The studies revealed that using AC Corona has no advantage over DC one, except that the AC discharge produced pulsed electric wind [Moreau et al. 2008)].

2.9.2 Dielectric Barrier Discharge Plasma Actuators (DBD)

Dielectric barrier discharge plasma actuator (DBD) is considered the most popular actuator, which has drawn the attention of many researchers since its perfection in 1995 by Roth's group. Unlike corona discharge actuators, DBD actuators cannot use DC high voltage because of the presence of the dielectric barrier in the gap between the electrodes, which stops the electric current and prevents sparks occurrence.

The standard design of DBD actuator is a single actuator, which is composed of two flat electrodes asymmetrically mounted on both sides of a dielectric plate. The upper electrode, the exposed electrode, is usually excited by an AC high voltage, while the lower one is usually grounded and encapsulated in order to prevent plasma generation on the both sides. When the applied voltage exceeds the breakdown voltage of the gas, ionization process starts. During ionization the gas molecules splits in to ions and electrons. It is the collision between the ions and the neutral particles that produce what is called electric wind [Kogelschatz, (2003), Moreau, (2013), Enloe et al. (2004), and Corke et al. (2008 and 2009)].

Different geometrical and electrical parameters affect the characteristics of the generated plasma, such as the width of the ground electrode, gap between the electrodes, excitation signal, applied voltage and the applied frequency. The standard design of the DBD actuator is shown in Fig. 2.9.

The physical explanation of the surface plasma generation was provided by Enloe et al. (2004). They found that the DBD plasma actuators are self-limiting because the charge is always opposing the applied voltage. They further explained that during the half cycle, for which the upper electrode is negative, electrons migrate towards the dielectric surface and the charge starts

to build up. On the other hand, the electrons move back towards the exposed electrode during the positive half cycle as shown in Fig. 2.10.
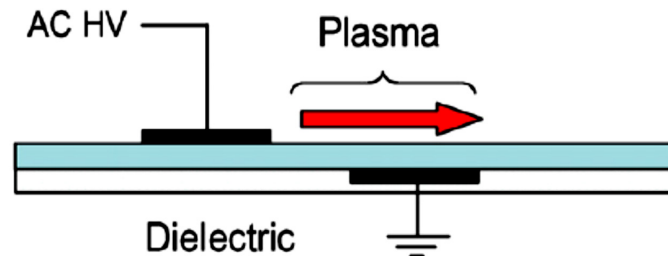
Figure 2.9 Standard dielectric barrier discharge DBD. [Enloe et al. (2004)]
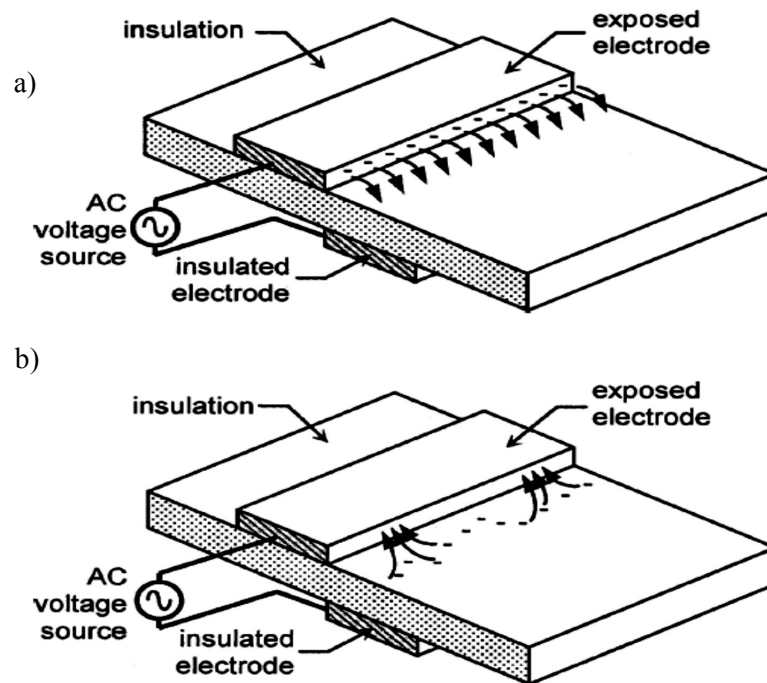
Figure 2.10 Self –limiting mechanism of DBD actuator, a) negative half cycle and b) positive   half cycle. [Enloe et al. (2004)]

The effect of number of electrical parameters has been investigated by many researchers in order to optimize the actuator design. The influence of supplied waveform on the electrical

characteristics of single DBD plasma actuator was investigated by Benard and Moreau (2012). Both sinusoidal and square waveforms with positive or negative ramps were examined. They observed that the sinusoidal waveform enhanced the velocity fluctuation. On the other hand, the mean generated electric wind and body force were higher when the square wave form was used.

To increase the induced electric wind by DBD plasma actuator, Forte et al. (2006) examined the effect of the gap between the exposed and the ground electrodes mounted on 2mm Plexiglas plate and the width of the ground electrode. The tested frequency and voltage 700 Hz and 20 kV respectively. They reported that, there is an optimum gap width of 5mm for their tested actuator and the maximum induced electric wind was 8 ms^{-1}. In addition, the wider the ground electrode is the larger plasma extension, which leads to increase the generated electric wind.

In an attempt to optimize the performance of DBD actuator, Thomas et al. (2009) investigated the effect of different parameters, such the amplitude of the applied voltage, the Frequency, ground electrode width, and the use of multiple actuators on the thrust generated by the DBD actuator. They showed that, using thicker dielectric material with lower dielectric constant impedes streamers formation because of the low current density near the dielectric surface. In addition, although the saturation of body force is higher at lowest tested frequency, lower applied voltage is needed to achieve certain body force at the same high frequency. Furthermore, optimum body force can be achieved using a saw tooth exposed electrode, and ground electrode of 50.4 mm width.

The influence of the active electrode shape on the mechanical performance of DBD plasma actuator was investigated by Hoskinson et al. (2009) and Hoskinson and Hershkowitz (2010). They examined both wire exposed electrodes of diameters ranging from 1mm to 0.13 μm and plane electrode. The results showed that using thin wire as an exposed electrode leads to an enhancement of the induced body force. They found that, unlike plate to plate configuration, fluid acceleration occurs on both positive and negative half cycles, when thin wire is used.

It has been shown that passive vortex generators are capable of delaying the T-S waves dominated laminar-turbulent transition on flat plate [Fransson et al. (2006) and Shahinfar et al. (2014)]. They found that the vortex generator can produce streamwise streaks that can effectively stabilize the unsteady perturbations. Plasma actuators can be a good candidate for this kind of

application because with plasma actuator both amplitude and the spatial extent can be adjusted Jukes and Choi (2012). Using streamwise oriented plasma actuators in order to produce spanwise forcing, Roth et al. (2000) demonstrated that this plasma actuator configuration can form unstable streamwise vortices. In addition, they found that as the input voltage increases, the vortices look more compact and develop faster.

Jukes and Choi (2012) investigated the use of dielectric barrier discharge plasma vortex generator actuators for flow control. Copper Strips were oriented in the streamwise direction with different yaw angles with respect to the incoming free jet. They found that this type of plasma actuators can successfully reduce the separation region. The maximum effect of plasma vortex generators is shown when the spanwise jet is perpendicular to the main flow direction.

Riherd and Roy (2013) investigated a new class of DBD plasma actuators that are known as serpentine DBD plasma actuator. Two flow features that have been previously reported both in quiescent [Durscher and Roy (2012), Wang et al. (2011)] and laminar boundary layer flow [Roy and Wang, (2008)] were reported. The first one is that this type of plasma actuators can produce a vectored jet comparable to the jet generated by plasma synthetic jet actuators [Santhanakrishnan and Jacob, (2007)]. The second is the counter rotating streamwise vortices that propagate downstream the actuator. In the current work a sine wave exposed actuator is used to control the vortex shedding noise of cut-in serration type airfoil trailing edge. Unlike plasma vortex generators, serpentine actuators generate a 3D flow which could be more effective for flow separation control.

Corke et al. (2010) investigated a three electrode DBD plasma actuator. His actuator design differ from that perfected by Moreau (2008) in that the ground electrode is used as exposed electrode and the high voltage exposed electrode is encapsulated as shown in Fig. 2.11. They demonstrated that, the plasma extended between the whole distance between the exposed electrode and the third one. In addition, the measured thrust is higher when the added electrode is connected to negative DC high voltage. Fig. 2.12 shows the tested actuator design and the measured thrust respectively.
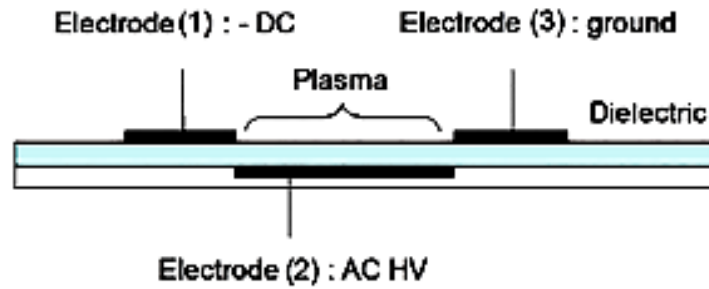
Figure 2.11 Schematic of slide discharge plasma actuator. [Corke et al. (2010)]
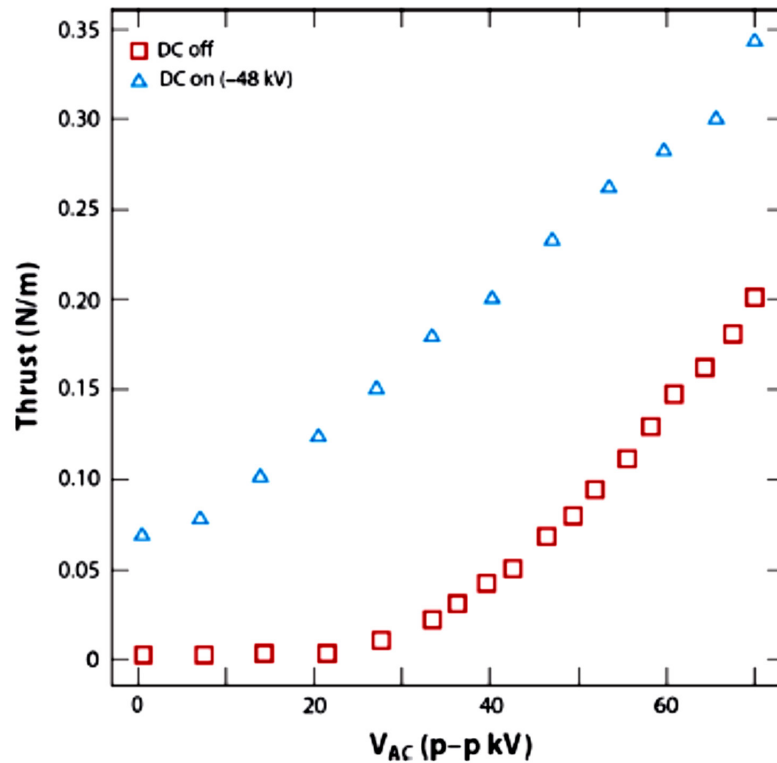
Figure 2.12 Thrust generated using plasma slide discharge. [Corke et al. (2010)]

2.9.3 Plasma Synthetic Jet Actuators (PSJA)

Same as the conventional single dielectric barrier discharge (SDBD), Plasma Synthetic Jet (PSJ) have been considered as one of the promising Active flow control techniques that can be useful for both subsonic and supersonic application. This actuator has no moving part and can produce

high speed pulse jet. The actuator was firstly perfected by a group from the Hopkins University lead by Grossman; they call it Plasma Spark Jet (PSJ) [Grossman et al. (2003)].

Similar to synthetic jet actuator, PSJ actuator is a solid state zero-net mass flux. It is composed of small chamber, electrodes and a jet orifice. PSJ cycle has three stages. The first stage, energy deposition stage, starts when a sufficiently high voltage is supplied to the electrodes and an arc is generated inside the cavity. This will lead to startup of the second stage when the gas inside the cavity electro thermally heats up which leads to rapid increase in air pressure. The high pressure air expels outside the cavity at high jet speed through the orifice. A partial vacuum is created inside the cavity after the initiation of the air jet, which causes the return of the air inside the cavity again and this is the end of the last stage, refresh stage, [Hopkins et al. (2013)]. Figure 2.12 shows the PSJ actuator cycle.
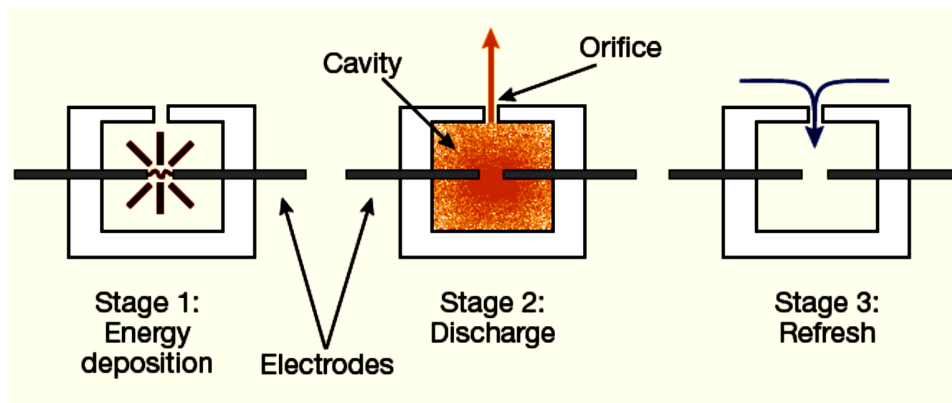
Figure 2.13 Plasma spark jet cycle. [Hopkins et al. (2013)]

Several experimental and theoretical have studied the effect of both the design of the power supply and different geometrical parameters on the actuator performance.

Zong et al. (2015) studied the effect of electrode distance, orifice diameter, and orifice height. They found that, for high jet velocity and longer jet duration the arc distance needs to be increased. The design of the orifice diameter depends on the controlled flow field. They noticed that strong perturbation with short duration jet is generated when small orifice diameter is used. While long lasting less intense jet is generated when small orifice diameter is used. The orifice height does not have big effect on the performance of the actuator.

The influence of energy dissipation in the discharge was investigated by Blinger et al. (2011). Both inductive and capacitive high voltage power supplies were designed in order to control the energy dissipation as can be seen in Fig 2.13. They reported that, using inductive power supply results in lower energy dissipation, relatively long discharge duration and lower jet velocity. On the other hand, capacitive one creates pulse spark and the energy is dissipated very quickly.

Seyhan et al. (2016) studied the effect of the duty cycle a novel spark plug plasma synthetic jet actuator. The tested actuator was spark plug covered by aluminum cap which has a cavity of 70 mm^3 and an orifice of 2 mm diameter. They reported that this actuator design generates a pulsed jet of 180 ms^{-1} at frequency of 100 Hz and 50% duty cycle.
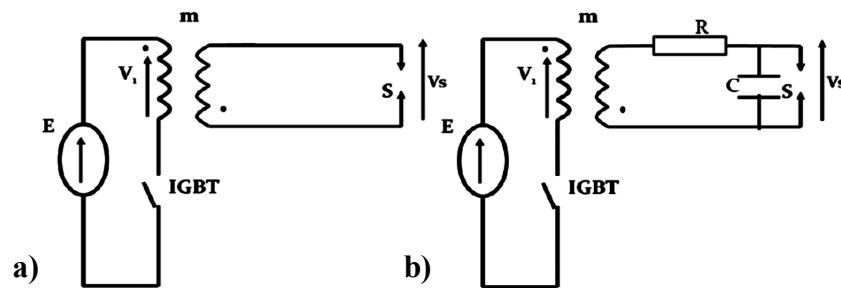
Figure 2.14 PSJ actuator a) Inductive and b) Capacitive power supplies. [Blinger et al. (2011)]

The development of the PSJ depends on two main issues. The first one is the efficiency of the actuator, which many researchers found to be low, needs to be addressed. This can be done be increasing the arc distance, which is found to be restricted by the input voltage. The second issue is the actuator limited affected region due to its size. In order to solve these problems a PSJ array is needed in order to implement the actuator in the practical applications. The use of conventional PSJ actuator circuit will not be efficient for an array of actuators, because most of the circuit energy is wasted in the current limiting resistor. In addition, it is difficult to use one power supply to drive the actuator array due to the negative resistance of the arc discharge channel.

In an attempt to solve the actuator array problem, Zhang et al. (2017) suggested a novel actuator circuit. The new circuit is similar to the traditional one except that the added relay circuit, which contains a capacitor and a resistor, connected in parallel as can be seen in Fig. 2.15. They reported that using this circuit results in operation of actuator array with only one power supply.
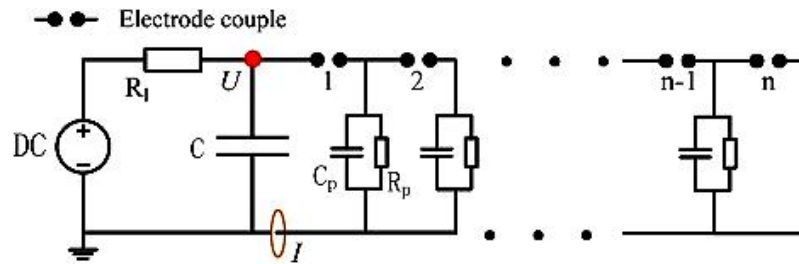
Figure 2.15 Multi-channel discharge circuit. [Zhang et al. (2017)]

2.10 Overview on Vortex Shedding Flow and Noise Control

Several studies have been published on vortex shedding control because of its association with many engineering applications. Different passive and active control techniques have been investigated to control vortex shedding behind two dimensional bluff bodies. A review on different active flow control techniques that has been implemented for vortex shedding and the associated noise control of two dimensional bluff bodies such as, circular cylinder and D-shape blunt trailing edge flat plate are presented in this section.

An early successful attempt to control flow separation was made by Prandtl in 1904. He noticed that the separation can be eliminated if the boundary layer is drawn out of near wall region. Active vortex shedding control methods can be divided into two categories:

- Direct wake modification.
- Vortex shedding suppression by controlling boundary layer separation.

Several active wake control techniques have been implemented to control the wake of bluff bodies by generation of secondary flow directly in the wake. For instance (steady suction and / blowing, Pulse jet, and Zero net mass flux (ZNMF) /synthetic jets.

According to Wood (1964), by introducing a secondary flow inside the wake region of blunt trailing edge profiled body, the profile drag is decreased and the strength of the Karman vortices is reduced. In addition, the onset of vortex formation occurs further downstream, when the injected air quantity is increased. Thus, the vortices are diffused before the formation of Karman Street.

Bearman (1967) examined the effect of base bleed on the flow over blunt trailing edge flat plate at free stream velocity of 25ms^{-1}. Base pressure, shedding frequency and hot wire measurement were conducted within the wake region. The results revealed that bleeding air in to the wake region can reduce the base drag to the third of its original value and the wake stabilizes.

Similar to the base bleed control mechanism, Castro (1971) used another approach, self-bleed mechanism, to control the flow in the wake behind perforated flat plat at Reynolds numbers ranging from 2.5 x 10^4 to 9 x 10^4. In this study, both drag and, vortex shedding frequency measurement were made and mean velocity, and turbulent intensity were measured using Hot-wire. The results of this study suggest that Karman vortex street dominates the wake region when a flat plate with law porosity is used. Furthermore, he noticed that increasing the size of the perforation leads to more air injection, which results in shifting the reverse flow region further downstream. These findings were confirmed by Inoue (1985), when he numerically simulated the same approach to control the wake of flat plate.

Using self-injection at the base of circular cylinder, Wong (1985) reported that the flow induced oscillations can be suppressed and the base pressure can be increased when base bleed is applied at the rear stagnation point of the cylinder. Two injection locations were investigated; the first one is at the rear stagnation point and the second one is positioned at an angle. From flow visualization tests, he observed that the mechanism of wake stabilization is the entrainment resulted from the backward movement of the fluid in the wake towards the separation region where it combines with shear layer.

El-Refaee (1994) investigated the effect of suction and blowing on boundary layer control of subcritical fluid over circular cylinder using boundary element method (BEM). The results showed that using a combination of steady/periodic suction and blowing system leads a substantial drag reduction. The most efficient system is found to be a sine function distribution of equal surface suction and blowing with suction discharge coefficient of 0.15.

Kim and Choi (2005) suggested a new approach to control vortex shedding from circular cylinder at low Reynolds numbers using distributed spanwise forcing. The forcing was provided on both upper and lower sides of the cylinder. Two phase differences were investigated; in phase and out of phase forcing. A wide range of Reynolds numbers were considered ranging from 40 to

3900. They reported that the in phase forcing is the most effective control method where a significant drag and lift fluctuation reduction were achieved for all the tested Reynolds numbers as can be seen in Fig. 2.16.

Kim et al. (2004) conducted both large eddy simulation (LES) and experimental investigation to study the effect of spanwise distributed forcing (suction and blowing) on the drag of a blunt trailing edge profiled body. Two spanwise forcing mechanisms were adapted in phase and out-of-phase. They measure the changes in the base pressure and drag at the trailing edge at low and high Reynolds numbers. They reported that, the results from the LES showed that using spanwise distributed forcing; a significant drag reduction and vortex shedding suppression are achieved. In addition, the results from both the experimental and the LES study showed that in-phase forcing is more effective than the out-of-phase one in terms of drag reduction. Fig 2.17 shows vortical structure from LES study of both in-phase and out-of-phase forcing

Henning and King (2005) investigated the use of alternating suction and blowing at the upper and lower edge of blunt trailing edge flat plate to reduce vortex shedding. The tests were carried out at free stream velocity of 9 ms^{-1}, thus the Reynolds number based on the plate height is equal to (4×10^4). The results revealed that the most effective actuation velocity was 0.3 of the free stream velocity. In addition, the vortex shedding is suppressed at scaled actuation frequency, $St_H = 0.17$. Although, the wake vortices were suppressed at this actuation frequency, the pressure fluctuation spectra showed the presence of new peaks at the actuation frequency and its harmonics.

Unlike continuous blowing and/ suction control technique, Synthetic jet provides pulsed jet of zero net mass flux into the controlled domain. Because of its ability to modify the surface shape and thus the surface pressure with a significant effect on flow separation, Amitay et al. (1997) performed one of the earliest steadies in the effect of fluidic actuator based on the synthetic jet principle on the flow separation over a circular cylinder. Two adjacent jet slots were flash mounted on the surface of circular cylinder, which can be rotated to adjust the angle between the jet and the free stream. They observed that, a closed recirculation region is formed when the synthetic is positioned at the front stagnation point and a displacement of the stream lines. When the synthetic jet was positioned at the rear stagnation point, the deficit region behind the cylinder become smaller and the separation was delayed.
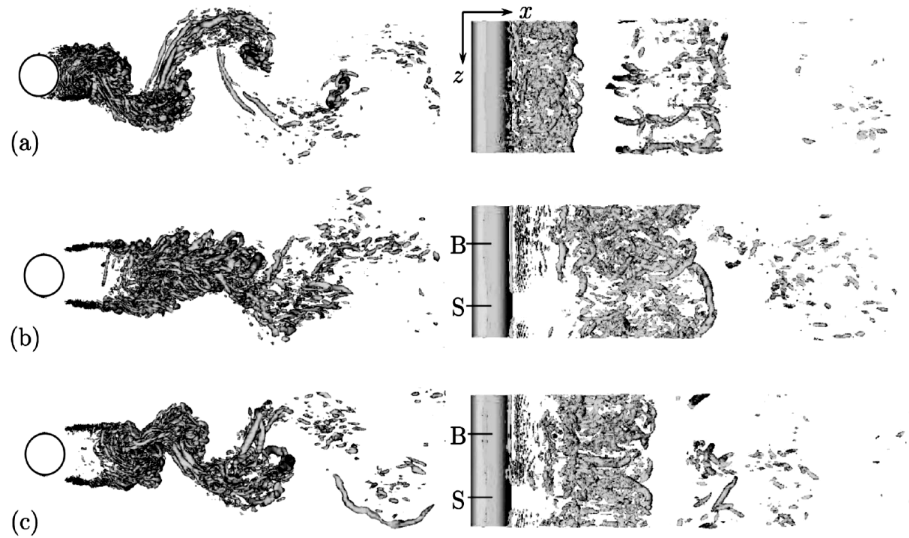
Figure 2.16 Vortical structures at Reynolds number 3900 of a) Uncontrolled case, b) In phase forcing c) out of phase forcing, B and S refers to the positions of maximum suction and blowing. [Kim and Choi (2005)]

Figure 2.17 Vortical structure of a) Uncontrolled case, b) In phase forcing case, and c) out of phase forcing case. [Kim et al. (2004)]

Many investigations were conducted on active flow control using synthetic jet near the separation point [Amitay et al. (1998), and Tensi et al. (2002)]. They found that the synthetic jet capable of delaying separation and modifying the drag coefficient even at high Reynolds numbers.

Wang et al. (2009) studied circular cylinder separation control and the flow structure affected by a synthetic jet. The synthetic jet placed at the front stagnation point and the jet is ejected against the main flow direction. The results showed that the front stagnation point is moved in the upstream direction and a closed envelope with a pair of vortices is formed in front of the stagnation point when Reynolds number is low. At higher Reynolds number the vortex pair still

presents near the front face of the cylinder and the front stagnation point moves further in the upstream direction.

Ma and Feng (2013) investigated the effect of synthetic jet actuator on the flow over circular cylinder using Particle Image Velocimetry (PIV). The jets were positioned at both the front and the rear stagnation points of the cylinder. The results showed that the presence of the synthetic jet alters the natural shedding frequency. Increasing the excitation frequency leads to domination of the synthetic jet on the entire domain.

More recently, Feng and Wang (2014) tested a cylinder with synthetic jet positioned at the front stagnation point at low Reynolds number. They investigated the effect of new control parameter, suction duty cycle factor (K), which represents the time ratio between the suction and blowing cycles on the characterization of the waveform. The found that the strength of the synthetic vortex pairs increases as the suction factor increases. In addition, actuation with K>1 leads to suppression of the vortex shedding and reduction in the drag coefficient, while for K>4, the wake region is dominated by anti-symmetric vortex shedding and shorter formation length.

Recently, a new active flow control technique has been hot research spot, namely Dielectric Barrier Discharge plasma actuators (DBD). Many researchers have investigated this technique because of its simple design, robustness, and for being easy to adapt. The atmospheric plasma actuator was first introduced be Roth et al. (1998). They designed a DBD plasma actuator that can operate at one atmospheric pressure and generates surface jet (electric wind) of several meters per seconds. DBD plasma actuators have been used as an active control technique to control several physical phenomena, such as Separation, vortex shedding, turbulence, drag reduction and lift augmentation. In the present study the use of DBD plasma actuators for flow and noise control of bluff bodies (fixed and natural separation point) will be reviewed in the next paragraphs.

The vortex shedding control from blunt trailing edge flat plate using single DBD plasma actuator is investigated by Nati et al. (2013). They tested four different configurations of plasma actuators, which are positioned at the trailing edge of the flat plate as shown in Fig. 2.18. The boundary layer was kept laminar on both upper and lower side of the plate and the tested Reynolds number, based on the thickness of the base at the trailing edge, for all tested cases was

from 3800 to 7300. They reported that, the tangential actuation in both upstream and downstream direction shows small effect on the vortex shedding structure. They found that the actuator with downward wind directed towards the center of the wake region is the most effective one, which leads to suppression of vortex shedding at free stream velocity of 5 ms^{-1}. In addition, the POD analysis showed that the total energy for the first and second modes, which is related to Karman spanwise large scale vortices, is significantly reduced when transverse plasma actuator is used.

McLaughlin et al. (2004) studied the effect of unsteady actuation of DBD plasma actuator to control wake of circular cylinder at Reynolds number of 7500. The plasma actuator was positioned at 90° on both sides of the cylinder. The forcing frequency of 5 kHz was modulated to 10.8 Hz, which was close to the natural shedding frequency for the cylinder at free stream velocity of 2 ms^{-1}. From the results of both smoke wire visualization and hot film measurements, they observed that flow separation from the cylinder can be delayed and the vortex shedding frequency can be altered and locked-in to the forcing frequency by controlling the amplitude/frequency of the actuation.
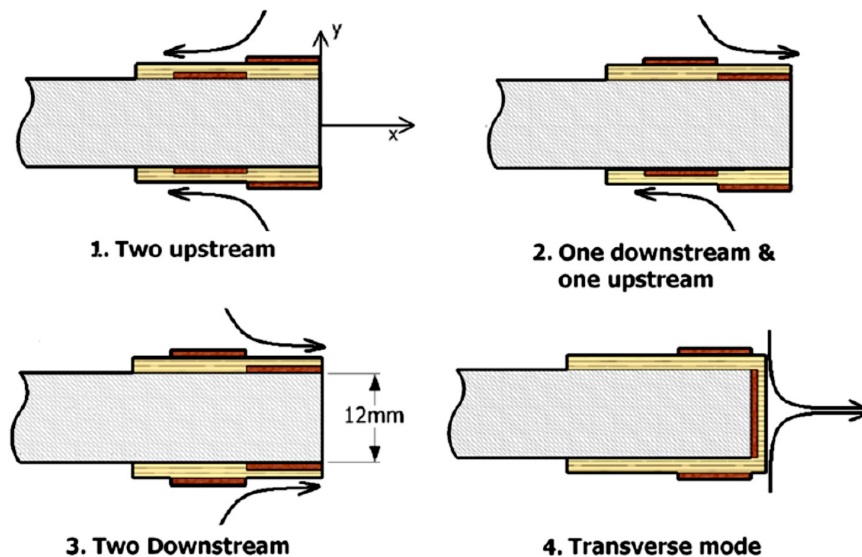
Figure 2.18 Plasma actuator configurations. [Nati et al. (2013)]

Extending their work on using DBD plasma actuator to lock in the vortex shedding of a circular cylinder using pulsed actuation, Munska and McLaughllin (2005) investigated the effect of SDBD plasma actuator at higher Reynolds numbers. A cylinder of 50 mm was tested at free stream velocity up to 30 ms^{-1}. The actuator was driven at burst frequency of 10 Hz and the

applied voltage was from 3 to 8 kV with 1 kV increment. They reported that pulsed plasma DBD actuator can modify the coherence of the vortex shedding along the span of the cylinder and change natural shedding frequency to that of the actuation, 10 Hz, when it is operated at the maximum applied voltage, 8 kV.

Thomas et al. (2006) used single DBD actuator to control flow separation and the unsteady vortex shedding from circular cylinder at free stream velocity $U_\infty = 4.5$ ms^{-1}. The effect of both steady and unsteady actuation was investigated with four actuators positioned at 90° and 135° two actuators on each sides of the cylinder. The results revealed that using SDBD plasma actuator with both steady and unsteady actuation can successfully suppress the vortex shedding. In addition, hot wire measurements showed that the turbulence intensity peak in the wake region is significantly reduced by both steady and unsteady actuation modes. Furthermore, the optimum actuation mode is achieved using the symmetric unsteady actuation of four actuator at St$_D$ = 1. Fig. 2.19 shows the effect of steady plasma actuation on the wake region of the cylinder using smoke wire visualization.
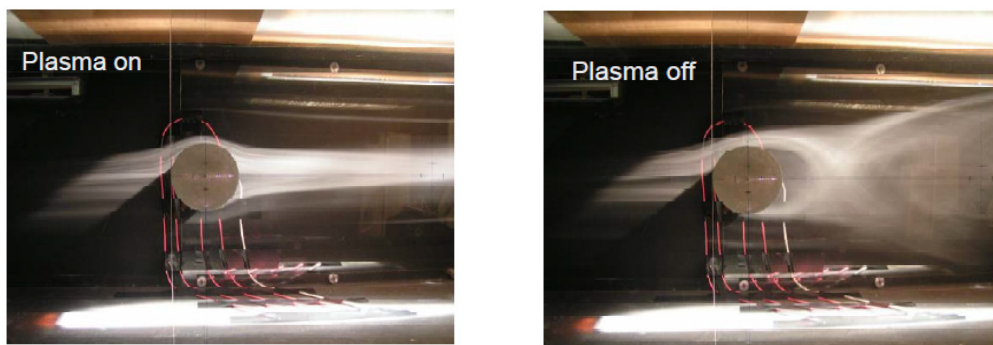
Figure 2.19 Cylinder flow visualization using smoke wire, Plasma of and steady symmetric actuation. [Thomas et al. (2006)]

Using Particle image velocimetry PIV, the effect of pulsed DBD plasma actuator on flow separation from circular cylinder was investigated by Jukes and Choi (2009). The tested cylinder has a diameter of 50 mm which and 300 mm long. The free stream velocity was set to 4.6 ms^{-1} and the corresponding Reynolds number based on the cylinder diameter is 15000. The maximum input voltage and frequency for the steady actuation were 3.5 kV, 33kHz, while the non-dimensional pulse frequency range of the unsteady actuation was from 0.1 to 2. The results showed that despite the low pulsing force that the actuator can generate, the unsteady actuation

successfully controls the wake of the cylinder. Due to the presence of plasma induced body force at critical forcing frequency above 0.6, the vortex shedding is eliminated. They believed that the reason of the suppression of the vortex shedding is due to the unsteady actuation of plasma actuator that leads to the generation of small scale vortices, which inhibit the roll up of the shear layer, thus stop it from entraining fluid from the opposite shear layer.

Instead of modulation of an AC power supply signal to drive pulsed SDBD plasma actuator, Chneck and O'Brien (2012) used capacitive DC power supply to control flow separation from circular cylinder. The cylinder was tested at Reynolds numbers based on the free stream velocity and cylinder diameter varying from 5×10^4 to 97×10^4. Two plasma actuators were positioned at 80° and 150° degree on both sides of the cylinder. The unsteady actuation non-dimensional frequency was from 0.32 to 1 which they correspond to frequencies from 69 to 334 Hz. The study revealed that operating the actuator at burst modes leads to significant flow control especially at low tested velocities. Increasing forcing frequency leads to remarkable reduction in wake width and depth. They also observed that the actuator performance decreases at highest tested Reynolds number of 97×10^4.

More recently, Akbıyık (2017) used segmented plasma actuator to produce spanwise forcing to control the wake of circular cylinder at low Reynolds number of 3900. The plasma actuators were mounted on the upper and lower sides of the cylinder with plasma jet at 80° measured from the front stagnation point. The actuators were distributed periodically in the spanwise direction with spacing of 4D between the actuators. They reported that forcing the flow using high power leads to substantial suppression in vortex shedding and reduction in the peak shedding frequency due to the increase in the vortex formation length.

Motivated by the need of aircrafts with low airframe noise, flow control of cylinders in tandem configuration has been investigated by many researchers. The nature of the flow between tandem cylinders in cross flow resulted from the unsteady flow separation and the large scale Karman vortices from the upstream cylinder and the following interaction with downstream cylinder shares several of the essential aspects of landing gear noise generation process, [Thomas et al. (2009)]. In addition to the Reynolds number, the ratio of the distance between the centers of the two cylinders to the cylinder diameter (L/D) plays an important role in the wake structure between two cylinders in tandem configuration. Comprehensive review of the flow regimes

between tandem cylinders, which have the same diameter, is given by Zdravkovich (1985). According to Zdravkovich, the nature of the wake between the cylinders and after the downstream cylinder at subcritical Reynolds numbers can be divided as follows:

- *L/D* < 1.1, for this range of spacing ratios the two cylinders have one wake and behave as a single bluff body.

- 1.1 < *L/D* <1.6, only the downstream cylinder has vortex shedding and a separation bubble occurs behind the upstream one.

- 1.6 < *L/D* <2.5, the separated shear layer from the upstream cylinder reattaches on the downstream cylinder and vortex shedding is observed behind the downstream cylinder.

- 2.5 < *L/D* < 3.2, intermittent vortex shedding is observed between the two cylinders, while a constant vortex shedding is detected in the wake of the downstream cylinder.

- 3.2 < *L/D* < 3.8, the gap between the cylinders has a bistable shedding changes between steady and intermittent shedding and constant vortex shedding is observed from the downstream cylinder.

- *L/D* > 3.8, both cylinders have constant vortex shedding in their wake with large pressure fluctuation is observed on the front face of the downstream cylinder.

Kozlov and Thomas (2011a) investigated the vortex shedding control from circular cylinder at Reynolds number of 85000. They investigated two types of plasma actuator configurations. The first one is the cylinder with spanwise oriented plasma actuator, which produces a streamwise jet in the main flow direction. The second configuration is plasma streamwise vortex generator (PSVG), which generates streamwise vortices when the actuator spanwise jet interacts with main flow. The first plasma actuator uses sawtooth waveform with 27.5 kV, while the second configuration uses sinusoidal waveform with 34.5 kV. The results show that both configurations can significantly suppress Kármán vortex shedding. A 14.2 dB and 11.2 dB reduction in the near field pressure fluctuations can be achieved when spanwise and streamwise oriented plasma actuators were used, respectively.

Extending their previous study in 2010, Kozlove and Thomas (2011b) experimentally examined the effect DBD plasma actuators on flow control of tandem cylinders at high Reynolds numbers. In this study, two cylinders with the same diameter (65 mm) were tested at two Reynolds

numbers 22000 and 172000. In order to have a steady vortex shedding from both cylinders, a spacing ratio L/D = 4 was chosen. Two configurations of plasma actuators were positioned only on the upstream cylinder at 90° measured from the front stagnation point. The first configuration was spanwise actuator that produces streamwise jet, while the other one is streamwise actuator, which generates streamwise vortices. The spanwise actuator was driven by sawtooth waveform of 27.5 kV and 1 kHz, while the streamwise actuator was powered by sinusoidal waveform of 34.5 kV and 500 Hz. They reported that the both plasma configurations lead to significant reduction in the width and the turbulence intensity of the wake on the downstream cylinder. In addition, the results showed that both actuators are effective at low Reynolds numbers. On the other hand, plasma actuator with streamwise jet is more effective at high Reynolds numbers. Figure 2.20 shows the effect of streamwise plasma electric wind configuration on the wake between the cylinders at Reynolds number 22000, which correspond to free stream velocity of 5 ms^{-1}.
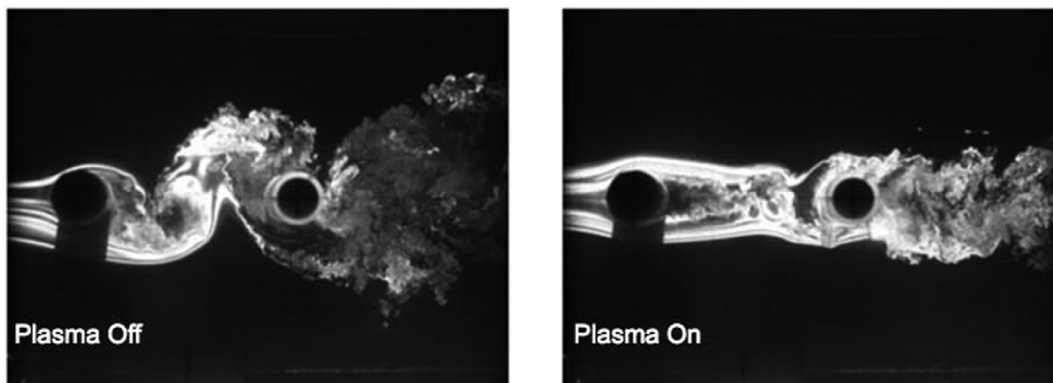
Figure 2.20 Smoke flow visualization at 5ms^{-1} [Kozlov and Thomas, (2011)]

In order to reduce unsteady wake interaction noise, which is resulted from the impingement of the wake of an upstream bluff body and the following interactions with a downstream body, active control techniques such as blowing and DBD plasma actuators have been investigated. Few researchers have investigated wake interaction noise control of both cylinder airfoil and tandem cylinders configuration and in cross flow, because they can be considered as a simplified generic flow geometry that has noise characteristics similar to the aircraft landing gear noise.

Jacob et al. (2005) conducted experimental study to investigate the rod-airfoil configuration in cross flow. The acoustic field, mean flow filed, and the instantaneous flow field was obtained

from the experimental measurements. The results showed that a spectral broadening occurs around the shedding frequency. They believed that the vortex stretching, splitting, and secondary vortices are responsible for the broad nature around the shedding frequency and the leading edge is the dominant noise source.

Experimental and numerical studies suggest that unsteady wake impingement with downstream body is responsible for the broadband noise generation. Wake interaction noise can be reduced either by reducing the turbulence in the wake region or be displacing it away from the downstream component. Siller et al. (2005) used blowing and suction near the leading edge of airfoil in order to modify the flow near the airfoil leading edge and to reduce wake interaction noise. They reported that using blowing at the leading edge of the airfoil is more effective than suction. Blowing leads to a reduction in the peak level at the mean shedding frequency, while suction increases the broadband noise level.

Angland et al. (2012) used distributed blowing to reduce wake interaction noise of cylinder-H beam configuration. They found that the tandem configuration produces significant broadband noise compared with isolated components. The results showed that the applied blowing to the surface of the cylinder from 60 to 150 degree leads to the suppression streamwise shear layer growth and the streamwise velocity fluctuation is reduced to half. The far field acoustic measurement revealed that blowing leads to a reduction in the broadband noise with maximum of 9.5 dBs around Strouhal number of 0.2. In addition, an averaged broadband noise reduction of 3 dB is achieved over frequency range $20 < f < 2$ kHz at Reynolds number of 2.7×10^5.

Single dielectric barrier plasma actuators have also been used for broadband noise reduction, as an active control technique. Huang et al. (2010) conducted an experimental study to control flow induced broadband noise emitted from a bluff body using a single DBD plasma actuator at Reynold number of 2.1×10^5. The tested model was cylinder and a torque link that resemble a simplified geometry of aircraft landing gears. The actuators were installed in a way to produce both upstream and downstream jet at an angle of 80° on both sides of the cylinder. The result suggests that using plasma actuator with electric wind generated in the upstream direction can reduce the broad band noise more effectively than the other configuration. The maximum reduction in OASPL is about 3 dB with upstream directed actuation while with the downward

only 1.7 dB is achieved. The performance of the actuator deteriorates when it is tested at higher free stream velocity 40 to 50 ms^{-1}.

2.11 Summary

An up to date overview on the related research was given in this chapter. The present study focuses on bluntness induced vortex shedding tonal noise and landing gear unsteady wake interaction noise as two examples of airframe flow induced sound.

Vortex shedding from bluff bodies such as circular cylinders (bodies of natural separation point) and blunt trailing edge bodies of fixed separation point is of great importance for many engineering applications. Many problems are associated with vortex shedding such as, drag increase, lift fluctuation, structural vibration, and noise. Examples on aerodynamic bodies subjected to vortex shedding are blunt trailing edge airfoils, which is used for wind turbine blade, and cylinders. Therefore, several active and passive flow control techniques has been investigated suppress/manipulate vortex shedding. Although active control techniques have proven to be more effective than the passive ones in many of flow control applications, they still possess some disadvantages such as, increased weight and complexity. A relatively new concept, which can eliminate some of the drawbacks of the active control techniques, is the use of plasma actuators. Plasma actuators have obtained their popularity because of their robustness, simple design, and wide working range of frequencies. Most of the plasma actuator studies focus on flow control.

Unlike vortex shedding control using plasma actuator, vortex shedding noise control has received little attention. Therefore, the present steady will focus on the following points:

- Using the DBD plasma actuator to reduce vortex shedding-induced tonal noise radiated from a flat plate with blunt trailing edge and an airfoil with cut-in type serrated trailing edge

- Using the DBD plasma actuator to control the narrowband tonal noise and wake interaction broadband noise radiated from single and tandem cylinders, respectively.

- To investigate and analyse flow mechanism related to the vortex shedding-induced noise using hot wire and PIV system.

Chapter 3

Experimental Setup

3.1 Introduction

In this chapter, a description of the experimental facilities and set-ups used in the present study will be given. In the study of the DBD plasma actuator for the vortex shedding noise control, both the aeroacoustic free field and fluid dynamic studies were conducted in the Brunel University London aeroacoustic facility (open jet wind tunnel and anechoic chamber). The experiments can be categorized into the aeroacoustic and fluid dynamic testing using far field condenser microphones, hot wire anemometry, and 2D Particle Image Velocimetry (PIV) system.

The organization of this chapter can be summarized as follows:

- A description of the aeroacoustic facility will be given in section 3.2.
- The measurement techniques will be discussed in section 3.3.
- Plasma generation system will be explained in section 3.5.

3.2 Aeroacoustic Facility

Far field noise measurements were conducted at the aeroacoustic wind tunnel. Both the vortex shedding tonal noise from a blunt trailing edge flat plate, NACA 0012 airfoil with cut-in serrated trailing edge, and tandem cylinders wake interaction broadband noise were investigated. Table 3.1 provides a summary of the acoustic and fluid dynamic tests.

Model	Velocity range	Angle of attack	Turbulence intensity	Test
Flat plate	$7.5 \leq U \leq 40$ ms^{-1} $0.75 \times 10^5 \leq Re_C \leq 4 \times 10^5$	0°	$< 0.3\%$	Flat plate Blunt Trailing edge vortex shedding noise, hot-wire, and PIV
NACA 0012	$7.5 \leq U \leq 40$ ms^{-1} $0.75 \times 10^5 \leq Re_C \leq 4 \times 10^5$	0°	$< 0.3\%$	NACA 0012 with cut-in serrated trailing edge & blunt trailing edge airfoil bluntness-induced noise.
Cylinder	10 ms^{-1} $Re_D = 1.1 \times 10^4$	-	$< 0.3\%$	wake interaction noise, hot-wire, and PIV

Table 3.1 Summary of aeroacoustic and flow tests.

3.2.1 Brunel Aeroacoustic Wind Tunnel Facility

The aeroacoustic facility includes an open jet wind tunnel situated inside a hemi-anechoic chamber, which has a dimension of 4 m x 5 m x 3.4 m. The cut-off frequency of the chamber is about 200 Hz. A 30 kW AC powered centrifugal fan that can produce a pressure rise of 8 kPa is used to obtain a maximum mass flow rate of about 3 kgs^{-1}. As shown in Fig. 3.1, the flow generated by the fan moves upward through an offset diffuser and then expands through a 90° bend duct, which has an aspect ratio ($AR = 1$). Then, the propelled air is acoustically treated by 10 m long silencer, which is positioned above the ceiling of the anechoic chamber. When the air leaves the silencer at the north side of the chamber, it is deflected by a 90° bend duct towards the floor. Another 90° bend duct is used to deflect the air in the horizontal direction and before it goes through a settling chamber, which is situated inside the anechoic chamber. Inside the settling chamber the air is conditioned by a series of woven wire mesh screens and honeycombs. When the air leaves the conditioning screens, it accelerates inside a nozzle, which has an outlet and an inlet cross sectional area of 867 mm x 867 mm and an outlet cross-sectional area of 100 mm x 300 mm respectively. The air jet is released inside the anechoic chamber with maximum velocity of 80 ms^{-1}. Finally, when the jet reaches the south side of the chamber, it is

deflected 90° upwards and is acoustically treated by a splitter type silencer, before exiting the anechoic chamber.
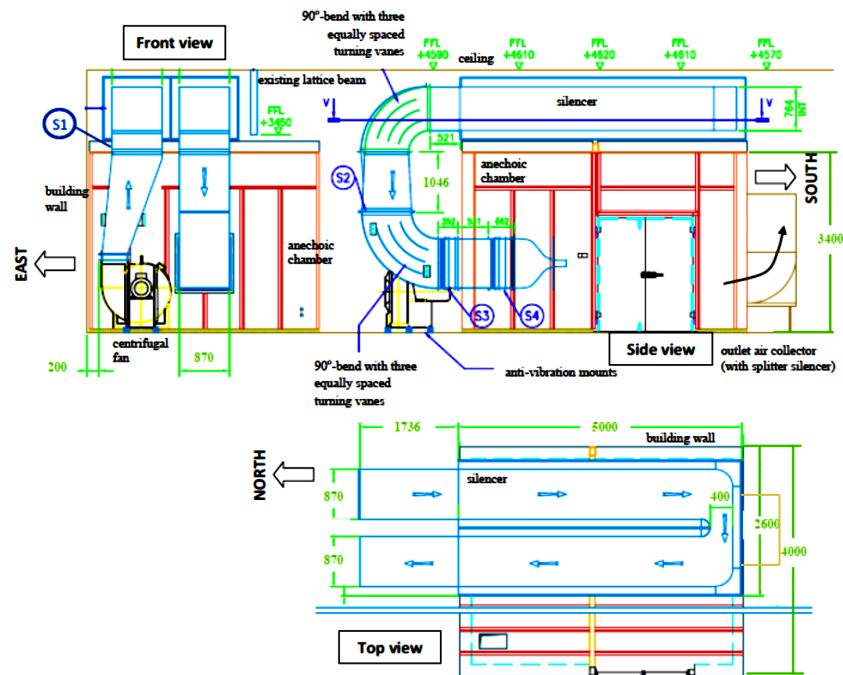
Figure 3.1 Top, front, and side views of Brunel University London aeroacoustic facility.
[Vathylakis et al. (2014)]

Different measurement techniques have been used in order to investigate the effect of the DBD plasma actuators on vortex shedding induced noise and the mechanism of noise reduction. These techniques will be discussed later in this chapter.

3.3 Acoustic Measurement Technique and Acoustic Metrics

All of the far field acoustic measurements were conducted using a ½ inch free field pre polarised condenser microphone (LarsonDavis 377B02), which has sensitivity of 50 mV/Pa (+/- 1.5 dB) and a dynamic range of between 15 and 146 dB. The microphone is placed at a distance of 1 m above the test model at mid span. A G.R.A.S. calibrator type 42AB is used to calibrate the microphone. The calibrator reference frequency and sound pressure level are 1 kHz and 142 dB, respectively. The experimental set up inside the anechoic chamber is illustrated in Fig. 3.2. The output signal from the microphone is pre-amplified using a preamplifier (426E01). Then, the signal is sampled at sampling frequency of 44 KHz for 10 seconds using a 16 bit analog to digital

(A/D) card. Analogue filter is used at a cut off frequency of 22 KHz. The acquired data is then exported to Matlab, where the power spectral density (PSD) of 1 Hz bandwidth is estimated using Welch's method from 1024 point Fast Fourier Transform (FFT), after windowing of the sampled data. The PSD of the measured mean-square acoustic pressure fluctuations can be derived from the following correlation function of the pressure fluctuations in the far field at a distance x_i from the source of sound:

$$R_{pp}(x_i, \tau) = \frac{1}{t_2 - t_1} \int_{t_1}^{t_1} p'(x_i, t) p'(x_i, t + \tau) dt \qquad (3.1)$$

where p' is the measured pressure fluctuations. By Fourier Transforming the correlation function (Eq. (3.1)), the PSD of the pressure fluctuations in the far field can be described as follows:

$$P_{xx}(f) = \int_{-T}^{T} R_{pp}(x_i, \tau) e^{-i2\pi f \tau} d\tau. \qquad (3.2)$$

Figure 3.2 Experimental set up inside the anechoic chamber.

The acquired noise data were converted into sound pressure level (*SPL*) which can be defined as follows:

$$SPL(f) = 10 \log_{10} \left(\frac{\overline{p'^2}}{p_o^2} \right) \qquad (3.3)$$

Where $\overline{p'^2}$ represents the mean-square of the pressure fluctuation and p_o is the air reference sound pressure, which has typical value of (20 µPa).

The mean-square of the pressure fluctuation $\overline{p'^2}$ can be calculated from the following equation:

$$\overline{p'^2} = \frac{1}{t_2 - t_1} \int_{t_1}^{t_1} p'(x_i, t) p'(x_i, t) dt \tag{3.4}$$

3.4 Fluid Dynamics Measurement Techniques

3.4.1 Hot Wire Anemometry System

In order to study the flow characteristics in the wake region of the test models, a constant temperature hot wire anemometry system was used. The hot wire was used to measure both the instantaneous velocity and the unsteady velocity power spectral density (PSD).

The data acquisition hardware represented by a 12 bit analog to digital card (TSI ADCPCI) was used to digitise the acquired signals. The acquisition and the transverse movement of the hot wire probe were controlled by the TSI software (Thermal pro). The movement of the probe within the investigated domain was controlled by the (TSI- Isel T2D model) 2-axis traverse system, which has an accuracy of 0.01mm in both directions. The alignment of both the hot wire probe and the traverse system was assured using digital inclinometer, which has an accuracy of 0.1^o.

Hot wire tests were conducted by two types of hot wire probes; straight single probe (DANTEC 55P11) and right angle probe (DANTEC 55P15). The hot wire probe is connected to a multi-channel constant temperature anemometer (CTA), DANTEC 55N80 model. The hot wire probe is made of tungsten wire, which has a diameter of 5 µm and length 1.25mm. In order to calibrate the how wire probe, the probe was positioned inside the potential core of the free jet without any object inside the jet. The calibration process can be described as follows:

- First, the anemometer channel bridge voltage was adjusted using DANTEC mini CTA spreadsheet. The required input parameters include, calibration temperature (T_c), flow temperature (T_a), probe wire resistance (R_{20}) and the overheat ratio which was kept the same for the cases at 1.8. This gives a typical wire temperature of about 300 C^o.

- Both the hot wire probe and a pitot-static tube were positioned in the free jet and the probe was aligned with static taps of the Pitot - static tube.

- The actual free jet velocity measured by Pitot - static tube and the voltage of the hot wire probe were recorded using the TSI thermal pro software. The free jet velocity was adjusted using a Furness FCO510 digital micro-manometer, which has an accuracy of 0.001Pa. Fig. 3.3 illustrates an example of a velocity- voltage calibration curve for a single hot wire probe. A schematic showing a typical set-up for the hot wire experiments is shown in Fig. 3.4.
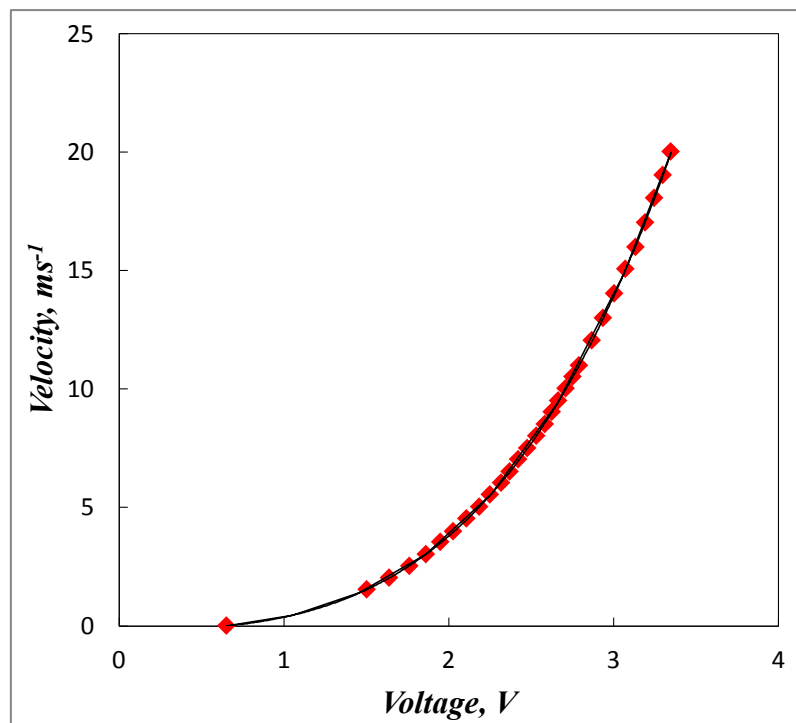
Figure 3.3 Single hot wire probe calibration curve.

The acquired hot wire voltage is corrected by temperature difference compensation using the following equation:

$$E_{corr} = E_{acq}(\frac{T_w - T_c}{T_w - T_a})^{0.5} \tag{3.5}$$

Where E_{corr} is the corrected hot wire probe voltage, E_{acq} is the acquired voltage, $(T_w, T_c,$ and $T_a)$ are the hot wire working temperature, calibration temperature, and flow temperature respectively. The relation between the corrected acquired voltage and measured

velocity can be determined by a fourth order polynomial fitting function, which can be expressed as:

$$U = C_o + C_1 E_{corr} + C_2 E_{corr}^2 + C_3 E_{corr}^3 + C_4 E_{corr}^4 \qquad (3.6)$$

Where C_o, C_1, C_2, C_3 and C_4 are coefficients that can be obtained from calibration curve.
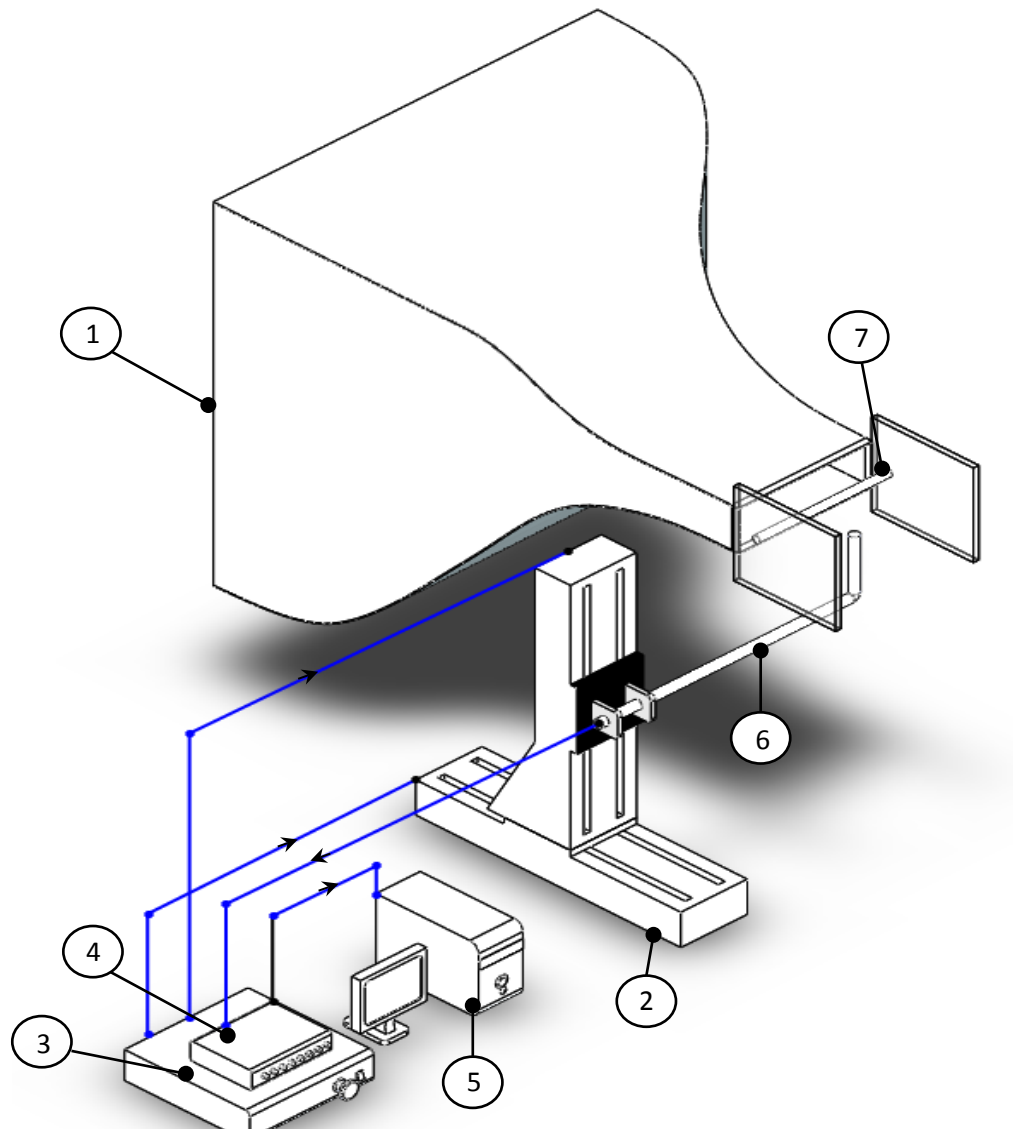
Figure 3.4 Schematic diagram of Hot wire experimental set up; 1) Nozzle, 2) 2D axis Traverse, 3) Traverse control, 4) CTA, 5) PC, 6) Hot wire probe holder, 7) Tested model.

3.4.2 Differential Pressure Transducer

Due to the filamentary nature of the plasma discharge, arcing may occur if the hot wire probe is close enough to the discharge region, which may severely damage not only the probe itself but also the anemometer hardware. Therefore the near wake region of the flow was investigated by a differential pressure transducer (Fig.3.5) which has pressure sensitivity between 0 and 10 mbar

Figure 3.5 Differential pressure Transducer.

A glass pitot tube, which has 1 mm inner diameter, was connected to one of the two ports of the pressure transducer using silicone tube to measure the total pressure while the other port was attached to a reference pressure tube (static ambient pressure) which was positioned near the tested model but away from flow region.

The free stream velocity is calculated using the following equation:

$$P_d = P_o - P = \frac{1}{2}\,\rho_{air}\,u^2$$

$$u = \sqrt{\frac{2*(P_o - P)}{\rho_{air}}} = \sqrt{\frac{2\rho_{water}*g*\Delta h}{\rho_{air}}} \tag{3.7}$$

where P_d, P_o, and P are the dynamic pressure, total pressure, and static pressure, respectively.

3.4.3 Particle Image Velocimetry (PIV)

Particle image velocimetry is considered as a powerful non-intrusive measurement technique, which can be used to measure the instantaneous flow characteristics of either 2D plane (Planar PIV) or 3D volumetric space (Tomographic PIV).

The working principle of a PIV system is based on tracking of small particles, which usually have a diameter between 1 and 5 μm. The tracing particles need to have high response to the flow behavior and to maintain the flow characteristics. These particles need to be illuminated in a plane of interest within the flow. A high intensity two laser sheet pulses are emitted from laser system with time difference of Δt between the pulses for particles illumination. Then, the light scattered from the illuminated particles is recorded on two separated frames by high speed Cross-Correlation Digital (CCD)-camera positioned perpendicular to the investigated flow plane and synchronized with laser pulses. The recorded images are transferred to a computer. Then the evaluation of the recorded frames starts by dividing them into small sub-areas known as "Interrogation areas". For each interrogation area, the displacement of the illuminated particles is determined by statistical techniques such as auto-correlation, cross-correlation, and adaptive correlation. The speed of the particle is calculated based on the particle displacement and the time difference between two subsequent frames.

The main components of the PIV system used in this thesis are as follows:

- As a source for the laser beam, a Litron Nd:YAG-Laser with maximum output energy of 800mJ was used. The range of wavelengths of the radiated laser is between (532 nm and 1064 nm).

- The laser has a maximum pulsing frequency of 15 Hz with minimum time between pulses of 4-6 ns. Using DANTEC optics provided with laser allows expanding the 5 mm laser beam to a light sheet of 1 mm thickness. The laser unit can be externally controlled via a Q-switch that is connected to the computer. This switch allows the user to define a number of laser important parameters such as, laser intensity and repetition rate.

- A DANTEC seeding generator is used to feed the flow with the tracing particles. The seeding generator working principle is based on open jet pumps. A high speed compressed air is supplied through capillary tubes into the generator's reservoir and results in a drop in the pressure, which causes a vacuum inside the reservoir. The generator disperses a seeding fluid to fine droplets of micrometer scale. The size of the seeding is of crucial importance in order to obtain a high quality data. Although large seeding particles are easy to be detected by the camera, they could slip especially in the regions of high frequency fluctuations. On the other hand, small seeding size allows seeding particles to follow the high frequency fluctuations in the flow and result in small slipping velocity (the velocity of the particles between two consecutive frames). Different types of seeding fluid can be used such as the paraffin, olive oil, and gear lubricant oil. In order to prevent oil layers build up on the sensitive devises, and the acoustic wedges inside the anechoic chamber, Polyethylene glycol (PEG) is used as a seeding fluid in the current thesis as this fluid has a high decay rate. Although PEG is considered as a water soluble fluid, the interior of the anechoic chamber were covered with a thin painting film to protect the acoustic wedges from contamination by oil. Before starting the experiment the chamber was filled with seeding particle, which were injected directly inside the chamber.

- A DANTEC CCD camera (FlowSense EO 2M) was used to capture the images of the seeding particles that are illuminated by the laser sheet in the field of interest. The camera can capture up to 44 frames per second (FPS) at full resolution of 1600 x 1200 pixels with pixel size of 7.4 µm. The camera is provided with Makro-Planar T*2/50mm Zeiss® lens with a minimum focusing distance of 0.24m. The camera was synchronized with the laser sheet pulses through a timer box, which was connected to the main computer.

3.4.4 PIV Set up

The objective of the PIV experiments is to measure the velocity field in the wake region of the blunt trailing edge flat plate and in between the tandem cylinders configuration. For the flat plate case, the measurements were carried out in (x,y) and (y,z) planes, while for the tandem cylinders, only (x,y) plane was investigated

The laser unit was positioned on a platform under the test model with the laser sheet parallel to the plane of interest. In order to trace the illuminated particles in the most efficient way, the CCD camera was situated at 90° with laser sheet plane as shown in Fig. 3.6. The first step in the measurement is the calibration. The calibration process of the PIV involves two main steps; camera calibration and laser alignment. In order to determine the dimension of the flow field image captured by the camera, a dot pattern calibration image of known dimensions was captured. The calibration image used for the flat plate wake study has a dimension of 100 mm x 100 mm, whereas in the case of tandem cylinders the calibration image has a dimension of 50 mm x 100 mm. Fig. 3.7 shows an example of the calibration target attached to the cylinder. In order to make sure that calibration target is perpendicular to the camera, the camera was focused on the whole calibration target. After taking the calibration image, the image was scaled from pixles to metrics by setting the scale factor.

The second step after the camera calibration is the laser sheet alignment. In order to make sure that the laser sheet is aligned with the test plane (e.g. (x,y) or (y,z) plane) at the desired position, a high-lighter marker was used to cover the lower edge of the calibration target. The high light marker was used in order to reflect the laser light and to make it visible, even when the full protection goggles is used. The laser is aligned when the laser sheet overlaps with the highlighted lower edge of the calibration target.

After finalising the calibration, the alignment, and setting the appropriate scale factor, a number of important parameters need to be determined such as the time between laser pulses, trigger rate, and number of frames to be captured. The time between the laser pulses is an important parameter. It describes the time delay between the first and the second captured frames, which plays an important role in particle displacement detection and it depends on the mean flow velocity. If the time delay between the laser pulses is too short, the particles in the second frame will occur at the same location as in the first frame. On the other hand, too long time delay will result in out-off plane velocity as the particles will leave the illuminated plane before the second pulse. The time delay for the current tests is 15 µs and it is based on the signal to noise ratio. The other parameter is the trigger rate. The trigger rate for the current set up is 15 Hz, which is the maximum value for the current system. In order to get high quality averaged velocity vectors the

number of acquired images is 530 images. Table 3.2 illustrates PIV set up parameters which were kept the same throughout the experiments.
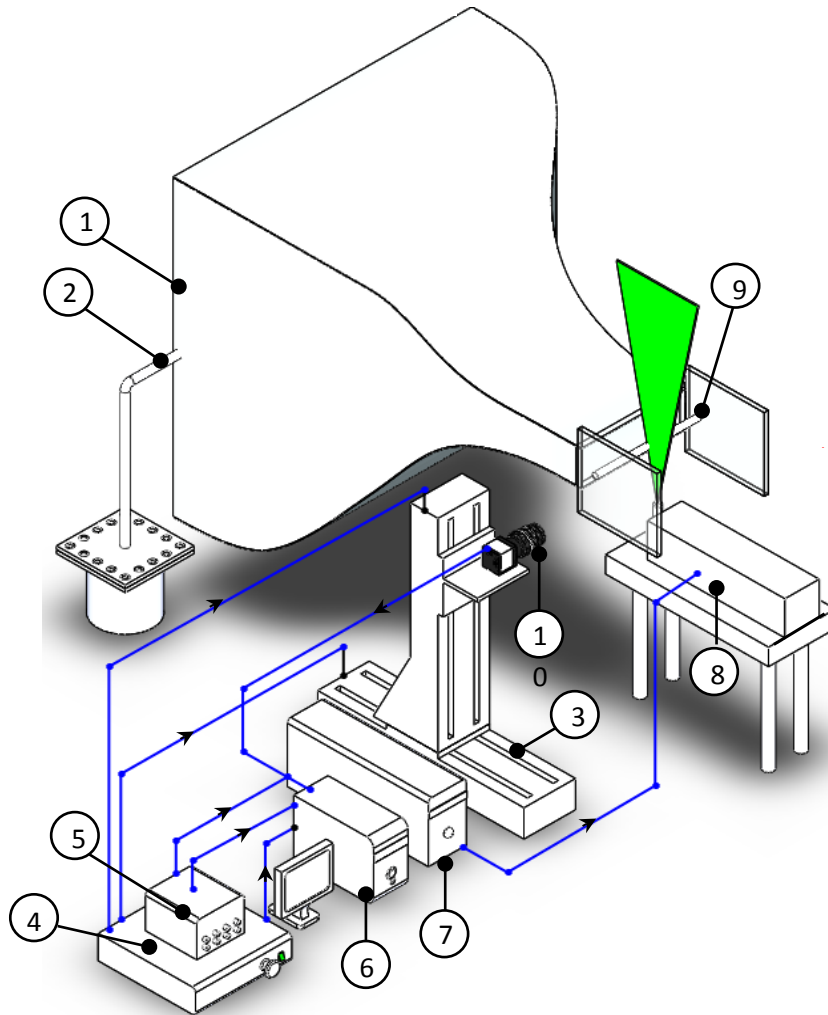
Figure 3.6 Schematic diagram of PIV experimental set up; 1) Nozzle, 2) Atomizer, 3) 2D axis Traverse, 4) Traverse control unite, 5) Synchronization box, 6) Workstation, 7) Laser cooling tower, 8) Nd:YAG-Laser, 9) Tested model, 10) CCD camera.
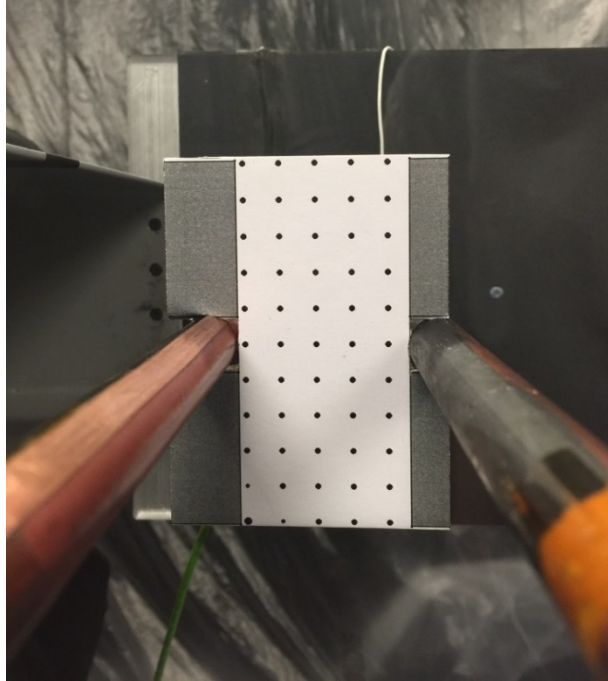
Figure 3.7 Calibration target.

Parameter	Value	unite
Droplet size	2	μm
Trigger rate	15	Hz
Time between laser Pulses	15 (Cross flow) 3.5 (Quiescent)	μs
Field of view	100 x 100 (flat plate) 50 x 100 (Cylinder)	mm
Analysis method	Adaptive correlation	-
Interrogation window size	32 x 32	pixel
Overlap	50	%
Number of captured frames	540	-
Refinement steps	2	-

Table 3.2 PIV set up parameters.

3.4.5 PIV Data Analysis

After the data acquisition, the flow field was reconstructed from the acquired image pairs. Image processing starts with identifying the interested field of view and masking out the unwanted regions (dark regions). In order to process the PIV images, a number of correlation method can be used such as, auto-correlation, cross-correlation, adaptive-correlation and average-correlation. These methods allow computing the instantaneous flow velocities in the two dimensional plane.

The analysis method used in the current thesis is the adaptive correlation method, which produces reasonably accurate flow results. During the analysis each image pair is divided into smaller windows called interrogation area (IA). Then the distance can be computed by comparing the particles between the successive images for each IA. This displacement can be determined by using the following equation:

$$R_{ii'}(x,y) = \sum_{-K}^{K}\sum_{-L}^{L} I\,(i,j)I'(i+x,j+y) \tag{3.8}$$

Where I and I' are the intensity of the first and the second frames, respectively. It can be seen that one cross correlation value can be obtained from the sum of the product of all of the overlapping pixels. When this operation is applied for a range of shift this will result in the formation of a correlation plane of $(2M+1)\,(2N+1)$. Unlike cross-correlation method, in the adaptive correlation method, the velocity vectors are calculated with the initial IA of size N multiplies the size of the final IA. Then the intermediate results are used as a source for the next smaller IA until the final size of the IA is reached. In the current study, the initial size of the IA is 64 x 64 pixels, whereas the final IA size is 32 x 32 Pixels using two refinement steps. Then the vector maps generated from applying the adaptive correlation are masked in order to remove the bad vectors generated from analyzing the previously masked regions. Finally, a single vector map is generated by combining the vector maps of each frame pair.

The averaged flow properties such as streamwise velocity u vertical velocity v, spanwise vorticity Ω, and turbulence intensity T_u and T_v are determined.

The spanwise vorticity and velocity fluctuation can be calculated using Eq. (3.9) and Eq. (3.10):

$$\Omega_z = \frac{\partial v}{\partial x} - \frac{\partial u}{\partial y} \tag{3.9}$$

$$T_u = \frac{u_{rms}}{U} \ , \ T_v = \frac{v_{rms}}{U} \tag{3.10}$$

3.4.6 POD Analysis

It was Lumley who introduced the Proper Orthogonal Decomposition (POD) analysis for the first time in Lumley, (1967). Different techniques have been used to perform the POD analysis. The POD technique that is used in the current study is called "Snapshot POD", which was first introduced by Sirovich (1987). The purpose of performing the POD analysis is to extract the information on the dominating flow features within the flow field. POD analysis has been used in several experimental and numerical researches to study the large coherent structures associated with vortex shedding phenomenon. Because of the existence of the large scale coherent structures represented by the von Karman vortex shedding in the current study, the POD method is considered to be a very efficient tool for the flow decomposition analysis.

The analysis of the POD modes consists of two steps; extracting the POD modes and projecting the unsteady part of the velocity components on the extracted modes. In the first part, the POD modes are obtained from a series of PIV snapshots captured under similar experimental conditions and in similar locations. Then the mean velocity field is calculated from the acquired snapshots, thus the mean mode is calculated. The mean velocity component is considered the zeroth mode in the analysis. The analysis of the other modes is performed on the fluctuated part of the each velocity components (u_{MN}, v_{MN}), where u and v are the streamwise and vertical velocity fluctuations and M and N are the coordinates position and number of snapshots, respectively. The unsteady part of the velocity field components can be obtained by subtracting the calculated mean velocity from all the acquired snapshots and result in U matrix.

$$U = \begin{bmatrix} u_{11} & u_{12} & \cdots & u_{1N} \\ \vdots & \vdots & \vdots & \vdots \\ u_{M1} & u_{M2} & \cdots & u_{MN} \\ v_{11} & v_{12} & \cdots & v_{1N} \\ \vdots & \vdots & \vdots & \vdots \\ v_{M1} & v_{M2} & \cdots & v_{MN} \end{bmatrix} \tag{3.11}$$

where the subscripts M and N refer to the coordinate position and the number of the snapshots, respectively (e.g. $u_{mn} = u\,(x_m, y_m, t_n)$).

Then the auto-covariance is created using as follows:

$$C = U^T U \tag{3.12}$$

And the corresponding eigenvalue can be determined from the following equation:

$$C\,A^i = \lambda^i\,A^i \tag{3.13}$$

Where A^i is the eigenvalue and the elements of the C matrix can be described as follows:

$$C_{jk} = \frac{1}{N}\,(u(x, t^j), u(x, t^k)), \qquad j, k = 1, \dots, N \tag{3.14}$$

Then, the solutions of the eigenvalues are ordered according to the size of the eigenvalues as follows:

$$\lambda^1 > \lambda^2 > \lambda^3 \dots > \lambda^N = 0 \tag{3.15}$$

The POD modes are constructed from the eigenvectors that are obtained from (3.11).

$$\Phi_i\,(X) = \frac{\sum_{n=1}^{N} A^i(t^n)\,u(X, t^n)}{\lVert \sum_{n=1}^{N} A^i(t^n)\,u(X, t^n) \rVert}\, , i = 1, \dots, N \tag{3.16}$$

The resulted solutions are organised with respect to the size of their eigenvalues (energy). The POD modes require a series of vector maps from which the energy (eigenvalues) are ordered with respect to the corresponding mode number from the highest to the lowest energy.

The second part is the projection of the fluctuating component on the extracted POD modes. The velocity vector map is reconstructed from the expanded mode matrix using both the extracted

POD modes and the vectors maps. The expansion factor (a_n) is obtained from the following equation:

$$a_n = \Psi^T u_n \tag{3.17}$$

Where Ψ^T is the mode matrix in which each column is represented by a POD mode (φ_i):

$$\Psi = [\varphi_1 \ \varphi_2 \ .... \ \varPhi_{N-1}] \tag{3.18}$$

The velocity can be reconstructed by the expansion of the fluctuated part as follows:

$$u_n = a_n \Psi \tag{3.19}$$

Finally, spatial distribution of the POD modes in terms of the streamwise and vertical velocity components can be obtained by projecting the extracted POD modes on the calculated velocity vectors. It can be seen that the total amount of the kinetic energy obtained from the velocity fluctuations in the snapshots for a certain POD modes is proportional to the related eigenvalue. The ordering of both the eigenvalues and eigenvectors ensures that the first modes are the highest energy modes (Eq. (3.12)). As a result, the first modes correspond to the large scale structures in the wake region.

3.5 Plasma Generation System

A high voltage, high frequency AC power supply (Minipulse 6) is used to generate the plasma. This power supply is capable of generating high AC voltages up to 60 kV peak-peak and the operating frequency range is between 5 and 20 kHz. The power supply consists of two parts; bridge convertor and transformer cascade. The input signal to this power supply is square wave while the output signal is sinusoidal. The input signal to the power supply is provided by a function generator (LeCroy wave station), which was also used to control the frequency of the output voltage. The maximum level of the output voltage and current that the power supply can provide depends on the connected load. Only the sinusoidal wave form was investigated in the current study due to the limitation of the power supply unit. Both the output voltage and current were monitored using a two channel oscilloscope (Tektronix TDS 1001C-EDU).

In order to reduce the effect of interference between the high voltage cable and the other signal cables (microphone and hot wire signal cables), the cable that was connected to the plasma system was shielded and separated from other cables. In addition, measurement equipment was located outside the anechoic chamber to reduce any possible effect of the electro-magnetic interference radiated by the plasma actuator. Furthermore, as the plasma requires high voltage to be produced, several measures were made in order to minimize the risk to the user. For instance, a number of cut-off switches were located inside and outside the chamber and good earthing was assured. In order to discharge any remaining charge on plasma surface, an earthing stick made of PTFE was used.

As Ozone is a by-product of the plasma generation, an ozone sensor (ECO SENSORS OS-4) is used to monitor the generated ozone level. The sensor was mounted outside the chamber on the side wall, because all the experiments were conducted while the plasma actuators were operated inside the closed anechoic chamber. After each experiment, the wind tunnel was kept running for about 10 minutes until the ozone sensor light turns green.

3.6 DBD Plasma Actuator Design

The tested plasma actuator in the current study is known as the Dielectric Barrier Discharge plasma actuator (DBD). This type of plasma actuators consists of two electrodes the first electrode is known as the exposed electrode while the second one is the ground electrode. The exposed electrode is usually connected to the high voltage power source, whereas the other one is connected to the ground. Both the exposed and ground electrodes used in the current study are made of copper and have thickness of 0.035 mm.

The ground electrode is usually separated from the exposed electrode by a dielectric material. The function of the dielectric layer is to prevent arcing occurrence between the exposed and the ground electrode and to allow for discharge accumulation near the exposed electrode. Different dielectric materials have been used for this type of actuators such as, glass, Perspex, PTFE, ceramic, and Kapton (film and tape). Two types of dielectric material were investigated in the current study; polycarbonate and Kapton tape. The electrodes can be arranged in either the symmetric or asymmetric configurations. When the electrodes are symmetrically arranged the plasma generates on both sides of the exposed electrode which results in generation of electric

wind in both directions. On the other hand, when plasma actuators are arranged asymmetrically, the plasma occurs on the exposed electrode edge that is close to the ground electrode. The tested DBD plasma actuators in the current study are asymmetrically arranged with no gap between the two electrodes, as shown in Fig. 3.8. More details on plasma configuration, and exposed electrode configurations will be given in Section 3.7.1.
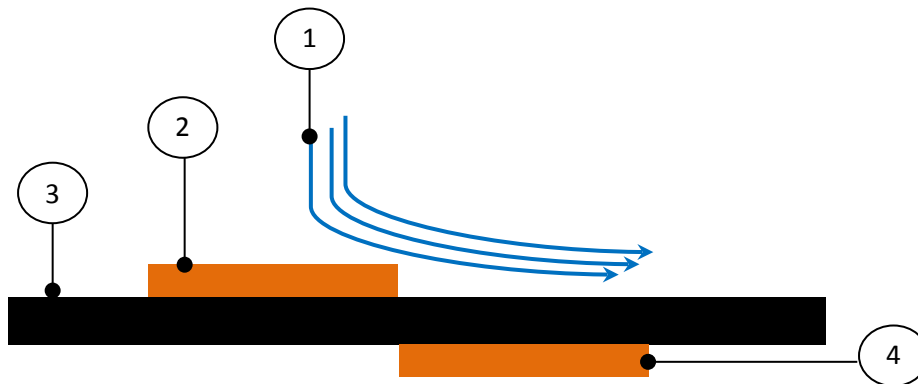
Figure 3.8 Typical asymmetric DBD plasma actuator; 1) Electric wind, 2) Exposed electrode, 3) Dielectric material, and 4) Ground electrode.

When a high AC voltage of $V_{(input)} \sim$ kV with a sinusoidal waveform of $f_{(input)} \sim$ kHz is supplied to the exposed electrode, a strong electric field is generated between the electrode. Thus, the air surrounding the exposed electrode is ionized and a region of approximately equal number of ions and electrons is generated. During the negative half cycle, electrons move from the exposed electrode towards the ground one. On the other hand, when the positive cycle begins, part of the electrons moves back towards the exposed electrodes. Because of this forward and backward movement of the electrons, a collision between the neutral and the ionized air particles will happen. Thus, a body force will be generated, which in turns produces an electric wind as a surface jet parallel to the flow direction.

3.7 Test Models

3.7.1 Flat Plate

In order to investigate the effect of DBD plasma actuator on the vortex shedding tonal noise phenomenon, a flat plate with blunt trailing edge have been designed. The designed plate is made of polycarbonate and has a chord length $C = 150$ mm and a width $B = 300$ mm. In order to

provide smooth entry to the incoming flow, a NACA 0012 airfoil leading edge is used as a leading edge of the flat plate, which is extended from the maximum thickness of the airfoil and has a blunt trailing edge of $H = 6$ mm.

In order to reinforce the plate, a sheet of steel plate is sandwiched in the middle. The plate was fixed between two side plates extending from the nozzle sides using three pins of 2.5 mm on each side, and was kept at zero incidents with respect to the incoming jet. Fig. 3.9 shows the schematic of the flat plate. The upper and lower sides of the plate were artificially tripped into turbulent boundary layer using rough sandpaper. The trip tape is positioned at 15mm from the leading edge of the flat plate and has length of 300 mm and width of 10 mm.

Three DBD plasma actuator configurations were investigated in the current steady. These actuators are named according to the electric wind direction. The first actuator is PA1 plasma actuator, which is supposed to generate electric wind parallel to the flow direction. The second plasma actuator configuration PA2 will generate electric wind in the downward direction. This actuator will draw the air from both upper and lower sides and the resulted vertical jet will merge in front of the blunt face producing a streamwise jet. The last plasma actuator is PA3. The exposed electrode of the PA3 configuration is composed of a number of short strips, which are equally spaced and distributed along the span of the flat plate. This actuator will generate spanwise perturbations, which lead to the generation of streamwise vortices. It will be shown later that the PA3 plasma actuator is the most efficient configuration in vortex-induced noise suppression at low voltages compared with the other configurations. More information about the plasma actuator components will be given in Chapter 4.
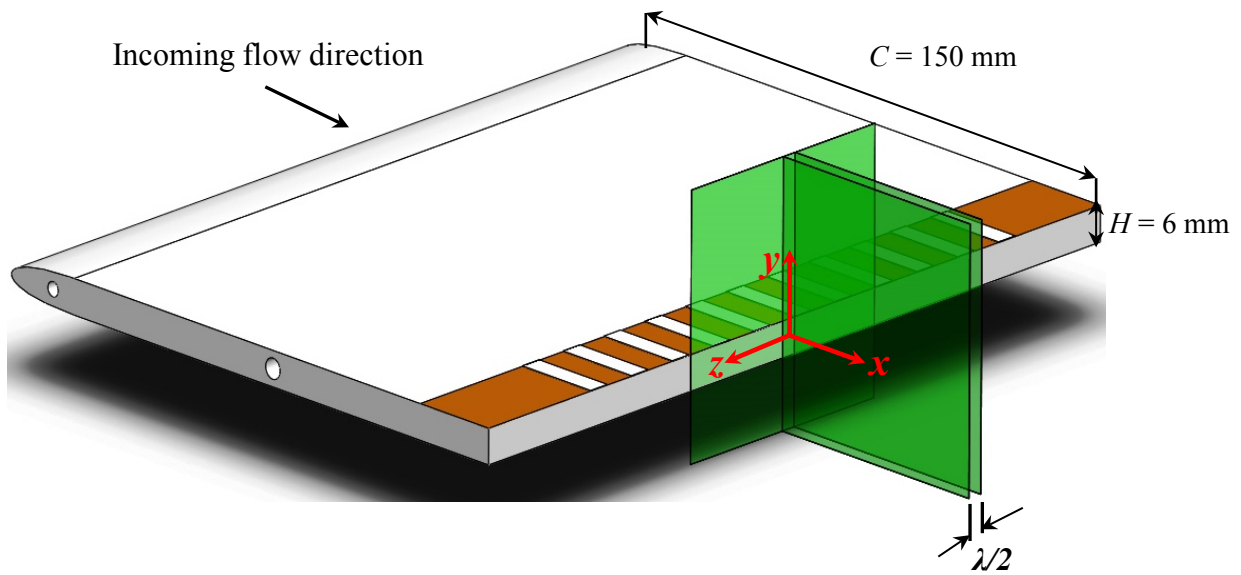
Figure 3.9 Blunt trailing edge flat plate with PA3 Plasma actuator with the investigated laser sheet planes.

3.7.2 NACA 0012 Airfoil

Turbulent boundary layer trailing edge noise usually occurs at high Reynolds number for non-separated turbulent flow. This noise has a broadband nature and scatters into the far field when the turbulent boundary layer convects over the trailing edge of the airfoil. As a passive control technique inspired by the silent flight of the owls, non-flat plate trailing edge serration has been used to control trailing edge noise. Despite the significant effect of the cut-out trailing edge serration on the trailing edge noise reduction, it radiates an additional noise of tonal nature, which is induced from the blunt section in the serration root. As an active flow control technique, the DBD plasma actuator is used to control non-flat plate trailing edge serration tonal noise. NACA 0012 airfoil with cut-in serrated trailing edge was used for a hybrid noise control experiment (active and passive).The airfoil is made of polycarbonate and has a chord length $C = 150$ mm and span $B = 300$ mm.

The airfoil has been designed to have two parts; main body part and trailing edge part. The main body part starts from the leading edge up to $x/C = 0.75$, whereas the second part has interchangeable trailing edge and starts from $x/C = 0.75$ and ends at $x/C = 1$. Two interchangeable trailing edges were designed; sharp and serrated trailing edges. Both the upper

and lower sides' boundary layer is artificially tripped to turbulent boundary layer using rough sand tape. The trip tape is positioned at 15 mm from the leading edge of the airfoil. The serrated trailing edge has been designed with a groove on both upper and lower sides in order to accommodate the plasma actuator. The grove extends along the span of the trailing edge and has a length of 290 mm and width of 15 mm. Unlike the PA3 plasma actuator used in the flat plate case, the exposed electrode that is used for the DBD plasma actuator in the current case has sinusoidal shape, which is supposed to produce a three dimensional plasma induced jet. The ground electrode is a straight copper strip of 280 mm length and 10 mm width. In order to improve the durability of the plasma actuator, the dielectric material used in this case is made of 1 mm thick polycarbonate sheet. The airfoil was placed at zero incident with relative to the incoming jet with velocities between 7.5 and 40 ms^{-1}. Figure 3.11 shows the 1) main body of airfoil, 2) and 3) are interchangeable sharp and cut-in serrated trailing edges, respectively.
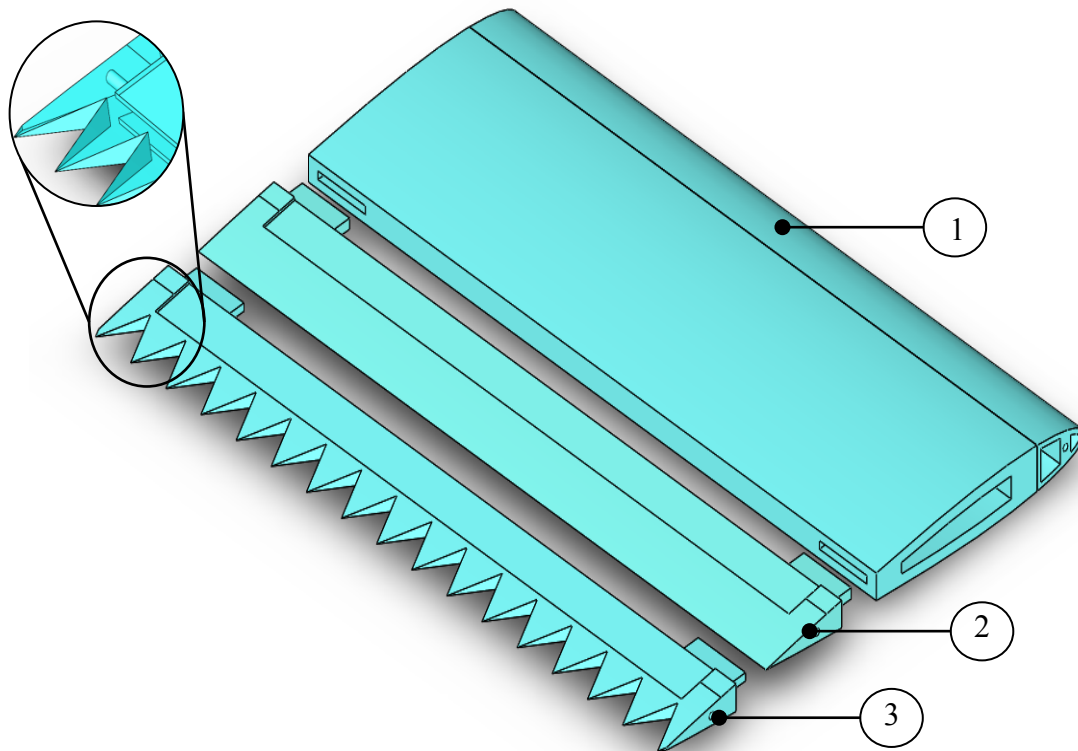
Figure 3.10 NACA 0012, 1) Main body, 2) Sharp trailing edge, 3) Serrated trailing edge.

3.7.3 Circular Cylinder

Motivated by the aircraft landing gear noise reduction, two cylinders in tandem configuration were investigated. The reason for choosing this setup is that the flow interaction between the two cylinders in tandem configuration is close to the flow nature that occurs when air flows over the aircraft landing gear. This type of interaction is likely to have significant role in the noise radiated from aircraft landing gear.

The DBD plasma actuator is used to control both the narrowband tonal noise and the interaction broadband noise radiated from two cylinders in tandem configuration. The cylinders have the same diameter and the distance between the centers of the two cylinders is $L/D = 4$. This spacing is chosen in order to ensure that each cylinder will independently produce vortex shedding [Zdravkovich, (1981)]. Both cylinders are made of polycarbonate tube and have diameter of 16 mm, length of 300 mm and 2 mm wall thickness. The cylinders were fixed by two side plates which are extended from the nozzle sides. A schematic of the tested cylinder is illustrated in Fig. 3.11.

Before testing the tandem cylinders case, the single cylinder is investigated first. The actuator was placed at different angles, θ_j range from 27° to 153°. The angles represent the place where the plasma jet is initiated and are measured from the front stagnation point. On the other hand, for the tandem cylinders case, three actuation set ups were investigated; 1) actuation of the upstream cylinder only, 2) the actuation of the downstream cylinder only, with plasma induced jet in the upstream direction (against the incoming flow direction), and 3) combination of 1 and 2, where both cylinders are simultaneously actuated. The cylinders were tested at free stream velocity of 10 ms^{-1} corresponding to a subcritical Reynolds based on the cylinder diameter of $Re_D = 1.1$ x 10^4.

a) Single cylinder

Upstream Cylinder (UC)   Downstream Cylinder (DC)

b) Tandem cylinders
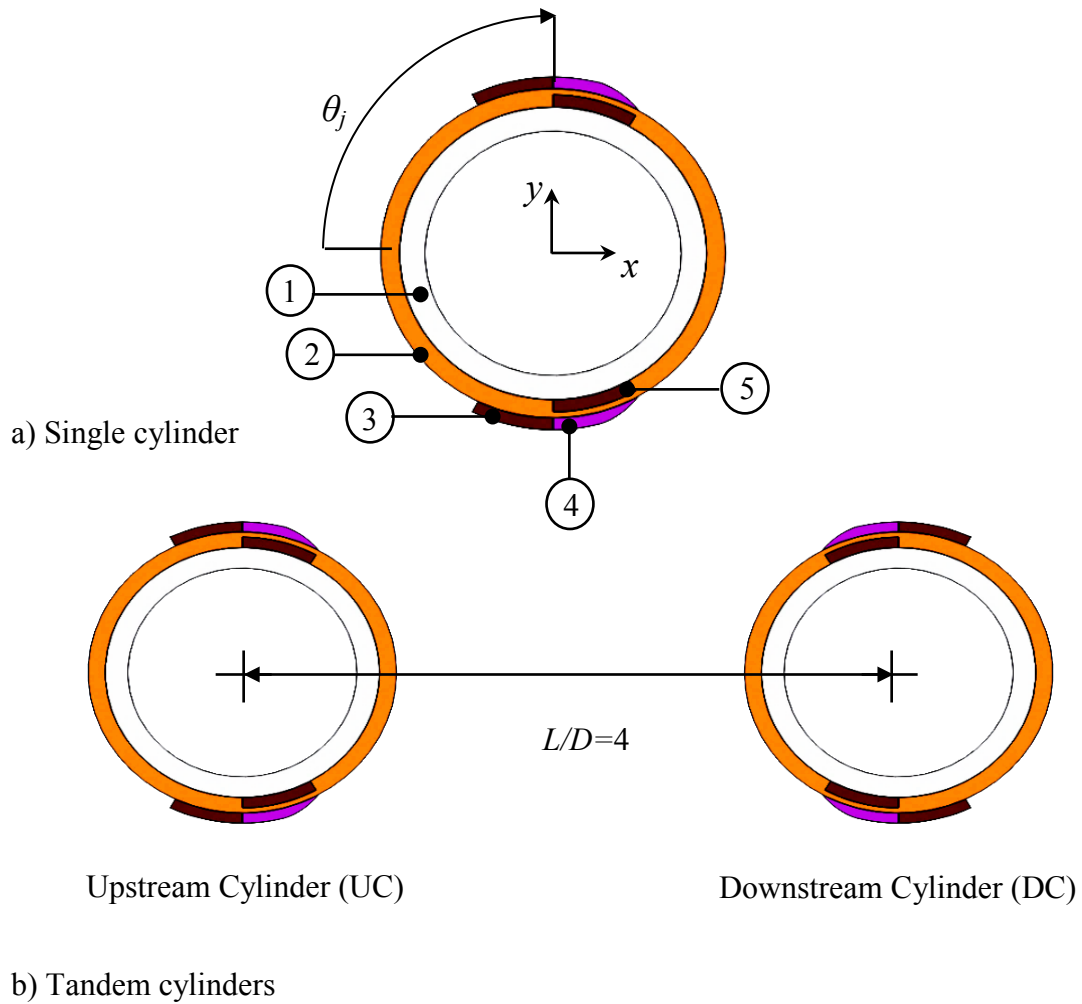
Figure 3.11 Schematic of the tested cylinder: 1) Polycarbonate cylinder, 2) Kapton tape, 3) Exposed electrode, 4) Plasma region, and 5) Ground electrode.

Chapter 4

Blunt Trailing Edge Flat Plate

4.1 Introduction

The findings of application of plasma actuator at the blunt trailing edge of a flat plate are presented in this chapter. The impact of three plasma actuator configurations, namely PA1, PA2 and PA3 on the aerodynamic noise and the hydrodynamic field is discussed. A description of the flat plate model and the plasma configurations used in the current study will be given in section 4.2. Flow characteristic and the design of the three configurations of plasma actuator will be provided in section 4.3. The aeroacoustic and hydrodynamic field results for the plasma actuators PA1, PA2, and PA3 will be discussed in sections 4.4, 4.5, and 4.6 respectively. The effect of spanwise actuation for the reduction of the bluntness-induced narrowband noise by a NACA 0012 blunt and with cut-in type serrated trailing edge airfoil will be given in section 4.7. Finally, a summary of all the experimental results will be provided in section 4.8.

4.2 Flat Plate Model and Plasma Configurations

A flat plate with a chord length of 0.15 m and width of 0.3 m is shown in Fig 4.1. The plate has and elliptic leading edge, the same as NACA 0012, which is used here to ensure a smooth entry for the incoming flow. The trailing edge of the flat plate is truncated and has a thickness of 0.006 m. In order to ensure a good level of two dimensionality of the flow over the flat plate, the flat plate was placed between two side plates at a zero incidence with respect to the incoming jet flow direction. In this study the boundary layer on the top and bottom surfaces of the plate were artificially tripped into turbulent using rough sandpaper. As a result, the vortex shedding from the blunt trailing edge is generated as a result of the roll up of the turbulent shear layer in the vicinity of the blunt trailing edge. The experiments conducted in this section were performed over Reynolds number range 0.75 and 4 x 10^5 based on the chord length.

The plasma actuator used in the current steady is a typical aerodynamic plasma actuator also known as the Dielectric Barrier Discharge plasma actuator (DBD). It is worth noting that the

main objective of this PhD work is to employ the existing technology of the DBD plasma actuator to produce the flow controlling jet, rather than focusing on the development of the DBD plasma actuator to produce a higher jet velocity. Therefore, the results presented here can be treated as a proof of concept for the benefit of DBD plasma actuator in the aeroacoustic field. Any positive outcomes demonstrated in this thesis will have a great impact in the future when a more advanced plasma actuator system is developed elsewhere; where higher output velocity for the flow-control jet can be realized. The plasma actuator adopted in this study basically has two electrodes. The first electrode is exposed to the air and is connected to a high-voltage power supply source, while the second electrode is usually grounded and covered by dielectric material. The dielectric material used in the current steady is the Kapton tape, which is known to have a high dielectric strength. The purpose of using the dielectric material is to prevent arc occurrence between the two electrodes and to allow for discharge-accumulation near the exposed electrode.

Three configurations of the plasma actuator were investigated in the current study. They are named according to the generated electric wind direction. The first plasma actuator, which generates a tangential plasma jet, is called PA1. In this configuration, the generated plasma along the surface of the grounded electrode draws a high momentum air from the free stream towards the wall near the blunt edge to modify the characteristics of the separated shear layer. The second configuration is called the PA2, which generates electric wind parallel to the blunt face of the trailing edge. This configuration is similar to the "transverse plasma" adopted by Nati et al. (2013). This particular design draws the air before it separates from the upper and lower side of the trailing edge, where the two downward jets merge into one jet towards the center of the wake region as shown in Fig 4.2. The last configuration is called the PA3, which generates electric wind in the spanwise direction. This actuator is situated at 4 mm away from of the trailing edge of the flat plate in the upstream direction. It has 13 copper strips of 30 mm (length) x 6 mm (width) on both the upper and lower surfaces. The distance between each two copper strips is 9 mm. The material used for the exposed and grounded electrodes through the course of this study is the copper tape.
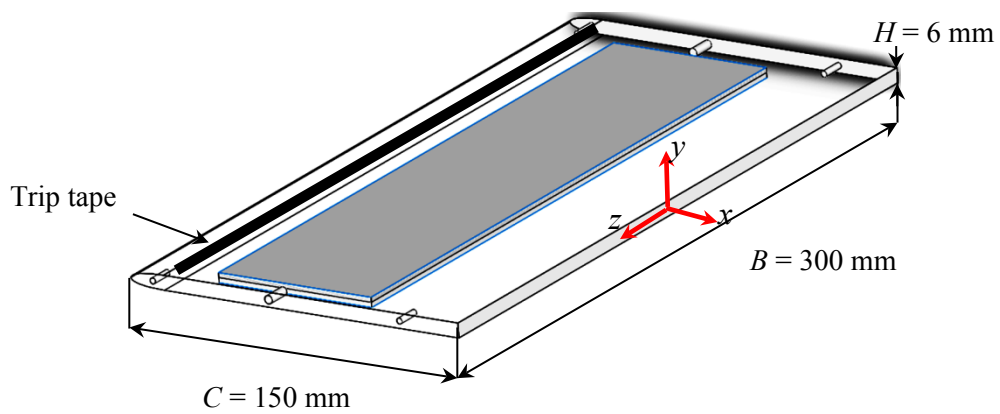
Figure 4.1 Flat plate model with blunt trailing edge investigated in the current study.

(a) PA1   (b) PA2

(c) PA3
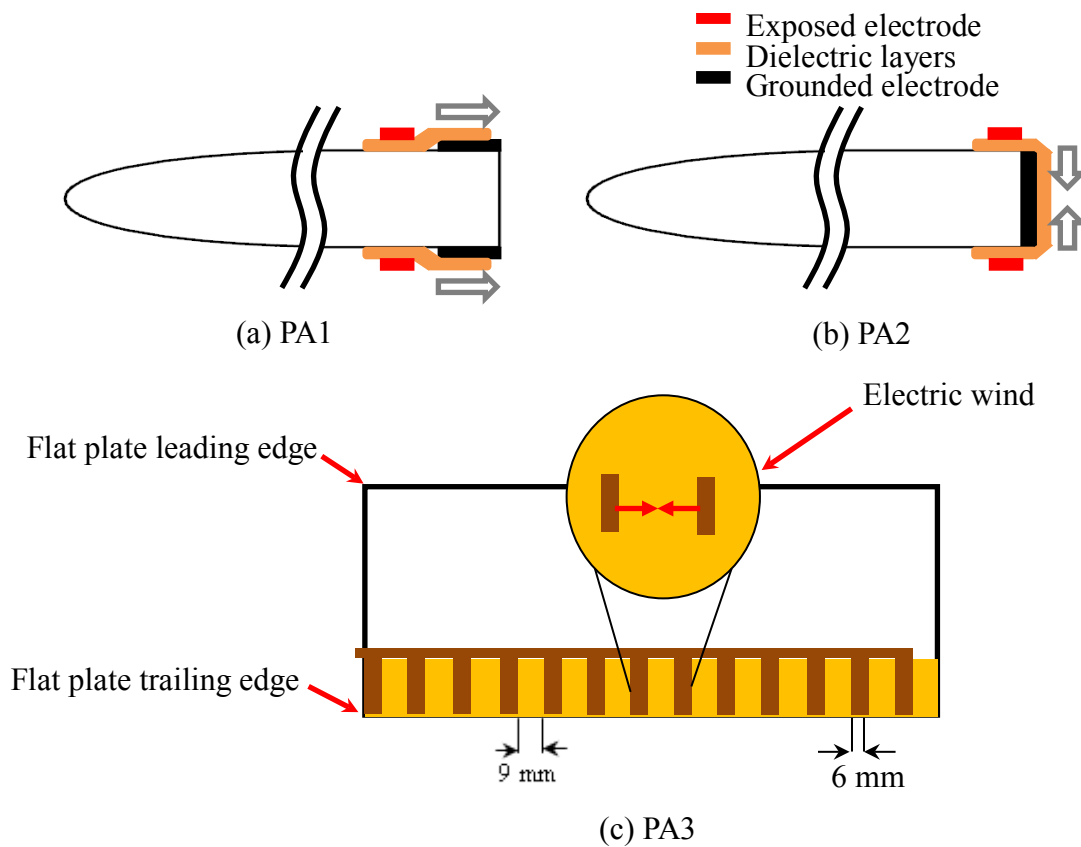
Figure 4.2 Plasma actuator configurations.

Parameter	PA1	PA2	PA3
Exposed electrode (length and width)	280 and 6 mm	280 and 6 mm	15mm and 6 mm
Ground electrode (length and width)	280 and 10mm	280 and 6 mm	280 and 10 mm
Dielectric thickness	0.125 mm	0.125 mm	0.125 mm
Applied voltages and frequencies	2.4 to 4.8 kV and 6 to 8 kHz		
Applied signal shape	Sinewave		

Table 4.1 Geometrical and electrical parameters of the plasma actuators.

4.3 Flow and Plasma Actuator Characterisation

4.3.1 Flow Characterisation

In order to determine the hydrodynamic properties near the trailing edge, velocity profile of the boundary layer were investigated near the trailing edge using hot wire. The measurement was conducted at 10 mm away from the trailing edge in the upstream direction (the zero position is at the center of the blunt base). The measured velocity profile is illustrated in Fig. 4.3.
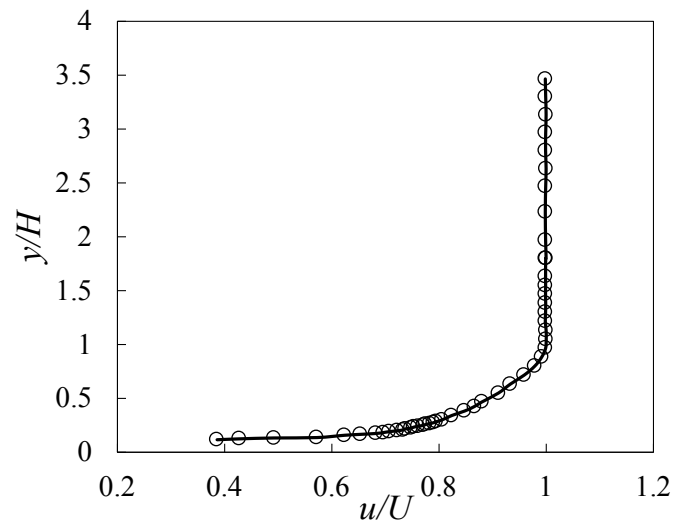
Figure 4.3 Boundary layer velocity profile on the upper surface at x = -10 mm from the trailing edge and at Re = 7.5 x 10^4.

The characteristics of the boundary layer were obtained from the velocity profile, Fig. 4.3. These parameters include the boundary layer thickness (δ_{99}), displacement thickness (δ^*), momentum thickness (θ), and shape factor (δ^*/θ). Note that δ_{99} is determined as the vertical position where $u = 0.99\ U_\infty$, where U_∞ is the free stream velocity. Table 4.2 demonstrates an overview of the boundary layer characteristics.

Parameter	Value	Unit
U_∞	7.5	ms^{-1}
δ_{99}	5.5	mm
δ^*	0.84	mm
θ	0.58	mm
δ^*/θ	1.45	-

Table 4.2 Boundary layer characteristics at x = -10 mm from the blunt trailing edge.

4.3.2 Plasma Actuator Characterisation

The parameters that can affect the performance of the plasma actuators (PA1, PA2, and PA3) can be divided into two categories; geometrical and electrical parameters. The geometrical parameters include; electrode width, length, thickness, and the separation distance between the exposed electrode and the grounded electrode. For the electrical parameters, these include the voltage, frequency, output voltage wave form, dielectric material, and dielectric thickness. The main aim of the current work is to reduce the aerodynamic noise generated by the vortex shedding. Before that, the overall sound pressure level (OASPL) is used to determine the best combination of the aforementioned geometrical and electrical parameters. Once the effective combination of the parameters has been identified, the same combination will be used for the rest of the tests. An intensive effort has been done on the DBD plasma actuator modification. Previous studies on the optimisation of plasma actuator suggest that four geometrical parameters can significantly affect the actuator efficiency. These are the thickness of the exposed electrode, width of the ground electrode, gap or the horizontal thickness between the electrodes, and dielectric thickness. Enloe et al. (2004) reported that the thickness of the exposed electrode can

significantly affect the electro hydrodynamic force generated by the plasma actuator. They found that using thinner exposed electrodes can lead to higher induced thrust compare with the wire-type exposed electrodes. Moreover, the wider the grounded electrode, the higher the induced electric wind. However, the width of the grounded electrode will increase the extension of the generated plasma before reaching a plateau. Post & Corke (2006) study the effect of the gap/the overlap between the exposed and the grounded electrodes. They suggest that using a small gap between the electrodes can lead to the formation of a more uniform plasma generation along the electrodes. Based on the findings of these studies, thin expose and grounded electrode and a zero gap between them were chosen to ensure a robust and uniform plasma generation.

Another important geometrical parameter is the dielectric thickness. Thick dielectric material allows for better electrical isolation so that higher driving voltages can be used. However, it will induce lower electric wind velocities compared with thin dielectric at equal voltage, [Forte et al. (2006)]. The effect of dielectric thickness on the aerodynamic noise reduction was evaluated based on the Overall Sound Pressure Level (OASPL) using different input voltages $V_{(input)}$ and input frequencies $f_{(input)}$. The value of the (OASPL) can be calculated by integrating the acoustic pressure fluctuation over a finite range of frequencies that correspond to the induced vortex shedding narrowband tonal noise (between 176 and 317 Hz) at $U = 7.5$ ms^{-1}. The relation between the number of the dielectric layers used, i.e. the total thickness and the ΔOASPL at $3 \leq V_{(input)} \leq 7.5$ kV, at a frequency of 8 kHz is demonstrated in Fig. 4.4. The ΔOASPL represents the difference in the OASPL between the plasma off case and the plasma on case. Therefore a positive ΔOASPL represents the reduction in the overall narrow band tonal noise level, and the opposite is true for the negative value for the ΔOASPL. It can be seen that as the $V_{(input)}$ increases the ΔOASPL increases as well, but reaches a plateau at the maximum input voltage. As shown in Fig. 4.4, the maximum tonal noise reduction was achieved at $V_{(input)} = 5.5$ kV between 3 and 4 layers of the dielectric material. Despite the possibility of not being the most optimum choice for the aerodynamic noise reduction, 5 layers of the dielectric material was finally chosen for the entire experiments. This is because it offers better electrical isolation and still producing a higher level of noise reduction when compared to the 6 layers case. The total thickness of the 5 layers of the dielectric film is about 0.125 mm, which is equivalent to $y^+ = 3.75$ near the blunt trailing edge. The skin friction coefficient, thereby the friction velocity as the scaling parameter, for the wall unit was calculated from the Clauser chart method.
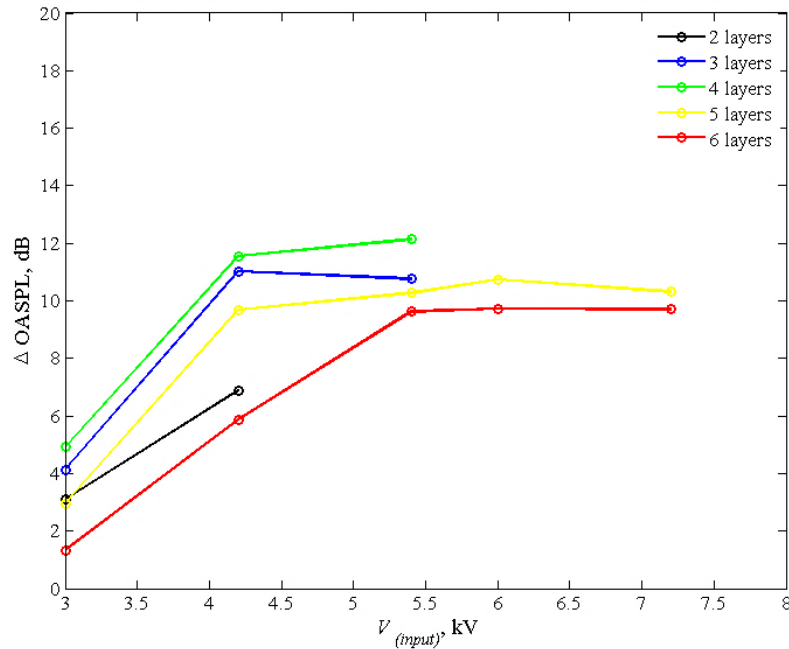
Figure 4.4 Effect of the number of the dielectric layers on ΔOASPL at different input voltages using PA2 plasma actuator and at f(input) = 8 KHz.
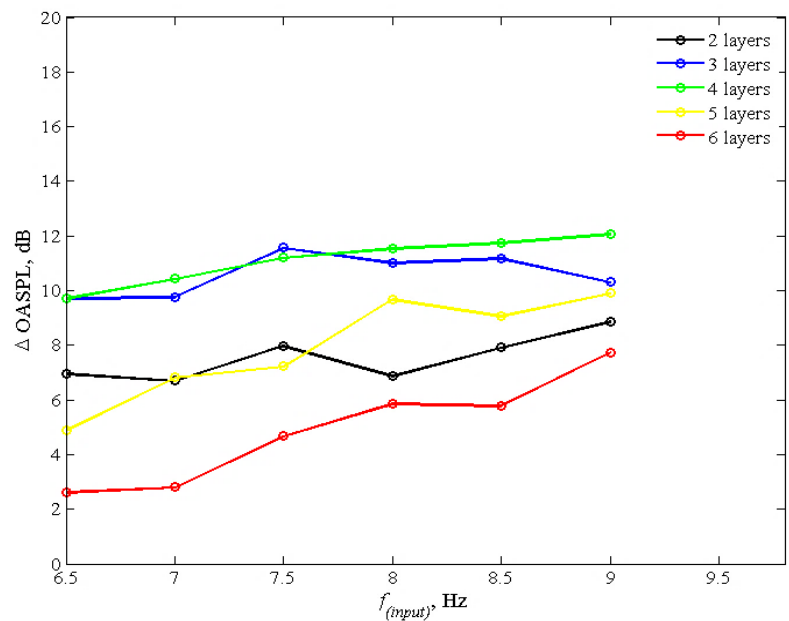
Figure 4.5 Effect of the number of the dielectric layers on ΔOASPL at different input frequencies and at V(input) =4.2 kV using PA2 plasma actuator.

The relation between the ΔOASPL and the number of dielectric layers at different range of input frequencies ($6.5 \leq f_{(input)} \leq 9$ kHz) was also investigated. As shown in Fig. 4.5, it can be seen that

the overall reduction in the vortex shedding tonal noise improves as $f_{(input)}$ increases. Although the maximum noise reduction was achieved at $f_{(input)}$ = 9kHz and 4 layers of the dielectric film, the entire experiments were conducted at $f_{(input)}$ = 8 kHz with 5 layers of the dielectric film because it provides a more uniform plasma discharge and is more stable in the plasma generation.

4.4 Acoustic and Hydrodynamic Fields –PA1

4.4.1 Acoustic Field Results

The effect of the plasma actuator PA1 on the aerodynamic noise of the flat plate with blunt trailing edge of H = 6 mm was investigated first. The experiment was conducted at free stream velocity U = 7.5 ms^{-1} and at zero incidence with respect to the incoming jet. For every increment of 0.6 kV, four input voltages between 2.4 and 4.2 kV and two excitation frequencies $f_{(input)}$ of 7 and 8 kHz were investigated. The frequency was non-dimensionalised by the bluntness H and the free stream velocity U. Figure 4.6 illustrates the Sound Pressure Level SPL spectra for both the plasma off "baseline case" and plasma actuator PA1. A distinct narrowband tonal noise peak at fH/U = 0.19, which correspond to acoustic frequency of 238 Hz can be seen in the spectra of the baseline case. This characteristic non-dimensional frequency is very close to the Strouhal number of the vortex shedding associated with the bluff bodies, [Sallet et al. (1967), Brinich et al. (1975), and Thomas et al. (2008)]. Therefore, the narrowband noise peak in the acoustic spectra of Fig. 4.6 is very likely to be related to the vortex shedding from the blunt trailing edge. When the flat plate is subjected to the plasma actuator PA1, the results show that plasma actuator PA1 has no significant effect on the bluntness induced vortex shedding tonal noise at $V_{(input)} \leq 3.6$ kV. However, moderate level of noise reduction of up to 2 ± 0.5dB can be achieved at the maximum input voltage and frequency, $V_{(input)}$ = 4.2 kV, $f_{(input)}$ = 8 kHz, respectively. The relation between the acoustic tonal noise and velocity field pertaining to the vortex shedding will be further explained in Section 4.4.2.
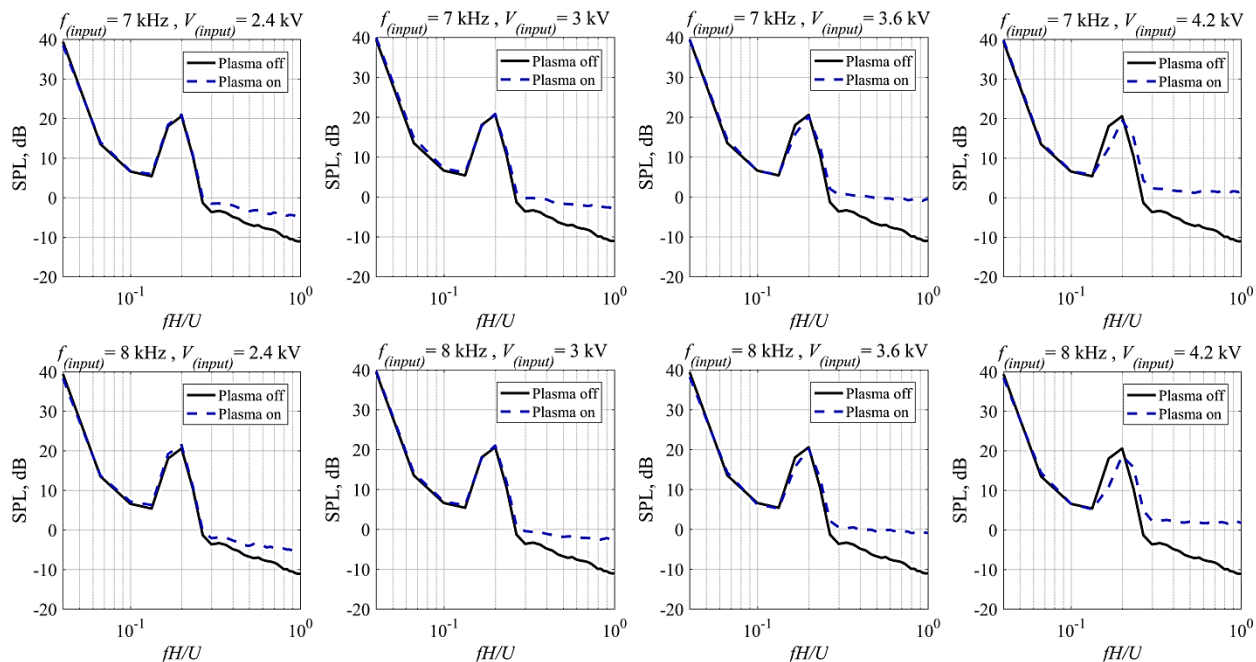
Figure 4.6 SPL spectra for the flat plate subjected to plasma actuator PA1 at free stream velocity U = 7.5 ms^{-1}, f$_{(input)}$ = 7, 8 kHz, and V$_{(input)}$ = 2.4-4.2 kV.

Despite the moderate level of noise reduction that can be achieved by this plasma configuration, PA1 was also tested at different free stream velocities $7.5 \le U \le 40$ ms^{-1} in order to compare its performance with the other plasma configurations, PA2 and PA3. The difference in the sound pressure level ΔSPL contours for the flat plate with and without plasma actuation are demonstrated in Fig. 4.7. Like the ΔOASPL defined earlier, the ΔSPL is the difference between the SPL of the baseline and plasma on cases. Therefore, positive ΔSPL value represents the reduction in the aerodynamic noise, and the opposite is true. The contours are divided into three different zones, A, B, and C. The first region is Zone A, which denotes the low frequency region. This region is characterized by ΔSPL values close to zero, which indicates that the current plasma actuator PA1 does not have significant effect on the acoustic field within this range of frequencies. The middle region, Zone B, represents the moderate frequency region, which denotes the upper and lower limit of frequency bandwidth (between 176 and 317 Hz) pertaining to the bluntness induces vortex shedding tonal noise. This region is characterized by slight reduction in the tonal noise as the $V_{(input)}$ from 2.4 to 4.2 kV for free stream velocities $U \le 15$ ms^{-1}.

The last region is the Zone C, which can be characterized by an increase in the broadband noise at the high frequency and low free stream velocity. There is also a distinct non-aerodynamic tone which occurs at the applied frequency $f_{(input)}$ and its harmonics at low free stream velocities. However, the radiation of the tone noise becomes less significant at the higher free stream velocities ($U \geq 20$ ms^{-1}). This is because the actuator self-noise has already been masked by the aerodynamic noise generated by the free jet and the blunt trailing edge of the plate.
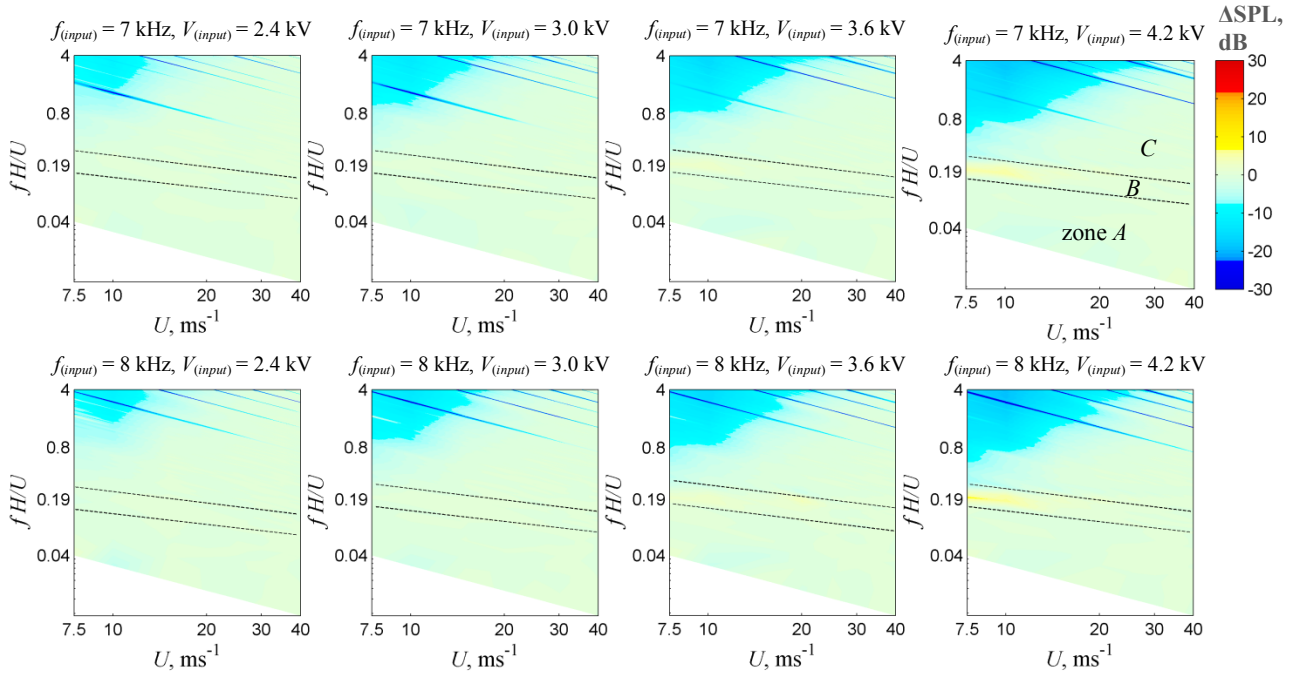
Figure 4.7 ΔSPL spectra by the PA1 plasma actuator operated at $f_{(input)}$ = 7, 8 kHz and $V_{(input)}$ = 2.4–4.2 kV at U = 7.5–40 ms^{-1}.

4.4.2 Hydrodynamic Field Results

4.4.2.1 Instantaneous Flow Field

The PIV results of the instantaneous streamwise velocity component, and the associated spanwise vorticity, Ω_z, for the flat plate subjected to the plasma actuator PA1 at $U = 7.5$ ms^{-1} are presented in Fig. 4.8 and 4.9 respectively. Note that $V_{(input)}$ = *4.2* kV and $f_{(input)}$ = *8* kHz respectively. These input voltage and frequency were chosen after considering the acoustic performance of the PA1 plasma actuator discussed earlier in Section 4.4.1.
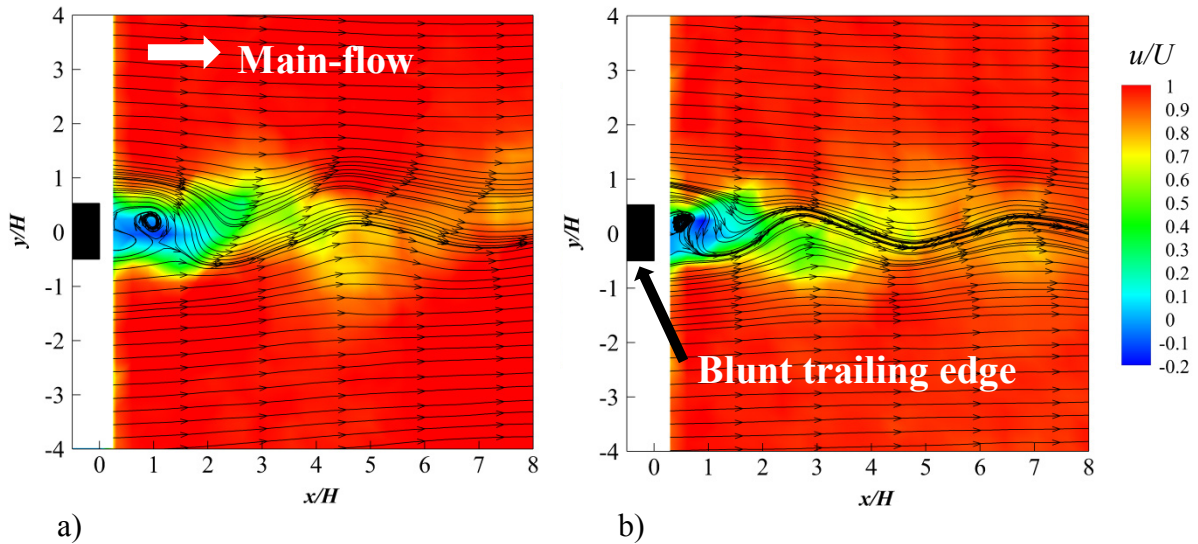
Figure 4.8 The instantaneous streamwise velocity component for the flat plate subjected to a) plasma off and b) plasma actuator PA1 at free stream velocity U = 7.5 ms^{-1}.
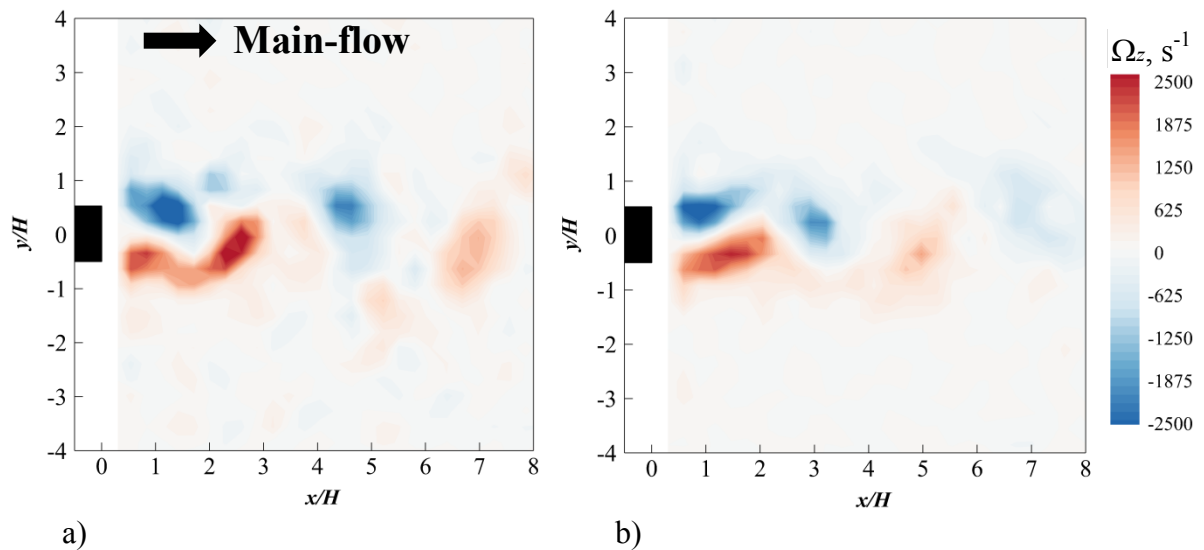
Figure 4.9 The instantaneous spanwise vorticity Ω_z component for the flat plate subjected to a) plasma off and b) plasma actuator PA1 at free stream velocity U = 7.5 ms^{-1}.

Due to the laser light reflection at the vicinity of the blunt trailing edge, the nearest streamwise location, where the PIV field of view (FOV) can still display the velocity field clearly is at $x/H \approx 0.3$ ($H = 6$ mm). It can be seen from Fig. 4.8a for the plasma off case, a wake deficit region is generated behind the blunt trailing edge of the flat plate and a recirculation region with non-convective air pocket presents just behind the blunt base. However, when plasma actuator PA1 is turned on, a wake region still can be seen behind the blunt trailing edge of the flat plate but the

non-convective air pocket shrinks and becomes closer to the trailing edge base as shown in Fig. 4.8b. This behavior is seen in the time-averaged streamwise velocity contour when the plate is subjected to plasma actuator Fig. 4.10b. In order to obtain more information about the effect of the plasma actuator PA1 on the wake region, time-averaged flow field and POD analysis were conducted. The time-averaged flow field results will be discussed in the next section.

Figure 4.9 shows the instantaneous spanwise vorticity field contours for the plasma off and plasma on cases. For the plasma off case, negative and positive shear layers separate from the top and the bottom edge of the flat plate trailing edge, respectively. These separated shear layers start to roll up and shed vortices in the wake region close to the blunt trailing edge of the flat plate as shown in Fig.4.9a. When the flat plate is subjected to the plasma actuator PA1, the results show that the vortex shedding in the wake region slightly becomes closer to the trailing edge of the flat plate, which suggests a small increase in the shedding frequency. This increase in the shedding frequency is seen in Fig. 4.6 when the plate is activated at $V_{(input)} = 4.2$ kV and demonstrated in the POD modes analysis, as shown in Fig.4.15b. More details will be provided in the Time averaged flow field study.

4.4.2.2 Time-Averaged Flow Field

PIV time-averaged flow quantities contours, such as the streamwise velocity, vertical velocity, spanwise vorticity, and unsteady velocity fluctuations for the flat plate subjected to the plasma off and plasma on (PA1) at free stream velocity $U = 7.5$ ms^{-1} will be addressed in this section. The uncertainty in the mean velocity reaches 0.8% of the free stream velocity. Both the mean velocity field and velocity fluctuations are non-dimensionalised by the free stream velocity U. Figure 4.10 illustrates the streamwise velocity component for the flat plate for both the plasma off and plasma on, PA1 case. Like the instantaneous flow field discussed earlier, the time-averaged streamwise velocity field shows the occurrence of the wake deficit region resulted from the separation of the shear layers from the blunt trailing edge for both the plasma off and plasma on cases. The actuation of PA1 does not have significant effect of the wake deficit region, where two symmetrical vortices still exist in the recirculation region even with the plasma actuation. These observations confirm what was seen in the SPL spectral where very small level of noise reduction could be obtained by PA1. The velocity contours in the normal

direction for both the plasma on (PA1) and plasma off cases are illustrated in Fig. 4.11. For both cases, the results show large opposing velocity in the transverse direction occurs at the end of the wake deficit region. The plasma actuator does not seem to affect the normal velocity field, consistent with the previous findings.

Figure 4.10 Time-averaged streamwise velocity component for the flat plate subjected to a) plasma off and b) plasma actuator PA1 at free stream velocity U = 7.5 ms^{-1}.

Next, the time-averaged spanwise vorticity field, Ω_z, is determined from the calculated mean velocity component for the flat plate. The time-averaged spanwise vorticity contours in the *x-y* plane for both the plasma off and plasma on cases are presented in Fig. 4.12. The contours of the spanwise vorticity for the plasma off case show that the separated shear layers from the blunt trailing edge of the flat plate produce a region of negative and positive vorticity of with highest intensity values encompassing, $\pm 0.2 \leq y/H \leq \pm 0.8$, and $x/H \leq 2.5$. When the plasma actuator PA1 is turned on, the same spanwise vorticity field as the plasma off case can be observed. In addition, it can be seen that the significant spanwise vorticity is almost parallel to the main flow direction and it does not correspond the shedding motion responsible for generation the tonal noise. The reason is that the PIV system has a low repetitive rate ($\sim$ 15Hz) compared with the vortex shedding frequency ($\sim 10^2$ Hz). Therefore it is unable to capture the unsteady motion. However, the unsteady motion of the vortex shedding can still be depicted vividly by the instantaneous spanwise vorticity field presented in Fig. 4.9.

The velocity fluctuation contours in the streamwise and normal directions in the wake flow were constructed and non-diemsionalised using the free stream velocity *U*. The streamwise velocity

fluctuations contours for both the plasma off and plasma on (PA1) are shown in Fig. 4.13. For the plasma off case, the results show that a region of high intensity of velocity fluctuations is generated where the shear layer separates from the upper and lower sides of the blunt trailing edge and extends in the downstream direction up to x/*H* ≈ 4. When the plasma actuator PA1 is turned on, the streamwise velocity fluctuations produce the same layout and intensity level as the plasma off case. The velocity fluctuations in the vertical direction are illustrated in Fig. 4.14. A region of high intensity of velocity fluctuation in the center of the wake region can be seen for both the plasma off and plasma on PA1. The low level of vertical velocity fluctuations throughout the near wake region, i.e. *x/H* ≤ 1 is due to the local non-recirculation flow at the vicinity of the blunt trailing edge. This configuration of the plasma actuator is not capable of reducing velocity fluctuations significantly in both the streamwise and normal directions.

Finally, the Proper Orthogonal Decomposion POD analysis is performed in order to capture the high energy, large coherent structures in the wake region after the blunt trailing edge. The contours of the highest energy modes, mode 1 and mode 2, colored by the velocity components in the streamwise and normal directions for the plasma off and plasma on cases, are presented in Fig. 4.15 and 4.16, respectively. Figure 4.15 shows the first mode in both *u* and *v* for the plasma off and plasma on (PA1). It can be seen that for the plasma off case, the first POD mode, for the streamwise velocity component demonstrates several anti-symmetrical structures that propagate alternately in the downstream direction. For plasma on case, although the high energy vortex shedding structures still exist in the wake region and exhibit the same trend as the plasma off case, the actuation of the plasma actuator PA1 reduces the spacing between the successive structures, which become more compact when compared to the plasma off case. On the other hand, the velocity component in the normal direction *v* for both the plasma off and plasma on cases has a symmetric pattern in the normal direction and alternate in the streamwise direction. Again for plasma on case, it can be seen that the plasma actuator is not capable to suppress the high energy vortex shedding structures in the wake region.

The second POD mode in the *u* and *v* velocity components for the plasma off and plasma on cases is presented in Fig.4.16. For both the plasma off and plasma on cases, on can notice that the high energy structures that appear in the wake region for plasma off case still exist even when plasma actuator PA1 is turned on, although these structures are now more compact.

Figure 4.11 Time-averaged normal velocity component for the flat plate subjected to a) plasma off and b) plasma actuator PA1 at free stream velocity U = 7.5 ms⁻¹.

Figure 4.12 Time-averaged spanwise vorticity contours for the flat plate subjected to a) plasma off and b) plasma actuator PA1 at free stream velocity U = 7.5 ms⁻¹.

Figure 4.13 Figure 4.13 Time-averaged streamwise unsteady velocity for the flat plate subjected to a) plasma off and b) plasma actuator PA1 at free stream velocity U = 7.5 ms^{-1}.

Figure 4.14 Time-averaged normal unsteady velocity for the flat plate subjected to a) plasma off and b) plasma actuator PA1 at free stream velocity U = 7.5 ms^{-1}.
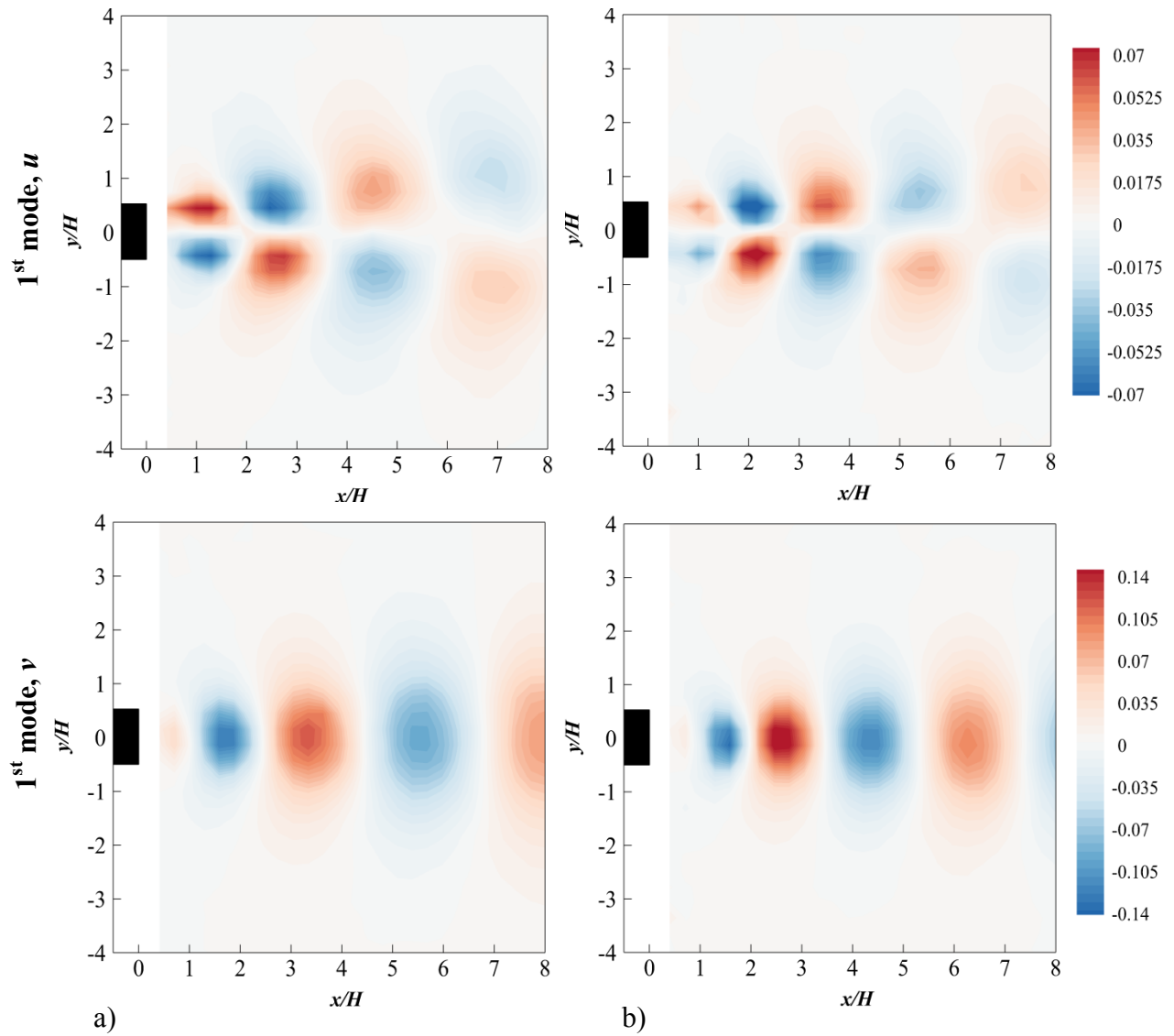
Figure 4.15 First POD mode in u and v for, a) plasma off and b) plasma actuator PA1 at free stream velocity U = 7.5 ms^{-1}, f$_{(input)}$ = 8 kHz and V$_{(input)}$ = 4.2 kV.
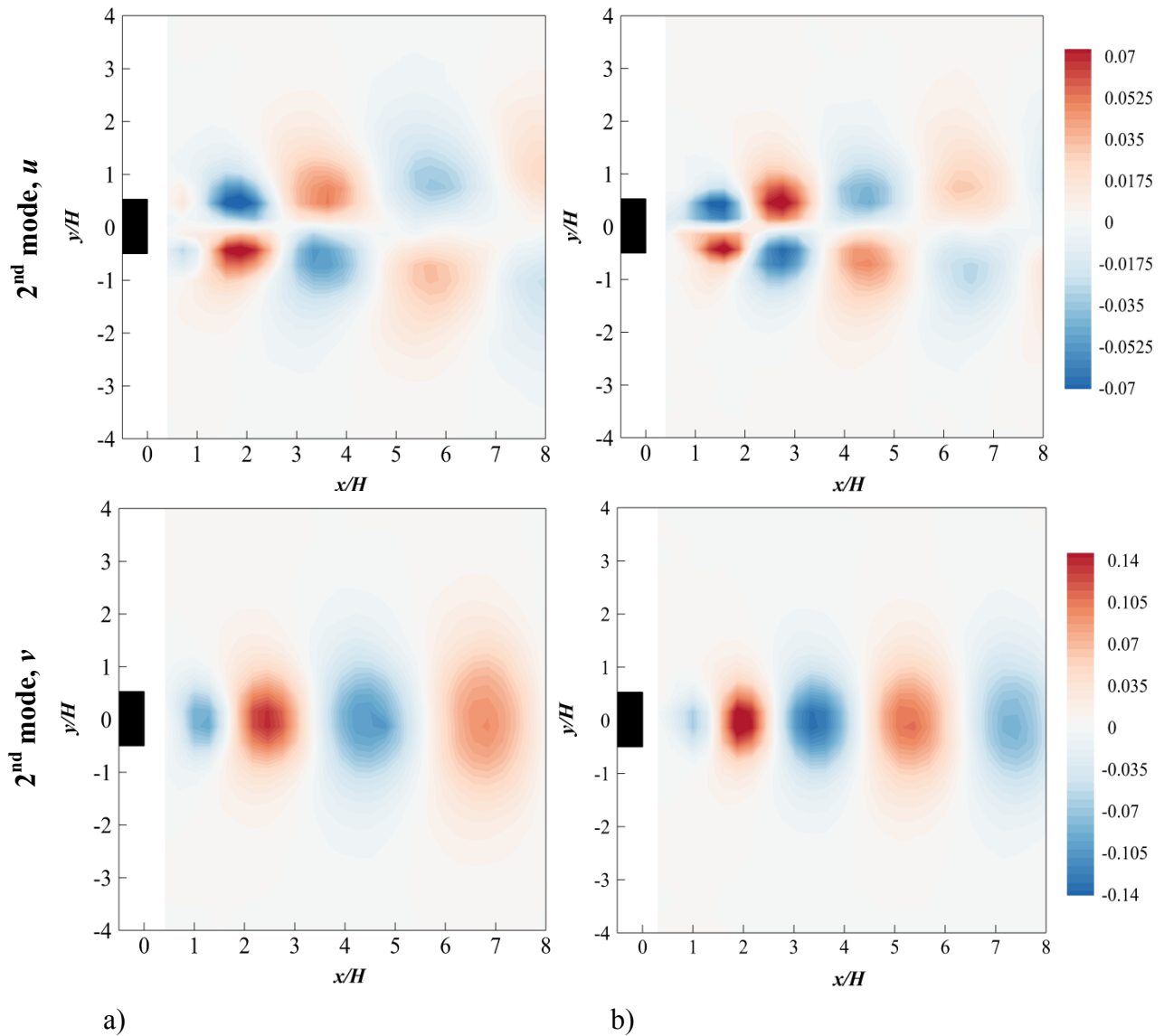
Figure 4.16 Second POD mode in u and v for, a) plasma off and b) plasma actuator PA1 at free stream velocity U = 7.5 ms^{-1}, f$_{(input)}$ = 8 kHz and V$_{(input)}$ = 4.2 kV.

4.5 Acoustic and Hydrodynamic Fields–PA2

4.5.1 Acoustic Field Results

The second configuration of the plasma actuator that was investigated in the current study is called the PA2. The effect of the PA2 plasma actuator on the SPL at $V_{(input)}$ = 2.4 - 4.8 kV and $f_{(input)}$ = 7 and 8 kHz for the flat plate with blunt trailing edge at U = 7.5 ms^{-1} is presented in Fig.4.17. The results show that as the $V_{(input)}$ increases from 2.4 to 4.8 kV the narrowband vortex

shedding tonal noise that exists in the baseline acoustic spectra level can be further suppressed. Figure 4.17 demonstrates an 8.3 ± 0.5dB reduction in the vortex shedding narrowband tonal noise for every 1 kV increase in the input voltage. Note that this linear trend is only correct for a certain range of input voltages 2.4kV ≤ $V_{(input)}$ ≤ 4.2 kV. It can be seen that there is no noise reduction at the lowest input voltage $V_{(input)}$ = 2.4 kV, while increasing the $V_{(input)}$ to 4.2 kV results in a 14.5 ±0.5dB reduction in the vortex shedding tonal noise. Further increase in the input voltage level to $V_{(input)}$ = 4.8 kV results in a slight improvement in the actuator performance with the maximum noise reduction of 15.2 ±0.5dB. Although, the difference in the tonal noise reduction between the $V_{(input)}$ = 4.2 and 4.8 kV is small, results to discussed later will show that the highest $V_{(input)}$ at 4.8 kV can lead to a better performance at higher free stream velocities U.

It will be interesting to investigate the effectiveness of the PA2 at higher free stream velocities 7.5 ≤ U ≤ 40 ms^{-1}. Figure 4.18 illustrates the contours of ΔSPL for the flat plate at $V_{(input)}$ = 2.4-4.8 kV, and two $f_{(input)}$ = 7 and 8 kHz. A positive ΔSPL means a reduction in the aerodynamic noise level, while the opposite is true. The domain of the ΔSPL contours is also divided in to three zones: A, B, and C, which are defined by both the free stream velocity and the dimensionless frequency fH/U. The result show that at low input voltage $V_{(input)}$ = 2.4 kV, no noise reduction can be achieved for all of the free stream velocities. When the input voltages $V_{(input)}$ increased to 3 kV, the maximum free stream velocity at which the plasma actuator still leads to a significant noise reduction is U = 10 ms^{-1}. At 3.6 kV, the corresponding maximum free stream velocity increases to U = 16 ms^{-1}. As the input voltage increases above 3.6 kV, the maximum free stream velocity at which the plasma actuator is still effective will increase as well. For instance, for $V_{(input)}$ = 4.2 - 4.8 kV, the maximum speed at which noise can still be reduced is 19 ms^{-1} and 22 ms^{-1} respectively. The results show that the $f_{(input)}$ has little effect on the level of the tonal noise reduction. It can be concluded that plasma actuator PA2 outperforms the plasma actuator PA1 in terms of the vortex shedding narrowband noise reduction.
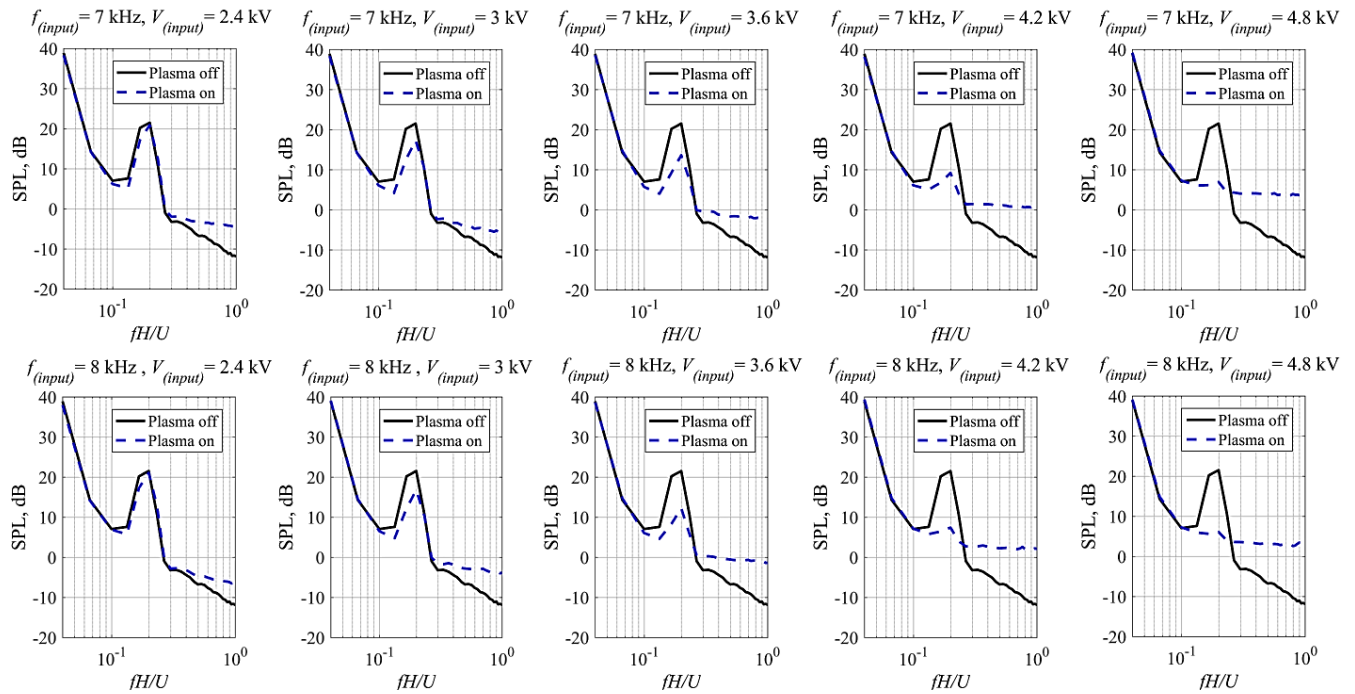
Figure 4.17 SPL spectra for the flat plate without plasma actuation (Plasma off) and with plasma actuation (PA2) at free stream velocity U = 7.5 ms⁻¹ at
V(input) = 2.4-4.8 kV, f(input) = 7 and 8 kHz.
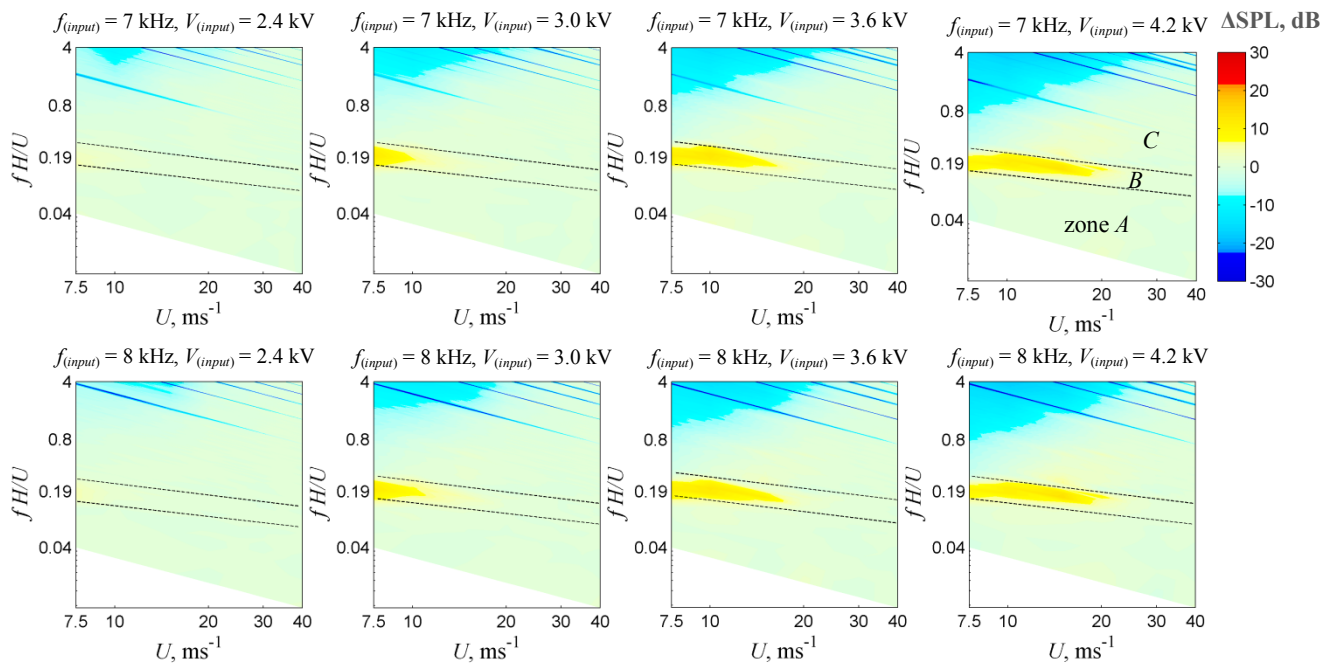
Figure 4.18 ΔSPL contours for the flat plate without plasma actuation (Plasma off) and with plasma actuation (PA2) at free stream velocity U = 7.5-40 ms⁻¹ at
V(input) = 2.4-4.8 kV, f(input) = 7 and 8 kHz.

4.5.2 Hydrodynamic Field Results

4.5.2.1 Instantaneous Flow Field

Before the investigation for the impact of the plasma actuator PA2 on the wake region behind the blunt trailing edge, the plasma actuator was activated at the quiescent, no flow condition at $V_{(input)}$ = 4.2 kV and $f_{(input)}$ = 8 kHz. Figure 4.19 demonstrates the electric wind generated by the plasma actuator PA2. The results clearly show that this plasma configuration is capable of generating an air jet $\hat{u}$ up to 1.8 ms^{-1}. The generated jet spreads uniformly as it propagates in the downstream direction and decays from 1.8 to 1.5 ms^{-1} within a longitudinal range of $0.5 \leq x/H \leq 4.5$. Although the induced plasma jet seems to be resilient enough to modify the wake region behind the trailing of the flat plate, it will be shown later that the mechanism of the tonal noise reduction is not entirely due to the direct momentum injection into the wake region.
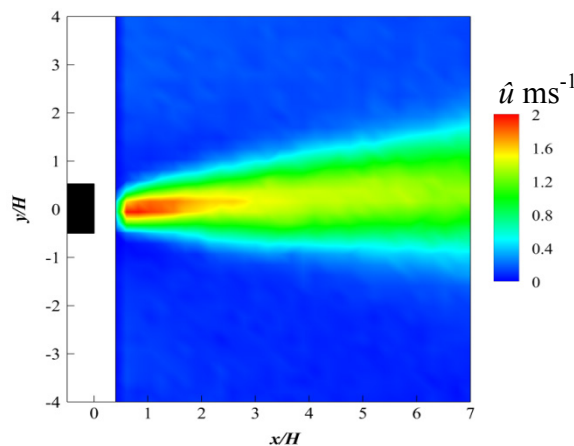
Figure 4.19 Plasma induced jet in quiescent air condition (no free jet) at where
$f_{(input)}$ = 8 kHz and $V_{(input)}$ = 4.2 kV.

In order to understand the mechanism of the aerodynamic noise reduction by the plasma actuator PA2, a number of flow measurements were conducted. The instantaneous streamwise velocity and spanwise vorticity contours behind the blunt trailing edge of the flat plate at U = 7.5 ms^{-1} are presented in Fig. 4.20 and 4.21, respectively. The tests were conducted at $V_{(input)}$ = 4.2 kV and at, $f_{(input)}$ = 8 kHz. This configuration is known to achieve high level of tonal noise reduction. From Fig. 4.20, it can be seen that when the plasma actuator is turned off a recirculation air pocket where $u/U \leq 0$ is generated behind the blunt trailing edge of the flat plate. This non-convective feature extends in the downstream direction directly behind the blunt base. However, when the plasma actuator PA2 is turned on, the recirculation region becomes larger in size and extends in

the downstream direction. This observation is seen in time-averaged streamwise velocity Fig.4.22b, where plasma actuation results in an elongation in the deficit region. Unlike the plasma off case, the separated shear layer from the upper and lower sides of the blunt trailing edge seems to be delayed in their interactions when the blunt trailing edge is subjected to the PA2 plasma actuator as shown in Fig. 4.21. This observation will be further discussed in the next section.
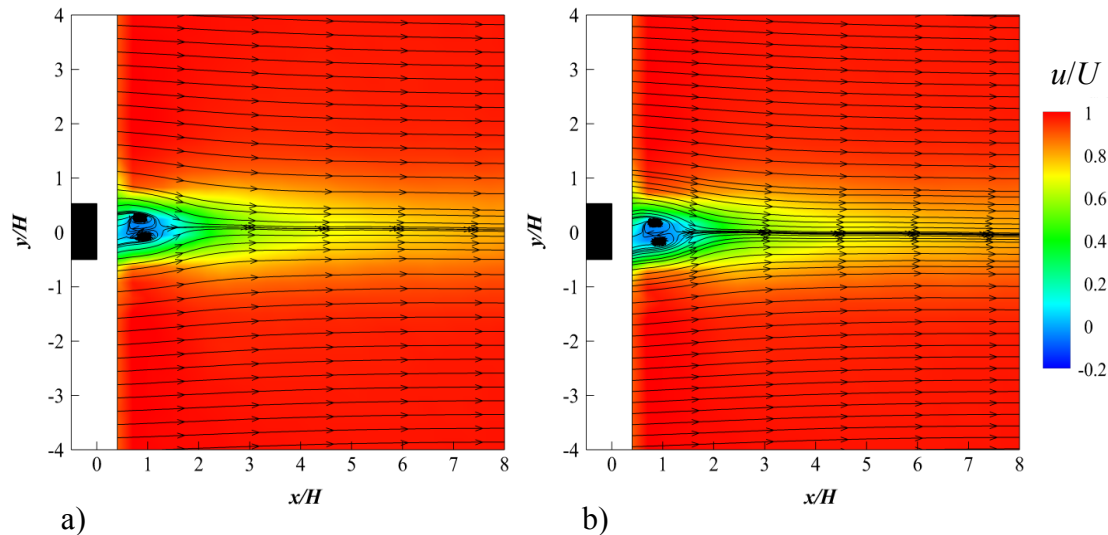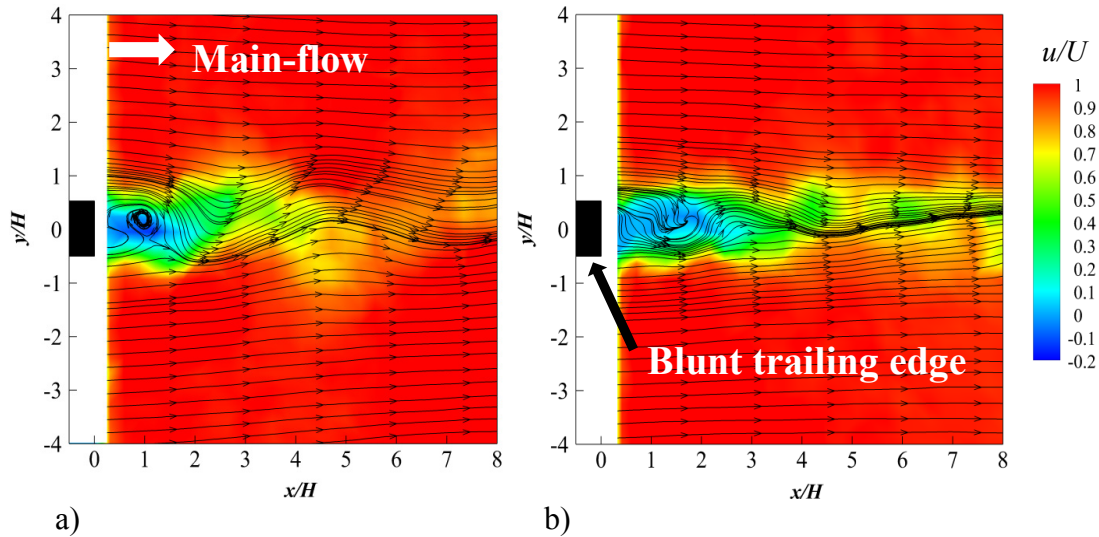

Figure 4.20 The instantaneous streamwise velocity component for the flat plate subjected to a) plasma off and b) plasma actuator PA2 at free stream velocity $U = 7.5 \text{ ms}^{-1}$.
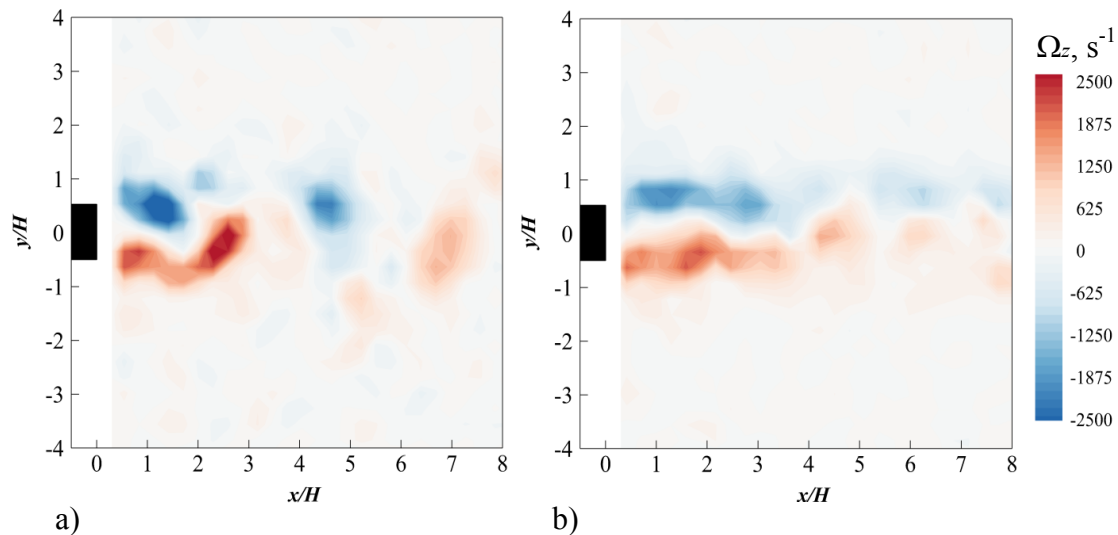
Figure 4.21 The instantaneous spanwise vorticity, Ωz, component for the flat plate subjected to a) plasma off and b) plasma actuator PA2 at free stream velocity $U = 7.5 \text{ ms}^{-1}$.

4.5.2.2 Time-Averaged Flow Field

The time-averaged flow quantities measured by PIV will be discussed in this section. The time-averaged streamwise velocity contours for the flat plate with blunt trailing edge at $U = 7.5$ ms^{-1} are presented in Fig. 4.22. The input voltage and frequency are $V_{(input)} = 4.2$ kV and $f_{(input)} = 8$ kHz, respectively. As discussed earlier, for the plasma off case, a recirculation region with streamwise velocity $u/U < 0$ is generated behind the blunt trailing edge. This region is related to the flow separation at the upper and lower sides of the blunt trailing edge, where the focal points of the re-circulating region are centered at $x/H \approx 1$. Further downstream the two separated shear layers start to interact with each other and form a convective shear flow where the streamwise velocity $u/U > 0$. However, when plasma actuator PA2 is turned on, one can notice that unlike the plasma off case, the recirculating air pocket now shifts from the blunt trailing edge in the downstream direction. The re-circulating region becomes larger in size, and its focal points are now at $x/H \approx 1.5$. This shift in the focal point of the recirculating region is due to the plasma induced jet, where the maximum induced-velocity is $\hat{u} \approx 1.8$ ms^{-1} directed in the center of the wake region at $x/H \approx 1$, as demonstrated in Fig. 4.19.

a)   b)
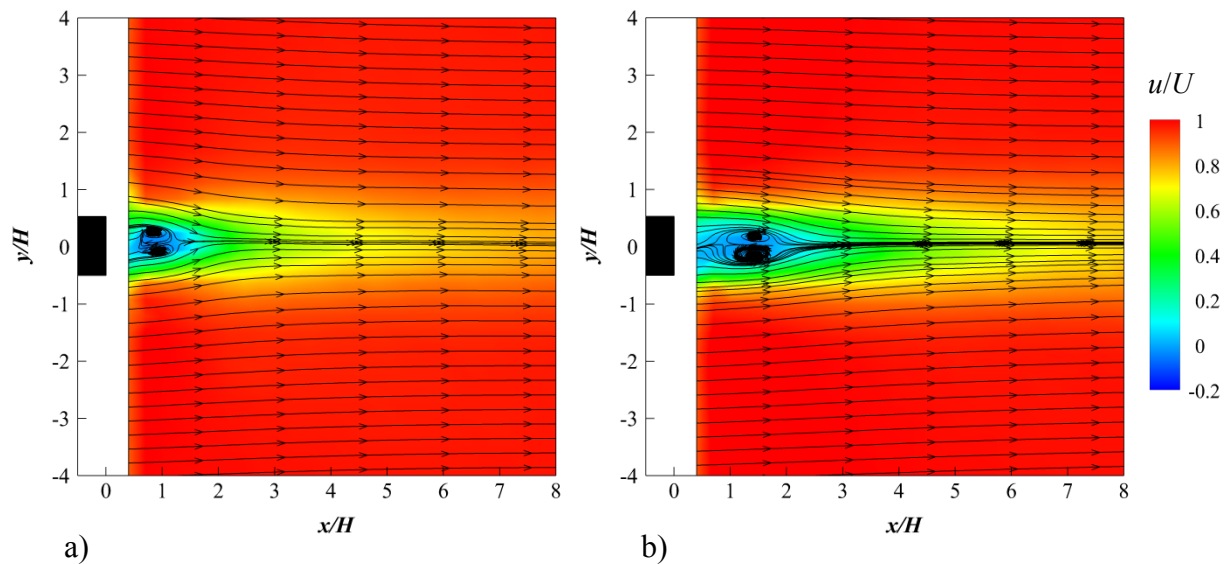
Figure 4.22 Time-averaged streamwise velocity component for the flat plate subjected to a) plasma off and b) plasma actuator PA2 at free stream velocity $U = 7.5$ ms^{-1}

The results in Fig. 4.22b suggest that the induced-plasma jet is not enough to reduce the velocity deficit through direct momentum injection to the wake, but rather a different mechanism is responsible for the vortex shedding noise reduction. A glass Pitot tube is used to allow a near

wake measurement at the vicinity of blunt face of the flat plate where both the hot wire and PIV data cannot reach due to the presence of the plasma discharge and reflection, respectively. The velocity profile was measured at four different streamwise positions, $x/H = 0.17$, $x/H = 0.5$, $x/H = 0.83$, and $x/H = 1.17$, ($x = 1, 3, 5$, and 7 mm from the blunt face of the plate). The results are presented in Fig. 4.23 (a-d). At $x/H = 0.17$, the velocity profile for plasma off case exhibits a predominantly zero value of $u/U = 0$, which corresponds to the recirculating air pocket previously observed in the mean velocity profile measured by the PIV, Fig. 4.22a. This is because the glass pitot-tube cannot measure the reverse flow, thereby returning a zero value when meet with such flow phenomenon. For plasma on case (PA2), the velocity profile measured at $x/H = 0.17$ clearly shows the slight streamwise jet produced by the plasma actuator. The plasma induced jet at $x/H = 0.17$ is $\hat{u} \approx 0.38$ ms^{-1}, which is significantly lower than $\hat{u} = 1.8$ ms^{-1} that is measured at even downstream location $x/H = 0.3$ in the quiescent condition presented earlier in Fig.4.19. Further downstream, at $x/H = 0.5$, 0.83, and 1.17, the results show that plasma-induced jet is completely vanished as demonstrated in Fig.4.23, respectively. These results contradict with the one demonstrated in Fig. 4.19, where a sustainable plasma induced jet can be observed in the quiescent flow condition. The above results show that the PA2 plasma actuator does not directly reduce the recirculating air pocket through direct momentum injection, but rather it pushes forward the vortices in the downstream direction away from the blunt base. The effect of the current plasma actuator is quite similar to the reported role of a splitter plate which has shown the ability to reduce and in some cases eliminate vortex shedding in the wake region of bluff bodies (flat plates and circular cylinders) [Apelt et al. (1973), Apelt and West (1975), and Hwang et al. (2003)].

Figure 4.24 shows the impact of the plasma actuator PA2 on the normal velocity component a $U = 7.5$ ms^{-1}. For the plasma off case, a region of high level of normal velocity component outside the separated region can be observed. However, for the plasma on case (PA2 actuator), it is quite clear that the downward plasma induced jet can reduce the level of the normal velocity components and push them further away from the trailing edge. As the vertical velocity represents the up-wash and down-wash movement of the fluid due to vortex shedding from the bluff body, the reduction and shifting in the vertical velocity value and position, respectively when PA2 plasma actuator is activated suggests that the intensity of the vortices is reduced. This agrees with the reduction in the tonal noise presented earlier in Fig. 4.17.

a) $x/H = 0.17$ ($x = 1$ mm)

b) $x/H = 0.5$ ($x = 3$ mm)

c) $x/H = 0.83$ ($x = 5$ mm)

d) $x/H = 1.17$ ($x = 7$ mm)
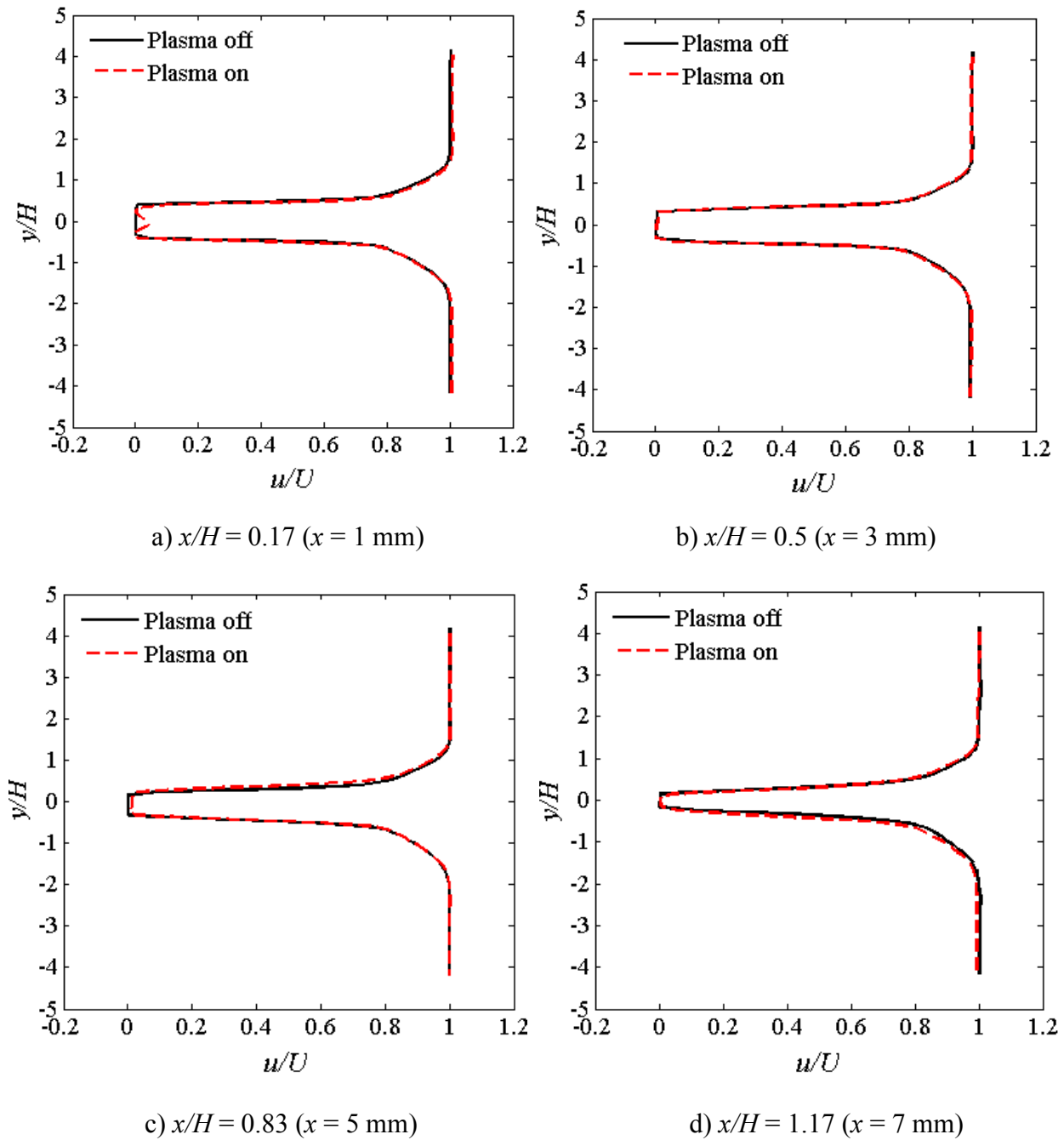
Figure 4.23 Mean wake velocity profiles measured by the glass-Pitot tube at U = 7.5 ms^{-1} when the PA2 plasma actuator is operated at f$_{(input)}$ = 8 kHz and V$_{(input)}$ = 4.2 kV.
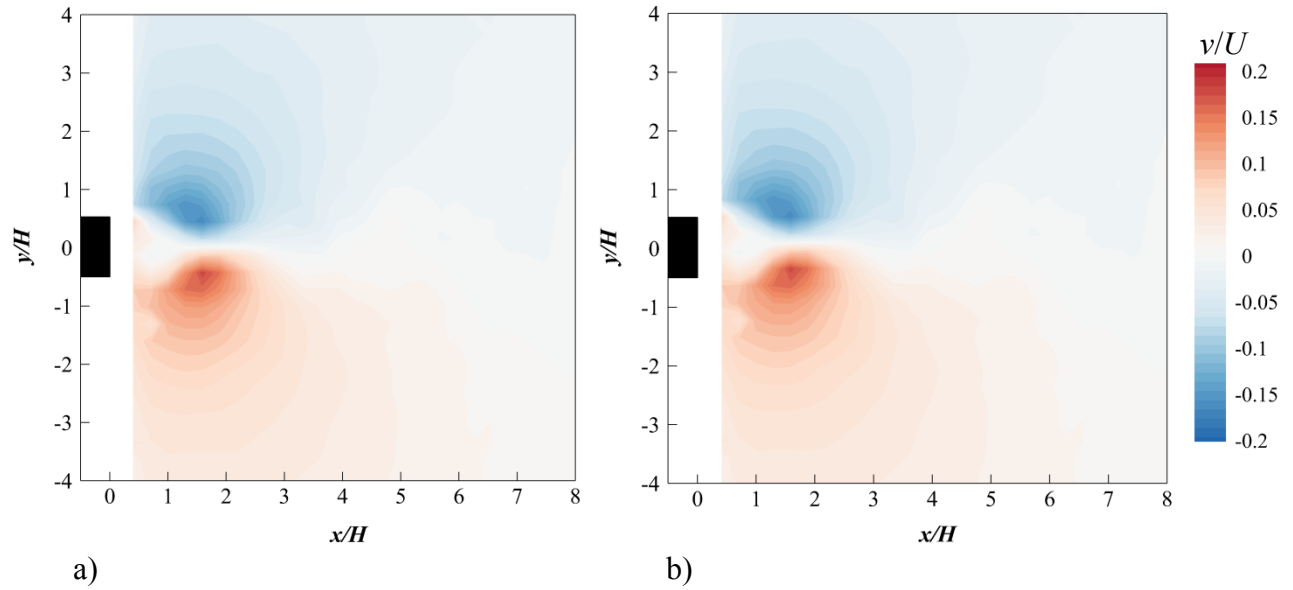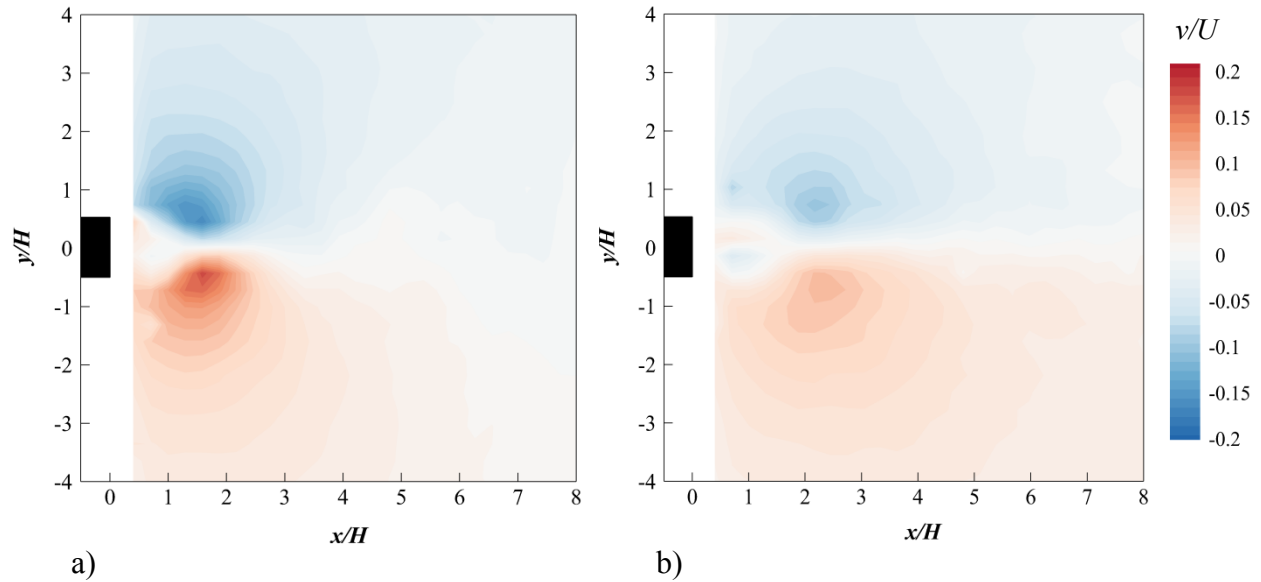
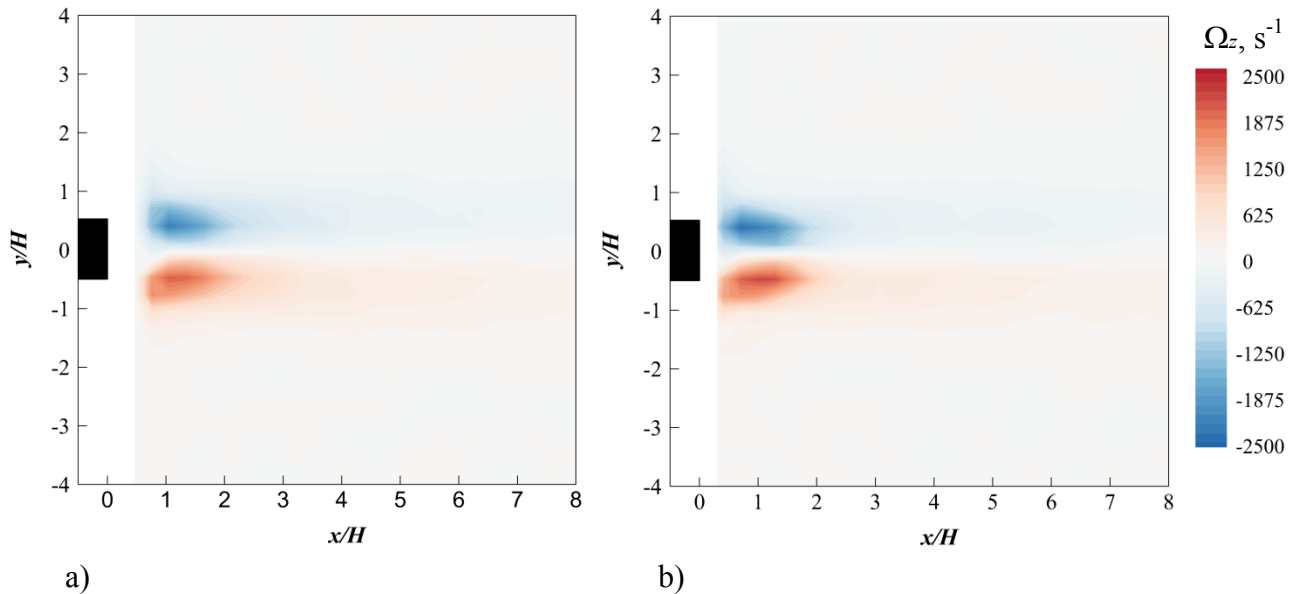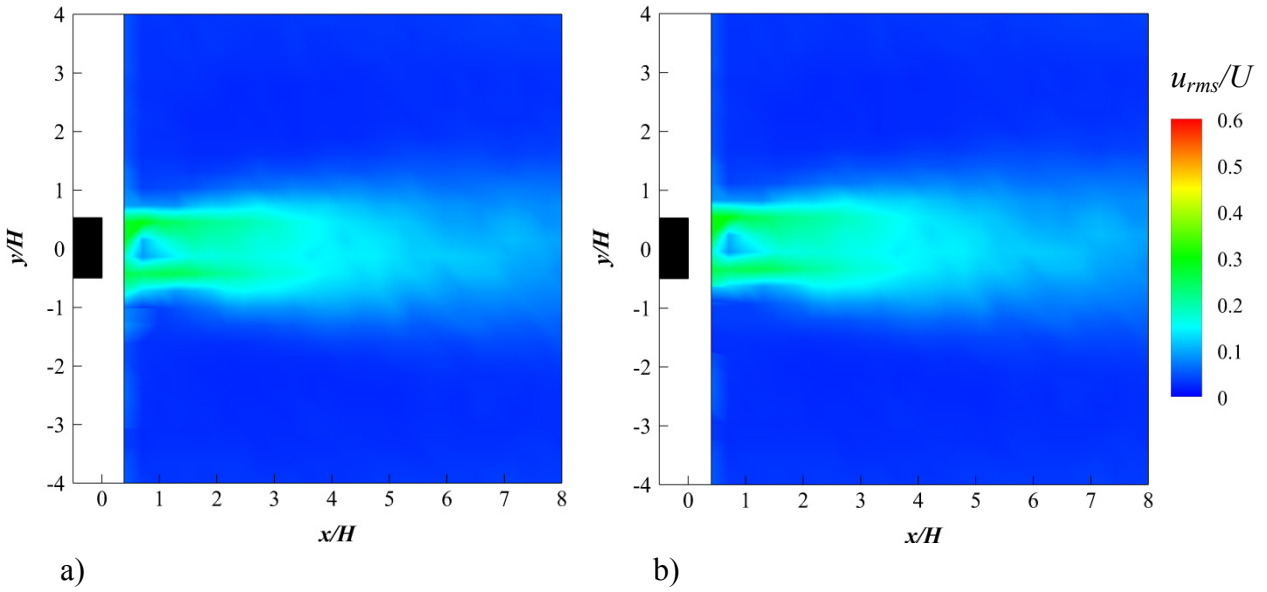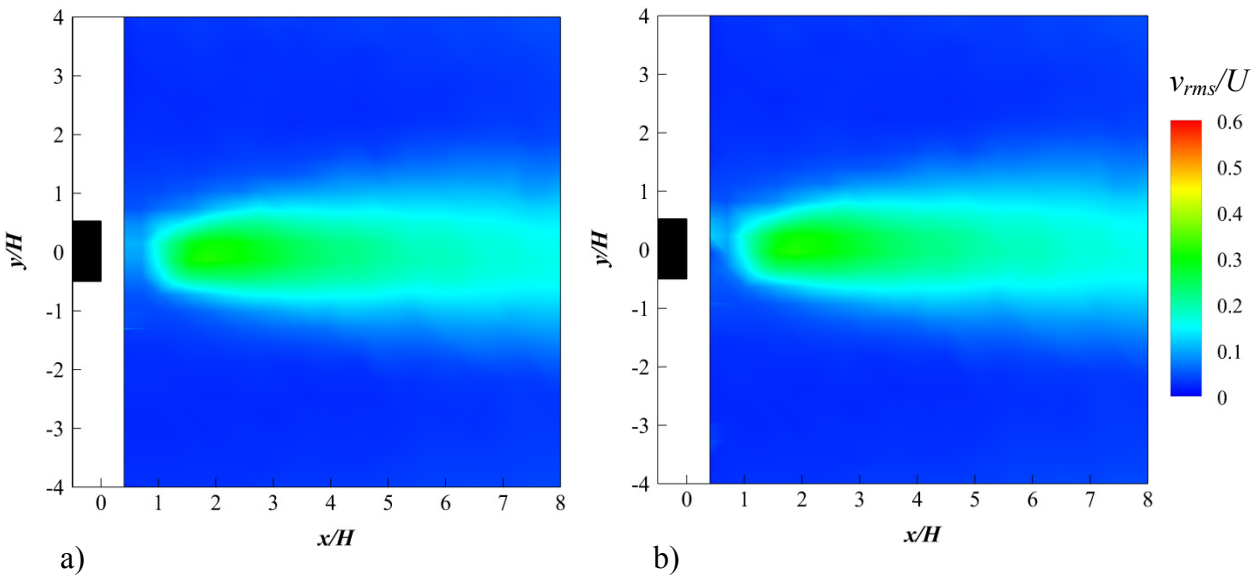*Figure 4.24 Time-averaged normal velocity component for the flat plate subjected to a) plasma off and b) plasma actuator PA2 at free stream velocity U = 7.5 ms^{-1} at f$_{(input)}$ = 8 kHz and V$_{(input)}$ = 4.2 kV.*

The spanwise vorticity contours, Ω_z, for the flat plate subjected to the plasma off and plasma actuator (PA2) are presented in Fig. 4.25. The input voltage and frequency are $V_{(input)}$ = 4.2 kV and $f_{(input)}$ = 8 kHz, respectively. The results show that for the plasma off case, a region of negative and positive spanwise vorticity is produced at the upper and lower sides of the blunt trailing edge, respectively. This spanwise vorticity has a maximum intensity at ($\pm 0.2 \leq y/H \leq \pm 0.8$) at streamwise location $x/H \leq 2.5$. The Karman vortices are originated from the roll up of the separated shear layer at some distance downstream of the blunt trailing edge. For the plasma off case, one can notice that vortex shedding is triggered after a short distance from the blunt face at $x/H \approx 2$, after this distance a sustainable oscillation can be observed (e.g. Fig. 4.20 and 4.21). These oscillating patterns in the wake region facilitate the radiation of the narrowband tonal noise into the far field. For the plasma on case (PA2), as can be seen in Fig 4.19, the plasma actuator produces jet to prevent the cross talk between the two separated shear layers. As a result the length of the separated shear layers, which form a region of negative and positive vorticity parallel to the main flow direction at the upper and lower sides of the blunt face, extends to a downstream location $x/H \approx 3.8$, as shown in Fig. 4.25b. This extension in the vortex shedding formation length could be the reason behind the overall reduction of the energy

for the wake instability (to be discussed in the POD analysis results). As a result, the level of the narrowband tonal noise is also reduced.
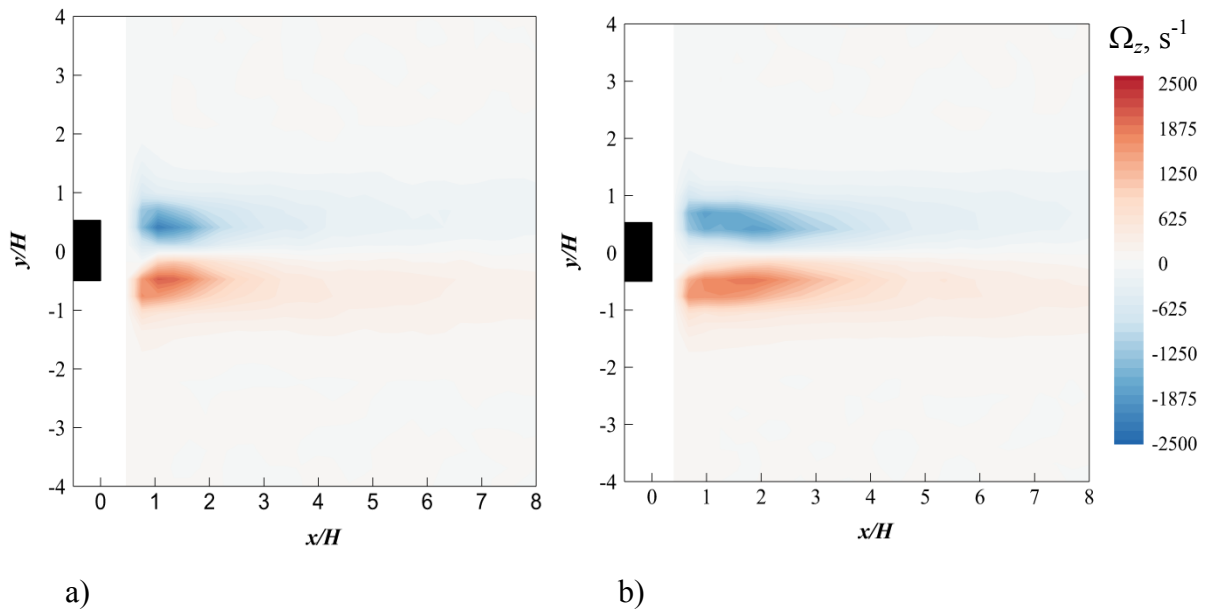
Figure 4.25 Time-averaged spanwise vorticity contours for the flat plate subjected to a) plasma off and b) plasma actuator PA2 at free stream velocity U = 7.5 ms^{-1} at f$_{(input)}$ = 8 kHz and V$_{(input)}$ = 4.2 kV

Hot wire measurements were conducted in the far wake region to verify the above interpretation of the vortex shedding noise reduction mechanism. The fluctuating velocity power spectral density for the plasma off and plasma on (PA2) cases is investigated at a streamwise location x/H = 4.17 and a normal location y/H = -1.17 at U = 7.5 ms^{-1}. The reason for choosing this large streamwise location is to ensure a safe distance between the hot wire probe and the plasma discharge so that electrical arcing will not occur. Figure 4.26a shows the fluctuating velocity PSD for the plasma off case. A significant peak at a reduced frequency fH/U = 0.19 can be observed which is similar to the acoustic narrowband vortex shedding tonal noise occurred in the SPL spectra in Fig. 4.17. This confirms that the narrowband tonal noise radiated into the far field is a by-product of the vortex shedding in the wake. When the flat plate is subjected to plasma actuator PA2 at $f_{(input)}$ = 8 kHz and $V_{(input)}$ = 4.2 kV, a maximum reduction in the narrowband peak of about 10 dB can be observed in the fluctuating velocity power spectral density, as shown in Fig. 4.26. In addition, the second harmonic of the main narrowband peak that otherwise occurs in the PSD for the plasma off case at fH/U = 0.38 is almost completely suppressed when the PA2 plasma actuator is activated.
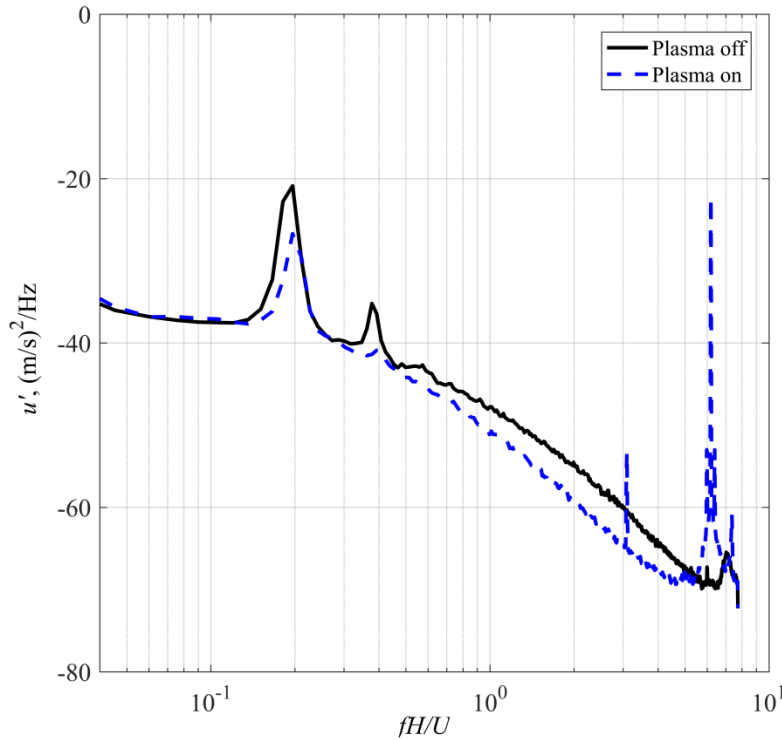
Figure 4.26 Wake fluctuating velocity PSD measured by the hot wire probe at $U = 7.5$ ms^{-1} when the PA2 plasma actuator is operated at $f_{(input)} = 8$ kHz and $V_{(input)} = 4.2$ kV. The measurement location is at $x/H = 4.17$ and $y/H = -1.17$.

Next, the fluctuations in the streamwise velocity and the normal velocity components contours are illustrated in Fig. 4.27. The velocity fluctuations are non-dimensionalised by the free stream velocity U. From Fig. 4.27, significant reductions in the velocity fluctuations in the streamwise and normal direction can be observed when the plasma actuator PA2 is switched on. This reduction in the energy of the wake vortex shedding by the plasma actuator PA2 is correlated to the reduction in the narrowband tonal noise observed in Fig. 4.17.

Now, in order to examine how the plasma actuator PA2 can affect the large coherent structure in the wake region, Fig. 4.28 illustrates the highest energy mode colored by the u and v velocity components from the POD analysis.

For the plasma off case, a high intensity anti-symmetry streamwise velocity component u and a symmetrical normal velocity component v can be observed. When the plasma actuator PA2 is turned on, the high energy structures for both the u and v velocity components are completely suppressed. This suppression of the high modes in the wake region is thus manifested in the significant reduction of the vortex shedding narrowband tonal noise radiation into the far field.
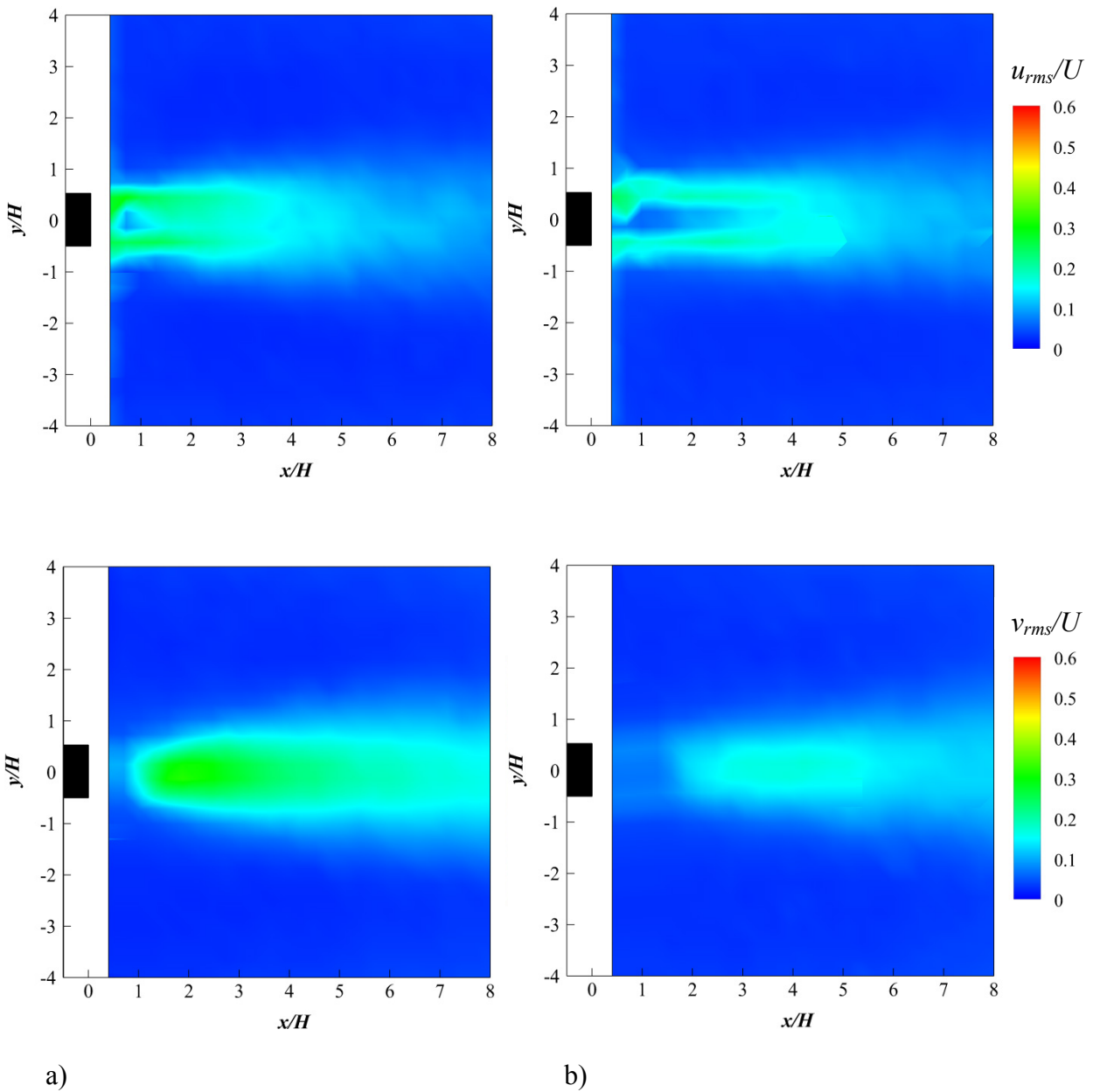
Figure 4.27 Time-averaged streamwise unsteady velocity for the flat plate subjected to a) plasma off and b) plasma actuator PA2 at free stream velocity U = 7.5 ms^{-1} at f$_{(input)}$ = 8 kHz and V$_{(input)}$ = 4.2 kV.
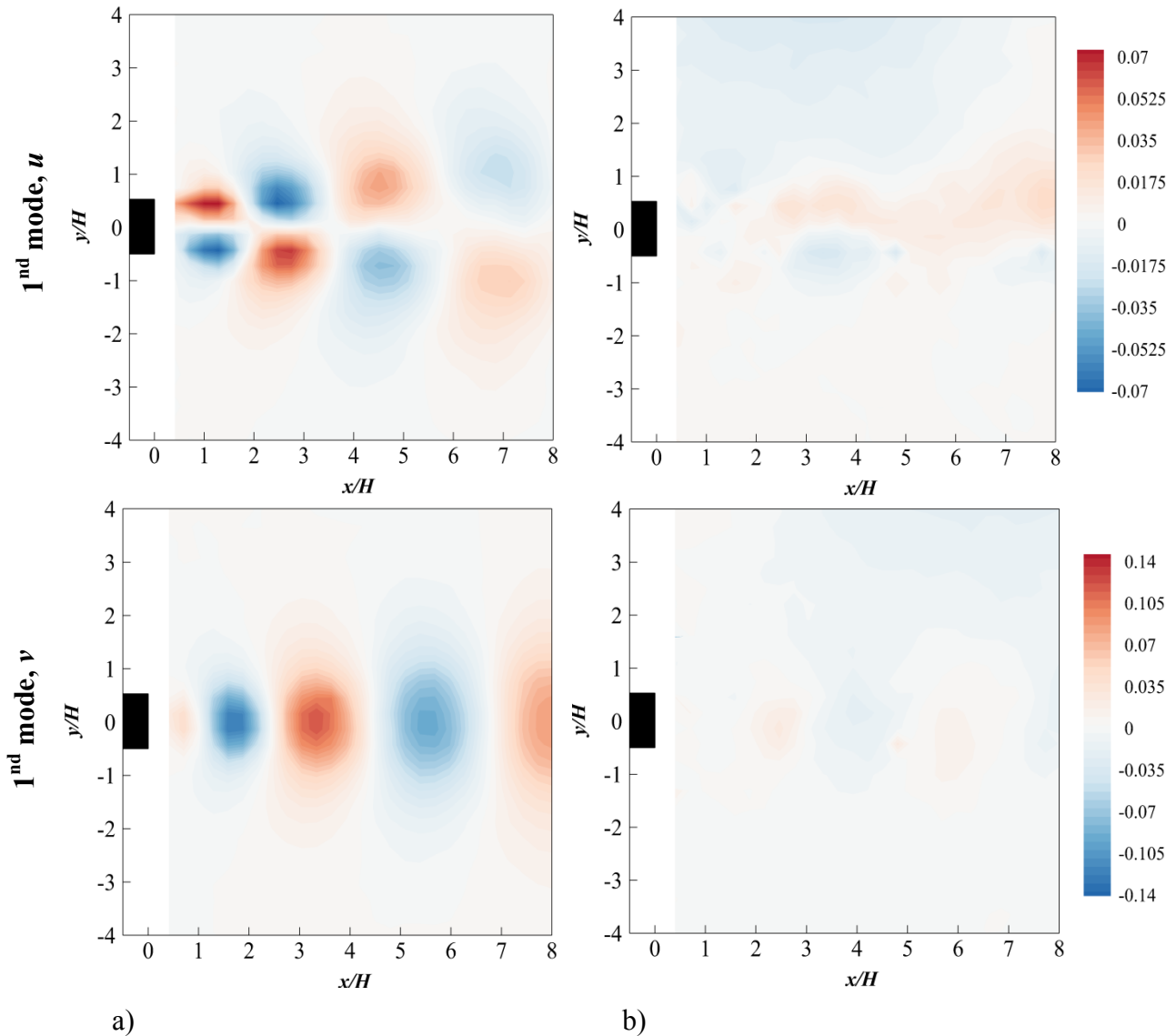
Figure 4.28 First POD mode in u and v for, a) plasma off and b) plasma actuator PA2 at free stream velocity U = 7.5 ms^{-1}, f$_{(input)}$ = 8 kHz and V$_{(input)}$ = 4.2 kV.

The energy contribution for the first twenty POD eigenmodes is presented in Fig. 4.29. It can be seen that the first two modes for the plasma off case represent the highest energy modes among the other eigenmodes, which is typical for flow with large coherent structures. When the plasma actuator PA2 is turned on, the energy contribution for these two modes (mode1 and mode 2) are reduced to about half of the value when no flow control is applied.
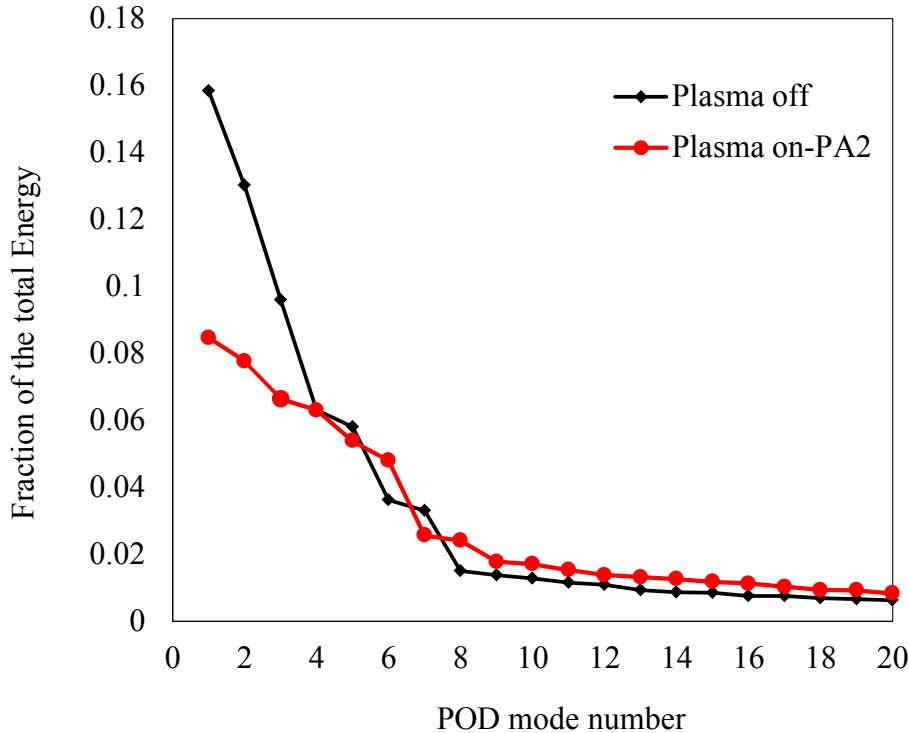
Figure 4.29 Energy contribution versus POD mode number for both plasma off and plasma on PA2 at free stream velocity U = 7.5 ms^{-1}, f$_{(input)}$ = 8 kHz and V$_{(input)}$ = 4.2 kV.

It has been shown in this section that the plasma actuator PA2 is capable of suppressing the vortex shedding tonal noise from the blunt trailing edge. Because the drag coefficient C_D is a by-product of the vortex shedding, it is interesting to examine the impact of the PA2 plasma actuator configuration on the drag coefficient. The wake velocity profile of both the mean and fluctuating components are used to calculate the C_D value, which can be decomposed to $C_D = C_{D(mean)} + C_{D(rms)}$. For a unit of span of the flat plate, C_D can be calculated as the following:

$$C_D = \frac{2}{C} \int_{-\infty}^{\infty} \frac{u}{U(x)} \left(1 - \frac{u}{U(x)}\right) dy + \frac{2}{C} \int_{-\infty}^{\infty} \left(\frac{u_{rms}}{U(x)}\right)^2 dy, \tag{4.1}$$

where $U(x)$ is the free stream velocity at the measurement point and C is the chord length of the flat plate. The first and second terms on the right hand side of Eq. (4.1) represent the $C_{D(mean)}$ and $C_{D(rms)}$, respectively. Now, the momentum thickness of the wake, θ, can be defined as:

$$\theta = \int_{-\infty}^{\infty} \frac{u}{U(x)} \left(1 - \frac{u}{U(x)}\right) dy \tag{4.2}$$

Therefore,

$$C_{D(mean)} = \frac{2}{c}\,\theta \tag{4.3}$$

The streamwise location where the wake profile is measured and used for C_D calculation is at $x/H = 1$. For the plasma off and plasma on cases, the $C_{D(mean)}$ values are 0.042 ±0.002 and 0.035 ±0.002 respectively. This produces a mean drag reduction of about 15%. It has been demonstrated in Fig. 4.26 that the broadband component of fluctuating velocity PSD for the plasma on case at reduced frequencies $fH/U \geq 0.38$ is constantly lower than the baseline case. As a result, the turbulence level of the far wake of the vortex shedding subjected to the plasma actuator PA2 will be lower. Therefore, it is expected that the near wake turbulence level will be reduced as well. At the same $x/H = 1$, the wake profiles for both the plasma off and PA2 plasma on cases produce the $C_{D(rms)}$ of 0.0071 ± 0.0003 and 0.0053 ±0.0003, respectively, which represents a reduction of 26% in the $C_{D(rms)}$.

4.6 Acoustic and Hydrodynamic Fields –PA3

4.6.1 Acoustic Field Results

In addition to the plasma actuators PA1 and PA2, another configuration of the plasma actuator is used in the current study. This actuator is configured so that it can locally modify the flow by generating spanwise perturbations. As described in Chapter 3, PA3 consists of a number of exposed electrode strips which are positioned on one common grounded electrode on both sides of the flat plate at the trailing edge. Von Karman vortices are considered as the primary instability in the wake region at low Reynolds number. However, at high Reynolds numbers, a secondary instability occurs in the wake beside the von Karman vortices. The characteristics of this instability depend on both the Reynolds number and the thickness of the bluff body. For more effective flow control, the spanwise periodicity or the wavelength of the passive or active (fluidic) devices should match the spanwise wavelength of the flow secondary instability. It has been found by Naghib-Lahouti et al. (2012) that at Reynolds number $Re_{(d)} = 2150$, the instability has a spanwise wavelength $(\lambda z/d) = 2.5$; where d is the characteristic length scale (thickness of the plate) and this instability can still exist even at Reynolds numbers up to $Re_{(d)} = 24000$. Based the thickness of the flat plate (H), in the current study, the Reynolds number ranges $3000 \leq Re_{(H)} \leq 16000$. Therefore, the spanwise distribution of the exposed electrodes is chosen to

have a periodicity of ($\lambda z/H$) = 2.5. The jet induced by this actuator will interact with the incoming flow and result in a vortical flow, which will then evolve in the streamwise direction in a mechanism similar to a vortex generator. In this section, the effect of the PA3 plasma actuator on the aerodynamic noise of blunt trailing edge flat plate will be investigated at U = 7.5-40 ms^{-1}. The input frequency and voltage levels used for the current actuator configuration are $f_{(input)}$ = 7, 8 kHz and $V_{(input)}$ =2.4-4.2 kV, respectively.

The SPL spectra for a flat plate subjected to the plasma off and plasma on (PA3) at free stream velocity U = 7.5 ms^{-1} is presented in Fig. 4.30. Similar to the previously tested plasma actuator configurations, (PA1 and PA2), the $f_{(input)}$ does not result in a significant effect on the actuator performance in terms of the aerodynamic noise reduction. At the lowest input voltage, $V_{(input)}$ = 2.4 kV, noise reduction of about 4 ±0.5dB can be observed. This level of noise reduction is high if compared with the plasma actuators PA1 and PA2 driven by the same voltage and frequency. When the input voltage is increased to $V_{(input)}$ = 3kV, the level of the narrowband tonal noise reduction is increased to 12 ±0.5dB. Note that, at the same input voltage $V_{(input)}$, the achieved noise reduction levels by both the PA1 and PA2 are ΔSPL = 0 and ΔSPL = 3.4 ±0.5dB, respectively. Based on these results, PA3 has so far outperformed both the PA1 and PA2 when they are subjected to the same input voltages. However, beyond that at $V_{(input)}$ = 3.6 and 4.2 kV, there is also no much difference in terms of the level of the tonal noise reduction i.e. ΔSPL = 12 ±0.5dB. It is also observed that increasing the $V_{(input)}$ will cause an increase in the non-aerodynamic broadband noise at fH/U > 0.3.

The ΔSPL achieved by the PA3 plasma actuator as a function of the reduced frequency fH/U and the free stream velocity U for the flat plate with blunt trailing edge is illustrated in Fig. 4.31. The free stream velocity covers U = 7.5-40 ms^{-1}, and the input frequency and voltage are $f_{(input)}$ = 7, 8 kHz and $V_{(input)}$ =2.4-4.2 kV, respectively. The results show that significant narrowband tonal noise reduction can still be achieved at higher free stream velocities, $U \approx$ 21 ms^{-1} when $V_{(input)}$ = 4.2 kV; at $U \approx$ 18 ms^{-1} when $V_{(input)}$ = 3.6 kV; at $U \approx$ 14 ms^{-1} when $V_{(input)}$ = 3.0 kV.
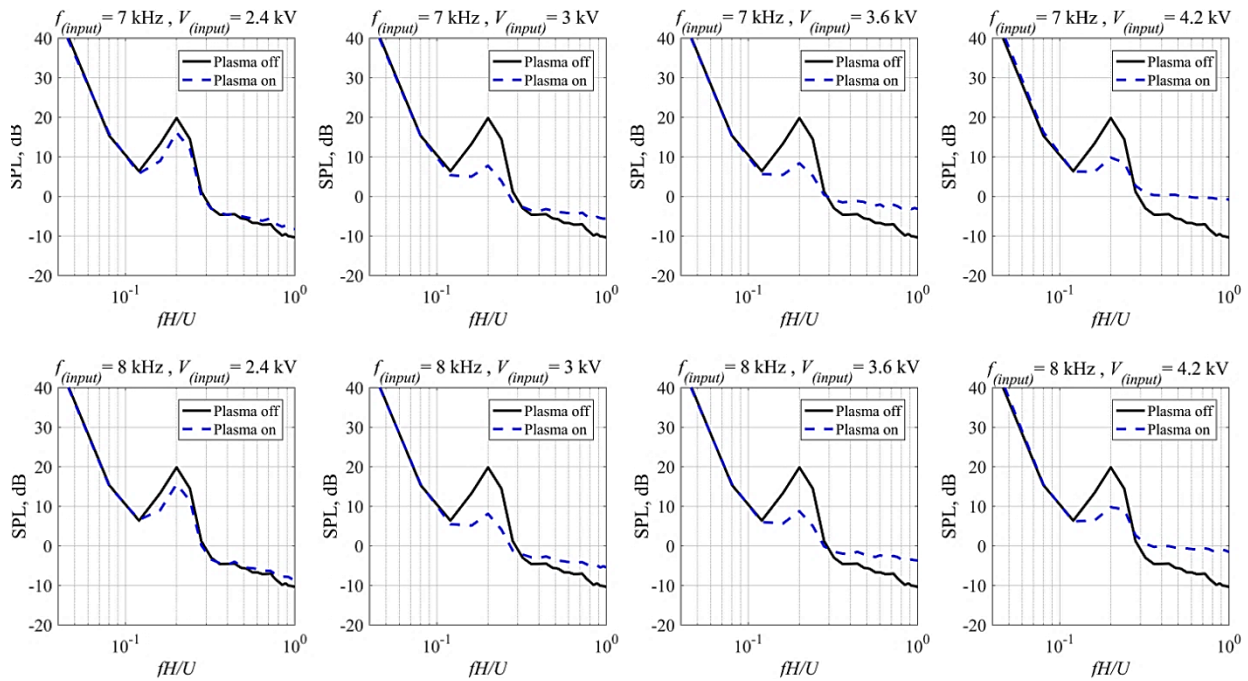
Figure 4.30 SPL spectra of the flat plate subjected to PA3 plasma actuator operated at $f_{(input)}$ = 7, 8 kHz and $V_{(input)}$ = 2.4–4.2 kV at U = 7.5 ms^{-1}.
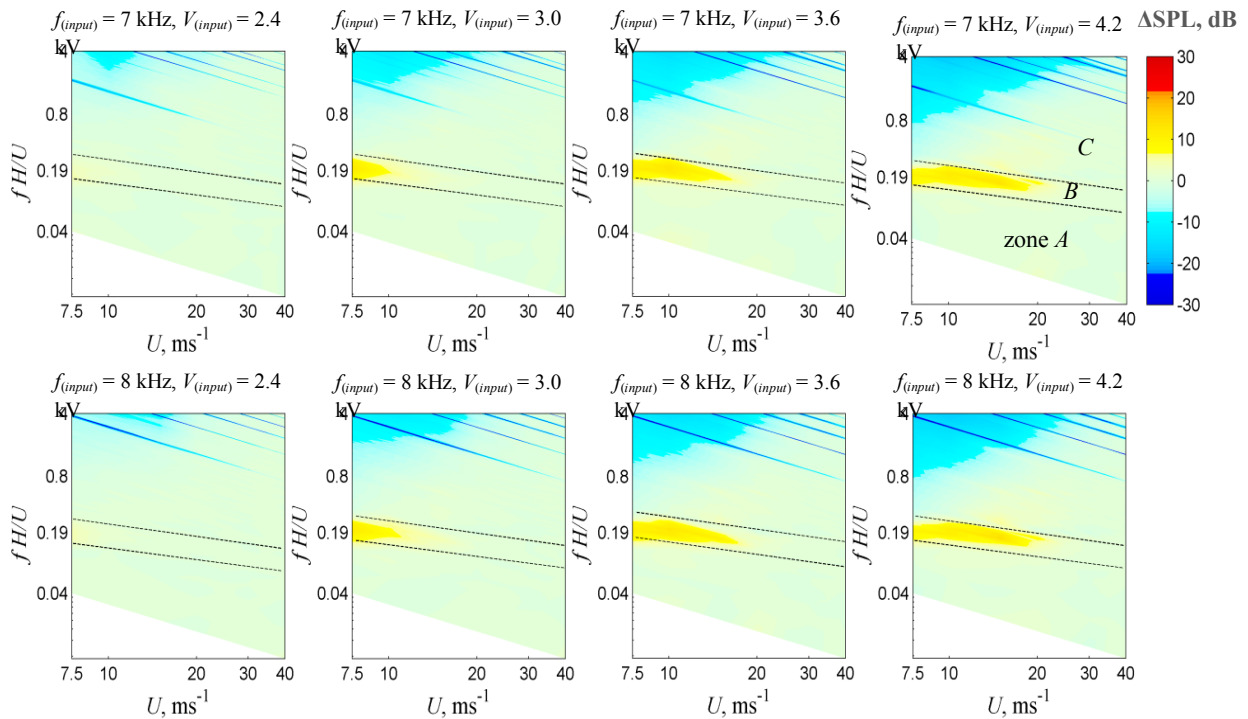
Figure 4.31 ΔSPL spectra for the flat plate subjected to PA3 plasma actuator operated at $f_{(input)}$ = 7, 8 kHz and $V_{(input)}$ = 2.4–4.2 kV at U = 7.5–40 ms^{-1}. The divisions for zones A, B and C are identical for all the contour maps.

4.6.2 Hydrodynamic Field Results

In order to clarify the mechanism of the narrowband tonal noise reduction achieved by the PA3 plasma actuator, instantaneous and average flow field results are presented in Section 4.6.2.1 and 4.6.2.2, respectively.

4.6.2.1 Instantaneous Flow Field

In order to explore the induced jet by the PA3 plasma actuator, a PIV measurement was conducted in y-z plane at $x/H = $ -1.5 from the blunt trailing edge under quiescent condition ($U = 0$). The vertical velocity contour induced by the PA3 plasma actuator at input voltage and frequency $V_{(input)} = 3.6$ kV and $f_{(input)} = 8$ kHz, respectively, is illustrated in Fig. 4.32. The result clearly shows that these spanwise distributed actuators can induce a vertical plasma jet of maximum velocity $\tilde{v} \approx 1.2$ ms^{-1}. The velocity contour is also superimposed with velocity vectors which clearly shows, that the actuator can ionize the air above each adjacent exposed electrodes. This reaction draws the flow towards the near wall region in the spanwise direction. Then, the drown flow from each adjacent electrodes will eventually merge and form a central vertical plasma jet at locations correspond to $z/H = \pm1.25$ and ±3.75. As a result of the interaction between the wall bounded and the spanwise airflow, a streamwise vorticity in the (x) axis direction is induced by each plasma actuator form on each side of the plasma vertical jet, as shown in Fig. 4.33. This behavior of streamwise oriented plasma actuator is previously reported by Jukes and Choi (2006), Jukes and Choi (2012), Choi et al. (2013) and Yokoyama et al. (2107).

Next, examples of the instantaneous velocity and spanwise vorticity field are presented. The instantaneous streamwise velocity contours for the flat plate subjected to the plasma off and PA3 plasma actuator operated at $U = 7.5$ ms^{-1} at $f_{(input)} = 8$ kHz *and* $V_{(input)} = 3.6$ kV are demonstrated in Fig. 4.34. The flow maps were obtained at two locations (i) and (ii), which refer to the center line between each pair of exposed electrodes and the edge of the exposed electrode, respectively It is worth noting that no measurements were carried out at location (iii), which refers to the region above the center of the exposed electrodes. The results show that when the plasma actuator is activated, the wake recirculation region generated as a result of the flow separation from the blunt trailing edge becomes less chaotic than the plasma off case. In addition, for the

PA3 plasma actuator at the spanwise locations (i) and (ii), an increase in the wake width can also be observed. This is also seen in the timed-averaged streamwise velocity Fig.4.36b, where an increase and decrease in the wake width can be seen at location (i) and location (ii). More details will be given in the time averaged flow field.
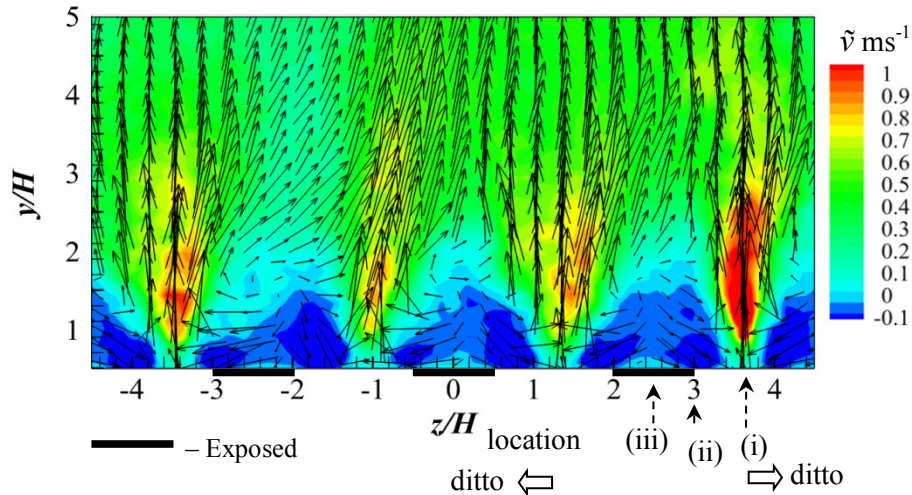
Figure 4.32 Instantaneous vertical velocity field generated by the PA3 plasma actuator at quiescent condition (i.e. U = 0) where $f_{(input)}$ = 8 kHz and $V_{(input)}$ = 3.6 kV. The dark blue region represents the wall-inward flow.
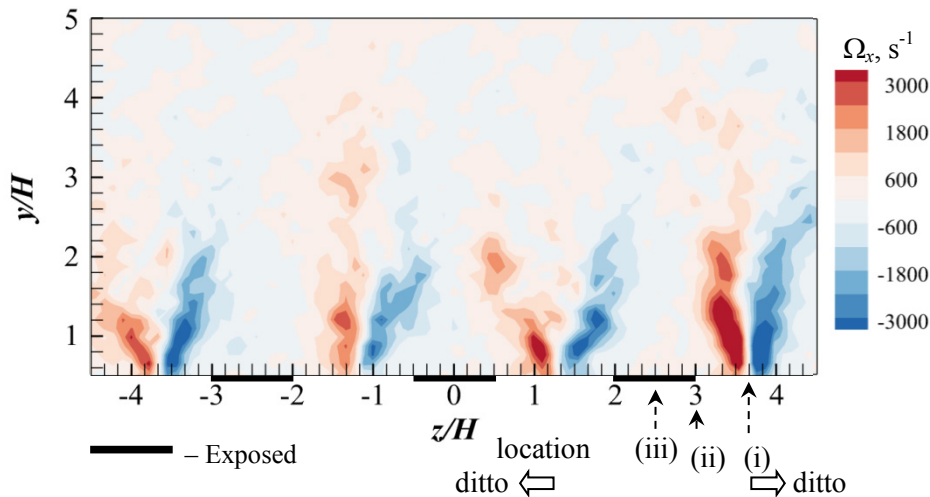
Figure 4.33 Instantaneous streamwise vorticity field generated by the PA3 plasma actuator at quiescent condition (i.e. U = 0) where $f_{(input)}$ = 8 kHz and $V_{(input)}$ = 3.6 kV.

Figure 4.35 shows, the corresponding spanwise vorticity, Ωz contours for the plasma off and plasma on (PA3) cases. A considerable effect of the plasma actuator PA3 on the vortex shedding is demonstrated at the two locations (i) and (ii). When the PA3 plasma actuator is turned on, the vorticity contours show no clear pattern of the coherent structures, which could otherwise be easily observed in the spanwise vorticity contours for the plasma off case. Although no

measurement was taken at location (iii), it is reasonable to assume that at this location no plasma-induced streamwise vortices exist locally. As a result there will not be any control to the bluntness-induced vortex shedding. This limitation could be alleviated by reducing the spanwise spacing of between each pair of exposed electrodes. This could result in a reduction in the effectiveness of the $V_{(input)}$ with respect to the PA3 plasma-induced jet, $\tilde{v}$ due to a large capacitance, which would be entailed across the whole plasma system.
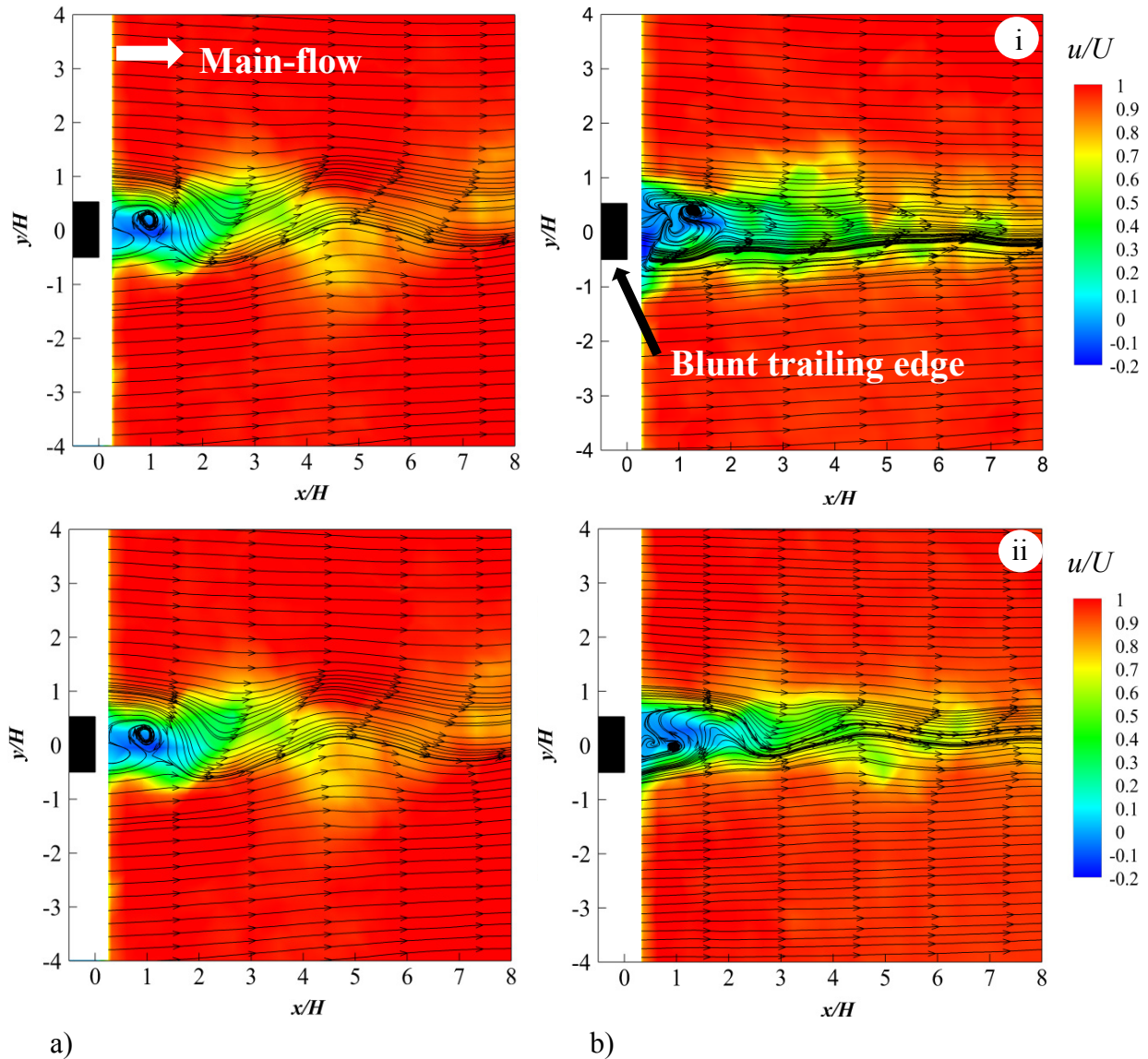
Figure 4.34 Instantaneous streamwise velocity contours for flat plate subjected to a) Plasma off, and b) Plasma on (PA3), location (i) and (ii) at free stream velocity of U = 7.5 ms^{-1}, at f$_{(input)}$ = 8 kHz and V$_{(input)}$ = 3.6 kV.
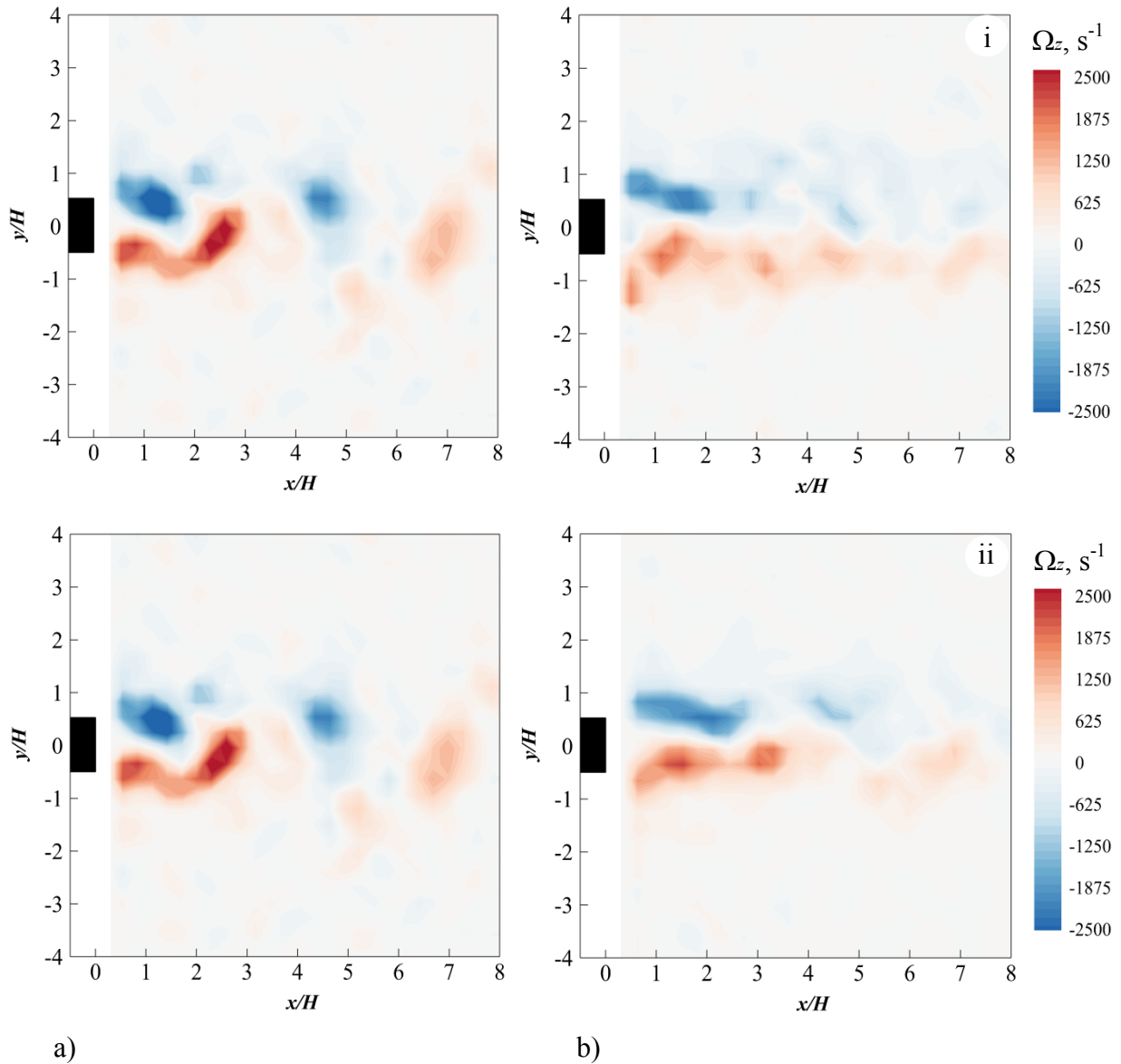
Figure 4.35 Instantaneous streamwise velocity contours for flat plate subjected to a) Plasma off, and b) Plasma on (PA3), location (i) and (ii) at free stream velocity of U = 7.5 ms^{-1}, at f$_{(input)}$ = 8 kHz and V$_{(input)}$ = 3.6 kV.

4.6.2.2 Time-Averaged Flow Field

The analysis of the time-averaged flow field at $U = 7.5$ ms^{-1} is presented in this section. The streamwise time-averaged velocity contours for the PA3 plasma actuator at two spanwise locations (i) and (ii) are demonstrated in Fig. 4.36.
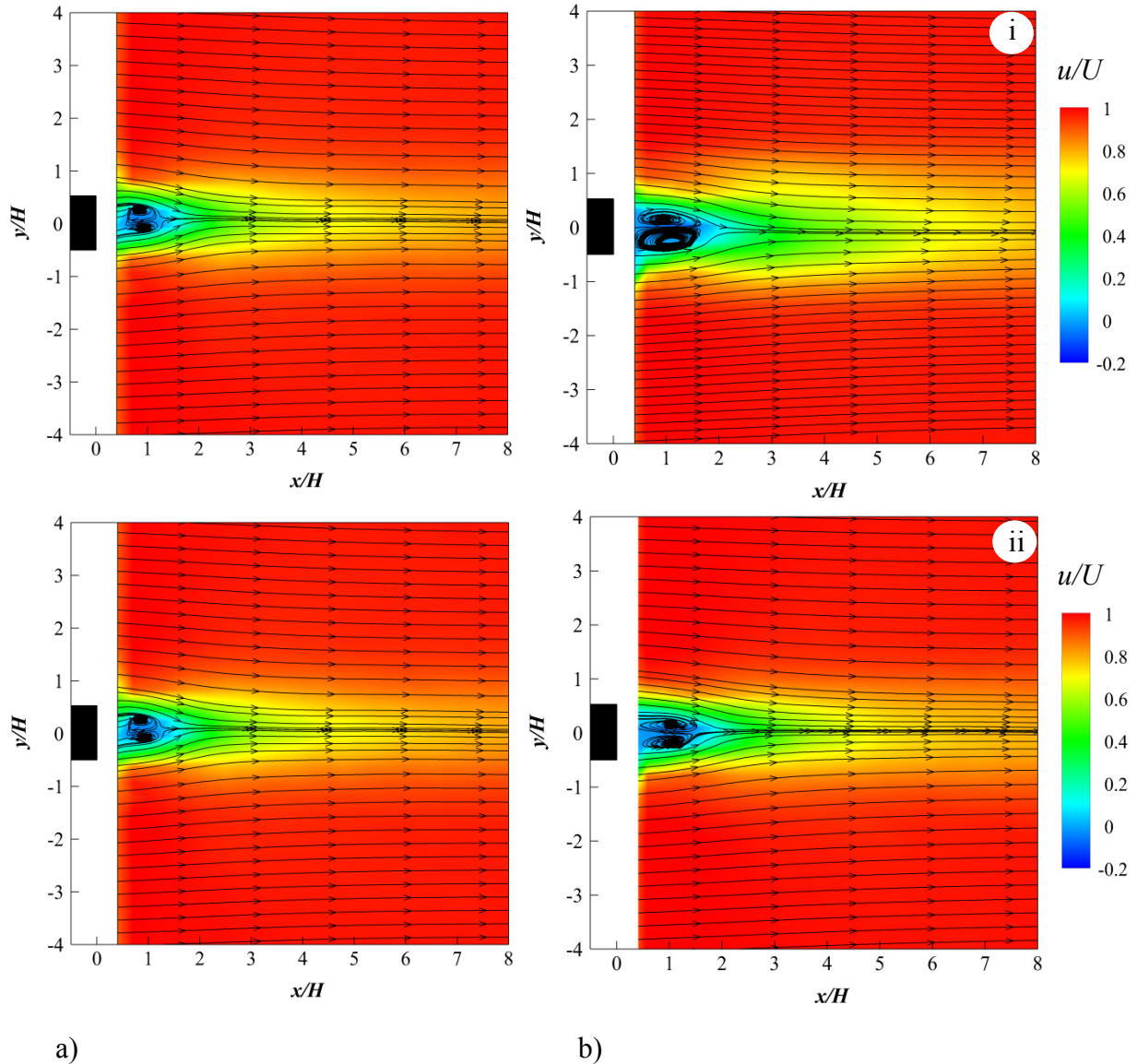
Figure 4.36 Time-averaged streamwise velocity contours for flat plate subjected to a) Plasma off, and b) Plasma on (PA3), location (i) and (ii) at free stream velocity of U = 7.5 ms⁻¹, at f(input) = 8 kHz and V(input) = 3.6 kV.

Figure 4.36 Time-averaged streamwise velocity contours for flat plate subjected to a) Plasma off, and b) Plasma on (PA3), location (i) and (ii) at free stream velocity of $U = 7.5 \ ms^{-1}$, at $f_{(input)} = 8 \ kHz$ and $V_{(input)} = 3.6 \ kV$.

From Fig. 4.36, the results show that for the PA3 case, at the spanwise location (i), both the length of the recirculation region and the thickness of the wake increase when compared to the plasma off case. The stream wise location of the recirculating air pocket for the plasma on case is extended to $x/H \approx 2.5$, while for the plasma off case the non-convective recirculating air pocket is closer to the blunt face of the trailing edge. For the second spanwise location (ii), one can notice that the recirculating region for the PA3 plasma actuator is extended more in the

downstream direction than the plasma off case. However, the wake width at this spanwise location is still the same as the plasma off case.

The time-averaged vertical velocity component contours at the two spanwise locations (i) and (ii) for the flat plate with and without the plasma actuation at $U = 7.5$ ms^{-1} are shown in Fig. 4.37. It can be seen that at both the spanwise locations, the vertical velocity is reduced when the plasma actuator PA3 is activated. However, the level of reduction in the vertical velocity at the spanwise location (ii), which refers to position at the edge of the exposed electrode, is larger than that at the center line between the two pairs of the exposed electrodes (location (ii)) and similar to the case where PA2 plasma actuator is activated, as demonstrated in Fig. 4.24.

Next, the time-averaged spanwise vorticity contours, Ω_z are shown in Fig. 4.38. It can be seen that for the plasma on (PA3) case, the two regions of negative and positive vorticity extend further in the downstream direction in a way similar to the vorticity field generated by the PA2 plasma actuator (Fig. 4.25). For the PA3 plasma actuator case, these significant vorticity regions extend up to $x/H \approx 2.5$, while for the PA2 plasma actuator the significant vorticity regions extend up to $x/H \approx 3.8$.

It is shown in Fig. 4.33, that due to the interaction between the wall bounded and the spanwise flow, streamwise counter rotating vorticity are generated on both sides of the plasma vertical jet under quiescent condition. When the main flow interacts with the spanwise plasma jet, the resulted streamwise vortices could be responsible for the significant tonal noise reduction by the PA3 plasma actuator (will be shown later in Fig. 4.39). PIV measurement was conducted in the y-z plane to investigate the development of the streamwise vortices generated by the PA3 plasma actuator under the presence of free stream velocity. Figure 4.39 shows the streamwise vorticity contours generated by the PA3 plasma actuator at $U = 7.5$ ms^{-1} and for two streamwise locations $x = 0$ and -12 mm (the zero position denotes the center of the blunt base). For both streamwise locations, the laser sheet illuminates the lower side of the flat plate in the y-z plane and the resulted flow field is turned upside down for clarity. It can be seen that the streamwise vortices generated by the PA3 plasma actuator still effective even at the edge of the flat plate. These projected vortices into the downstream direction could interrupt the spanwise coherence of the bluntness induced vortex shedding and weaken the narrow band vortex shedding tonal noise

as demonstrated earlier in Fig.4.30. This will later be compared with the POD mode analysis for the PA3 plasma actuator.
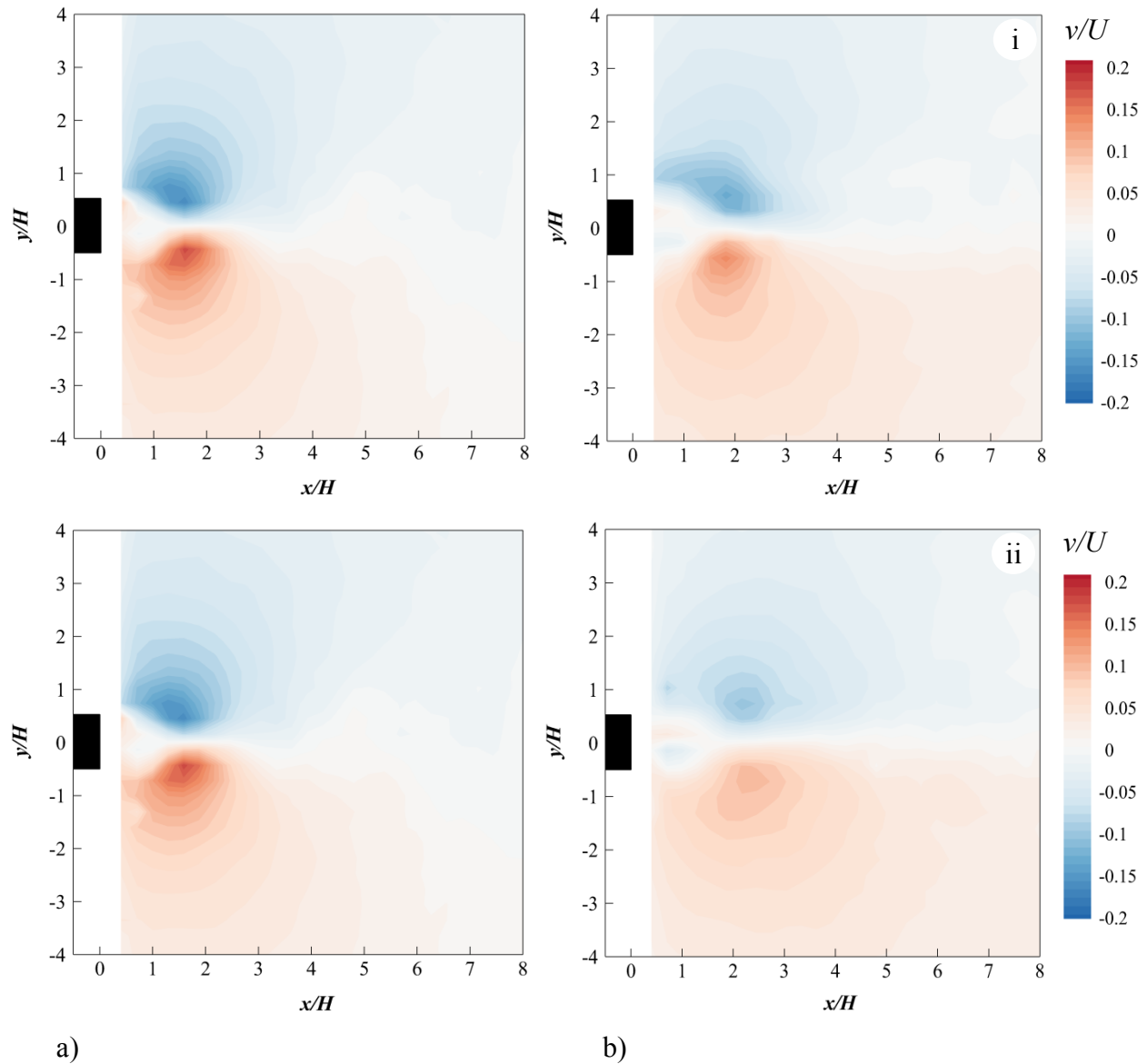
Figure 4.37 Time-averaged vertical velocity contours for flat plate subjected to a) Plasma off, and b) Plasma on (PA3), location (i) and (ii) at free stream velocity of U = 7.5 ms^{-1}, at f$_{(input)}$ = 8 kHz and V$_{(input)}$ = 3.6 kV.
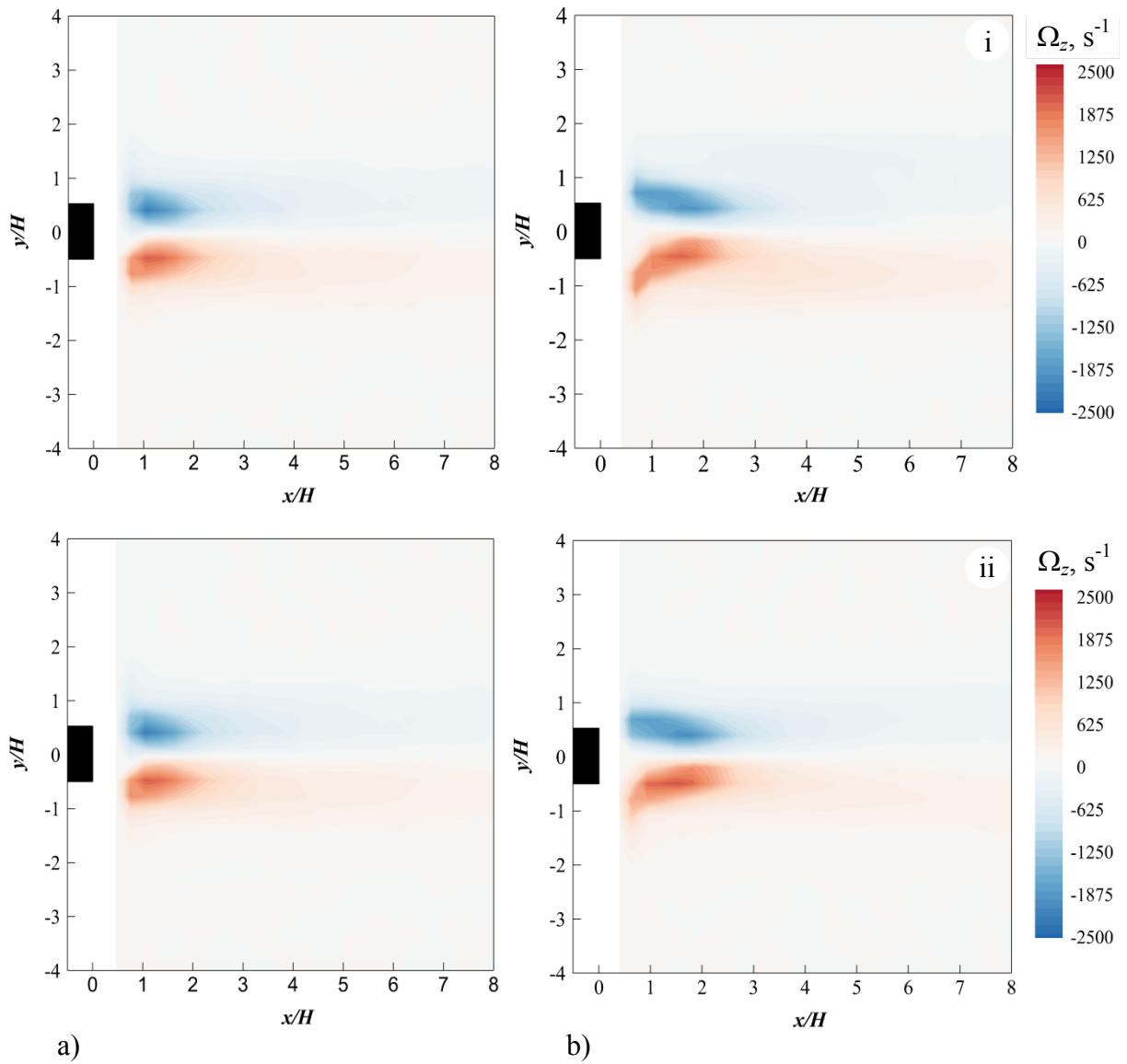
Figure 4.38 Time-averaged spanwise vorticity contours for flat plate subjected to a) Plasma off, and b) Plasma on (PA3), location (i) and (ii) at free stream velocity of U = 7.5 ms⁻¹, at f(input) = 8 kHz and V(input) = 3.6 kV.
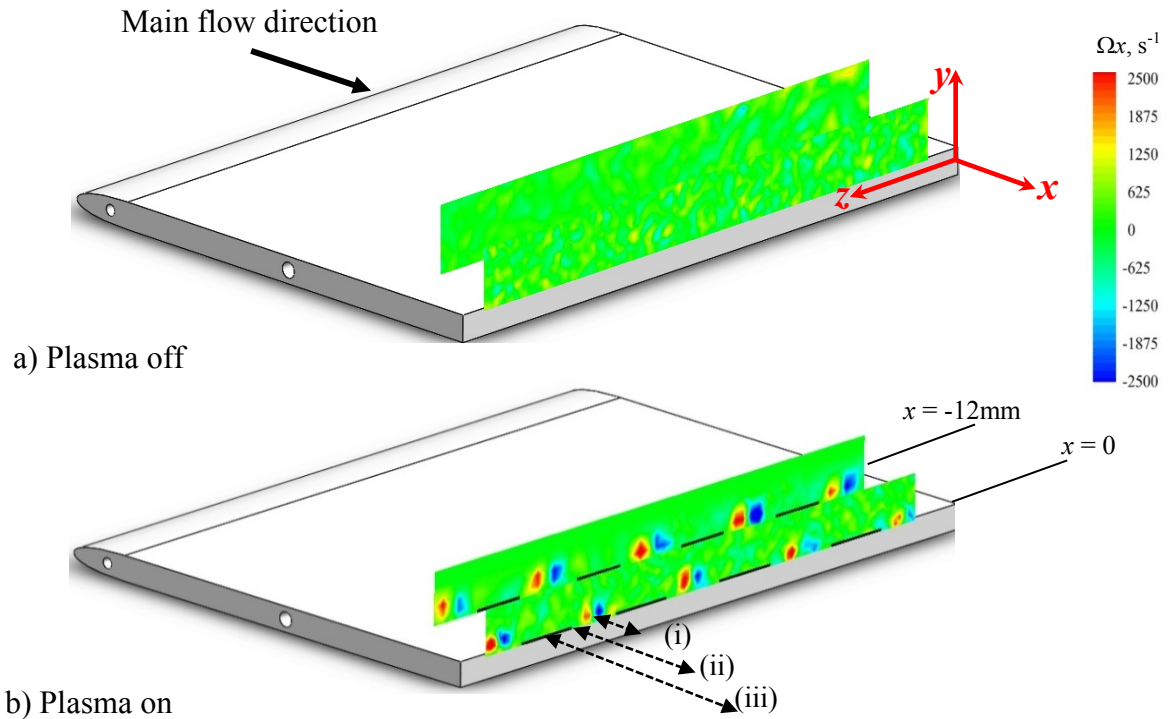
Figure 4.39 Time-averaged streamwise vorticity fields generated by the PA3 plasma actuator at U = 7.5 ms^{-1} where $f_{(input)}$ = 8 kHz and $V_{(input)}$ = 3.6 kV. Drawings are not to scale.

The impact of the PA3 plasma actuator on the energy structures in the wake region is investigated. Figures 4.40 and 4.41 illustrate the effect of the PA3 plasma actuator on the highest energy modes in the u and v velocity components of the wake flow, respectively. The result shows that at spanwise locations (i) and (ii), the large energy structures that occur in the wake region for the plasma off case are totally suppressed in both u and v velocity components. Because these structures are the projection of the bluntness induced vortex shedding, the suppression of these features explains the significant noise reduction that is achieved by the PA3 plasma actuator.

The energy contribution for the first twenty POD eigenmodes is presented in Fig. 4.42. The first two modes for the plasma off case have the highest energy among the other eigenmodes. For the plasma actuator PA3, the energy contributions for mode1 and mode 2 are reduced to nearly half the value of the plasma off case. In addition, the induced streamwise vortices by the plasma actuator PA3 at the spanwise location (i) results in the largest reduction in the energy for the first twelve modes when compared to the spanwise location (ii), which is at the edge of the exposed electrodes. It is expected that the spanwise configuration of the plasma actuator will be the most

optimum when the spanwise spacing between the exposed electrodes is small, this allowing a greater disruption of the coherence of the vortex shedding at the spanwise direction.
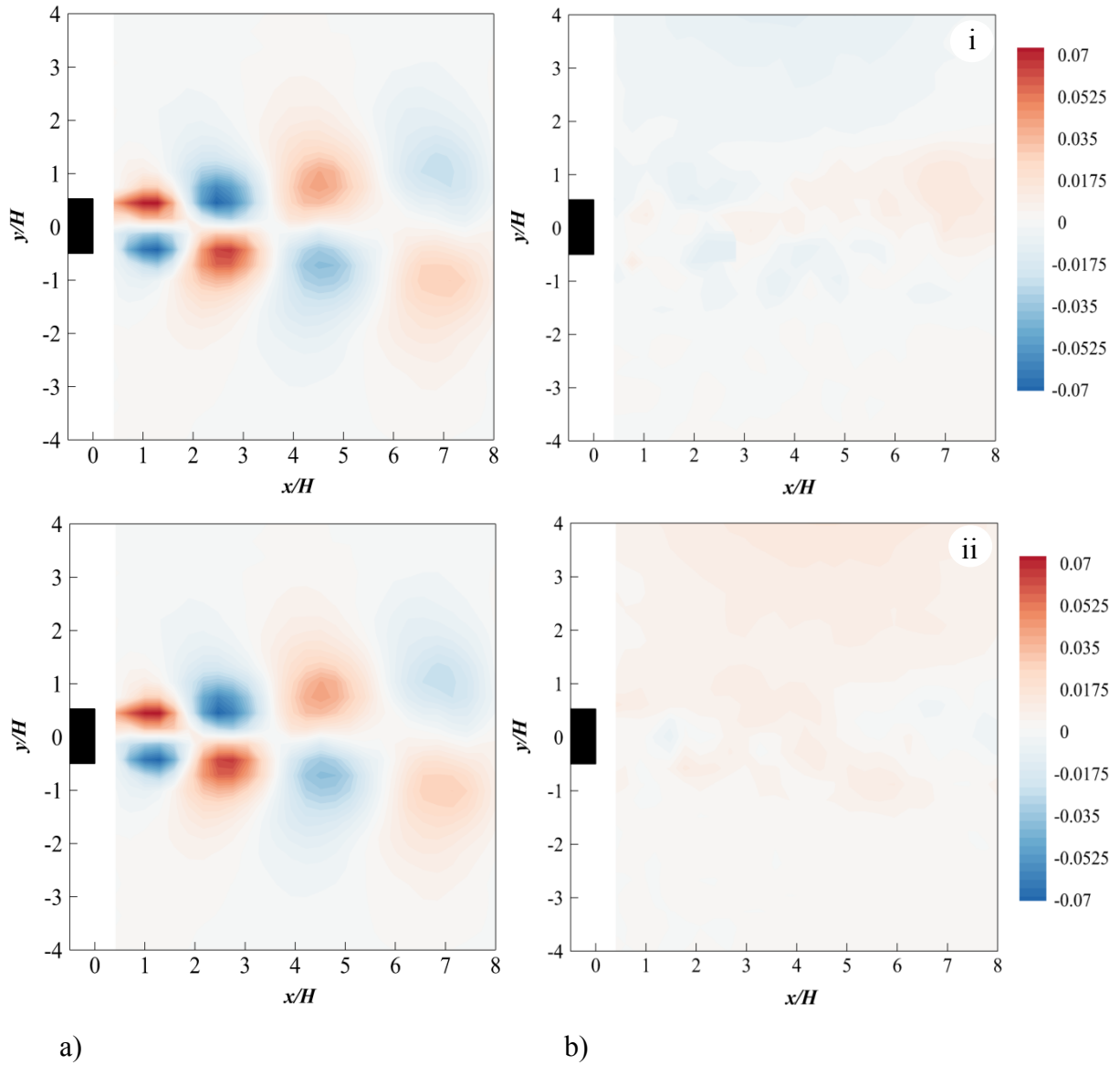
Figure 4.40 First POD mode in u for, a) plasma off and b) plasma actuator PA2 at location (i) and (ii) at free stream velocity U = 7.5 ms^{-1}, f$_{(input)}$ = 8 kHz and V$_{(input)}$ = 3.6 kV.
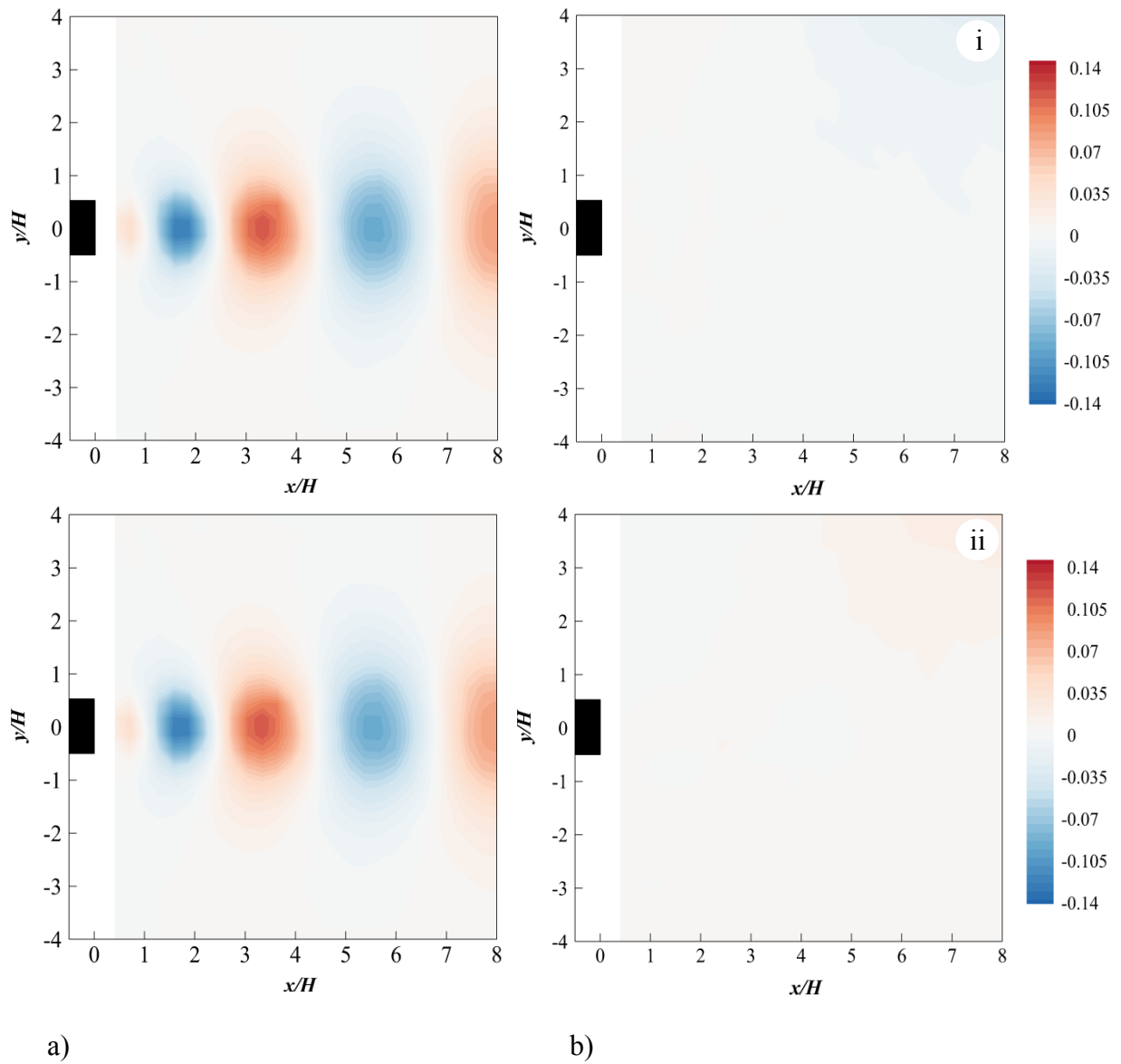
*Figure 4.41First POD mode in v for, a) plasma off and b) plasma actuator PA2 at location
(i) and (ii) at free stream velocity U = 7.5 ms^{-1}, f$_{(input)}$ = 8 kHz and V$_{(input)}$ = 3.6 kV.*
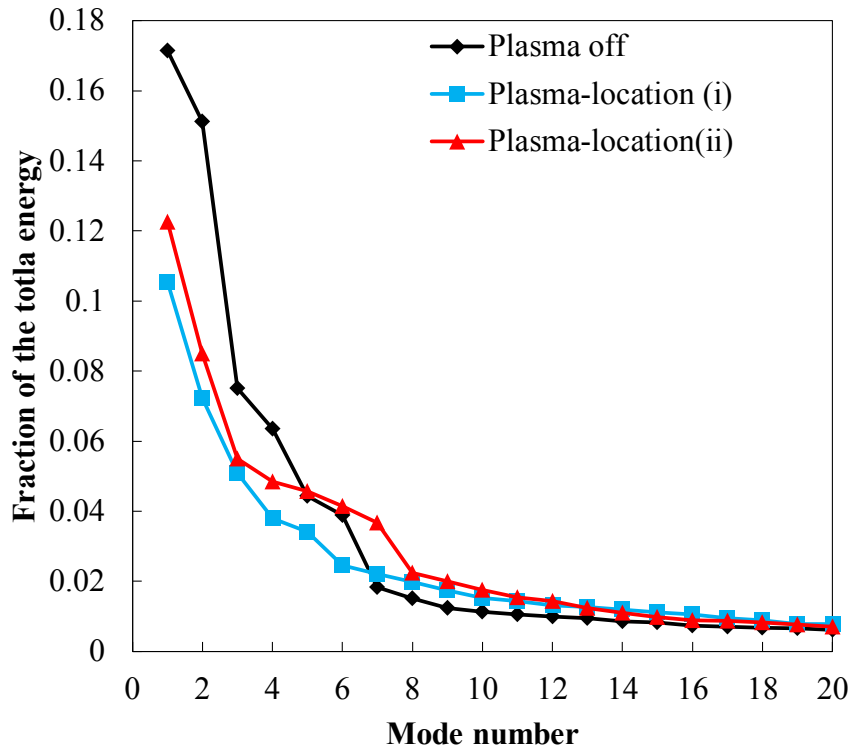
Figure 4.42 Energy contribution versus POD mode number for both plasma off and plasma on PA3 for location (i) and (ii) at free stream velocity U = 7.5 ms^{-1}, f$_{(input)}$ = 8 kHz and V$_{(input)}$ = 3.6 kV.

4.7 NACA 0012 Airfoil

4.7.1 Airfoil with Cut-In Serrated Trailing Edge

It has been shown that both the plasma actuators PA2 and PA3 successfully reduce bluntness-induced vortex shedding narrowband tonal noise by either preventing the interaction between the two separated shear layers from the blunt trailing edge, or injecting the streamwise vortices into the wake region, respectively. One of the aerodynamic bodies that are also associated with the vortex shedding is the thick airfoil with blunt trailing edge. This type of airfoil is used for wind turbine blade, due to several advantages, such as better structural strength, less manufacturing complexity, and lower blade weight. Another example of aerodynamic body that is subjected to the vortex shedding problem is an airfoil with cut-in type trailing edge serration. This type of airfoil has successfully been used for controlling the

turbulent boundary layer trailing edge noise. However, it is been found that a cut-in type serrated trailing edge can also produce narrowband vortex shedding tonal noise (Chong et al, 2013). In this section, surface DBD plasma actuator is used in conjunction with cut-in type serrated trailing edge. It should be noted that the plasma actuator is not primarily used for the reduction of the turbulent broadband noise, but rather it is used to alleviate the extraneous vortex shedding tonal noise as a result of introducing the cut-in type serration

4.7.1.1 Test Models and Plasma Actuator Configurations

NACA 0012 airfoil with sharp and cut-in type serrated trailing edge was used in the current investigation. As demonstrated in Chapter 3, the airfoil has a chord length of 150 mm and span of 300 mm. The airfoil is 3D printed and has two parts; 1) the main body and 2) trailing edge. The serrated trailing edge used in the current study has the following parameters; a serration amplitude ($2h$) of 20 mm, serration wavelength (λ) of 18.7 mm, and serration angle (φ) of 25°. The experiments were carried out at free stream velocity range $7.5 \leq U \leq 40$. The airfoil is placed at zero angle of attack with respect to the incoming free jet.

Although it has been shown earlier in this chapter that the downward (PA2 plasma actuator) and spanwise actuations (PA3 plasma actuator) both successfully control bluntness-induced vortex shedding tonal noise, the spanwise actuation is chosen for the current study that involves the cut-in serration airfoil. The reason of choosing spanwise actuation rather than the downward one is that the downward actuator is not straight forward to be implemented to the serrated trailing edge airfoil. The spanwise actuators are flash-mounted on both sides of the serrated trailing edge, where grooves of 1mm on both sides of the trailing edge were fabricated to account for the electrode and dielectric thicknesses. A 1mm thick polycarbonate plastic sheet is used as dielectric material on which both the exposed and grounded electrodes are positioned. The grounded electrode is straight copper tape of 280 mm length and 10 mm width. A new design of the exposed electrode of sinusoidal shape is adopted, which involves three different sinusoidal wavelengths. The plasma actuators will be named according to the exposed electrode shape, as shown in Fig. 4.43. The dimensional characteristics of the exposed electrodes are illustrated in table 4.3.

Trip tape

EE1 exposed electrode
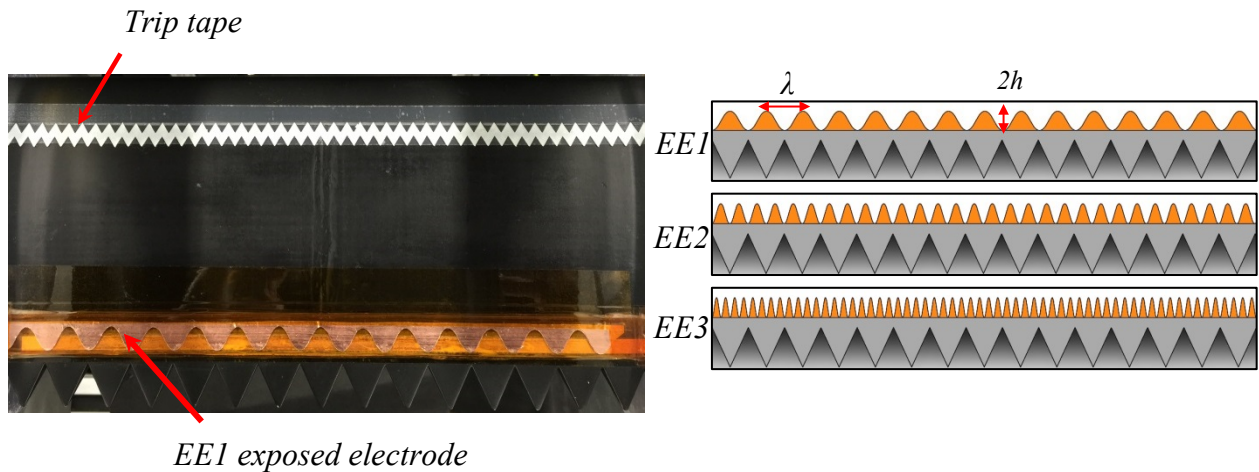
Figure 4.43 Exposed electrode configurations.

Plasma actuator	Exposed Electrode	
	λ (mm)	2h (mm)
EE1	18.6	10
EE2	9.3	10
EE3	4.6	10

Table 4.3 Geometrical characteristics of the exposed electrode.

4.7.1.2 Discussion of Results

The acoustic results for the three plasma actuator configurations (*EE1, EE2, and EE3*) will be demonstrated in this section. The impact of the plasma actuator *EE1* on the self-noise airfoil compared with cut in serration is presented in Fig. 4.44. The figure shows a comparison of the SPL spectra among the baseline case (sharp trailing edge airfoil), airfoil with serrated trailing edge only, and airfoil with serrated trailing edge and plasma actuator *EE1*. The acoustic results were obtained at U = 20 ms^{-1} and at input frequency $f_{(input)}$ = 8 kHz, and at input voltage $V_{(input)}$ = 8.5 kV. The results show that a broadband spectral is produced by the airfoil with sharp trailing edge, which is generated as result of the turbulent boundary layer scattered into sound at the sharp trailing edge of the airfoil. When the serrated trailing edge is attached to the airfoil, the turbulent boundary layer-trailing edge noise is reduced at $0.2 < fH/U < 1$. However, a distinct tonal noise can be found at $0.1 < fH/U < 0.2$ which is within the Strouhal number pertaining to the wake vortex shedding produced by a blunt trailing edge, which is the focus of the current

study. When *EE1* plasma actuator is implemented to the serrated trailing edge no significant reduction in the tonal noise can be observed (ΔSPL = 2 ±0.5dB). The tonal noise peak is also shifted towards a higher frequency to *fH/U* = 0.19 (the tone peak for the cut-in serrated trailing edge only occurs at *fH/U = 0.18)*.
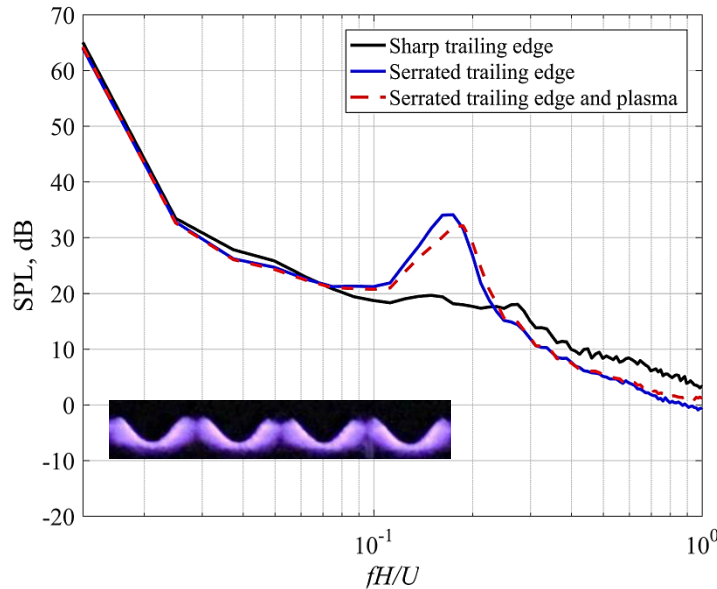
Figure 4.44 SPL spectra for NACA0012 airfoil with cut-in serrated trailing edge subjected to plasma actuator EE1at V$_{(input)}$ = 8.5 kV and at f$_{(input)}$ = 8 kHz.

The *EE1* plasma actuator was also tested at higher free stream velocities $7.5 \leq U \leq 40$ ms^{-1}. Figure 4.45 demonstrates the difference in sound pressure level ΔSPL between the serrated trailing edge airfoil (plasma off case) and the plasma on case. The positive values represent the reduction in the SPL and the opposite is true. The results show that the actuator can still reduce the bluntness induced tonal noise (*fH/U* < 0.2) up to $U = 10$ ms^{-1}. However, the non-aerodynamic self-noise generated by the electrical charge of the plasma actuator at $U \leq 10$ ms^{-1} is quite significant at *fH/U* > 0.8. The actuator self-noise becomes less significant at higher velocity, because it is masked by the aerodynamic jet and airfoil trailing edge noise.

Another plasma configuration is called the *EE3*. This actuator has a sinusoidal exposed electrode with the smallest wave length (λ = 4.6 mm) among the other plasma actuator configurations (*EE1* and *EE2*). Figure 4.46 shows the SPL spectra for the *EE3* plasma actuator at $U = 20$ ms^{-1}. It can be seen that this plasma actuator configuration is capable of reducing the level of the tonal noise

by about $\Delta SPL = 6 \pm 0.5$dB. Figure 4.47 shows the ΔSPL contours for Plasma actuator *EE3* at different free stream velocities. The results show that a significant noise reduction is achieved at $U \leq 10$ ms^{-1}.
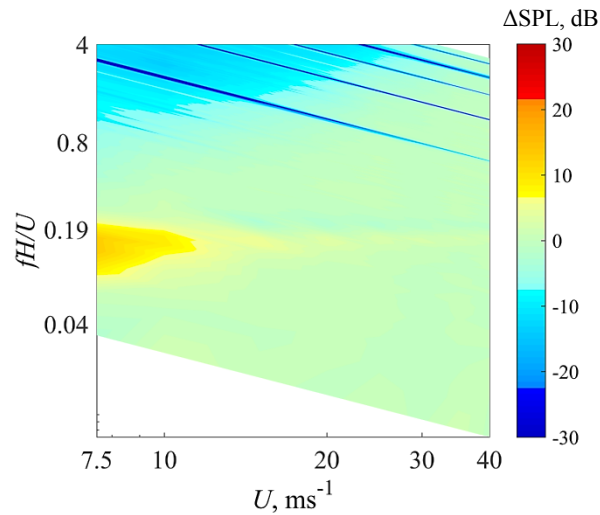
Figure 4.45 ΔSPL contours for NACA0012 airfoil with cut-in serrated trailing edge subjected to plasma actuator EE1 at V$_{(input)}$ = 8.5 kV and at f$_{(input)}$ = 8 kHz.
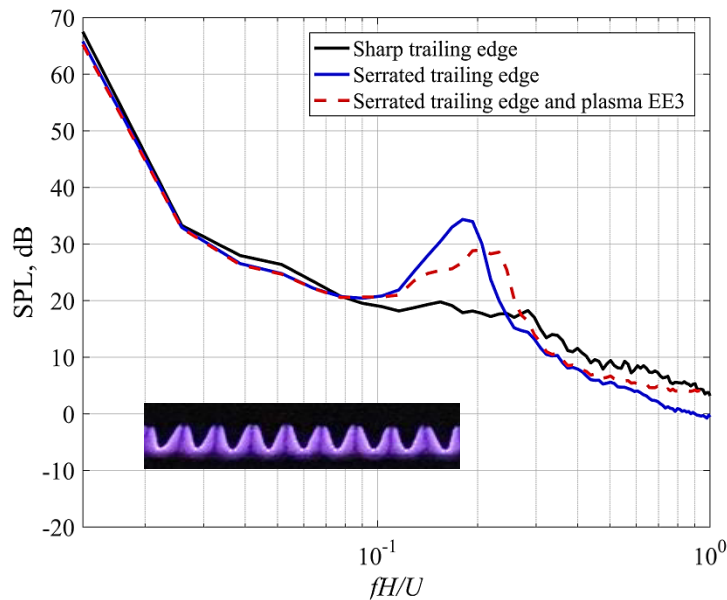
Figure 4.46 SPL spectra for NACA0012 airfoil with cut-in serrated trailing edge subjected to plasma actuator EE3 at V$_{(input)}$ = 8.5 kV and at f$_{(input)}$ = 8 kHz.
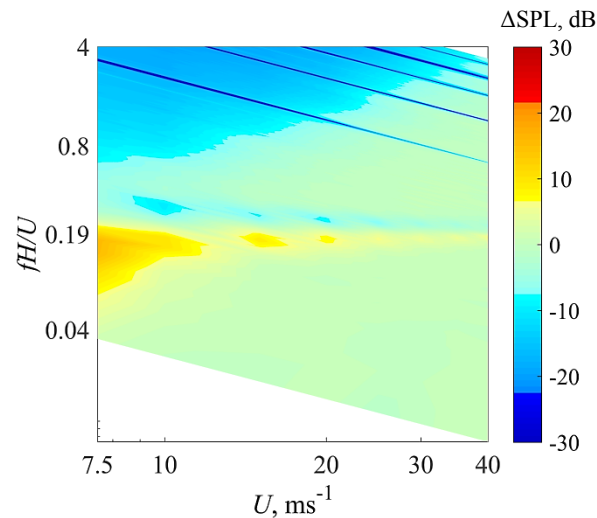
Figure 4.47 ΔSPL contours for NACA0012 airfoil with cut-in serrated trailing edge subjected to plasma actuator EE3 at $V_{(input)}$ = 8.5 kV and at $f_{(input)}$ = 8 kHz.

Finally, SPL spectra for the plasma actuator *EE2* is shown in Fig. 4.48 and 4.49. The results show that the *EE2* plasma actuator can significantly reduce the tonal noise at $U \geq 7.5$ ms^{-1} by approximately 9 ±0.5dB. This particular configuration represents the most optimal configuration for the reduction of the tonal noise generated by the cut-in serrated trailing edge. Unfortunately, the PIV system was not available during the experiment for the cut-in type serrated airfoil. As a result no flow field measurements could be done effectively to help explaining the mechanism of the current test.
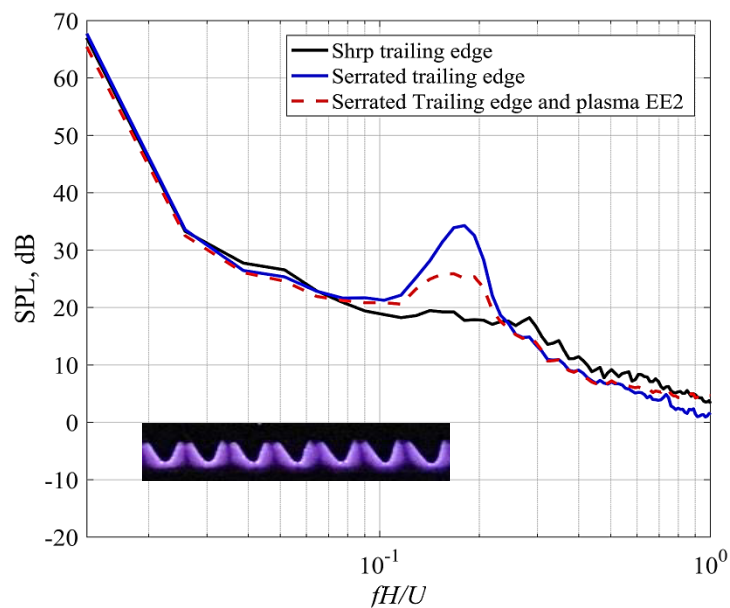
Figure 4.48 SPL spectra for NACA0012 airfoil with cut-in serrated trailing edge subjected to plasma actuator EE2 at $V_{(input)}$ = 8.5 kV and at $f_{(input)}$ = 8 kHz.
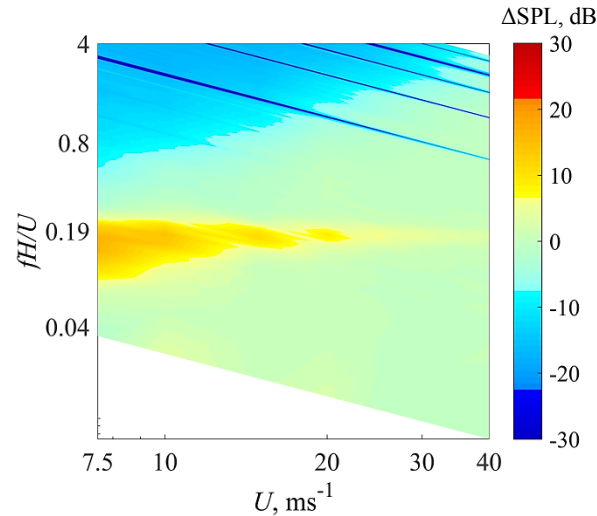
Figure 4.49 ΔSPL contours for NACA0012 airfoil with cut-in serrated trailing edge subjected to plasma actuator EE2 at $V_{(input)}$ = 8.5 kV and at $f_{(input)}$ = 8 kHz.

4.7.2 Airfoil with Blunt Trailing Edge

This section focuses on the impact of the DBD plasma actuator on the bluntness induced vortex shedding tonal noise radiated from NACA 0012 airfoil with a truncated trailing edge. The blunt trailing edge airfoil is formed by cutting off the rear part of the NACA 0012 airfoil at x/C = 0.87. The airfoil was tested at $7.5 \leq U \leq 40$ ms^{-1}. Because the *EE2* DBD plasma actuator used for the serrated trailing edge resulted in a good tonal noise reduction, the same configuration has been adapted for the current truncated trailing edge airfoil. The input voltage and frequency in the current study are 8.5kV and 8 kHz, respectively.

4.7.2.1 Acoustic Results

The SPL spectra of a NACA 0012 airfoil with a truncated trailing edge subjected to the *EE2* plasma actuator is shown in Fig. 4.50. For the plasma off case at U = 7.5 ms^{-1}, a distinct tonal noise peak at fH/U = 0.17 can be found in the SPL spectra. When the plasma actuator *EE2* plasma actuator is activated, the tonal noise generated from the truncated trailing edge is totally suppressed and a maximum tonal noise reduction of 14.5 ±0.5dB can be achieved. When the free stream velocity is increased to 10 ms^{-1}, the results show that the tonal noise can still be successfully reduced by 12.5 ±0.5dB and the peak is shifted towards the high frequency region. Further increasing the free stream velocity to $15 \leq U \leq 40$ ms^{-1} would result in no reduction in the tonal noise, as shown in Fig. 4.51.This could be due to the increase in the strength of the

wake instabilities when the free stream velocity increases. As a result, the streamwise vortices that are generated by the plasma actuator will not be strong enough to interrupt the spanwise coherence of the bluntness-induced vortex shedding.
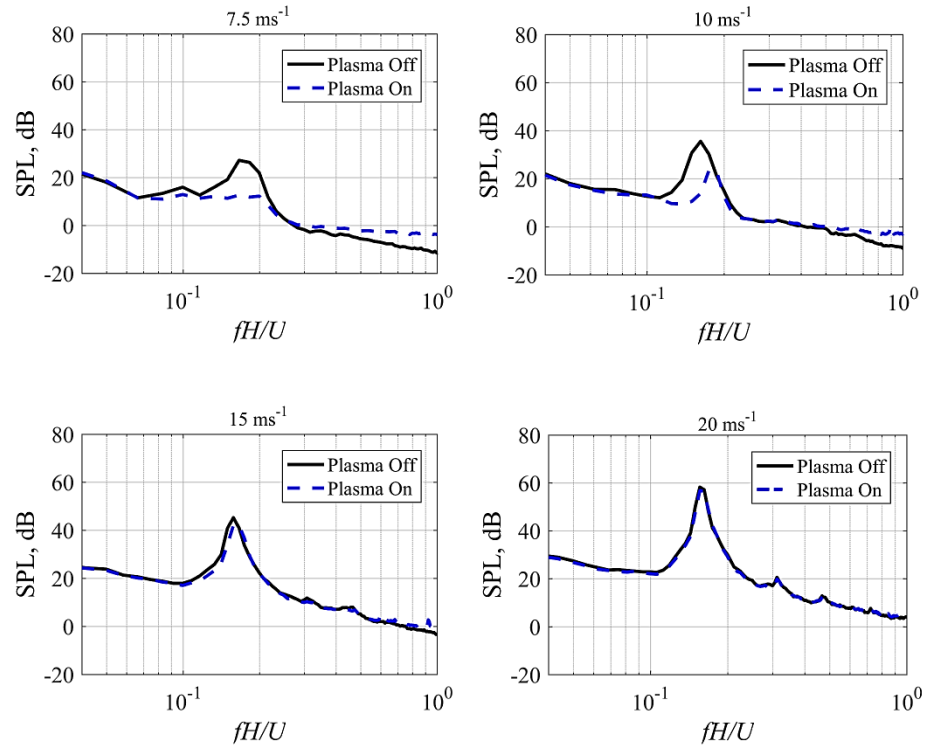
Figure 4.50 SPL spectra for NACA0012 airfoil with truncated trailing edge subjected to plasma actuator EE2 at $V_{(input)}$ = 8.5 kV and at $f_{(input)}$ = 8 kHz.
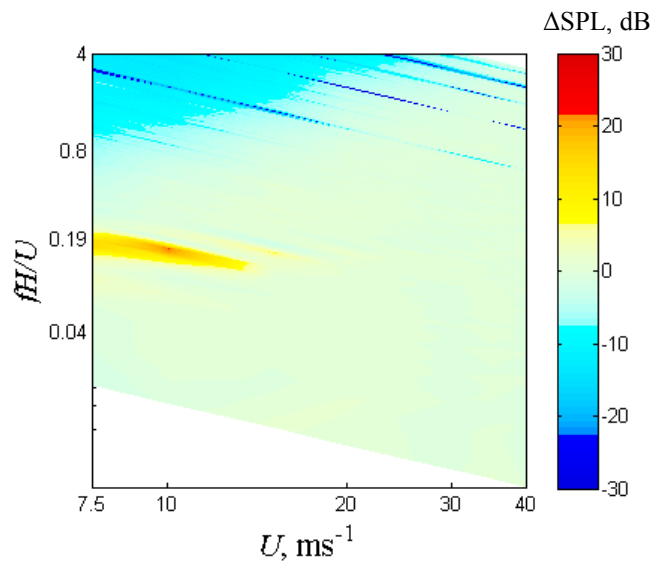
Figure 4.51 ΔSPL contours for NACA0012 airfoil with truncated trailing edge subjected to plasma actuator EE2 at $V_{(input)}$ = 8.5 kV and at $f_{(input)}$ = 8 kHz.

4.8 Summary

This chapter focuses on the impact of the surface dielectric barrier discharge DBD plasma actuators on the bluntness-induced narrowband tonal noise for the blunt trailing edge of a flat plate as well as an airfoil with cut-in type serrated trailing edge. The models were tested at free stream velocity $7.5 \leq U \leq 40$ ms^{-1} at Reynolds number base on the chord length 0.75 x $10^5 \leq Re_C \leq 4$ x 10^5. For the flat plate with blunt trailing edge, three configurations of the plasma actuator were investigated. These are the PA1, PA2, and PA3 plasma actuators. Each actuator configuration has its own unique electric wind generation method. The PA1 will produce tangential electric wind, while the PA2 generates downward electric wind directly into the center of the wake. Finally, PA3 is designed to generate ionic wind in the spanwise direction.

Both the flow and noise studies were performed in the aeroacoustic facility at Brunel University London. As the plasma actuator self-noise is proportional to the level of the input voltage, the input voltages were kept relatively low at $V_{(input)} < 5$ kV, to keep the actuator noise to the minimum and to align with trend of developing active flow control actuators that do not need high input voltages. In addition to the input voltage and frequency, the effect of dielectric thickness on the plasma actuator performance in terms of the overall sound pressure level (OASPL) was investigated. The results show that using 5 layers of Kapton tape can ensure adequate insulation between the exposed and grounded electrodes, while maintaining good noise reduction performance. In addition, increasing both the voltage and input frequency leads to increase in the noise reduction.

The sound pressure level (SPL) spectra for the flat plate with blunt trailing edge showed that a distinct narrowband tonal noise peak associated with the plasma off baseline case occurs at a reduced frequency $fH/U = 0.19$ across the free steam velocities range $7.5 \leq U \leq 40$ ms^{-1}. This frequency is similar to the vortex shedding Strouhal number of bluff body.

Results for the first plasma actuator configuration (PA1) show that this configuration is not very effective. It has been found that the maximum noise reduction that this plasma actuator can achieve is only about 2 ±0.5dB. However, an interesting aeroacoustic phenomenon has been observed when the flat pate is subjected to the PA1plasma actuator. POD analysis shows that the large coherent structures in the wake region are more compact when the flat plate is subjected to

the PA1 plasma actuator compared with the plasma off case, which indicates an increase in the shedding frequency, which is indeed manifested in the acoustic spectra.

The second plasma actuator investigated in this study is the PA2 plasma actuator. This actuator is expected to produce electric wind in the downward direction, and subsequently inject a streamwise jet directly into the wake region. From the quiescent test of this plasma configuration, it has been shown that the maximum streamwise jet that the actuator can produce is about 1.8 ms^{-1}. Although the velocity generated by the PA2 plasma actuator is less than that reported in the literature, the actuator has shown significant performance in terms of suppressing the bluntness vortex shedding tonal noise. For instance, at $U = 7.5$ ms^{-1}, and at input voltage of 4.2 kV, about 14.5 ±0.5dB reduction of the tonal noise can be achieved. This is confirmed by the results from the POD analysis of the first mode where a dramatic reduction in the energy of the large coherent structures in the wake region has been observed. In addition, the wake velocity profiles indicate that the mean and fluctuating components of the drag can be reduced by 15 % and 26 %, respectively.

Both the PIV and Pitot tube measurements of the near wake region indicate that the mechanism of the far field noise reduction by the PA2 actuator is not related to the direct injection of high momentum fluid into the wake region, but rather the induced plasma jet prevents the two separated shear layers from interacting with each other in the region close to the blunt trailing edge of the flat plate. Moreover, it has been shown that the plasma induced jet decays quickly after a short distance from the trailing edge when the free stream flow is present. This is also confirmed by the hot wire far wake measurement of the wake velocity fluctuation, where a reduction in the vortex shedding peak at Strouhal number 0.19 occurs in the fluctuating velocity power spectral density. This hydrodynamic Strouhal number is similar to the acoustical Strouhal number observed in the far field noise of the SPL spectra.

The last plasma actuator investigated in the current study is PA3. From the quiescent measurement result, it has been found that this plasma actuator is capable of producing a vertical plasma jet with counter rotating vortices on both sides of the jet, which are generated as a result of the interaction between the spanwise and the wall normal jet. These counter rotating vortices are projected into the wake region under the presence of free stream flow. It is believed that the interaction between these projected counter-rotating vortices with the bluntness-induced vortex

shedding plays an important role in the far field tonal noise reduction. This configuration of the plasma actuator has shown better performance in terms of tonal noise reduction compared to the PA2 plasma actuator at lower input voltages. For instance, a tonal noise reduction of 12 ±0.5dB can be achieved when PA3 actuator is used at input voltage of only 3 kV compared to 3.4 ±0.5dB reduction by PA2 at the same input voltage. However, when the input voltage is further increased to 4 and 4.2 kV, no significant tonal noise reduction can be achieved.

The POD analysis of the flow field subjected to the plasma actuator PA3 has shown a significant reduction in the energy of the large coherent structures in the wake region. This absence of the high energy structures in the wake region is believed to be the reason of the reduction in the bluntness induced far field tonal noise. However, there are regions where no streamwise vortices are generated, which are related to the location (iii) in Fig. 4.33. Therefore, these untreated regions will contribute to the overall far field tonal noise radiation, due to the existence of bluntness induced vortex shedding downstream of the exposed electrode in the wake region.

Next, the impact of the distributed spanwise forcing by the plasma actuator on an airfoil with cut-in type serrated trailing edge is investigated. The PA3 plasma actuator was chosen for the reduction of cut-in serration bluntness-induced vortex shedding tonal noise. Three different actuators were investigated, which are named according to the exposed electrode configuration; *EE1*, *EE2*, and *EE3*. Instead of using straight exposed electrode, a new sinusoidal one has been investigated. The reason of selecting this configuration is that this class of plasma actuator can generate 3D flow in the region close to the serration similar to the serpentine plasma actuators. Different wavelength has been investigated; λ = 18.6 mm for *EE1* actuator, λ = 9.3 mm for *EE2* actuator, and λ = 4.6 mm for *EE3* actuator. The acoustic results show that the *EE2* plasma actuator outperforms both *EE1* and *EE3* plasma actuator in terms of the bluntness-induced tonal noise reduction. A 9 ±0.5dB noise reduction can be achieved by the *EE2* plasma actuator compare to 2 and 6 ±0.5dB by the *EE1* and *EE3*, respectively. The *EE2* plasma actuator configuration is adapted for the reduction of bluntness-induced vortex shedding tonal noise produced by an airfoil with a truncated trailing edge. The results show that at 7.5 and 10 ms^{-1}, a maximum tonal noise reduction of 14.5 ±0.5 dB and 12.5 ±0.5dB, respectively can be achieved. The plasma actuator performance deteriorates when it is tested at higher free stream velocities $15 \le U \le 40$ ms^{-1}.

Chapter 5

Circular Cylinder

5.1 Introduction

In this chapter, both the aeroacoustic and hydrodynamic field results of a single cylinder and two cylinders in tandem configuration subjected to DBD plasma actuator are presented. A description of the tested models and the specifications of plasma actuator used in the current study will be given in section 5.2. Section 5.3 is devoted to the acoustic and flow filed experimental results for the single cylinder. The acoustic and flow field results for two cylinders in a tandem configuration will be presented in section 5.4. A summary of all of the results will be provided in section 5.5.

5.2 Tested Models

In the current study, both the aeroacoustic and flow investigations were conducted simultaneously at the same aerocoustic facility. The tested models used in the current study are single circular cylinder and two circular cylinders in tandem configuration. The cylinders have a diameter of 16 mm and length of 300 mm. For the case of two tandem circular cylinders, the horizontal distance between the cylinders was fixed to $L/D = 4$, where L is the distance from center to center and D is the cylinder diameter. This ratio was chosen in order to ensure that each cylinder produces vortex shedding that is independent of each other [Arie et al. (1983) and Zdravkovich (1985)]. In order to ensure the two dimensionality of the flow, the cylinders were placed between two side plates, which extend from the nozzle side walls. Both acoustic and flow control tests were conducted at relatively low subcritical Reynolds number based on the cylinder diameter $Re_D = 1.1 \times 10^4$ (Free stream velocity $U = 10$ ms^{-1}). At this Reynolds number, the flow separates on the cylinder at 80° from the front stagnation point (designated as 0° location) and the cylinder has strong and periodic vortex shedding afterwards.

The dielectric barrier discharge plasma actuator DBD used in the current study is composed of two electrodes; the exposed and ground electrodes. Both electrodes have a length of 280 mm

(extends in the spanwise direction of the cylinder) and width of 6 mm. For both test models (single and tandem cylinders), the actuators were positioned in a way that plasma induced jet is induced at different angles (measured from the front stagnation point) before and after the separation line, $\pm 27^o \leq \theta_j \leq \pm 153^o$. The models of single and tandem cylinders with plasma actuator were described in Chapter 3 (Fig. 3.11).

Thomas et al. (2008) and (2006), Kim and Wang (2009), Kozlov and Thomas (2011) studied the impact of DBD plasma actuator on the large coherent structures in the wake of circular cylinder at subcritical Reynolds number range 2.2 x $10^4 \leq Re \leq 17.2$ x 10^4 (free stream velocity $U = 5$ ms^{-1}). They reported that plasma actuator is capable of eliminating vortex shedding using both steady and unsteady actuation. However, because of the limitations of their experimental facility, and perhaps not their main research objectives, no far field acoustic measurements were made. Although the Reynolds number used in the current study is lower than those reported in the literatures, it is still within the range of subcritical Reynolds numbers. The aim of the current study is to provide information about the impact of plasma actuator on the narrowband tonal and wake interaction broadband noise radiated from single cylinder and two cylinders in tandem configuration, respectively and to clarify the mechanism of noise reduction. The acoustic and hydrodynamic results for the single cylinder and two cylinders in tandem configuration will be discussed next.

5.3 Single Cylinder

5.3.1 Acoustic Results

In this section, flow induced aerodynamic noise from a single cylinder will be investigated. The cylinder was tested at free stream velocity $U = 10$ ms^{-1} with Reynolds number based on the free stream velocity and cylinder diameter $Re_D = 1.1$ x 10^4. Before the effect of DBD plasma actuator on the aerodynamic noise induced by vortex shedding from the cylinder is discussed, the findings of surface oil flow visualization will be presented first.

The surface flow visualization experiment was conducted to identify the angle at which the flow separates from the cylinder wall and to make sure that the presence of the plasma actuator does not trip the flow. Figure 5.1 shows the results of oil flow visualization over circular cylinder at

free stream velocity $U = 10$ ms^{-1}. It can be seen that when mean the flow is present, the oil moved until it reached the indicated red dashed line, which represents the separation line. The flow separates at a separation angle $\theta_s = 75^\circ$ and reattaches at $\theta_r = 90^\circ$, which is in reasonable agreement with Yokuda and Ramaprian (1990) who reported that for Reynolds numbers $10^4 \leq Re \leq 10^5$, the wake is fully turbulent and laminar flow separation occurs at an angle $\theta_s = 75^\circ$-80°. Thus the current plasma actuator does not affect the flow over the cylinder. Although reported literature [Sato et al. (2013) and Che et al. (2015)] suggests that the position of the plasma actuator for optimum flow control is normally when the actuator is placed close to the separation point. In the current investigation, the plasma actuators were positioned at various angles before and after the separation point on both top and bottom half of the cylinder $(\pm 27^\circ \leq \theta_j \leq \pm 153^\circ)$ in order to identify the effect of different plasma induced jet positions on the aerodynamic noise induced by vortex shedding in the wake of the circular cylinder.

a) Without flow ($U = 0$ ms^{-1})

b) With flow ($U = 10$ ms^{-1})
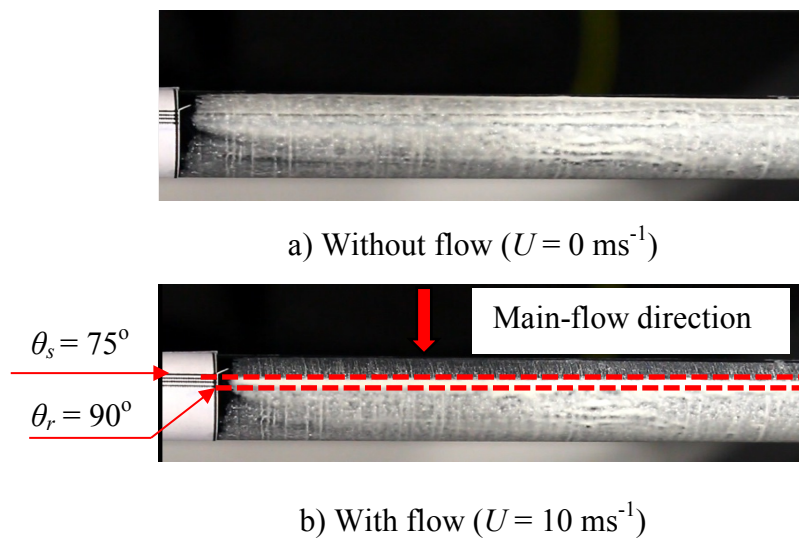
Figure 5.1 Surface oil flow visualization over circular cylinder at free stream velocity $U = 10$ ms^{-1}.

The effect of DBD plasma actuator on the aerodynamic noise generated by vortex shedding from circular cylinder at free stream velocity $U = 10$ ms^{-1} was investigated first. The input voltage and frequency are $V_{(input)} = 6$ kV and $f_{(input)} = 8$ kHz respectively. Figure 5.2 presents the sound pressure level SPL for both baseline "plasma off" and "plasma on" case against Strouhal number fD/U, where f is the frequency, D is the cylinder diameter and U is the free stream velocity. The actuator was placed at different angles measured from the front stagnation point $\pm 27^\circ \leq \theta_j \leq \pm 70^\circ$, where "$\theta_j$" represents the angle at which plasma induced jet initiates. It can be seen that for

plasma off case a significant narrowband tonal peak occurs in the SPL spectra at Strouhal number $fD/U = 0.185$, which is close to that normally associated with vortex shedding from bluff bodies of about 0.2, [Sumer and Fredsoe, (1997)]. In addition to the main peak another small peak that is believed to be the third harmonic of the main tone occurs at $fD/U = 0.545$. It will be shown later in flow field measurements that the first three harmonics occur in the unsteady velocity power spectral density (PSD) spectra. The presence of the of the harmonic peaks in the acoustic spectra agrees with the numerical steady results reported by Khalighi et al. (2010) and Eltaweel et al. (2014), who successfully captured the main shedding frequency and its first three harmonics for a single cylinder. For plasma on case the results show that for actuators positioned at angles $\theta_j \leq \pm 90^o$, no noise reduction can be achieved. However, as the actuator azimuthal angle increases, both main and the third harmonic peaks are shifted towards the high frequency region. This could mean that the plasma actuator at these positions may alter the wake vortex structure to some extent, although this remains for future investigation. When the actuator is placed at $\theta_j = \pm 90^o$ downstream the separation angle, the result show that the main tonal peak noise is reduced by about 9 ± 0.5dB and shifted towards a high frequency $fD/U = 0.223$, while a total suppression of the secondary peak can be seen, as shown in Fig. 5.3. A major suppression of the main peak harmonic can be observed as well. When the plasma actuator is placed further downstream the separation angle at $\theta_j = \pm 110^o$, the reduction in the narrowband tonal peak noise becomes less compared with the plasma actuator at $\theta_j = \pm 90^o$. The maximum noise reduction that can be achieved when the actuator is placed at this position is about 6.5 ± 0.5dB compare to 9 ± 0.5dB at $\theta_j = \pm 90^o$. When the actuator angle is increased to 125° and 133°, one can notice that the main tonal peak noise in the SPL spectra is reduced by up to 11 ± 0.5dB at $\theta_j = \pm 125^o$ and 12 ± 0.5dB at $\theta_j = \pm 133^o$. In addition, a total suppression of the third harmonic of the main tonal peak noise can be seen at $fD/U = 0.545$. This reduction in the main tonal peak in the current steady is in good agreement with near field acoustic measurements reported by Kozlov and Thomas (2009). They found that the plasma actuator can effectively reduce the tonal noise by 12.6 dB using the same actuator design of the current work. Finally, for the last actuator position, $\theta_j = \pm 153^o$, the results show that although the actuator is still capable of reducing the main tonal noise, the level of reduction is not as significant. However, the third harmonic at $fD/U = 0.545$ can still be suppressed. By far, the acoustic results have shown that the current plasma actuator setup is capable of reducing the

main peak tonal noise level induced by the vortex shedding from the cylinder. Although the narrowband tonal noise is reduced when the actuator is placed at $\theta_j = \pm90^o$, $\pm110^o$, $\pm125^o$, and $\pm153^o$, the actuator that was placed at $\theta_j = \pm133^o$ is chosen for the flow field study using both the PIV and hot wire because it led to the highest level of noise reduction compared with the other tested angles. It is worth noting that the main tonal frequency subjected to the plasma on case is shifted to a slightly higher value for the azimuthal angles $\pm70^o \leq \theta_j \leq \pm90^o$. Increasing the azimuthal angle $\theta_j > 90^o$ leads to a reduction in the radiated main tone frequency until it becomes similar or slightly less than the baseline "plasma off case". This interesting phenomenon of shedding frequency variation has been reported by many experimental and numerical studies at high and low Reynolds numbers. For instance, Roshko (1955), Apelt et al. (1973), and Apelt and West (1975), reported that using splitter plate of different lengths in the wake region of a circular cylinder leads to a variation in the vortex shedding frequency. This variation is accompanied by an elongation of the wake deficit region and an increase in the base pressure.
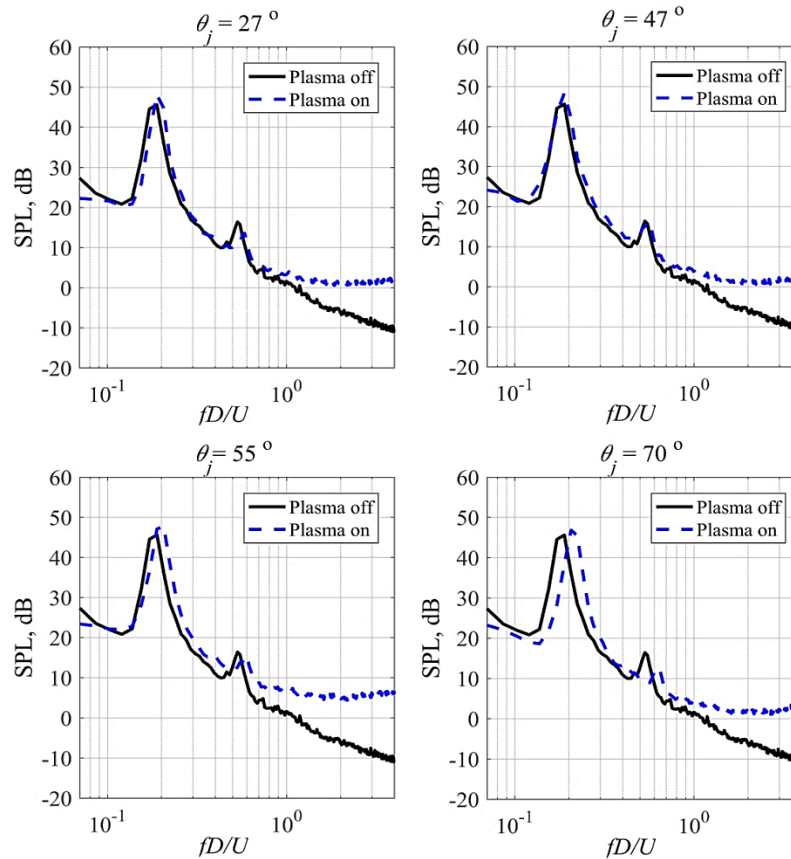
Figure 5.2 SPL spectra for a single cylinder subjected to DBD plasma actuator at angles measured from the front stagnation point $\pm27^o \leq \theta_j \leq \pm70^o$ at free stream velocity $U = 10 \ ms^{-1}$ and at $V_{(input)} = 6 \ kV$ and $f_{(input)} = 8 \ kHz$.
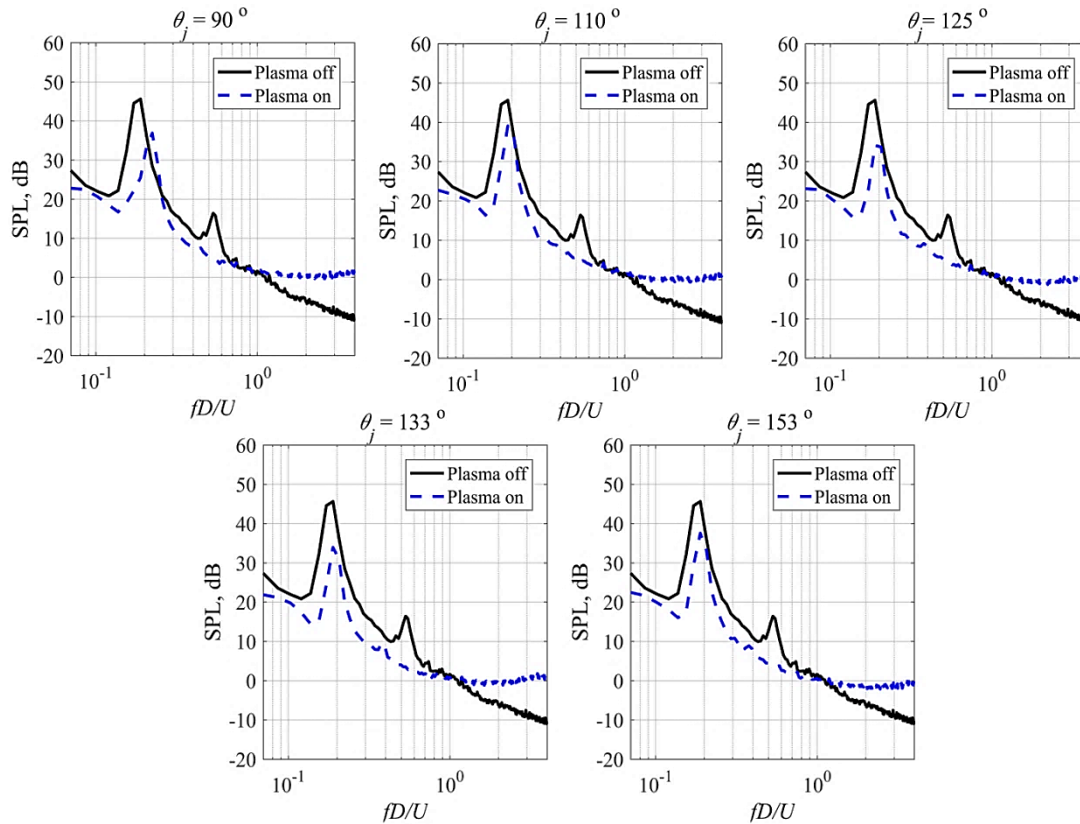
Figure 5.3 SPL spectra for a single cylinder subjected to DBD plasma actuator at angles measured from the front stagnation point± 90° ≤ θ$_j$ ≤ ±153° at free stream velocity U =10 ms^{-1} and at V$_{(input)}$ = 6 kV and f$_{(input)}$ = 8 kHz.

5.3.2 Flow Results

5.3.2.1 Instantaneous Flow Field

In the previous section, it has been shown that maximum noise reduction for single cylinder can be achieved when the plasma actuator is placed at an angle of θ_j = 133°. In order to get general idea about the effect of plasma actuator on the wake region, the instantaneous streamwise velocity field and the spanwise vorticity in the wake region of a single cylinder subjected to DBD plasma actuator placed at θ_j = ±133° and at a free stream velocity U = 10 ms^{-1} will be presented in this section. Figures 5.4a-b presents the instantaneous streamwise velocity field for both the plasma off and plasma on cases respectively, in the *x-y* plane. The input voltage and frequency are the same at $V_{(input)}$ = 6 kV and $f_{(input)}$ = 8 kHz, respectively. For the plasma off case, the instantaneous flow field result shows that a recirculating and non-convective flow region ($u/U \leq 0$) is formed as a result of flow separation from the cylinder's upper and lower wall

surfaces. In addition, a large spatial variation of the velocity deficit can be seen in the wake region of the Plasma off case. This is also seen in Fig. 5.7a where the recirculation region occurs just after the cylinder base. For the plasma on case, a large and longer recirculating region in the wake region behind the cylinder can be seen. The wake region now exhibits smaller spatial variation of the velocity deficit when compared with the plasma off case, as shown in Fig. 5.4b. This also confirmed in time-averaged streamwise velocity (Fig. 5.7b) where the dead air pocket is elongated further in the downstream direction under plasma actuation.

Figure 5.4 Instantaneous streamwise velocity for single cylinder subjected to a) Plasma off and b) Plasma on case at free stream velocity U = 10 ms⁻¹ at $V_{(input)}$ = 6 kV and $f_{(input)}$ = 8 kHz.

The corresponding instantaneous spanwise vorticity contours measured in the *x-y* plane in the wake region of the circular cylinder for both the plasma off and plasma on cases are demonstrated in Fig. 5.5a-b. For the plasma off case, two regions of negative and positive vorticity are generated as a result of the separation of the shear layers from the upper and lower surface of the cylinder, respectively. It can also be seen that the separated shear layers start to roll up near to the cylinder back. On the other hand, for the plasma on case, the vorticity contour shows that the separated shear layers extend in the downstream direction away from the cylinder rear face. This confirms what was seen earlier in Fig.5.4b. This flow behavior for plasma off and on cases is seen in the time averaged spanwise vorticity, which shows that when plasma actuator

is turned on the roll up process starts further downstream the cylinder base compared with plasma off case, as shown in Fig. 5.10. More details will be provided in the next section.

Figure 5.5 Instantaneous spanwise vorticity for single cylinder subjected to a) Plasma off and b) Plasma on case at free stream velocity U = 10 ms⁻¹ at V$_{(input)}$ = 6 kV and f$_{(input)}$ = 8 kHz.

5.3.2.2 Time-Averaged Flow Field

Time-averaged flow field quantities obtained from the PIV measurements, such as the streamwise velocity, vertical velocity, spanwise vorticity, velocity fluctuations, and POD modes will be presented in this section. Before the discussion of the time-averaged flow field results, PIV study was conducted to measure plasma induced jet at quiescent condition. The input voltage and frequency are $V_{(input)}$ = 6 kV and $f_{(input)}$ = 8 kHz, respectively. The uncertainty in the mean velocity is as high as approximately 0.9 % of the free stream velocity. Figure 5.6 presents the plasma induced streamwise velocity contours for single cylinder at quiescent condition. The plasma induced jet from the upper and lower actuators merge at the center line of the cylinder producing a streamwise jet. The jet core velocity extends from $0.2 \leq x/D \leq 0.75$, where at $x/D \approx 0.2$, a maximum induced jet velocity of $\hat{u} \approx 2$ ms⁻¹ can be observed, while further downstream at $x/D \approx 0.75$ the induced jet decays to about $u \approx 1.6$ ms⁻¹. Although the plasma induced jet is reduced by 20%, it has been shown from the instantaneous spanwise vorticity (Fig. 5.5) and the streamwise velocity contours (Fig. 5.4) that the plasma actuation led to an

increase in the vortex shedding formation length compared with the plasma off case (This point will be demonstrated clearly in the next few paragraphs). This could mean that the plasma induced jet affects the wake flow when the main flow is present. This effect will be further investigated in the analysis of the time-averaged flow quantities in the next paragraph.
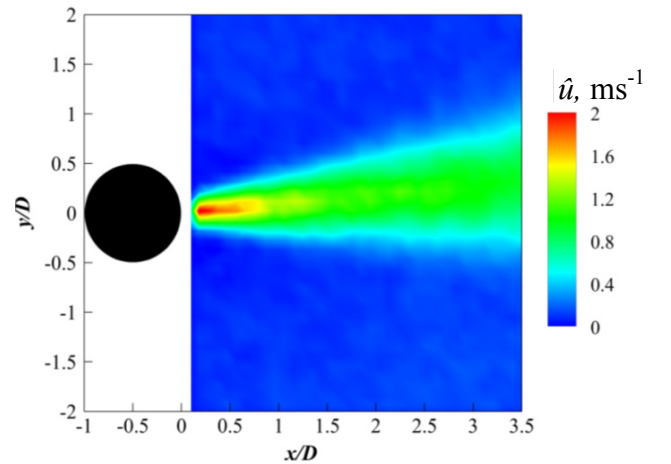
Figure 5.6 Plasma induced streamwise velocity contours for single cylinder subjected to plasma actuator at $V_{(input)} = 6$ kV and $f_{(input)} = 8$ kHz.

The time-averaged streamwise velocity contours superimposed with the streamlines for the cylinder subjected to plasma off and plasma on cases at free stream velocity $U = 10$ ms^{-1} are presented in Fig. 5.7a-b. For the plasma off case, it can be seen that a wake region with two semi-symmetric vortices is formed behind the cylinder due to the separation of the boundary layer. The center of the recirculation (the focal point, F) occurs at a streamwise location $x/D \approx 0.5$. When the plasma actuator is activated, the focal point is shifted to $x/D \approx 1$. This effect of plasma actuator on the flow in the wake region behind the cylinder is similar to the reported effect of a splitter plate in the wake region of bluff bodies (cylinder and flat plate). It has been shown that using a splitter plate can successfully inhibit the interaction between the separated shear layers and elongates the wake region. Akili et al. (2008) found that by placing a splitter plate in the wake region of circular cylinder at $Re = 6300$ the wake region elongates as the length of the splitter plate is increased and the focal points significantly is moved into the downstream direction with the saddle point (the point where intensive fluctuations occur) is located at the trailing edge of the splitter plate. Their findings agree with time-averaged streamwise velocity contours in the current steady Fig. 5.7a-b where a clear shift of the focal point can be seen with the vertical distance between them is about 0.5D when the cylinder is subjected to plasma

actuation compared with the plasma off case. This suggests that the plasma actuator could inhabit the cross talk between the separated shear layers in a way similar to what a splitter plate can do. Figure 5.8 shows a comparison between the plasma off and plasma on cases of the wake half width obtained from the streamwise velocity field. The results show that plasma actuation can lead to an increase in the near wake half width compared with the plasma off case ($0.5 \leq x/D \leq 1$). However, further downstream, plasma actuation results in a reduction in the wake half width ($x/D > 1$). The results in Fig. 5.8 demonstrates that, at $0.5 \leq x/D \leq 1$, the thickening of the wake half width for the plasma on case could be caused by case the lack of interaction between the separating shear layers. At $1.25 < x/D < 3$, the thinning of the wake half width for plasma on case is could be due reduction in the size of the large scale structures that are otherwise prominent in the plasma off case.

a)   b)
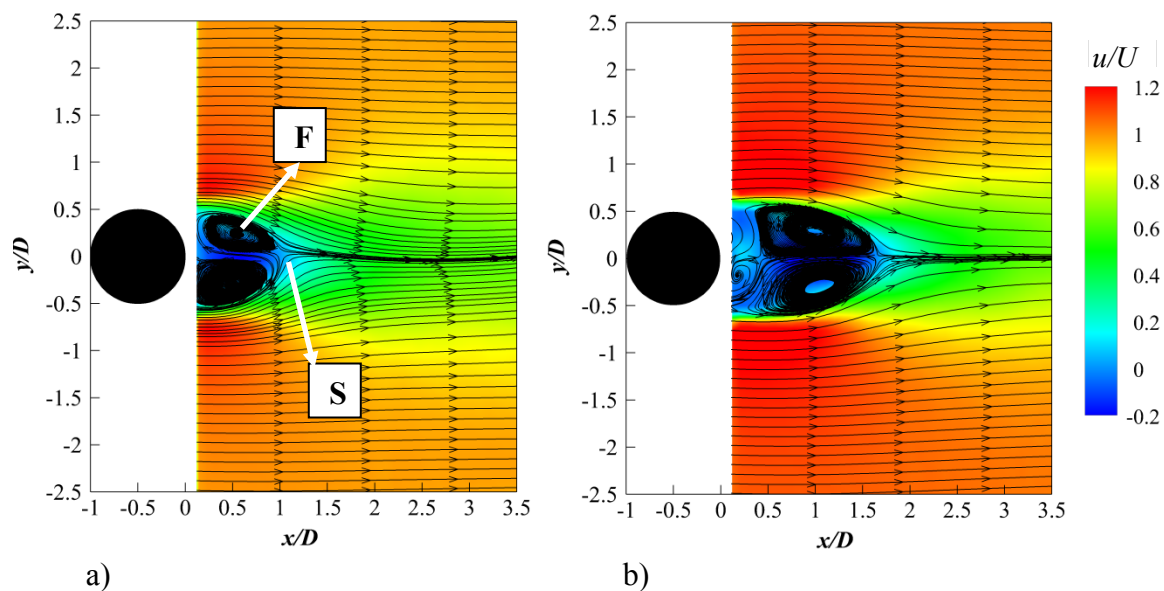
Figure 5.7 Time-averaged streamwise velocity for single cylinder subjected to a) Plasma off and b) Plasma on case at free stream velocity $U = 10\ ms^{-1}$ at $V_{(input)} = 6\ kV$ and $f_{(input)} = 8\ kHz$.

Next, the impact of plasma actuator on the vertical velocity is presented in Fig. 5.9. It can be seen that for the plasma off case, the vertical velocity, which represents the upward and downward movement of the flow resulted from the vortex shedding in the wake region has a maximum value at streamwise location $x/D \approx 1$. This represents the end of the recirculation region and the start of the convective shear flow and this point also is known as the saddle point, as demonstrated earlier in Fig. 5.7a. For the plasma on case, a clear shift of the maximum value

of the vertical velocity in the downstream direction up to $x/D \approx 1.5$, which also agrees with the results presented earlier in Fig. 5.7b, where the plasma actuation leads to the elongation of the recirculation region and a shift in the saddle point to the same streamwise location $x/D \approx 1.5$. This suggests that the plasma on case can delay the roll up of the separated shear layers as will later be shown in the vorticity contours in the next paragraph. Indeed the corresponding vertical fluctuating velocity field also manifests the same picture.
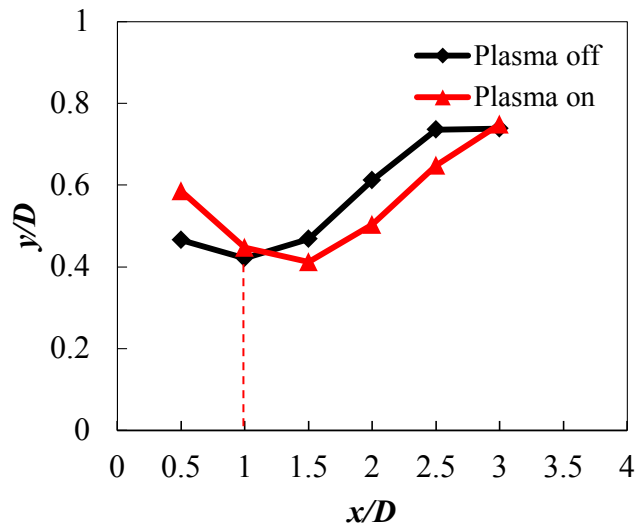
Figure 5.8 Comparison of plasma off and plasma on of streamwise evolution of the wake half width at $U = 10\ ms^{-1}$ at $V_{(input)} = 6\ kV$ and $f_{(input)} = 8\ kHz$.

a)   b)
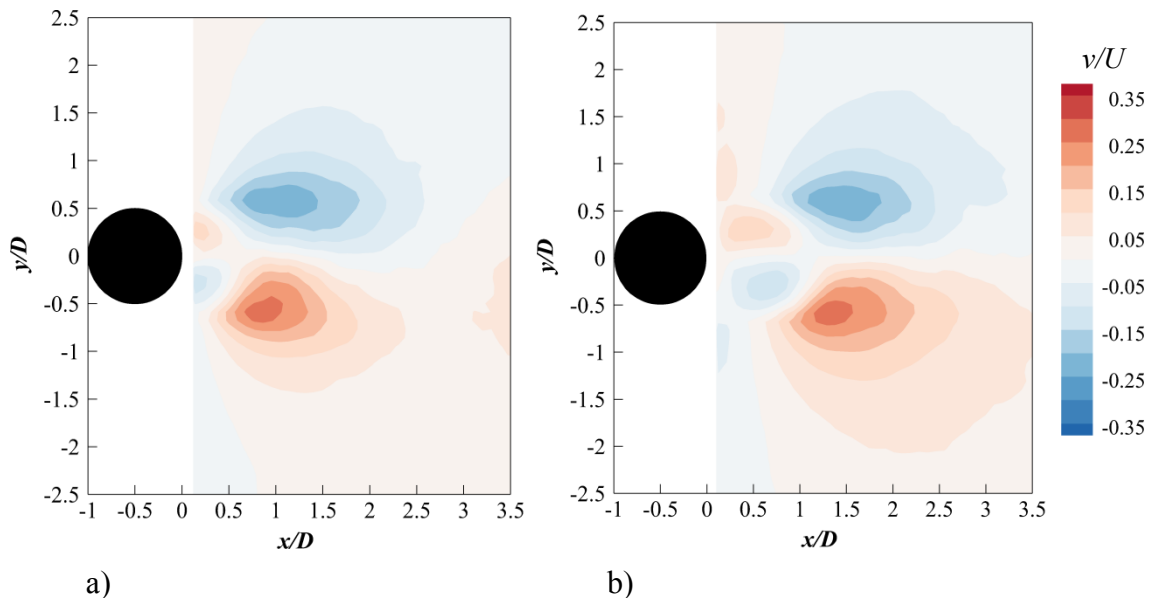
Figure 5.9 Time-averaged vertical velocity for single cylinder subjected to a) Plasma off and b) Plasma on case at free stream velocity $U = 10\ ms^{-1}$ at $V_{(input)} = 6\ kV$ and $f_{(input)} = 8\ kHz$.

The impact of plasma actuator on the spanwise vorticity filed is presented in Fig.5.10. For plasma off case the separated shear layers from the upper and lower sides of the cylinder starts to interacts directly after the base of the cylinder. The effective region of the spanwise vorticity extends to a streamwise location of $x/D \approx 1$. However, for the plasma on case, the spanwise vorticity region extends further in the downstream direction up to $x/D \approx 1.5$ where the entrainment of the shear layers occurs. Because the Karman vortex shedding occurs as result of the roll up of the separated shear layer at certain distance from the cylinder, the short vorticity length implies that the vortex shedding is triggered close to the cylinder (as demonstrated earlier in the instantaneous vorticity contours Fig 5.5a). This suggests that when plasma actuator is activated, the plasma induced jet inhibits the interaction between the separated shear layers up to a streamwise location $x/D \approx 1.5$ where vortex shedding will be triggered further downstream and the oscillation of the separated shear layers starts. This behavior also reported by Kawai (1990) and Akili et al. (2008) who found that using a splitter plate elongates the separated shear layers and significantly suppresses the flapping. Eltaweel et al. (2014) reported that the vortex shedding from the cylinder is the main acoustic source. Thus any suppression of these vortices or any movement away from the cylinder will result in a reduction vortex shedding tonal noise. In the current study the spanwise Karman vortices are shifted away from the cylinder back. This could be the reason of the reduction in the tonal noise peak demonstrated earlier in Fig. 5.3.
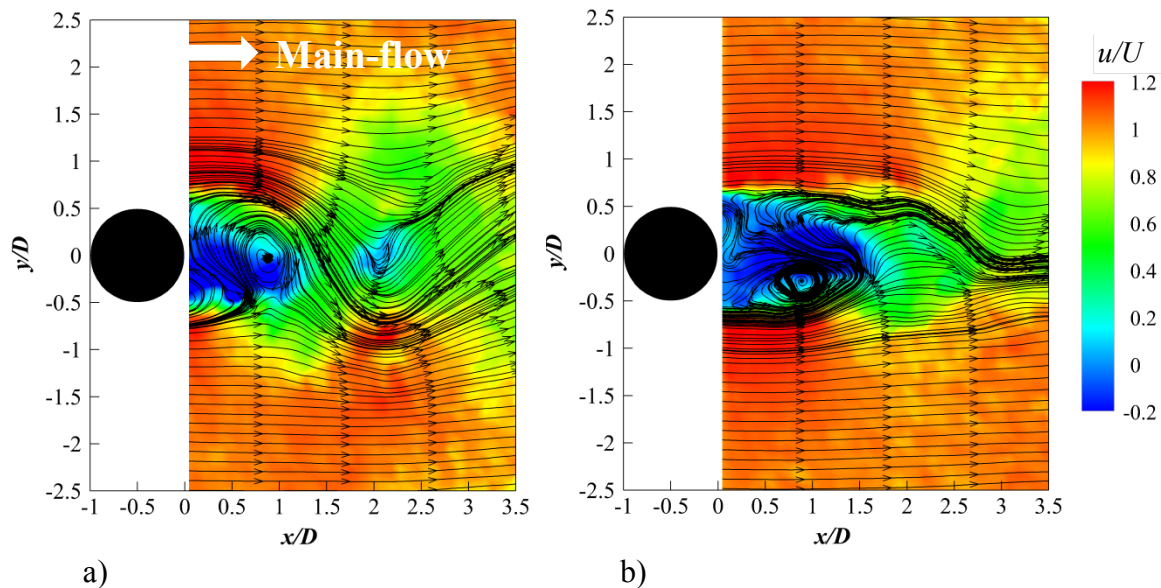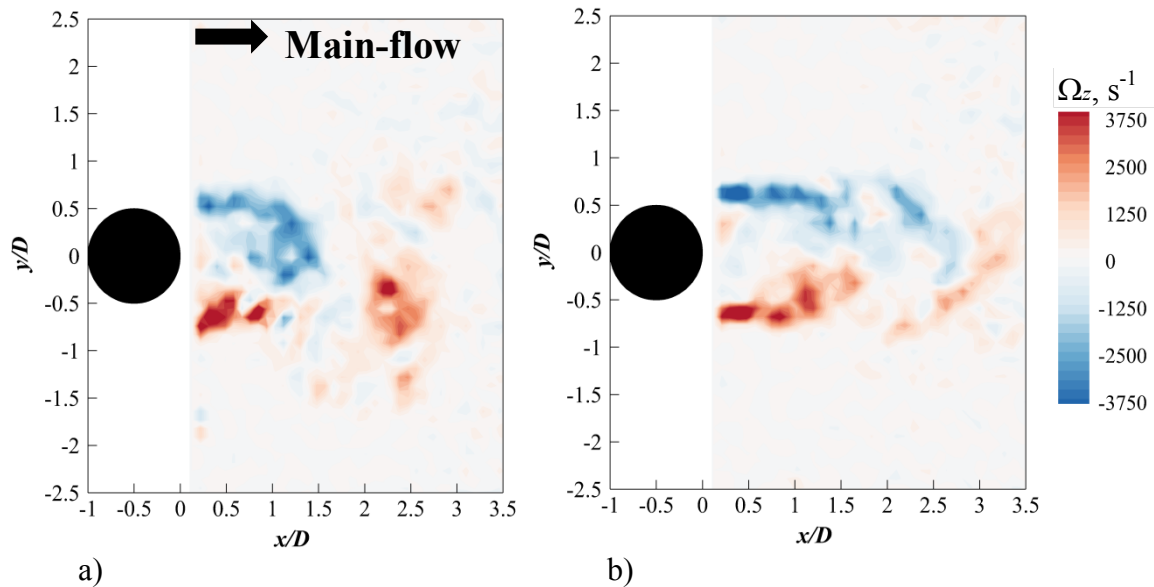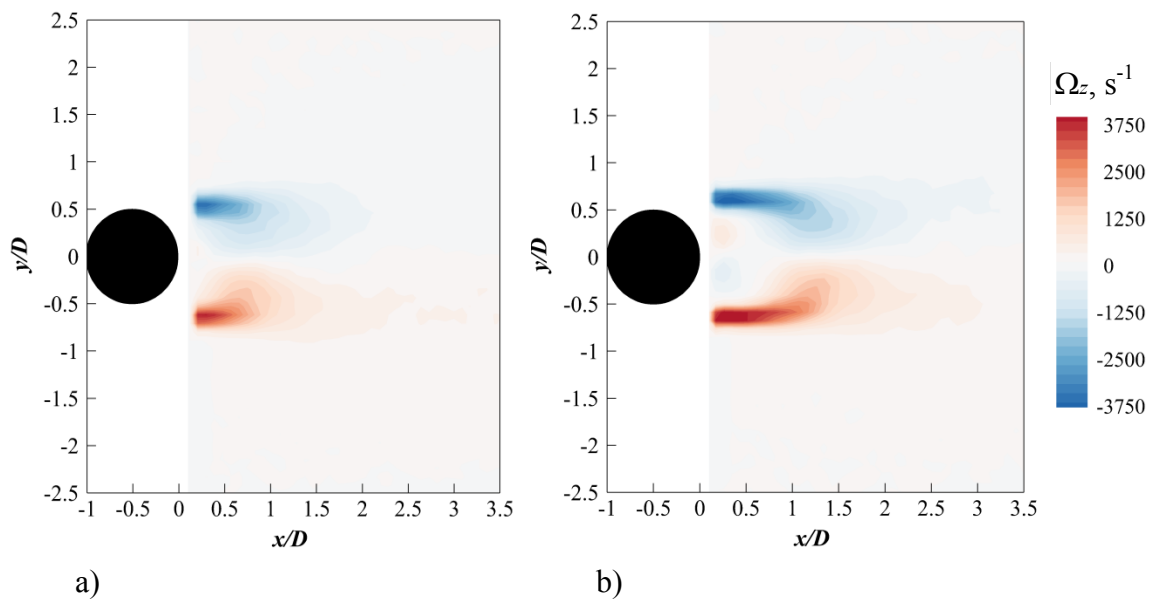

Figure 5.10 Time-averaged spanwise vorticity for single cylinder subjected to a) Plasma off and b) Plasma on case at free stream velocity U = 10 ms^{-1} at V$_{(input)}$ = 6 kV and f$_{(input)}$ = 8 kHz.

In order to prove the above interpretation, hot wire measurements were conducted to measure the unsteady velocity power spectral density for both the plasma off and plasma on cases in the wake region of the cylinder at six different streamwise locations x/D = 0.75, 1.125, 1.5, 1.875, 2.25, and 2.5 at free stream velocity U = 10 ms^{-1}. The nearest position for the hot wire probe at x/D = 0.75 which corresponds to 12 mm from the back of the cylinder, is still within the range of the spanwise vorticity of significance in the wake region produced by the cylinder. Figure 5.11 shows that for the plasma off case, a distinct peak can be seen in the unsteady velocity power spectral density at Strouhal number of fD/U = 0.188 which is very close to the narrowband tonal noise peak at fD/U = 0.185 as demonstrated in the in the acoustic spectra seen earlier in Fig. 5.2 and Fig. 5.3. This confirms that the narrowband tonal noise peak in the SPL spectra is generated as a result of the vortex shedding from the cylinder. When the plasma actuator is activated, at streamwise location close to the cylinder x/D = 0.75 (12 mm), a reduction of up to 15 dB in the narrowband peak of the unsteady velocity power spectral density can be observed. Further downstream, at x/D = 1.125 (x = 18 mm), the narrowband peak is reduced by at least 24.44 dB, while a reduction of 9.2 dB can be seen at the streamwise location x/D = 1.5 (x = 24 mm). One can also notice at x/D >1.5, three peaks which correspond to the second, third, and the forth harmonic of the dominant main tone occur in the PSD. It is also observed that, the harmonic of the main peak is almost suppressed at x/D = 1.125 and reduced at x/D = 1.5. Moreover, for the plasma on case, the broadband component of the fluctuating velocity power spectral density is consistently lower than the baseline "plasma off "case throughout the Strouhal number range. This implies that the turbulence level in the wake region of the cylinder has been reduced when the plasma actuator is turned on. At a further downstream locations, x/D = 1.875, 2.25, and 2.5, where vortex shedding will be present even for plasma on case, the narrowband peak in the power spectral density can still be reduced by about 4.6 dB, 4 dB, and 4.8 dB, respectively. Figure 5.12 presents the streamwise and vertical velocity fluctuations in the wake region of the cylinder. For the plasma off case, in Fig. 5.12a a pair of high streamwise velocity fluctuations can be observed up to x/D = 1. These correspond to the separated shear layer from the cylinder upper and lower sides. On the other hand, for the plasma on case in Fig.4.12b, a significant reduction in the streamwise velocity fluctuations in the near wake region can be seen. The vertical velocity fluctuations contours for the plasma off and plasma on cases are shown in Fig. 5.12c-d. The results show that a significant reduction in the vertical velocity fluctuations can

be seen in the center of the wake after the recirculation region, where the large scale coherent structures start to shed. These findings confirm the dramatic reduction in the narrowband peak in the fluctuating velocity power spectral density at x/D = 0.75 demonstrated earlier in Fig. 5.11. By comparing Fig. 5.12a and Fig. 5.12b, as well as Fig.5.12c and Fig. 5.12d, one can notice that the streamwise velocity fluctuation is better representative for the separating shear layer, while the vertical velocity fluctuation is more associated with the vortex shedding event. This reduction in the energy of the wake region that is associated with the activation of plasma actuator indicates that the plasma induced jet leads to flow reattachment and reduces the unsteadiness in the near wake region which results in noise reduction, Kozlov and Thomas (2009).
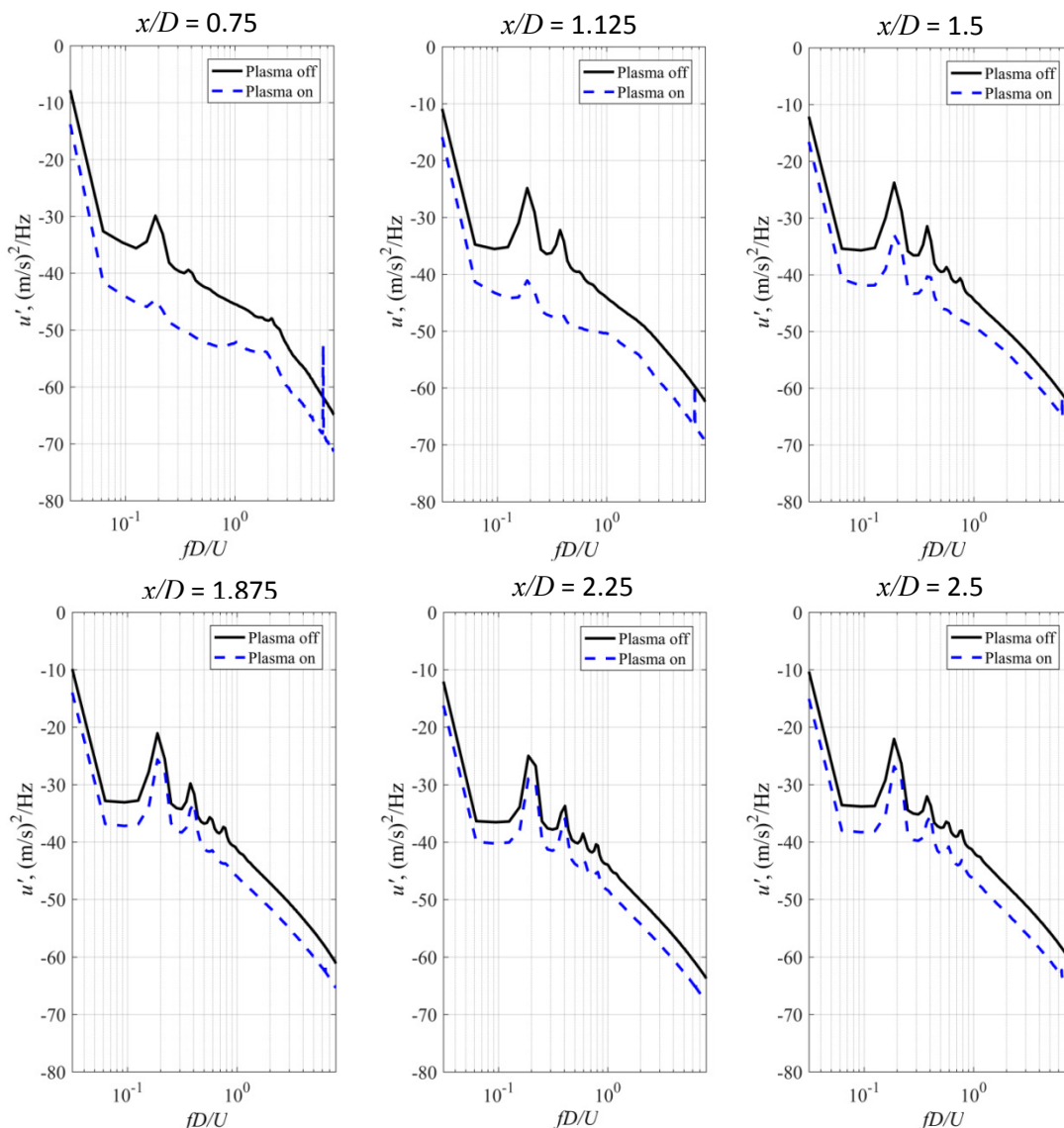
Figure 5.11 Unsteady velocity PSD for single cylinder subjected to Plasma off and Plasma on case at free stream velocity U = 10 ms^{-1} at V $_{(input)}$ = 6 kV and f$_{(input)}$ = 8 kHz.

a) plasma off   b) plasma on

c) plasma off   d) plasma on
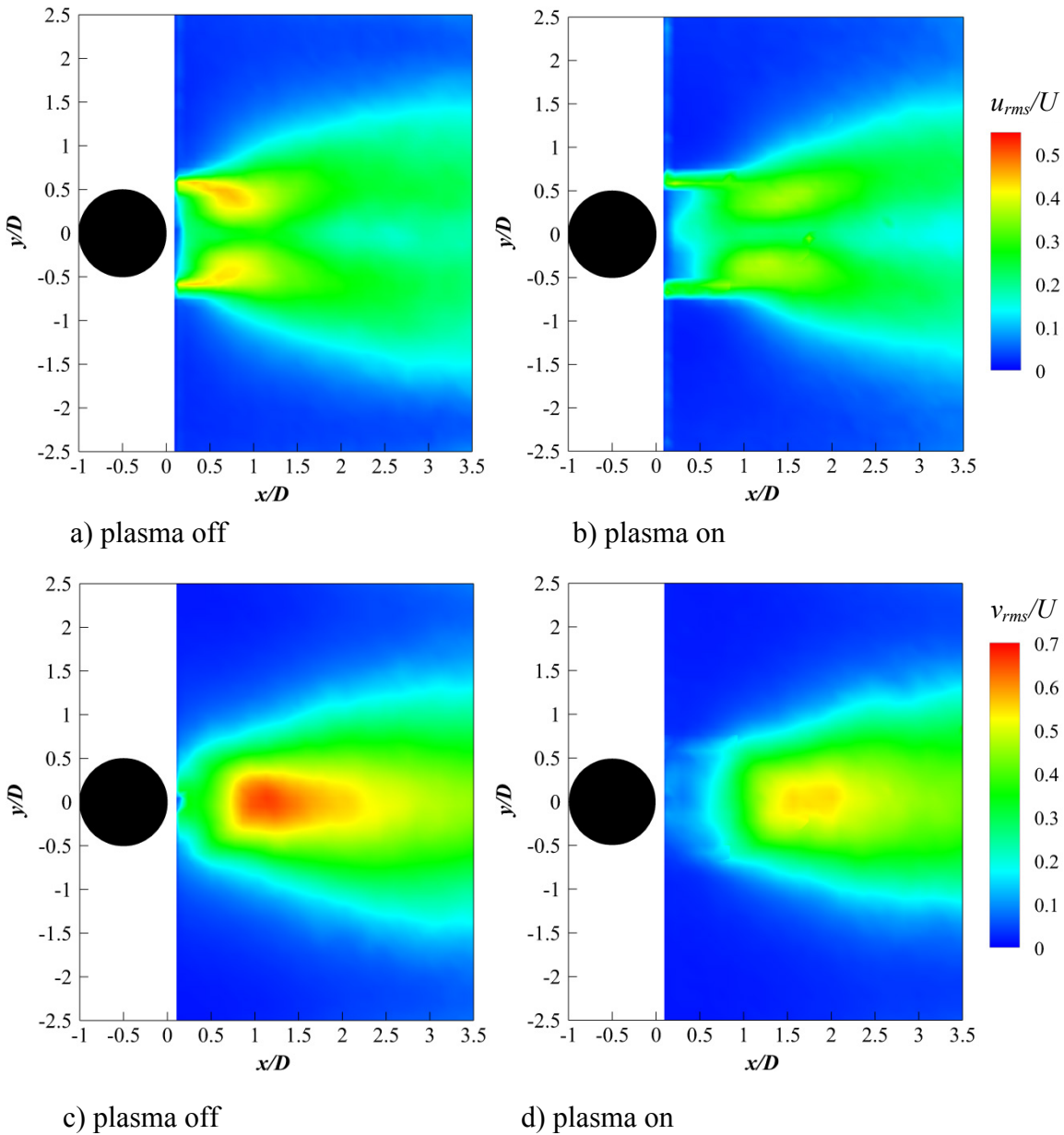
Figure 5.12 Time-averaged (a-b) streamwise velocity fluctuation, (c-d) vertical velocity fluctuations, for Single cylinder subjected to Plasma off and Plasma on case at free stream velocity $U = 10 \text{ ms}^{-1}$ at $V_{(input)} = 6 \text{ kV}$ and $f_{(input)} = 8 \text{ kHz}$.

Next, a comparison between the plasma off and plasma on cases for the streamwise and vertical velocity fluctuations at streamwise locations $x/l_f = 0.5$ is presented in Fig. 5.13. The streamwise location is non-dimensionalised by the vortex formation length l_f, which is the distance from the back of the cylinder to the position of maximum streamwise fluctuation in the center of the wake region. The results show that significant reduction in both the u_{rms}/U and v_{rms}/U fluctuating velocity components can be achieved, with the largest reduction occurs at vertical velocity

fluctuations. These results agree with the hot wire measurements, which showed a consistent reduction in the fluctuating velocity power spectral density, as demonstrated in Fig. 5.11.
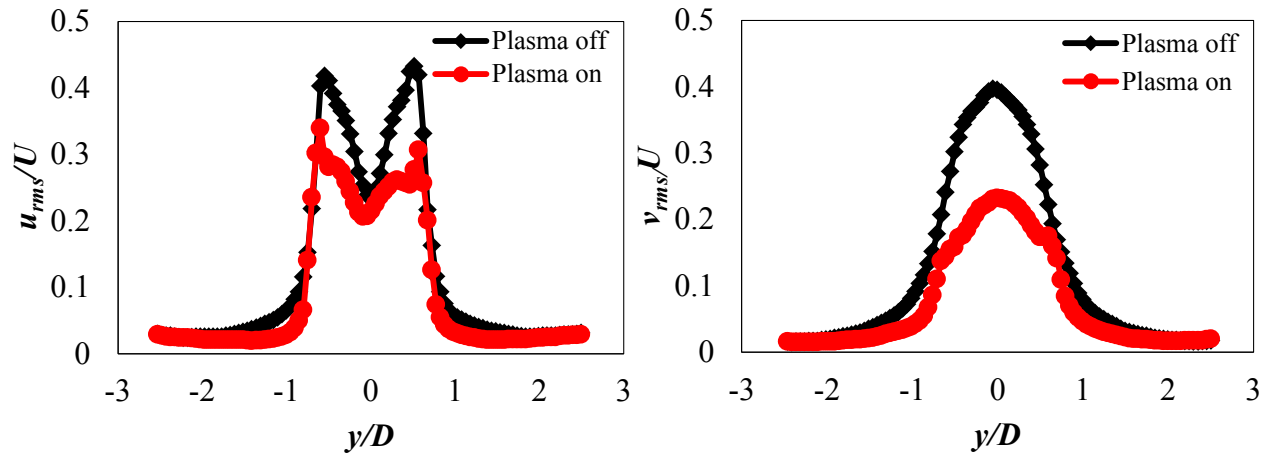
Figure 5.13 Time-averaged streamwise (left) and vertical (right) velocity fluctuations for Single cylinder subjected to a) Plasma off and b) Plasma on at x/l$_f$ = 0.5 at free stream velocity U = 10 ms^{-1}.

Finally, POD analysis has been made to capture the most energetic modes and the corresponding spatial distribution in the wake region of the cylinder. The spatial distribution of the first and second modes, the most energetic modes, in terms of the streamwise and vertical velocity components, *u* and *v,* respectively, for both the plasma off and plasma on cases are presented in Fig. 5.14 and 5.15, respectively.

For the plasma off case in Fig. 5.14a, it can be seen that the first and second most energetic modes manifest two rows of anti-symmetric patterns which alternately propagate in the downstream direction. In addition, the intensity of the mode dissipates as they propagate downstream. The location of the highest intensity mode is consistent with location of the maximum streamwise velocity fluctuations demonstrated earlier in Fig. 5.12a. For the plasma on case in Fig. 5.14b, the results show that the first pair of the modes slightly elongated compared with the plasma off case. This observation again agrees well with maximum streamwise velocity fluctuations demonstrated in Fig. 5.13b. Moreover, one can notice that the first and second modes of plasma on case exhibit a change in sign when compared with the plasma off case.
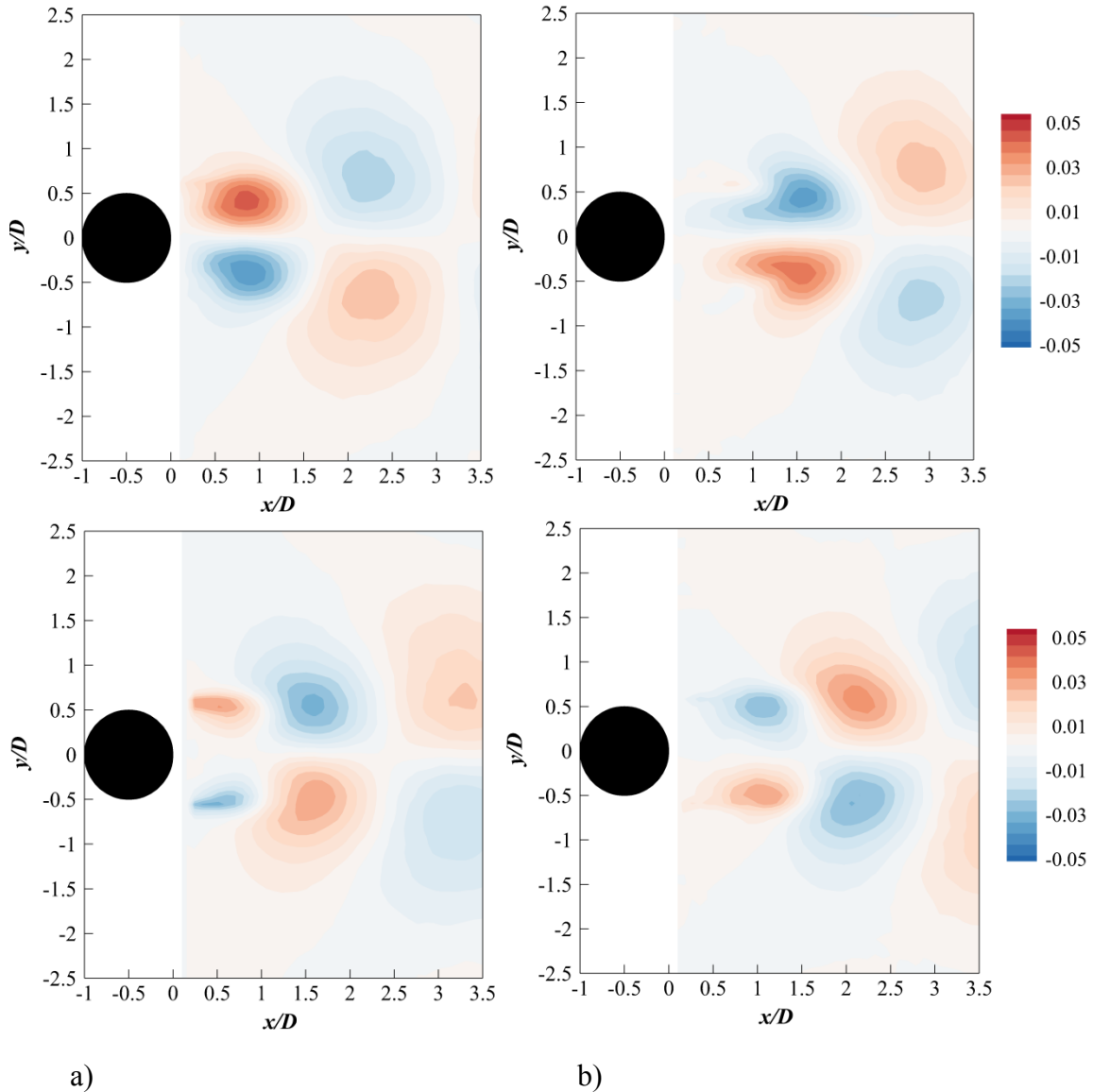
Figure 5.14 POD first (top) and second (bottom) modes in terms of the streamwise velocity for the cylinder subjected to a) plasma off and b) plasma on at free stream velocity U = 10 ms⁻¹ at V(input) = 6 kV and f(input) = 8 kHz.

The spatial distribution of the most energetic modes, the first and second mode, in terms of the vertical velocity component for the plasma off and plasma on cases are shown in Fig. 5.15a-b. The results show that a row of symmetrical patterns in the vertical direction can be observed for both plasma off and plasma on cases. These patterns alternately propagate in the downstream direction. It can be seen for the plasma off case, that the intensity of the first pattern in the first and second modes is reduced and its sign is changed.

In general, the analysis of the POD modes returns the same patterns as the time-averaged mean velocity, velocity fluctuation, and the spanwise vorticity for the streamwise and vertical velocity components, respectively. Using the plasma actuator does not seem to reduce the level of the POD mode, but it does alter the spatial distribution of the different modes and this indicates the change in the vortical structure in the wake range.

a)   b)
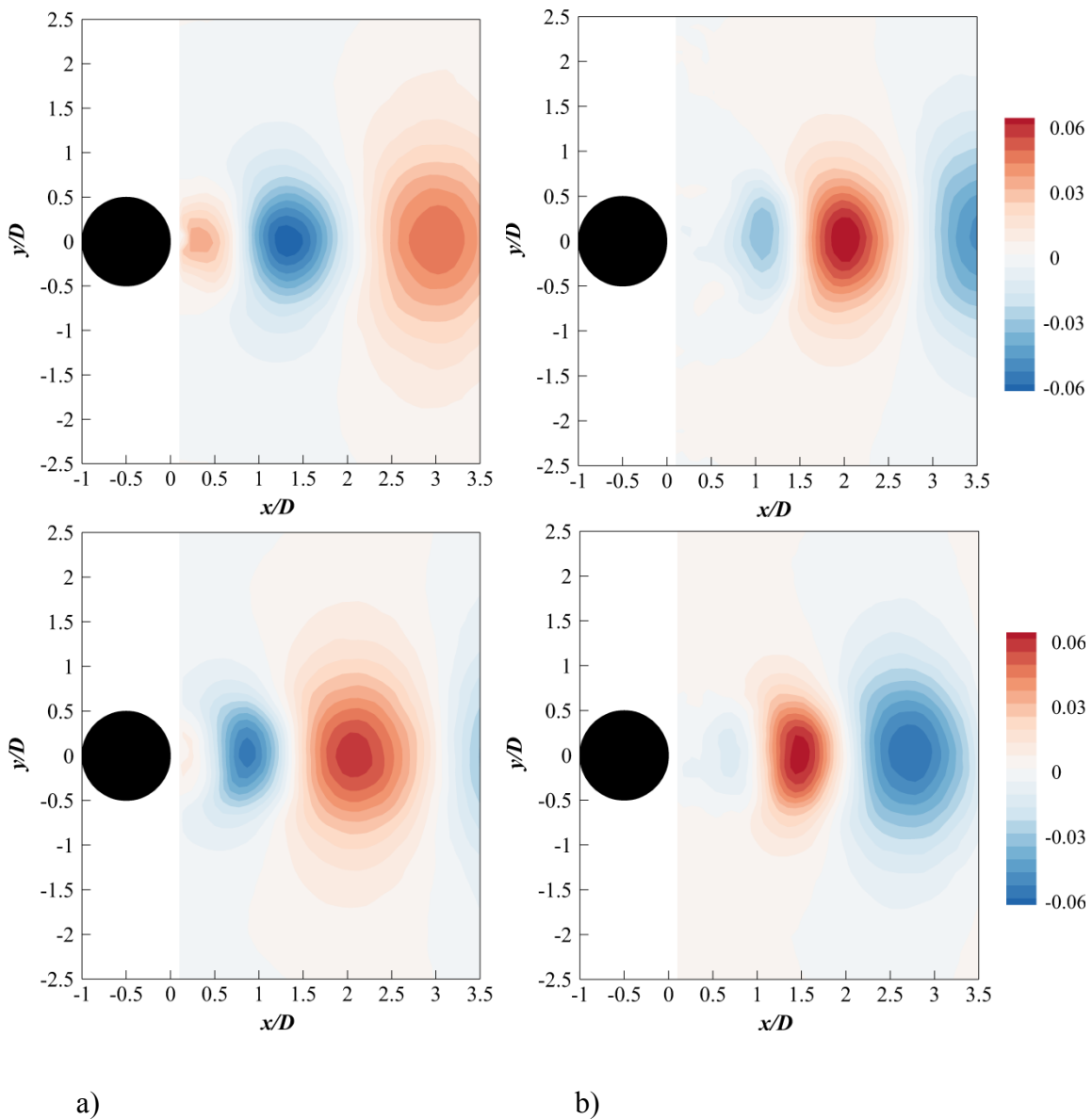
Figure 5.15 POD first (top) and second (bottom) modes in terms of the vertical velocity for the cylinder subjected to a) plasma off and b) plasma on at free stream velocity U = 10 ms⁻¹ at V₍input₎ = 6 kV and f₍input₎ = 8 kHz.

5.4 Tandem Cylinders

The acoustic and flow results for two cylinders in a tandem configuration will be presented in this section. The experiments were performed at free stream velocity $U = 10$ ms^{-1}, corresponding to a Reynolds number based on the cylinder diameter D and the free stream velocity, $Re_D = 1.1$ x 10^4. The input voltage and frequency for the plasma actuators on both upstream and downstream cylinders remains the same $V_{(input)} = 6$ kV and $f_{(input)} = 8$ kHz, respectively.

5.4.1 Acoustic Results for the Plasma off Case

The acoustic results of the tandem are presented in this section. Three cases, namely the actuation of the upstream cylinder only, the actuation of the downstream cylinder only and actuation of both downstream and upstream cylinders, were investigated. In addition, for each case, the effect of the plasma induced jet azimuthal angle (measured from the front stagnation point), θ_j was investigated as well. For the acoustic tests, the azimuthal angles are $\pm 27^o \le \theta_j \le \pm 153^o$.

Before discussing the acoustic results of the two cylinders in tandem configuration case with the upstream cylinder actuated only, the Sound Pressure Level SPL for tandem cylinder for plasma off case will be examined first. Figure 5.16 presents the SPL spectra for tandem cylinders, upstream cylinder only, downstream cylinder only and free stream jet noise (without cylinder) with the side plates attached to the nozzle. The result shows that the SPL spectra when the upstream cylinder only is placed in the cross flow has a distinct narrowband peak and its harmonic at Strouhal number of $fD/U = 0.185$ and 0.545, respectively. This observation agrees with the acoustic results for a single cylinder in cross flow demonstrated earlier in Fig. 5.2 and 5.3. When the downstream cylinder only is placed in the cross flow, the results show that the SPL spectra has the same main narrowband peak and its harmonic as the case where only the upstream cylinder is in the cross flow. On the other hand, the SPL spectrum for the tandem cylinders can be divided into two regions. The first one occurs at $fD/U = 0.155$, where a significant narrowband tonal peak can be observed, which has an amplitude higher than that of the single cylinder. The second region is represented by a broadband noise at Strouhal number $0.28 \le fD/U \le 1.6$. This broadband noise region is believed to be generated by the interaction of the turbulent wake originated from the upstream cylinder with the front face of the downstream

cylinder. The broadband interaction noise and the narrowband tonal noise are the focus of the current study.
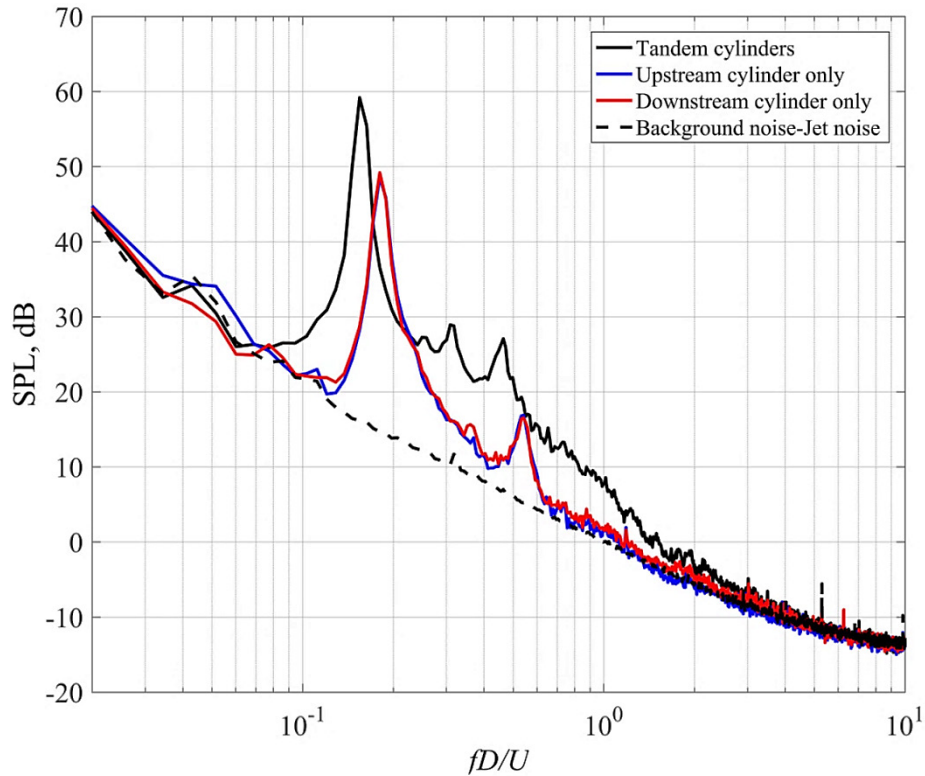
Figure 5.16 SPL spectra for single upstream cylinder, single downstream cylinder, tandem cylinders and free jet noise without plasma actuation at free stream velocity U = 10 ms⁻¹.

5.4.1.1 Upstream Cylinder-Downstream Actuation

The results of the effect of the plasma induced jet on the tonal and broadband noise of two cylinders in tandem configuration will be investigated. Figure 5.17 presents the SPL spectra for tandem cylinders with only the upstream cylinder is subjected to the actuation of the plasma actuator with a plasma jet in the downstream direction. The results show that for angles less than 70°, a moderate reduction in the aerodynamic noise up to 4 ±0.5dB can be achieved. One can also notice that the main narrowband noise peak is shifted towards a slightly higher frequency $fD/U = 0.172$, when the plasma induced jet is at azimuthal angle, $\theta_j = \pm27^o$, $\pm47^o$, and $\pm55^o$. When the plasma actuator is placed at $\theta_j = \pm70^o$, the main narrowband tonal noise peak is reduced by about 9 dB and shifted to an even higher frequency $fD/U = 0.189$. The level of the interaction broadband noise $(0.28 \leq fD/U \leq 1.6)$ remains the same. For Strouhal number

fD/U ≥ 1.4, the actuator self-noise, which is a non-aerodynamic actuator self-noise can be observed.
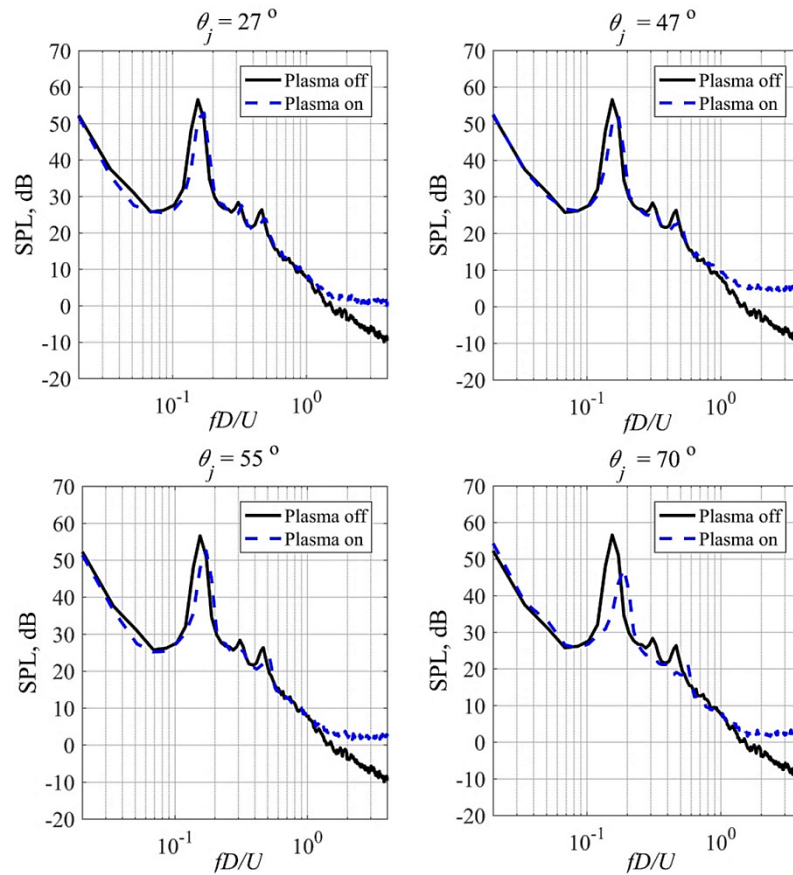
Figure 5.17 SPL spectra for tandem cylinders with the upstream cylinder only subjected to plasma off and plasma on cases at azimuthal angles ($\pm27^o \le \theta_j \le \pm70^o$) at free stream velocity $U = 10$ ms^{-1} and at $V_{(input)} = 6$ kV and $f_{(input)} = 8$ kHz.

When the plasma actuator is placed at $\theta_j = \pm90^o$, the main narrowband tonal peak is reduced by about 7.8 ±0.5dB and shifted towards a higher frequency *fD/U* = 0.189. In addition, it can be seen that the second and third harmonic of the main peak are reduced as well. However, when the plasma actuator is placed at a higher azimuthal angle $\theta_j = \pm110^o$, the narrowband tonal noise peak is reduced by only 4 ±0.5dB compared to 7.8 ±0.5dB when the actuator is placed at $\theta_j = \pm90^o$. In addition, vortex shedding frequency becomes similar to the shedding frequency of the baseline "plasma off" case. Further increasing the azimuthal angle of the plasma actuator to $\theta_j = \pm125^o$ results in a significant reduction in the narrowband tonal noise by up to 15 ±0.5dB and a shift towards a lower frequency *fD/U* = 0.1375 In addition, a good reduction in the interaction broadband noise of about 4 ±0.5dB at $0.22 \le fD/U \le 1.1$ can also be observed. This reduction in the narrowband and the broadband noise level is very close to the reduction that is

reported by Eltaweel et al. (2014). They reported that the vortex shedding noise can be reduced by 16 dB when the plasma actuator on the upstream cylinder is activated. At azimuthal angles $\theta_j = \pm133^o$, the plasma induced jet results in a slightly less reduction in both the levels of the narrowband tonal noise as well as the interaction broadband noise than that at $\theta_j = \pm125^o$. In addition, the second and third harmonics are slightly reduced. When the plasma actuator is placed at $\theta_j = \pm153^o$, there is hardly any reduction of the narrowband tonal noise and the interaction noise. It seems that the most optimized location to place the plasma actuator is at $\pm125^o \leq \theta_j \leq \pm133^o$, the range over which is relatively similar to the single cylinder case discussed in Section 5.3.1. The interesting thang that one can notice in the acoustic spectra is that the plasma actuator angle $\theta_j = \pm110^o$ can be considered as a critical which divide the variation of Strouhal number into two regions. The first one is the region where the plasma actuator induced jet is at $\theta_j < \pm110^o$ has higher shedding frequency than the plasma off case. The second one is the region that has lower shedding frequency than the baseline case when the plasma induced jet is at $\theta_j > \pm110^o$.
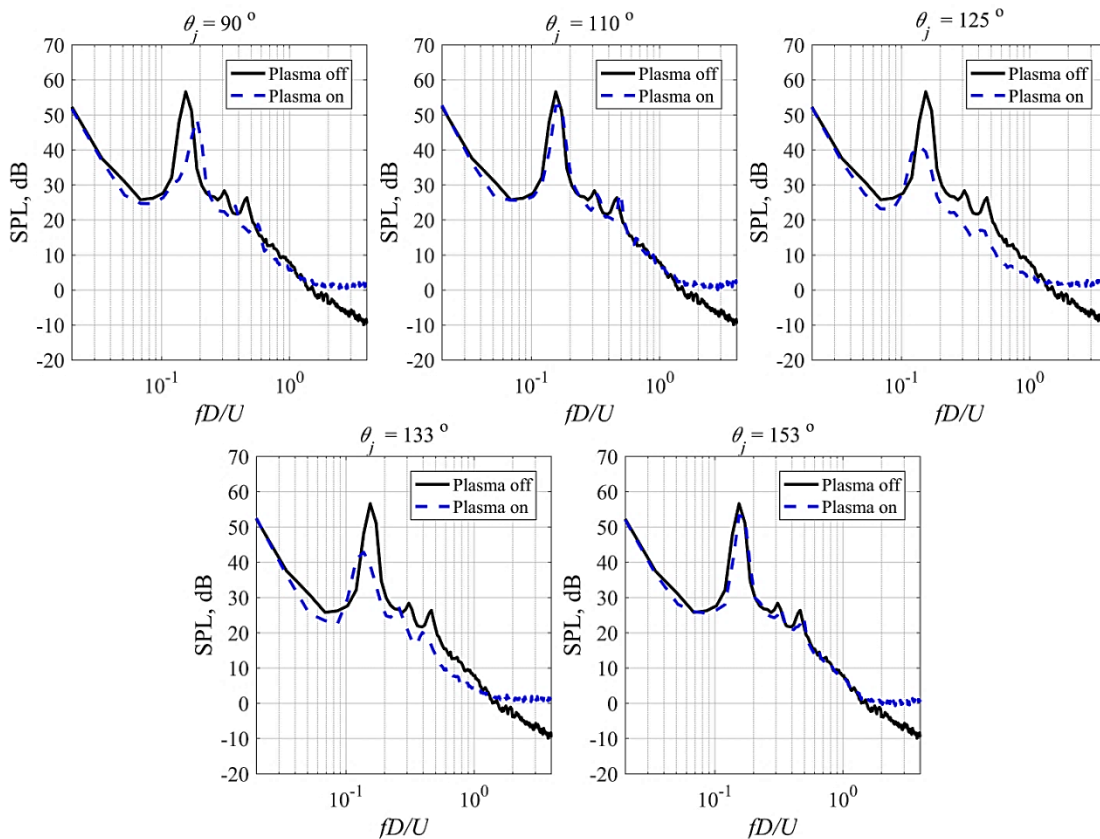
Figure 5.18 SPL spectra for tandem cylinders with the upstream cylinder only subjected to plasma off and plasma on cases at azimuthal angles ($\pm90^o \leq \theta_j \leq \pm153^o$) at free stream velocity $U = 10\ ms^{-1}$ and at $V_{(input)} = 6\ kV$ and $f_{(input)} = 8\ kHz$.

This interesting phenomenon was also seen when a single cylinder is placed in a cross flow demonstrated earlier in Fig. 5.3. One of the most successful passive vortex shedding control techniques that has received a lot of attention is the splitter plate. This plate can be attached to the base of the bluff body or detached with a gap between the plate leading edge and the base of the bluff body. The objective of using the splitter plate is the stabilize separation point and inhibit the interaction between the separated shear layers. The variation of plate length at a certain flow Reynolds number has shown an interesting phenomenon similar to the effect of plasma actuator on the wake region of the circular cylinder (single and Tandem configuration). It has been reported by [Roshko (1955), Apelt et al. (1973), Apelt and West (1975)] that changing the length of the plate leads to an appreciated Strouhal number variation. The effect of the plasma actuator on the flow will be discussed later in this chapter.

Figure 5.19 SPL spectra for tandem cylinders with only the downstream cylinder is subjected to plasma actuator placed at azimuthal angles ($\pm 27^o \leq \theta_j \leq \pm 70^o$) at free stream velocity $U = 10\ ms^{-1}$ and at $V_{(input)} = 6\ kV$ and $f_{(input)} = 8\ kHz$.

5.4.1.2 Downstream Cylinder- Upstream Directed Actuation

Figures 5.19 and 5.20 show the acoustic spectra for the tandem cylinders measured at $U = 10$ ms^{-1} with plasma induced jet is directed against the incoming flow at different azimuthal angles $\pm 27^o \leq \theta_j \leq \pm 153^o$ on the upper and lower sides of the downstream cylinder. From Fig. 5.19, it can be seen that when the plasma actuator is placed on the downstream cylinder with the plasma induced jet directed in the upstream direction at azimuthal angles $\pm 27^o \leq \theta_j \leq \pm 70^o$, the effectiveness of the plasma actuator is less compared with the case where the actuator is placed on the upstream cylinder, as demonstrated in Section 5.4.1.1. The most important take out from Fig. 5.19 is that an injection of the plasma set in an opposing direction has little effect on the incoming shedding flow (i.e. the wake flow from the upstream cylinder). Moreover, the plasma jet also fails to achieve any beneficial effect on the interaction broadband noise. Figure 5.20 shows the SPL spectra for the cases where the actuator is placed at azimuthal angles $\pm 90^o \leq \theta_j \leq \pm 153^o$. The results show that when the plasma actuator is placed at $\theta_j = \pm 90^o$, a moderate reduction in the narrowband tonal noise peak of up to 2 ± 0.8dB can be achieved. However, no significant reduction in the interaction broadband noise can be observed at this angle. Further increase in the actuator azimuthal angle can affect neither the narrowband tone noise, nor the interaction noise. The lack of effect on the acoustic spectra when the plasma actuator is placed at $\pm 90^o \leq \theta_j \leq \pm 153^o$ suggests that the wake flow produced by the downstream cylinder has been modulated by the wake flow from the upstream cylinder. For the PIV tests, the azimuthal angle $\theta_j = \pm 55^o$ is chosen as it provides slightly better effect than the other tested angles. It is likely that the wake flow pertaining to the downstream cylinder no longer in the vortex shedding mode, hence the plasma actuator at $\pm 90^o \leq \theta_j \leq \pm 153^o$ would have no significant effect on the aerodynamic noise under the current actuator configuration, this will be shown later in the POD analysis where a clear change in the sign of the high energy structures can be seen. The conclusion that can be drawn from the acoustic results is that the activation of the upstream cylinder is more effective than the activation of the downstream one in terms of noise reduction. This agrees with the results from the numerical study conducted by Eltaweel et al. (2014). They found that for the baseline "plasma off "case both the flow and acoustic fields are dominated by the vortex shedding from the upstream cylinder and the impingement of the wake on the downstream cylinder. They also reported that the activation of the upstream cylinder can

effectively suppress vortex shedding noise by delaying separation which results in a more stable wake. In addition, they suggested that further noise reduction can be achieved by applying plasma actuator on both cylinders. Therefore, the simultaneous actuation of both upstream and downstream cylinders was conducted (to be discussed in next section).
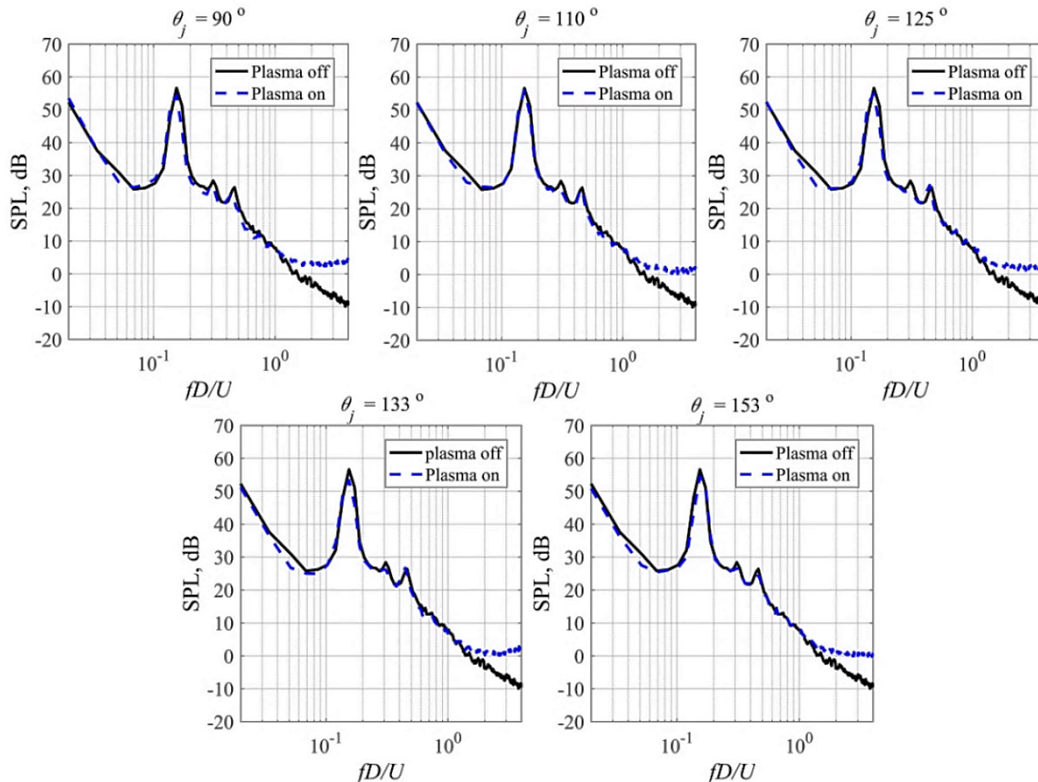
Figure 5.20 SPL spectra for tandem cylinders with only the downstream cylinder is subjected to plasma actuator placed at azimuthal angles ($\pm90^o \leq \theta_j \leq \pm153^o$) at free stream velocity U = 10 ms^{-1} and at V$_{(input)}$ = 6 kV and f$_{(input)}$ = 8 kHz.

5.4.1.3 Upstream and Downstream Cylinders Simultaneous Actuation

In the previous sections, the effect of plasma actuator placed only on the upstream and on the downstream cylinder was investigated separately for the radiated noise. In this section, the effect of the simultaneous actuation of both the upstream and the downstream cylinders will be investigated. The actuator on the upstream cylinder induces plasma jet in the downstream direction at an azimuthal angle now denoted by θ_{UCj}. While the actuator on the downstream cylinder is configured in a way that the plasma induced jet is in the upstream direction against

the main flow. The corresponding azimuthal angle for the plasma actuator is now denoted as θ_{DCj}. The results of the sound pressure level are presented in Fig. 5.21 and 5.22
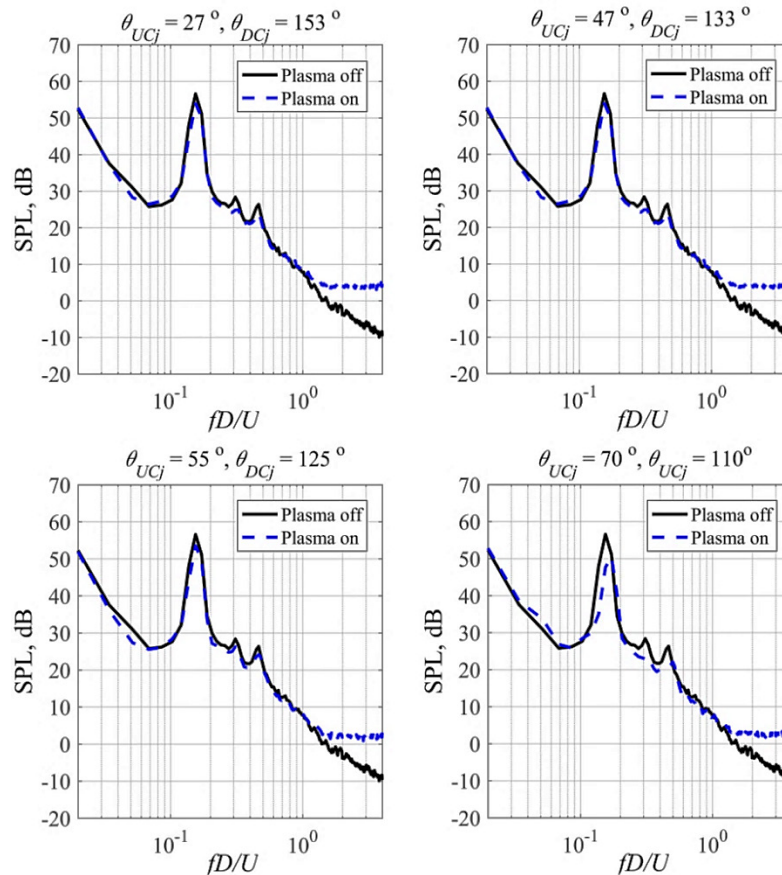
Figure 5.21 SPL spectra for tandem cylinders with the upstream and downstream cylinders are subjected to plasma actuator placed at azimuthal angles ($\pm 27^o \leq \theta_{UCj} \leq \pm 70^o$) and ($\pm 153^o \leq \theta_{DCj} \leq \pm 110^o$), respectively at free stream velocity $U = 10$ ms^{-1} and at $V_{(input)} = 6$ kV and $f_{(input)} = 8$ kHz.

It can be seen that when the plasma actuator is placed at ($\theta_{UCj} = \pm 27^o$, $\pm 47^o$, and $\pm 55^o$) and at ($\theta_{DCj} = \pm 153^o$, $\pm 133^o$, and $\pm 125^o$) on the upstream and downstream cylinders, respectively, no significant reduction in the narrowband tonal noise or the interaction broadband noise can be observed. When the plasma actuator angle is increased to $\theta_{UCj} = \pm 70^o$ for the upstream cylinder and to $\theta_{DCj} = \pm 110^o$ for the downstream cylinder, the SPL spectrum shows that a reduction of up to 6 ± 0.5dB in the narrowband tonal noise can be achieved. In addition, it can be seen that both the second and the third harmonic are reduced by up to 5 ± 0.5dB. However, no significant reduction of the interaction noise can be observed. In addition, as the plasma actuator angle increases, the frequency of the primary peak increases. This can clearly be seen when the plasma

actuator is placed at $\theta_{UCj} = \pm70^o$ and $\theta_{DCj} = \pm110^o$ up to the azimuthal angle $\theta_{UCj} = \pm110^o$ and $\theta_{DCj} = \pm70^o$. Then the frequency reduces when the actuator is placed at $\theta_{UCj} = \pm125^o$ and $\theta_{DCj} = \pm55^o$. Roshko (1955), Apelt et al. (1973), Apelt and West (1975) reported that when a splitter plate is attached to the base of a cylinder the shedding frequency varies with the length of the plate. When the azimuthal angle of the plasma actuator on the upstream and downstream cylinders is changed to $\pm90^o$, a reduction of 6 ±0.5dB and a shift towards high frequency region in the narrowband tonal noise can be observed, as illustrated in Fig. 5.22. Similarly, there is no reduction in the broadband component for this configuration. For the upstream and downstream cylinders with plasma actuator placed at $\theta_{UCj} = \pm110^o$ and $\theta_{DCj} = \pm70^o$, respectively, both the narrowband tonal noise and the broadband noise are not affected by the plasma actuation. However, when the actuator is placed at $\theta_{UCj} = \pm125^o$ on the upstream cylinder and at $\theta_{DCj} = \pm55^o$ on the downstream cylinder, the tonal noise peak can be reduced by 16 ±0.5dB and an average reduction of up to 6 ±0.5dB in the broadband noise can be seen over the frequency range of $0.22 \leq fD/U \leq 1.1$. Most importantly, having both cylinders subjected to the plasma actuation simultaneously higher broadband noise reduction can be achieved compared with the case when the plasma actuator is placed at $\theta_j = \pm125^o$ on the upstream cylinder only. This improved performance could be because the plasma jet induced at $\theta_{DCj} = \pm55^o$ successfully acts as a virtual fluidic shield in front of the downstream cylinder. Thus, the wake generated by the upstream cylinder, after being displaced by the plasma jet at $\theta_{UCj} = \pm125^o$, would again be further displaced by the upstream jet at $\theta_{DCj} = \pm55^o$. This behavior will be further investigated in the next section. For plasma actuator placed at larger azimuthal angle, $\theta_{UCj} = \pm133^o$ and $\theta_{DCj} = \pm47^o$ on the upstream and downstream cylinders, respectively, the tonal and broadband noise reduction level is same as the case when the upstream cylinder is only actuated at $\theta_j = \pm133^o$. Further increase in the plasma actuator angle to $\theta_{UCj} = \pm153^o$ and $\theta_{DCj} = \pm27^o$, would result in no significant reduction in the tonal and broadband noise, as shown in Fig. 5.22. Moreover, the case when the plasma actuator is placed at $\theta_{UCj} = \pm110^o$ and $\theta_{DCj} = \pm70^o$ can be considered as the critical angle in the tandem cylinder case. For the case of simultaneous actuation of the plasma actuators for the upstream and downstream cylinders, the combined configuration of $\theta_{UCj} = \pm125^o$ and $\theta_{DCj} = \pm55^o$ represents the most optimized and this will be further investigated for the corresponding flow behaviors in Section 5.4.2.4.
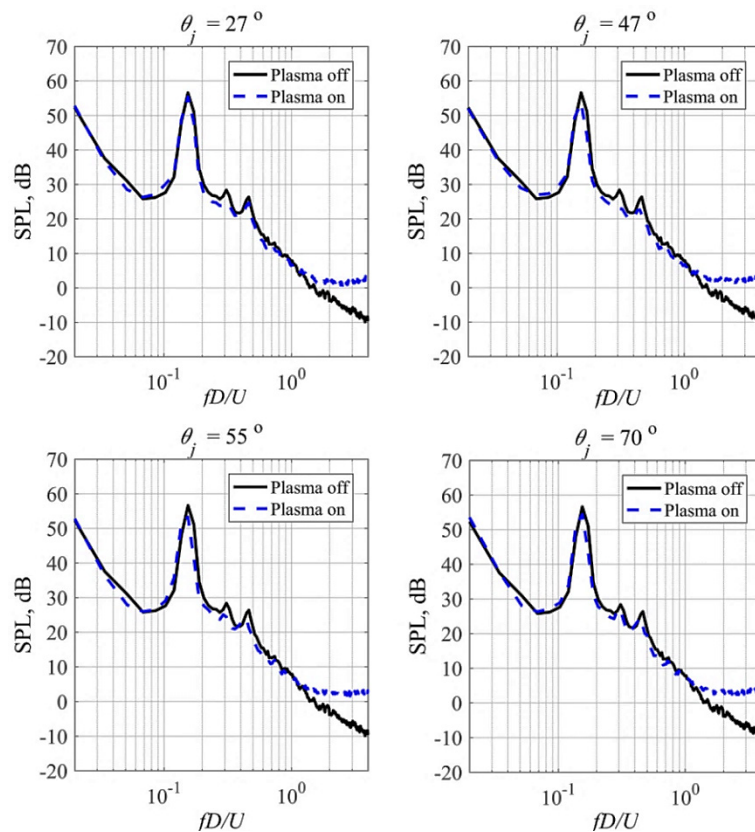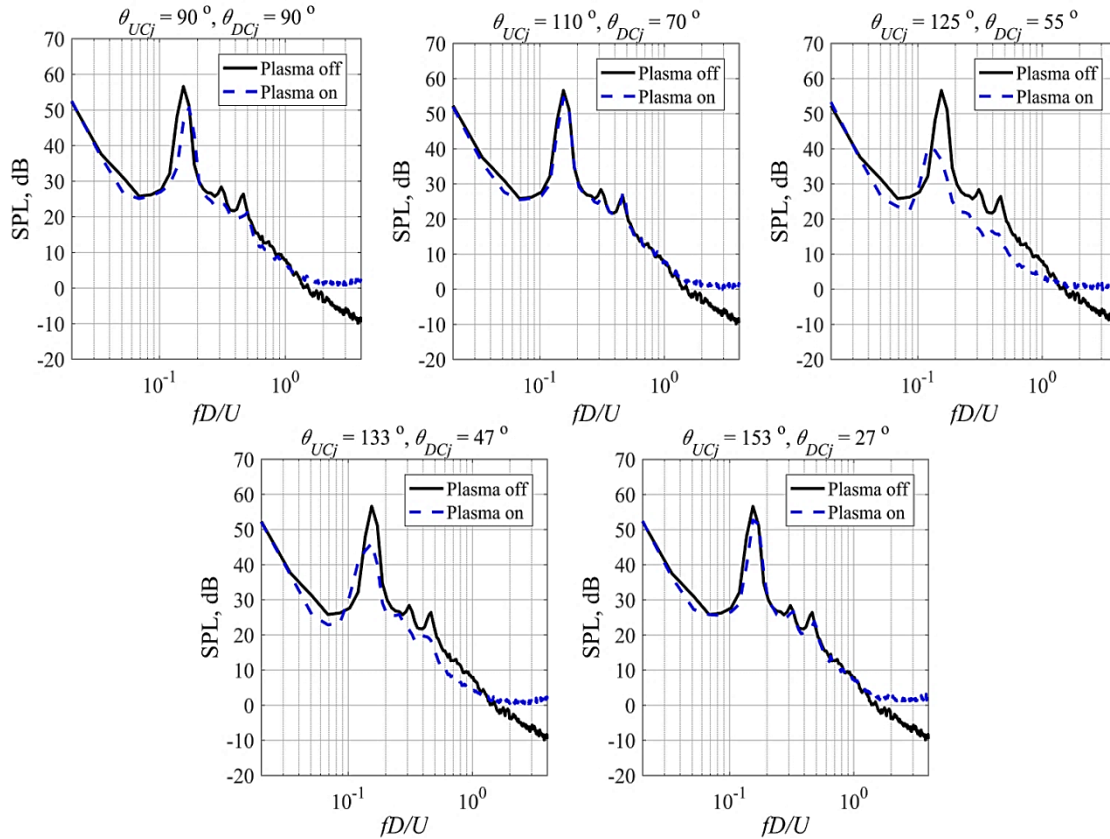
Figure 5.22 SPL spectra for tandem cylinders with the upstream and downstream cylinders are subjected to plasma actuator placed at azimuthal angles ($\pm90 \leq \theta_{UCj} \leq \pm153^{o}$) and ($\pm90^{o} \leq \theta_{DCj} \leq \pm27^{o}$), respectively at free stream velocity $U = 10~ms^{-1}$ and at $V_{(input)} = 6~kV$ and $f_{(input)} = 8~kHz$.

5.4.2 Flow Results

In this section, the instantaneous and the time-averaged flow results obtained from the PIV measurements for the tandem cylinders subjected to the plasma actuation will be presented. The test cases were chosen according to the acoustic performance presented earlier in Section 5.4.1. The first case is where only the upstream cylinder is subjected to the plasma actuation at $\theta_{UCj} = \pm125^{o}$, while the second case is the actuation of the downstream cylinder at $\theta_{DCj} = \pm55^{o}$. The last case is where both the upstream and downstream cylinders are actuated at $\theta_{UCj} = \pm125^{o}$, and $\theta_{DCj} = \pm55^{o}$, respectively.

5.4.2.1 Instantaneous Flow Measurement

The instantaneous flow field for the two cylinders in the tandem configuration subjected to various configurations of plasma actuator at free stream velocity $U = 10$ ms^{-1} will be presented here. Figure 5.23 shows the instantaneous streamwise velocity and spanwise vorticity fields for the plasma off case, upstream cylinder (uc) subjected to plasma actuator placed at $\theta_{UCj} = \pm125^{o}$, downstream cylinder (dc) with plasma actuator placed at $\theta_{DCj} = \pm55^{o}$ and both cylinders subjected to plasma actuation at $\theta_{UCj} = \pm125^{o}$, and $\theta_{DCj} = \pm55^{o}$.

From Fig. 5.23, it can be seen that a recirculation zone occurs in the wake region of the upstream cylinder and the wake width increases as the flow advances in the downstream direction. This observation is confirmed in the time-averaged streamwise velocity Fig. 5.24a, where the deficit region occurs just behind cylinder base for the plasma off case. When the upstream cylinder is subjected to the plasma actuation the recirculation region between the cylinders extends and two anti-symmetric vortices move closer towards the downstream cylinder, this is also seen in the Fig. 5.24b, where the deficit region is extended in the downstream direction near to the front face of the downstream cylinder. When the downstream cylinder, is subjected to the plasma actuation, the wake topography between the cylinders is quite similar with the baseline case. In addition, there is an increase in the wake width which is also seen in Fig. 5.33 and 5.34 when compared with plasma off case.

The last actuation case is the simultaneous actuation of both the upstream and downstream cylinders. From Fig. 5.23, it can be seen that when the plasma actuators are turned on the recirculation region extends even further in the downstream direction and an increase in the wake width can also be seen in the near wake region compared with both plasma off case and the case when only the upstream cylinder is subjected to the plasma actuator. This is also seen in the time-averaged streamwise velocity contours in Fig. 5.43b where the wake extends in the downstream direction and the wake width increases near the back of the upstream cylinder and decreases near the front face of the downstream cylinder, as shown in Fig. 5.44.

The instantaneous spanwise vorticity for the plasma off and plasma on cases are also shown in Fig. 5.23. It can be seen that for the plasma off case, two regions of shear layer with the negative and positive spanwise vorticity are formed from the upper and lower sides of the upstream

cylinder, respectively, and they start to roll up just after the cylinder base. The flow trend for this case is similar to the time-averaged spanwise vorticity contours that are seen in Fig. 5.26a, where the roll up process of shear layers starts just near the base of the upstream cylinder. On the other hand, when the upstream cylinder is subjected to plasma actuation, both the separated shear layers extend in the downstream direction and the roll up starts away from the cylinder base. This is also demonstrated in the time-averaged spanwise vorticity contours for the upstream cylinder activation case where the activation of the upstream cylinder leads to the elongation of the two separated shear layers in away similar to what is seen in the instantaneous spanwise vorticity in Fig. 5.23. The role of this increase in the vortex formation length will be investigated in details in the time-averaged spanwise vorticity for plasma on case in the next section.

The actuation of the downstream cylinder with the plasma induced jet directed in the upstream direction leads to a slight change in the separated shear layers compared with the plasma off case. This observation is also seen in the time average spanwise vorticity shown in Fig. 5.36, where the two separated shear layers shows a slight change in the length of the separated shear layers compared with plasma off case.

The simultaneous actuation of both upstream and downstream cylinders results in an elongation the separated shear layers in the downstream direction away from the upstream cylinder base. This elongation of the separated shear layers is clearly seen in time averaged spanwise vorticity shown in Fig. 5.46.

5.4.2.2 Time-Averaged Flow Field-Upstream Cylinder Actuation

In this section, the time-averaged flow results such as, the streamwise and vertical velocity, spanwise vorticity, velocity fluctuations, and POD modes, will be demonstrated. Figure 5.24 shows the streamwise velocity contours for both the plasma off and plasma on cases where the upstream cylinder only is subjected to the actuation. The results show that when the plasma actuator is off, a region of non-convective velocity ($u/U \leq 0$) occurs in the wake of the upstream cylinder with the saddle point occurs at $x/D \approx 1$, after this location the separated shear layers start to interact with each other. The result is very similar to the single cylinder case in Fig. 5.7a.
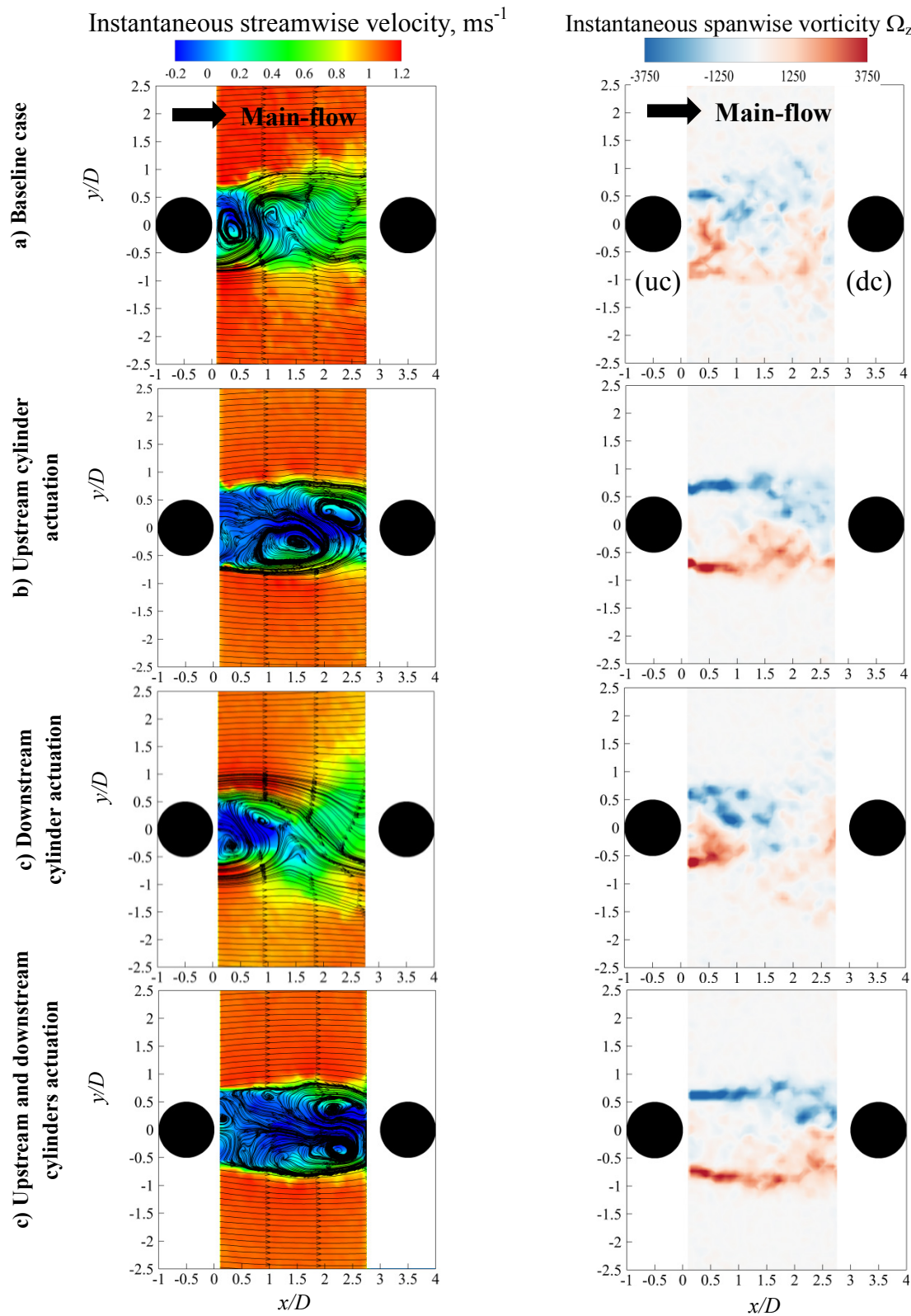
Figure 5.23 Instantaneous streamwise velocity and spanwise vorticity for tandem cylinder subjected to plasma actuator at U = 10 ms^{-1} and at V$_{(input)}$ = 6 kV and f$_{(input)}$ = 8 kHz.

This suggests that the downstream cylinder in the tandem case has little effect on the vortex formation in the wake region pertaining to the upstream cylinder. However, when the plasma actuator is on, the recirculating zone extends significantly in the downstream direction and two large symmetrical vortices almost cover the whole gap between the two cylinders. In addition, the focal point occurs further downstream compared with the baseline "plasma off" case. Moreover, two saddle points can be identified. The first one is near the base of the upstream cylinder while the other one is near the front of the downstream cylinder. This elongation of the recirculation region has been previously reported by many researchers who used a splitter plate to control vortex shedding from bluff bodies [Apelt et al. 1973 and Apelt and West (1975)]. They reported that this elongation is a clear evidence of separation delay and drag reduction [Milano et al. (2000)].

Next, the vertical velocity contours are shown in Fig. 5.25. It can be seen that for the plasma off case, large vertical velocity values occur beyond the separation region towards the center of the wake. The "converged" flow between the top and bottom sides of the cylinder is reflected to the rolling up of the separating shear layers the recirculating pockets. Unlike the single cylinder case, the presence of the downstream cylinder leads to occurrence of a noticeable level of vertical velocity near the front face of the downstream cylinder. When the plasma actuator is turned on, the wake flow near the upstream cylinder exhibits a weak "diverged" pattern, i.e positive vertical velocity at the top side of the cylinder, and negative velocity at the bottom side. A much weaker "diverged" flow pattern only appears at a more downstream location $x/D = 2$. This indicates the delay in the roll up of the shear layer when the plasma actuator is on. It is worth noting that there is a change in the sign of the vertical velocity near the front face of the downstream cylinder. This suggests that the plasma actuator can affect the vortex shedding mode.

Figure 5.24 Time-averaged streamwise velocity contours for tandem cylinders with upstream cylinder is only actuated subjected to a) Plasma off and b) Plasma on case at free stream velocity U = 10 ms^{-1} at V$_{(input)}$ = 6 kV and f$_{(input)}$ = 8 kHz.

Figure 5.25 Time-averaged vertical velocity contours for tandem cylinders with upstream cylinder is only actuated subjected to a) Plasma off and b) Plasma on case at free stream velocity U = 10 ms^{-1} at V$_{(input)}$ = 6 kV and f$_{(input)}$ = 8 kHz.

Now, the time-averaged spanwise vorticity component of the flow field is plotted in Fig. 5.26, for both the plasma off and plasma on cases. For the plasma off case, it can be seen that two regions of negative and positive spanwise vorticity are generated as a result of the separation of

the shear layers from the upper and lower sides of the upstream cylinder, respectively. The separated shear layers start to roll up streamwise location $x/D \approx 1$. One can notice that the vorticity strength for the tandem cylinder case is less than that for the single cylinder demonstrated earlier in Fig. 5.10a. This could be due to the presence of the downstream cylinder, which could affect the vortex shedding from the upstream cylinder. When the plasma actuator is turned on, the strong vorticity region extends further in the downstream direction up to $x/D \approx 1.5$. As the Karman vortex shedding starts after the roll up of the separated shear layer, it can be seen that for the plasma off case, vortex formation starts at a relatively short distance from the back of the cylinder, while the vortex formation is triggered at a much further downstream location when the plasma actuator is activated. This increase in the vortex formation length will cause a reduction in the turbulence intensity of the unstable wake, to be shown later. Unlike the single cylinder case, the presence of the downstream cylinder leads to the extension of the separated shear layers further downstream. This increase in the vortex formation length translates to the reduction in the frequency of the main narrowband tonal noise when the upstream cylinder only subjected to the plasma actuation at $\theta_j = \pm 125^{\circ}$, as shown in Fig. 5.18.

Hot wire measurements were also conducted in order to investigate the unsteady velocity power spectral density in the wake region between the two cylinders for both the plasma off and plasma on cases at four different streamwise locations $1.125 \le x/D \le 2.25$ ($18 \le x \le 36$ mm) at free stream velocity $U = 10$ ms^{-1}. As shown in Fig. 5.27, it can be seen that for the plasma off case, a distinct narrowband peak and its second harmonic occur in the velocity fluctuation PSD spectra at the Strouhal number $fD/U = 0.156$ and 0.313, respectively. These values are very close to the narrowband tonal noise peak observed earlier in the acoustic spectra in Fig. 5.18 under the same mean flow conditions. This confirms that the narrowband tone peak seen in the acoustic spectra is mainly caused by the vortex shedding from the upstream cylinder. On the other hand, for the plasma on case, the results show that at $x/D = 1.125$ and 1.5, the main narrowband peak is reduced by 13 dB and 9 dB, respectively. However, the plasma actuator becomes less effective at a streamwise locations $x/D = 1.875$ and 2.25, where the narrowband peak is reduced by 4.7 dB and 4.2 dB, respectively. It can be seen that at reduced frequency $fD/U > 0.3$, the broadband component of the fluctuating velocity power spectral density for the plasma on case is less than the baseline case, which means that turbulence level in the wake region has been reduced by the plasma actuation. Thus the broadband noise peak earlier noticed in the acoustic results is

reduced. The interaction broadband noise is more associated with the turbulence intensity of the flow near the stagnation point. Although there is no data at the vicinity of the downstream cylinder, the trend in Fig. 5.27, as well as the other flow results to be presented next, could be used to conjecture that the turbulence level of the wake near the stagnation point at the downstream cylinder will still be lower when subjected to plasma actuator on the upstream cylinder. Because the key to any noise reduction is the delay or suppression of the separation and the associated unsteadiness in the wake region, the achieved reduction in the turbulence intensity under the activation of the plasma actuator will result in a reduction in the level of the interaction broadband noise at $\theta_j = \pm 125^\circ$, as observed earlier in Fig. 5.18.

a)   b)
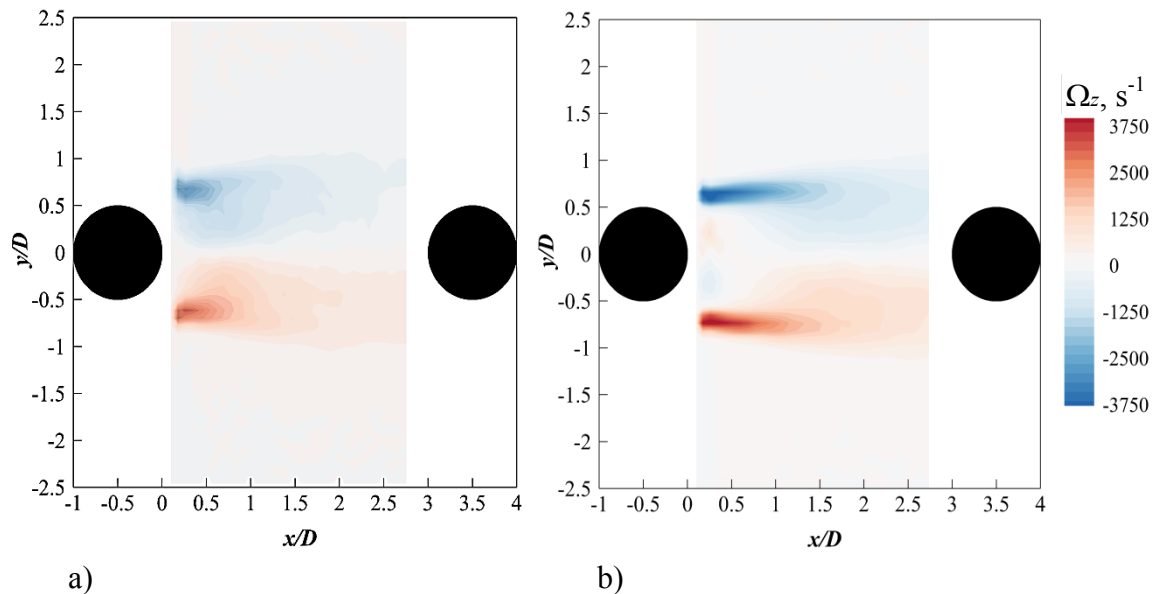
Figure 5.26 Time-averaged spanwise vorticity contours for tandem cylinders with upstream cylinder is only actuated subjected to a) Plasma off and b) Plasma on case at free stream velocity U = 10 ms^{-1} at V$_{(input)}$ = 6 kV and f$_{(input)}$ = 8 kHz.

Next, the effect of plasma actuation on the streamwise and vertical velocity fluctuation obtained from the PIV measurements are presented in Fig. 5.28 and 5.29, respectively. For the plasma off case, the results show a region of high streamwise velocity fluctuation in the wake of the upstream cylinder. This high turbulence intensity region is generated as result of the separated shear layers from the upper and lower sides of the upstream cylinder. One can also notice that the turbulence intensity for the tandem cylinder case is much larger than that of the single cylinder demonstrated earlier in Fig. 5.12a.
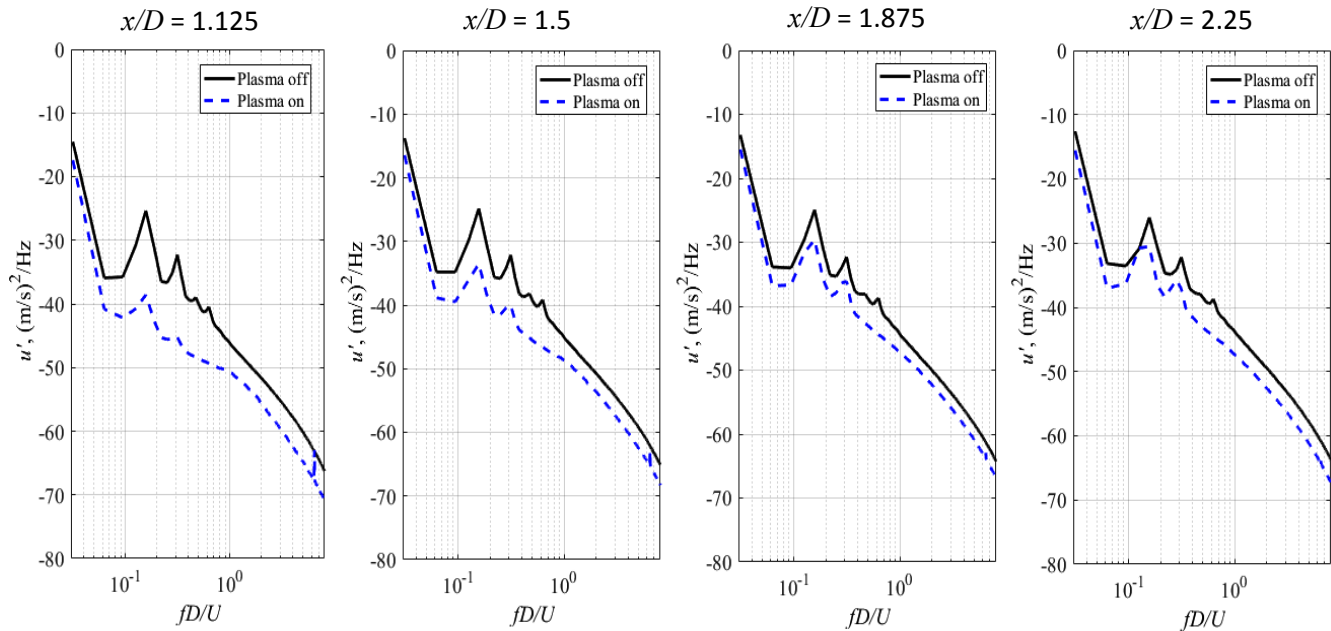
Figure 5.27 Velocity fluctuation PSD spectra for tandem cylinders with upstream cylinder is only actuated for Plasma off and Plasma on case at free stream velocity U = 10 ms⁻¹ at V(input) = 6 kV and f(input) = 8 kHz.

This difference is due to the presence of the downstream cylinder, which can affect the wake vortex shedding from the upstream cylinder. This explains the significant increase in the interaction broadband noise radiated from the tandem cylinder when compared to the single cylinder case seen earlier in Fig. 5.16.When the plasma actuator is activated, the streamwise velocity fluctuations in the near wake region are significantly reduced due to the plasma induced jet. This observation corroborates the hot wire results presented earlier in Fig. 5.27. Figure 5.29 shows the vertical velocity fluctuations in the region between the two cylinders. It can be seen that for the plasma off case, large vertical velocity fluctuations occurs in the center of the wake region of the upstream cylinder, where vortex shedding begins. However, when the plasma actuator is activated, a significant reduction in the vertical velocity fluctuations in the near wake region can be observed. Further in the downstream direction at a streamwise location $x/D > 1$, a noticeable level in the vertical velocity fluctuations can be seen. This indicates that the vortex shedding, albeit with a lower intensity level, starts to shed at this location in the downstream direction.
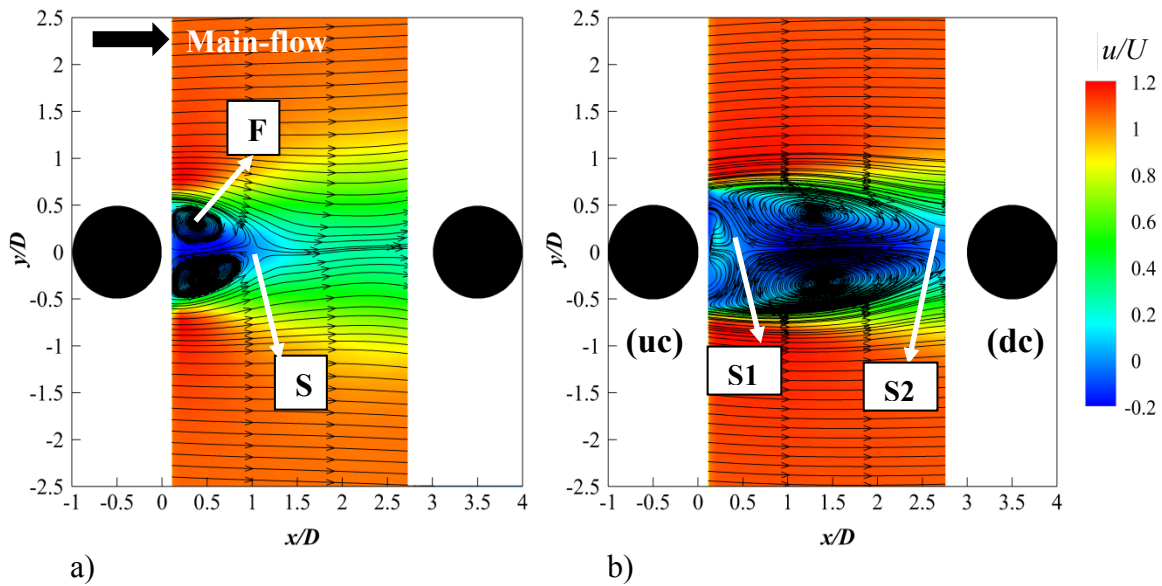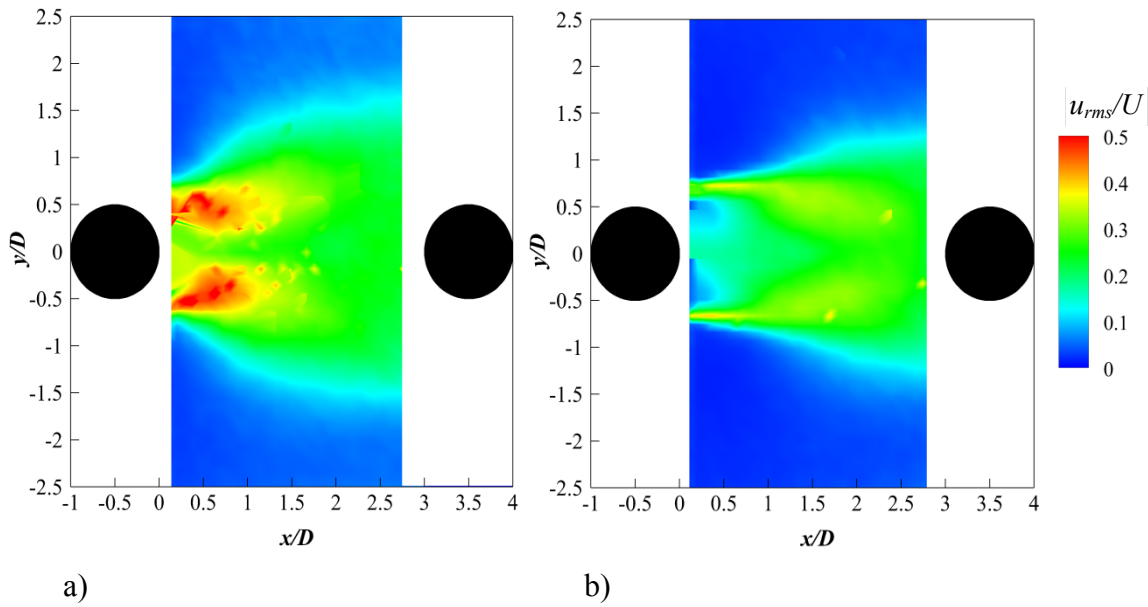
Figure 5.28 Time-averaged streamwise velocity fluctuations contours for tandem cylinders with upstream cylinder subjected to a) Plasma off and b) Plasma on case at free stream velocity $U = 10\ ms^{-1}$ at $V_{(input)} = 6\ kV$ and $f_{(input)} = 8\ kHz$
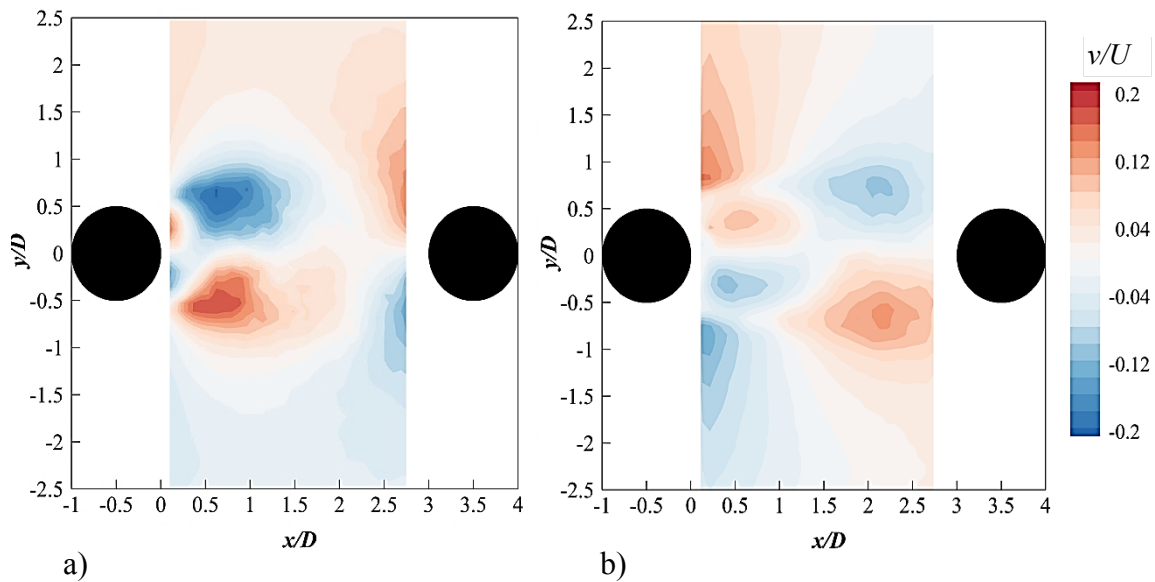

Figure 5.29 Time-averaged streamwise velocity fluctuations contours for tandem cylinders with upstream cylinder subjected to a) Plasma off and b) Plasma on case at free stream velocity $U = 10\ ms^{-1}$ at $V_{(input)} = 6\ kV$ and $f_{(input)} = 8\ kHz$.

Figure 5.30 shows the streamwise and the vertical velocity fluctuations along the center of the wake region between the cylinders. From Fig.5.30a-b it can be seen that the activation of the plasma actuator leads to a reduction in the turbulence intensity near the front face of the downstream cylinder when compared to the plasma off case. Because the wake interaction

broadband noise is related to the interaction between the turbulent wake and the downstream cylinder, the reduction in the broadband noise (Fig. 5.18) is due to the reduction in the turbulence intensity near the front face of the downstream cylinder. Figure 5.30b shows that when the plasma actuator is turned on, a dramatic reduction in the vertical velocity fluctuation especially in the near wake region can be observed. This confirms that the delay in the vortex shedding seen earlier in Fig. 5.26b results in a reduction in the vertical velocity fluctuation, which leads to a reduction in the narrowband tone noise level. This is also manifested in the reduction of the narrowband tonal noise seen earlier in Fig. 5.18, when the upstream cylinder only subjected to the plasma actuation at $\theta_{UCj} = \pm 125^{\circ}$. The effect of the plasma actuation on the wake region represented by the increase in the formation length is very similar to the reported effect of a splitter plate as passive vortex shedding control device by Apelt and west (1975).

a) Streamwise velocity fluctuation   b) Vertical velocity Fluctuation
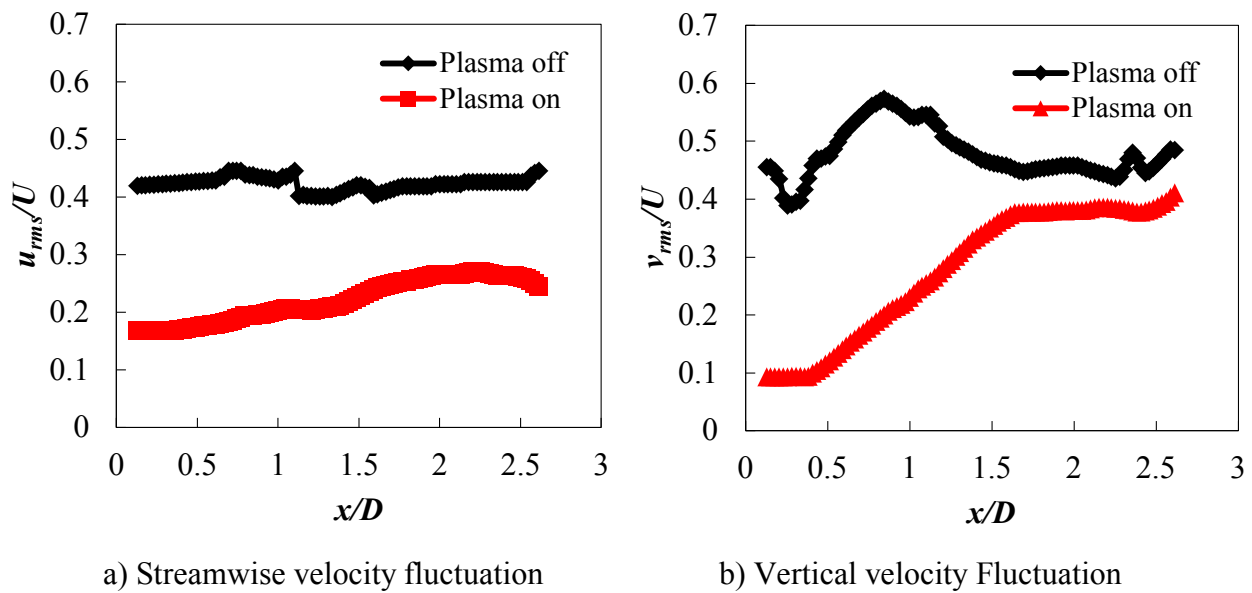
Figure 5.30 streamwise and vertical velocity fluctuations along the center of the wake region between the cylinders.

The POD analysis has been performed to capture the large scale high energy structures in the wake region between the two tandem cylinders at $U = 10$ ms^{-1} *and at* $V_{(input)} = 6$ kV *and* $f_{(input)} = 8$ kHz. Figure 5.31 and 5.32 show the spatial distribution of the first and second modes in terms of the streamwise and vertical velocity components, u and v, respectively. Figure 5.31 shows that for plasma off case, two rows of anti- symmetrical structures which propagate

alternately in the downstream direction can be observed. The intensity of these patterns decreases as it convects in the downstream direction. However, for the plasma on case, in the near wake region, the large scale patterns have less energy and a change in sign occurs compared with the baseline case. The streamwise location of the beginning of the vortex shedding structures when subjected to the plasma actuation, occurs at $x/D \approx 1.5$ compared with the plasma off case which occurs at $x/D \approx 1$. This increase in the location where the vortex shedding starts agrees with spanwise vorticity result, which showed that the plasma actuation leads to an increase in the vortex formation length to a streamwise location $x/D \approx 1.5$, see Fig. 5.26b. This reduction in the energy of the near wake vortex shedding patterns corroborates the reduction in the turbulence intensity demonstrated earlier in Fig. 5.28, 5.29 and 5.30.

Figure 5.32 shows the POD first and second modes in terms of the vertical velocity component, v for both the plasma off and plasma on cases. For the first modes, the results for the plasma off case show that a row symmetrical patterns in the vertical direction, but alternatingly develop in the downstream direction. When the plasma actuator is activated, the energy of the patterns in the near wake region is reduced and a change of sign occurs when compared with the plasma off case. However, the intensity of these structures increases as they develop in the downstream direction. This reduction in the energy of the vortex shedding patterns is manifested in the reduction in the wake turbulence level as observed in Fig. 5.30b.

To conclude, both PIV and hot wire results confirm that the activation of the plasma actuator on the upstream cylinder both primary peak and the broadband component can be reduced. The mechanism of the noise reduction is the reduction in the large scale vortex shedding structure size and the increase in the vortex formation length which is associated with a significant reduction in the intensity of the wake unsteadiness that impinge on the front face of the downstream cylinder. The interesting thing about using plasma actuator as an active vortex shedding control is that the effect of this particular technique on the wake region is very similar to the reported effect of the splitter plate. Both the splitter plate and the plasma actuator result in an elongation of the wake region behind the bluff body. This elongation indicates that the vortex formation length is increased and the vortices are pushed downstream which is a clear evidence of delayed separation and drag reduction Apelt and West (1975).
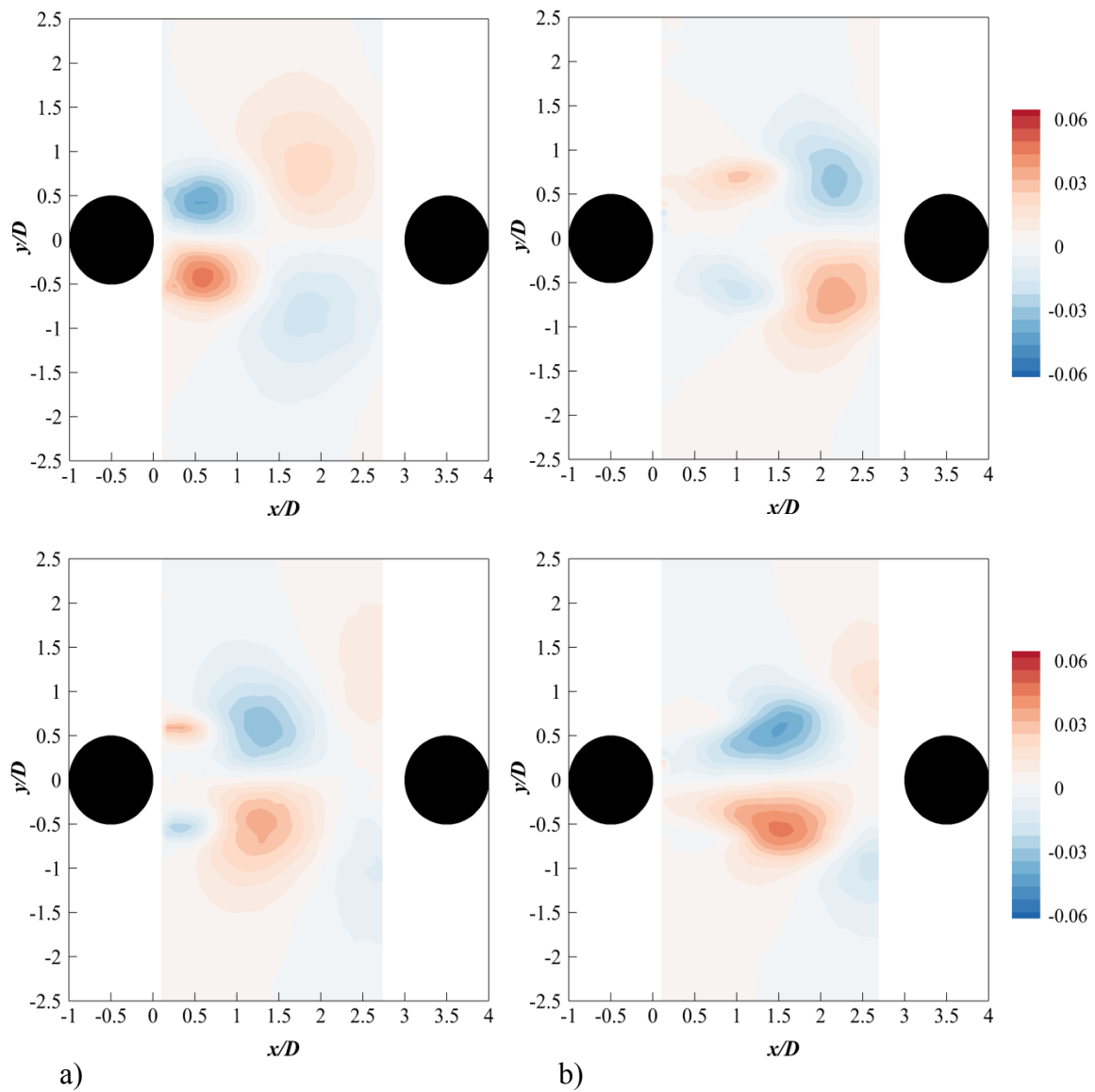
Figure 5.31 POD first (top) and second (bottom) modes in terms of the streamwise velocity for tandem cylinders with upstream cylinder subjected to a) Plasma off and b) Plasma on case at free stream velocity U = 10 ms^{-1} at V$_{(input)}$ = 6 kV and f$_{(input)}$ = 8 kHz.
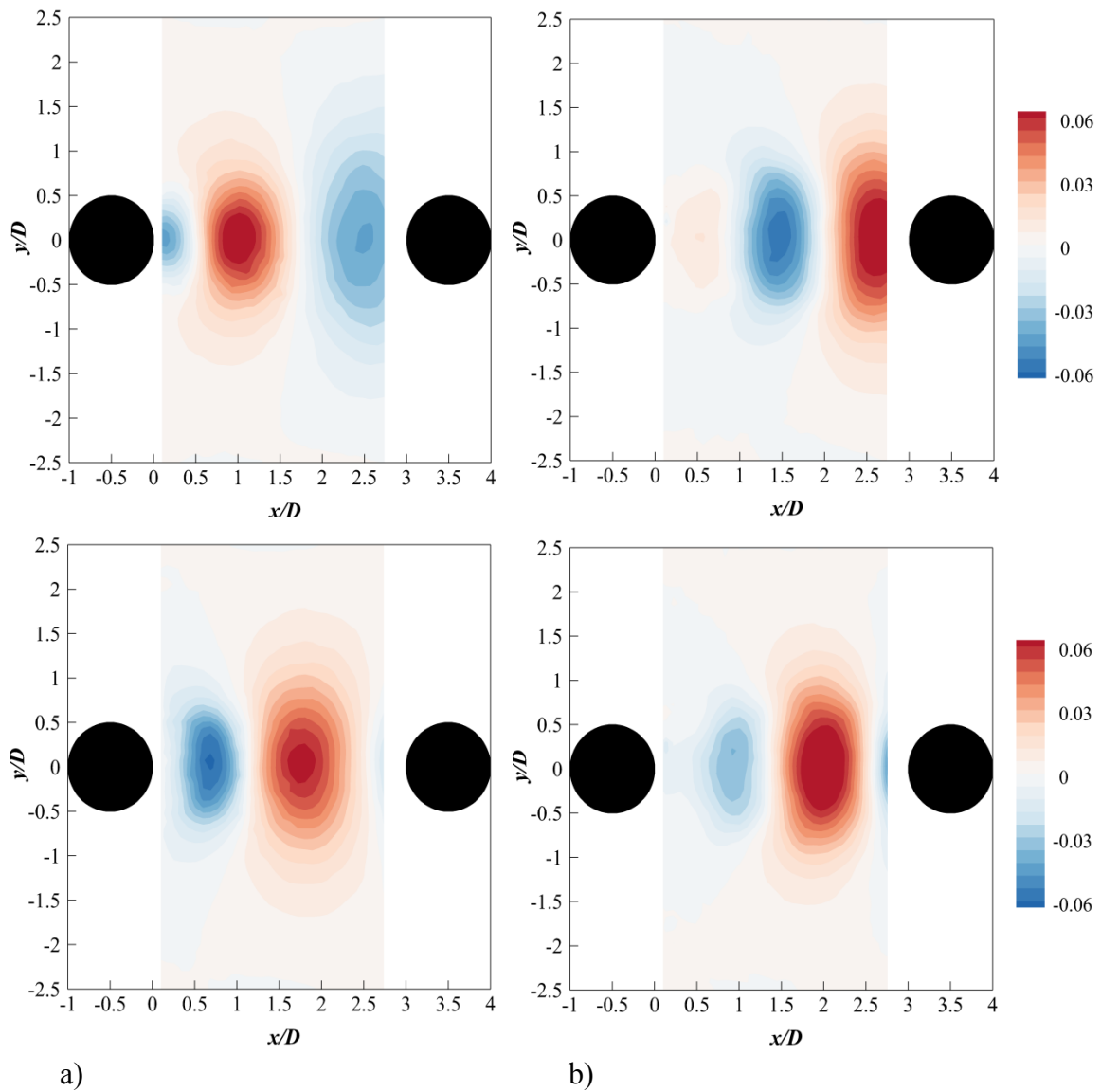
Figure 5.32 POD first (top) and second (bottom) modes in terms of the vertical velocity component, v for tandem cylinders with upstream cylinder subjected to a) Plasma off and b) Plasma on case at free stream velocity U = 10 ms⁻¹ at V$_{(input)}$ = 6 kV and f$_{(input)}$ = 8 kHz.

a)   b)

5.4.2.3 Time-Averaged Flow Field - Actuation of the Downstream Cylinder

This section presents the time-averaged flow results for the tandem cylinders with the downstream cylinder subjected to the plasma actuator placed at an azimuthal angle $\theta_{DCj} = \pm55^\circ$ on both the upper and lower sides of the cylinder. The actuator is situated in a way to induce the plasma jet in the upstream direction against the main flow.

The streamwise velocity component, u contours superimposed by the streamlines for both the plasma off and plasma on cases at free stream velocity $U = 10$ ms^{-1} are shown in Fig. 5.33. Like the plasma off case, a recirculating and non-convective region in the wake of the upstream cylinder for the plasma on case can be observed. It can also be seen that the vortex formation length is slightly shifted further in the downstream direction compared to the plasma off case. Moreover, when the plasma actuator is activated, an increase in the near wake half width can be seen at $x/D < 2$ when compared to the plasma off case. This could be due the upstream directed plasma-induced jet, which could result in an early separation (reduces the separation angle). Further downstream in the wake region at $x/D > 2$, a reduction in the wake half width can be observed, as shown in Fig. 5.34. This reduction in the wake half width suggests that this plasma configuration can affect the vortex shedding mode by the upstream directed plasma-induced jet.

The vertical velocity component, v contours for both the plasma off and plasma on cases are demonstrated in Fig. 5.35. Generally speaking, the vertical velocity component for both the plasma off and plasma on cases are similarly behaved except that a reduction near the front face of the downstream cylinder can be observed for the plasma on case. This reduction in the vertical velocity value occurs at $x/D \approx 2$, where the wake half width is reduced as observed earlier in Fig. 5.34.

The spanwise vorticity contours in the wake region between the two cylinders for both plasma off and plasma on cases are illustrated in Fig. 5.36. Again, there is no much difference between the two cases except that a slight extension in the vorticity for the plasma on case. This slight extension of the vortex recirculating zone leads to the light reduction in the narrowband vortex shedding frequency seen earlier in Fig. 5.19.
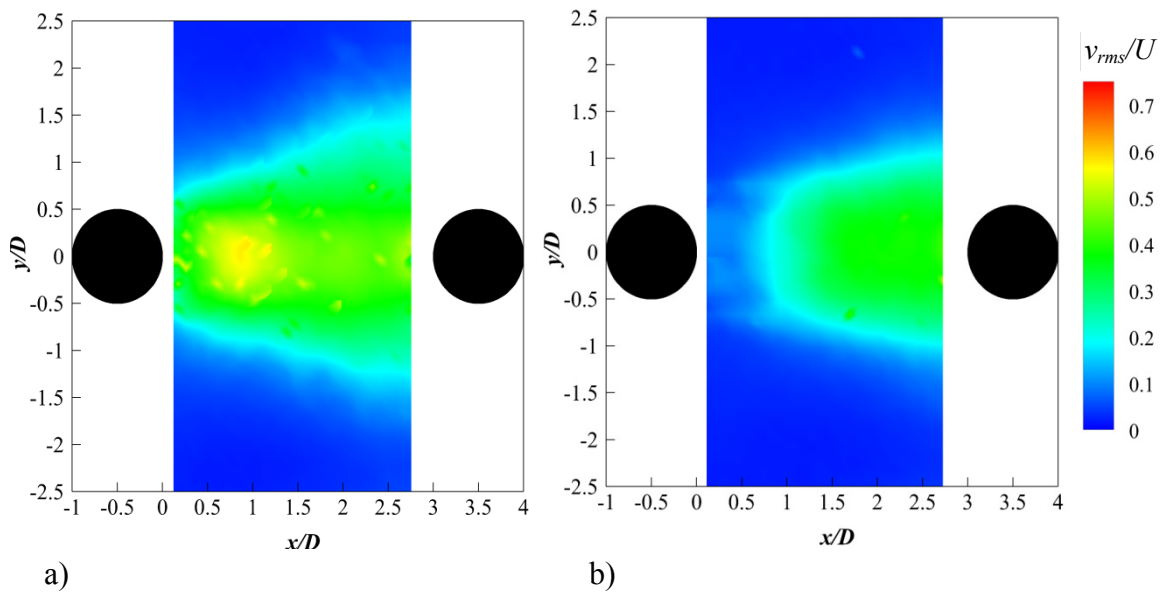
Figure 5.33 Time-averaged streamwise velocity contours for tandem cylinders with downstream cylinder is only subjected to a) Plasma off and b) Plasma on case at free stream velocity U = 10 ms⁻¹ at V_(input) = 6 kV and f_(input) = 8 kHz.
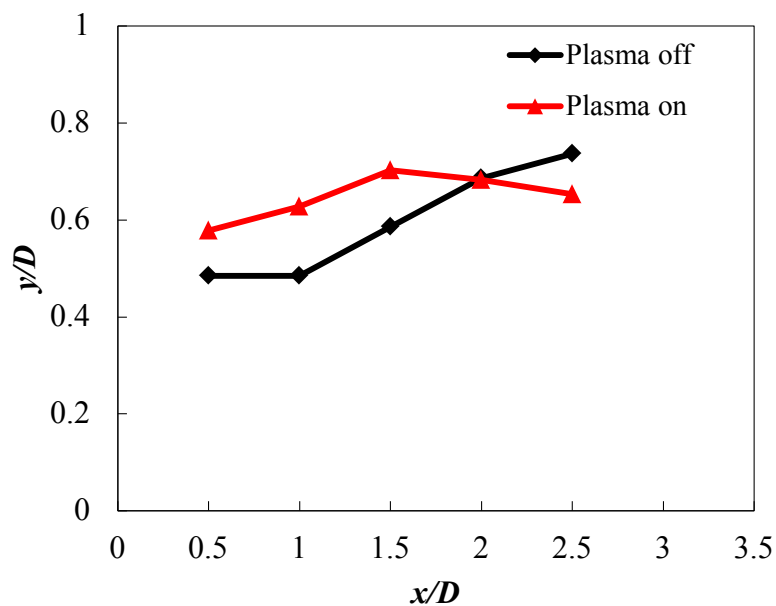
Figure 5.34 Comparison between plasma off and plasma on of streamwise evolution of wake half width for tandem cylinders with downstream cylinder only subjected to the plasma off and plasma on case at U = 10 ms⁻¹ at V_(input) = 6 kV and f_(input) = 8 kHz.

Figure 5.35 Time-averaged vertical velocity contours for tandem cylinders with downstream cylinder is only subjected to a) Plasma off and b) Plasma on case at free stream velocity $U = 10\ ms^{-1}$ at $V_{(input)} = 6\ kV$ and $f_{(input)} = 8\ kHz$.
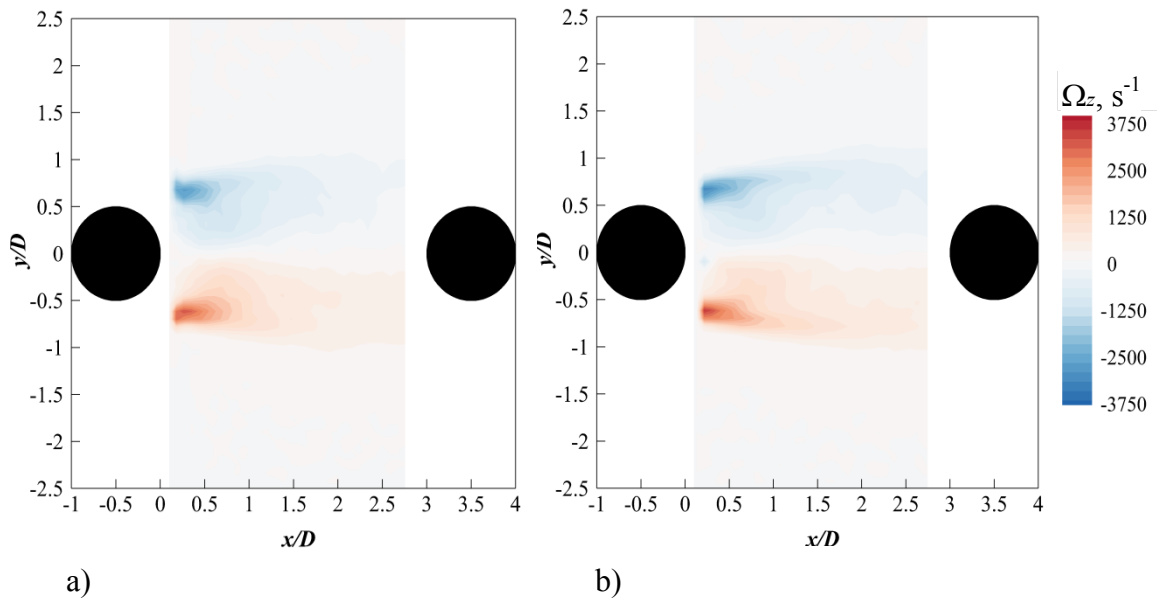
Figure 5.36 Time-averaged spanwise vorticity contours for tandem cylinders with downstream cylinder is only subjected to a) Plasma off and b) Plasma on case at free stream velocity $U = 10\ ms^{-1}$ at $V_{(input)} = 6\ kV$ and $f_{(input)} = 8\ kHz$.

Figure 5.37 shows the streamwise velocity fluctuations for both the plasma off and plasma on cases at free stream velocity $U = 10\ ms^{-1}$. It can be seen that unlike the plasma off case, a slight reduction in the streamwise velocity fluctuations in near wake region can be seen, when the plasma actuator is activated. However, further downstream in the wake region the velocity

fluctuations start to increase again, especially near the center of the front face of the downstream cylinder.

Figure 5.37 Time-averaged streamwise velocity fluctuations contours for tandem cylinders with downstream cylinder is only subjected to a) Plasma off and b) Plasma on case at free stream velocity $U = 10\ ms^{-1}$ at $V_{(input)} = 6\ kV$ and $f_{(input)} = 8\ kHz$.

Figure 5.38 shows the vertical velocity fluctuation for the plasma off and plasma on cases. For the plasma off case, the results show a region of relatively high velocity fluctuation in the center of the wake region between the two cylinders at streamwise location $x/D \approx 1$. For the plasma on case, the results show that a slight reduction in the vertical velocity fluctuations at the same streamwise location can be observed. The streamwise and vertical velocity fluctuations at various streamwise locations $0.5 \leq x/l_f \leq 2.5$ are presented in Fig. 5.39 and 5.40, respectively. From Fig. 5.39 it can be seen that this plasma configuration can slightly reduce velocity fluctuation at $x/l_f = 0.5$. Further downstream at $x/l_f > 2$, a noticeable increase in the turbulence intensity near the center of the front face of the downstream cylinder. Because of the relation between the streamwise velocity fluctuations and the separated shear layer, the results suggest that this plasma actuator configuration does not have any significant influence on the separating shear layer. This explains the weak effect of the current configuration on the narrowband tonal noise level seen earlier in Fig. 5.20. Figure 5.40 shows the vertical velocity fluctuation at the same streamwise locations. It can be seen that when the plasma actuator is turned on, a reduction in the vertical velocity fluctuation at $x/l_f \leq 2$ can be seen. However, further downstream, a slight

reduction in the velocity fluctuation can be achieved. This is manifested in the slight reduction in the interaction broadband noise demonstrated in Fig. 5.19.

Figure 5.38 Time-averaged vertical velocity fluctuations contours for tandem cylinders with downstream cylinder is only subjected to a) Plasma off and b) Plasma on case at free stream velocity $U = 10 \ ms^{-1}$ at $V_{(input)} = 6 \ kV$ and $f_{(input)} = 8 \ kHz$.

Next, the POD analysis for the streamwise velocity component is shown in Fig. 5.41, which illustrates the effect of plasma actuation on the large scale and high energy structures in the wake region between the cylinders. Generally, the spatial distribution and the energy levels for the modes are similar, except that there is a switch in the sign between the plasma off and plasma on case. The scenario is demonstrated in the POD modes for the vertical velocity component in Fig. 5.42. The phenomenon of sign changing for the POD modes also happens for the case when the plasma actuator is activated at the upstream cylinder (see Fig. 5.31 and 5.32). Although it is not completely understood yet what causes the change in sign for the POD modes when subjected to the plasma actuation, it is clear that the plasma induced jet can exert certain level of effect to the wake vortical structure. Some can be significant (e.g. the upstream cylinder actuation, as well as the simultaneous actuation of the two cylinders cases), and in this particular case when the plasma actuation is at the downstream cylinder only, the spatial distribution and the energy level of the modes are quite similar. These are generally manifested quite well in the corresponding acoustical results. Particularly, the narrowband tonal noise remains unchanged at this particular plasma actuator configuration
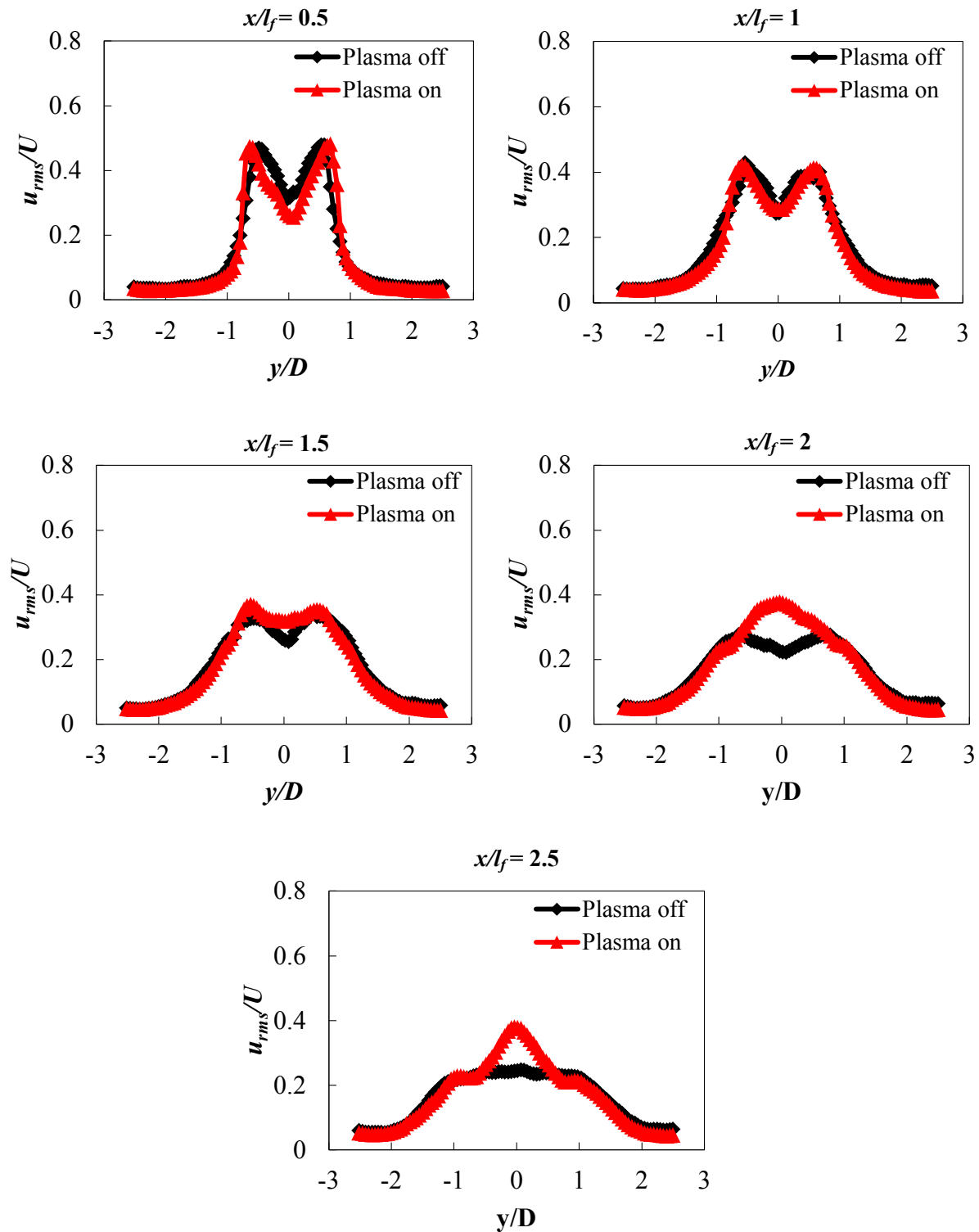
Figure 5.39 Streamwise velocity fluctuations at various streamwise locations $0.5 \leq x/l_f \leq 2.5$ for the tandem cylinders with the upstream cylinder only subjected to the plasma actuation at free stream velocity $U = 10 \ ms^{-1}$ at $V_{(input)} = 6 \ kV$ and $f_{(input)} = 8 \ kHz$.
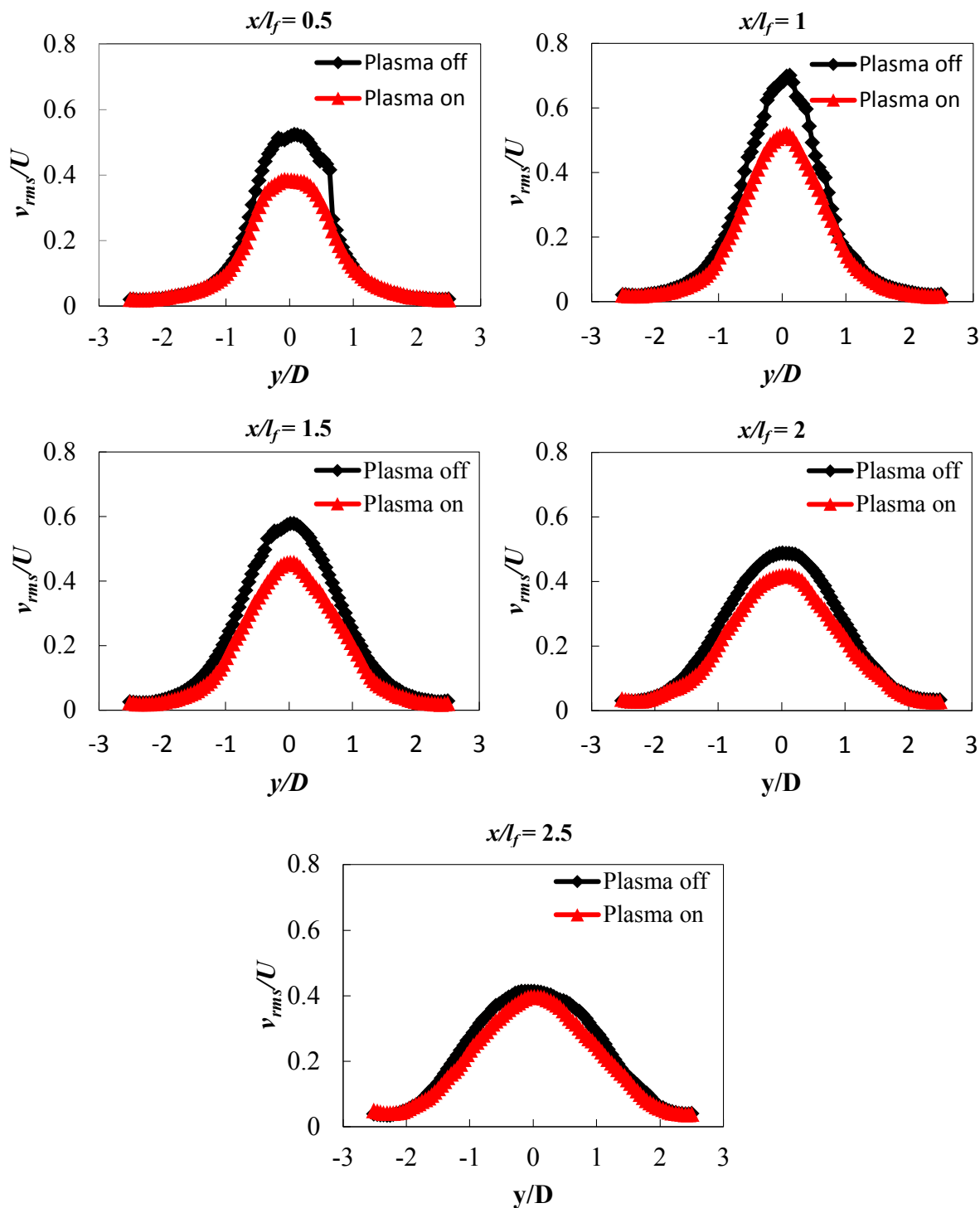
Figure 5.40 vertical velocity fluctuations at various streamwise locations 0.5 ≤ x/l$_f$ ≤ 2.5 for the tandem cylinders with the upstream cylinder only subjected to the plasma actuation at free stream velocity U = 10 ms^{-1} at V$_{(input)}$ = 6 kV and f$_{(input)}$ = 8 kHz.
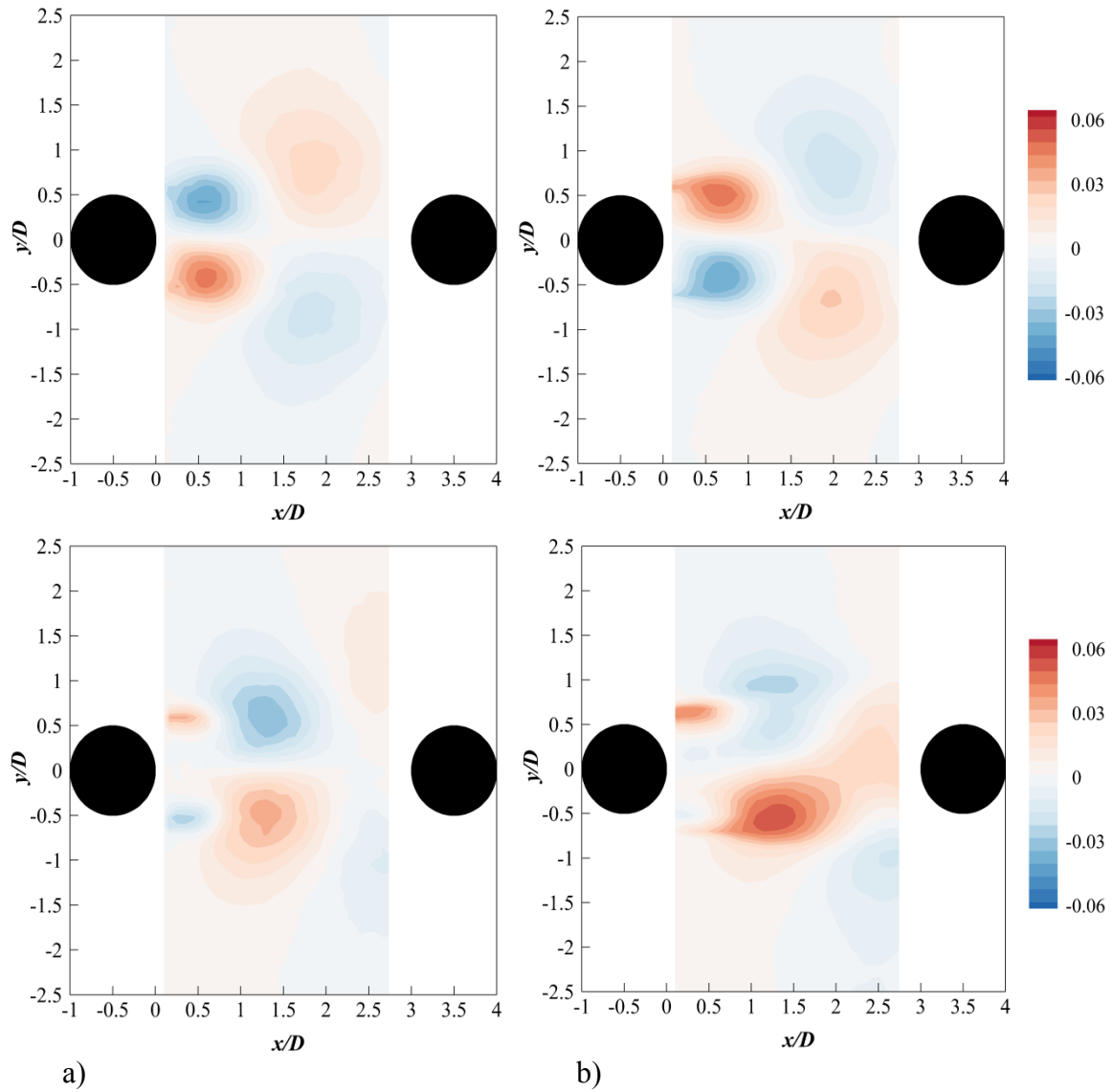
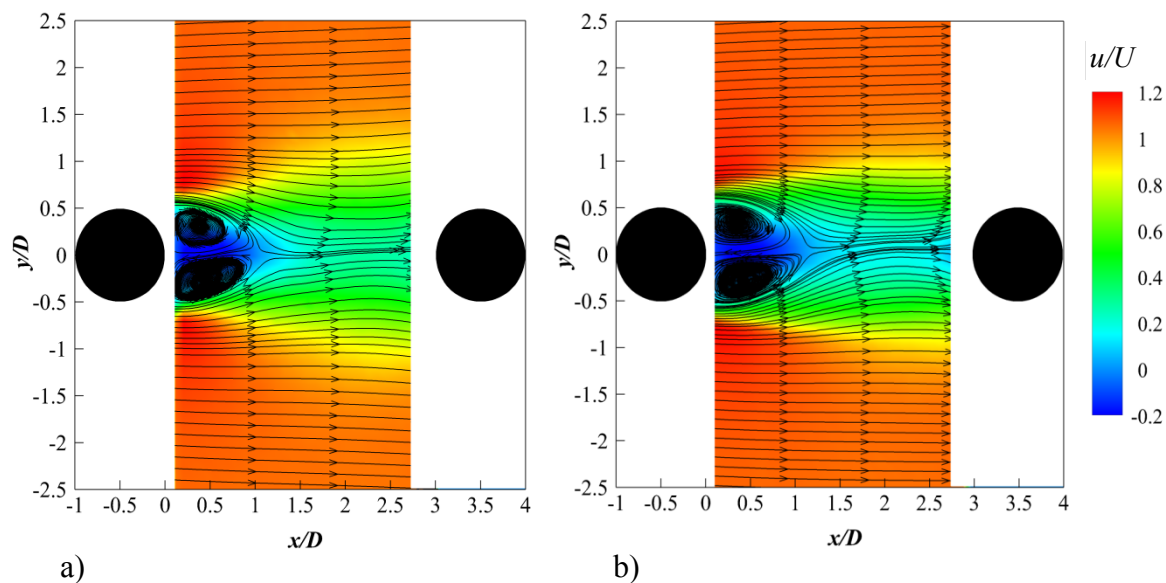*Figure 5.41 POD first (top) and second (bottom) modes in terms of the streamwise velocity for tandem cylinders with downstream cylinder subjected to a) Plasma off and b) Plasma on case at free stream velocity U = 10 ms^{-1} at V$_{(input)}$ = 6 kV and f$_{(input)}$ = 8 kHz.*
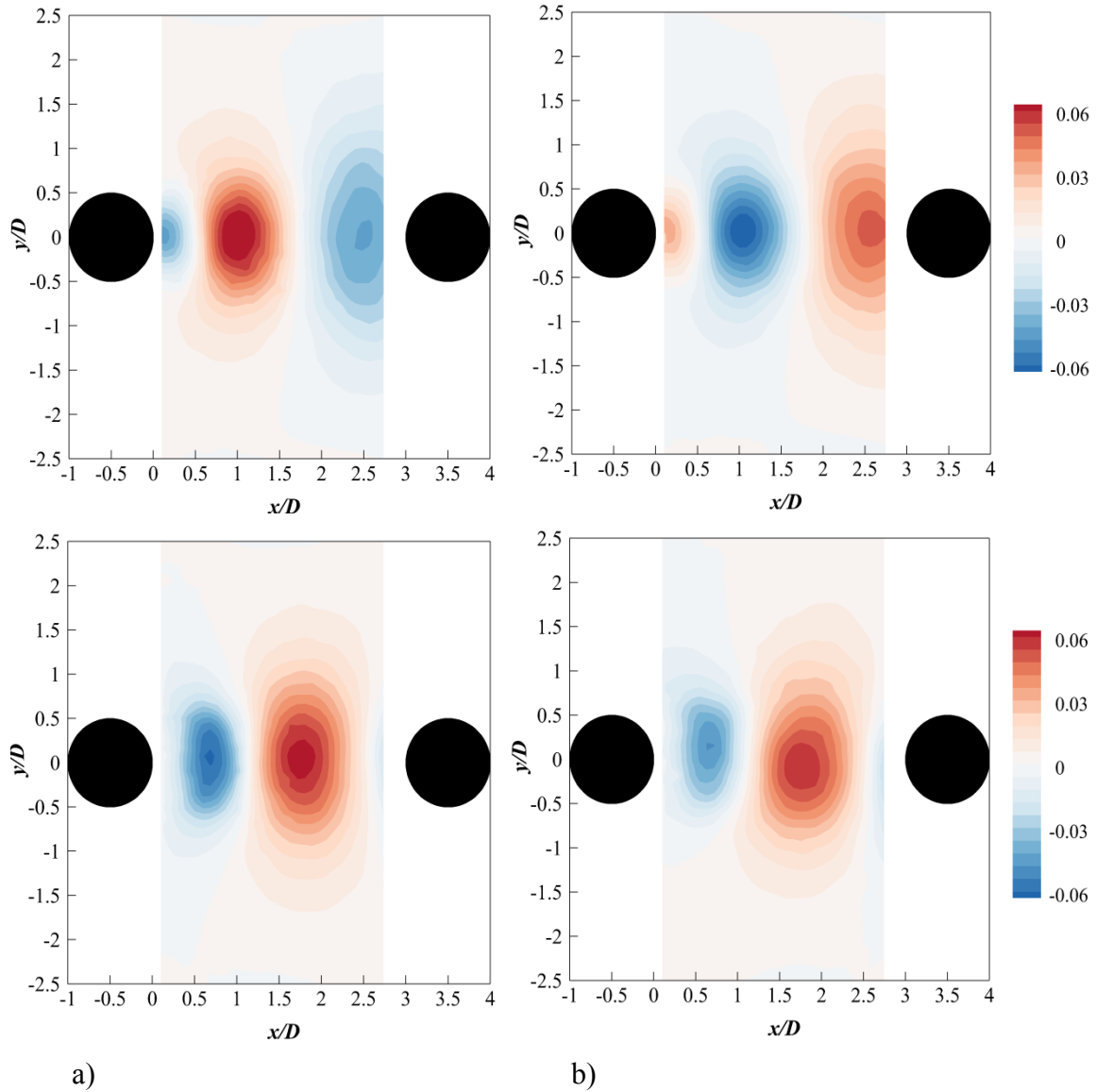
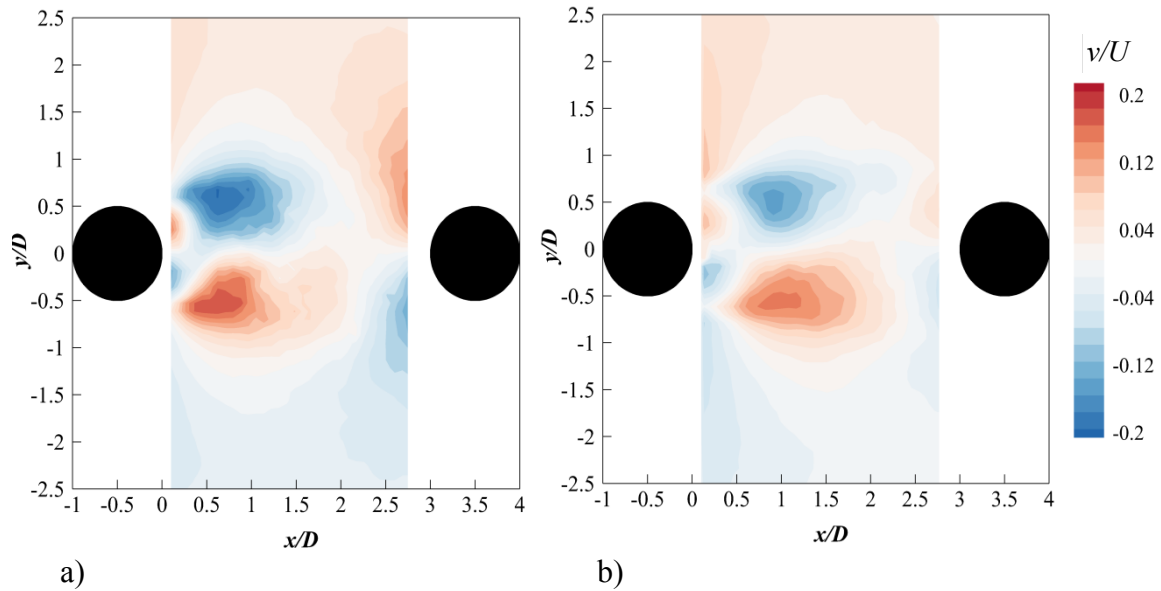*Figure 5.42 Figure 5.42 POD first (top) and second (bottom) modes in terms of the vertical velocity for tandem cylinders with downstream cylinder subjected to a) Plasma off and b) Plasma on case at free stream velocity U = 10 ms^{-1} at V$_{(input)}$ = 6 kV and f$_{(input)}$ = 8 kHz.*

5.4.2.4 Time-averaged flow field- actuation of both cylinders

This section will focus on the time-averaged flow fields for the tandem cylinders with plasma actuator placed on the upstream and downstream cylinders at azimuthal angle $\theta_{UCj} = \pm125^o$ and $\theta_{DCj} = \pm55^o$, respectively. The plasma induced jet on the upstream cylinder is directed towards the downstream direction while the plasma induced jet on the downstream cylinder is directed towards the upstream direction. The cylinders were tested at free stream velocity $U = 10$ms^{-1} and

at $V_{(input)}$ = 6 kV and $f_{(input)}$ = 8 kHz. Figure 5.43a-b presents the streamwise velocity contours superimposed with streamlines for both plasma off and plasma on cases. Unlike the plasma off case, when the plasma actuator is on, the recirculating air pocket enlarges and extends in the downstream direction and two large, counter-rotating, and symmetrical vortices occur between the two cylinders. Moreover, it can be seen that the width of the recirculating region near the front face of the downstream cylinder increases compared with the case where only the upstream cylinder is actuated as demonstrated earlier in Fig. 5.24b. In addition, one can also notice that the focal points are shifted more downstream to approximately $x/D \approx 2.25$.

a)   b)
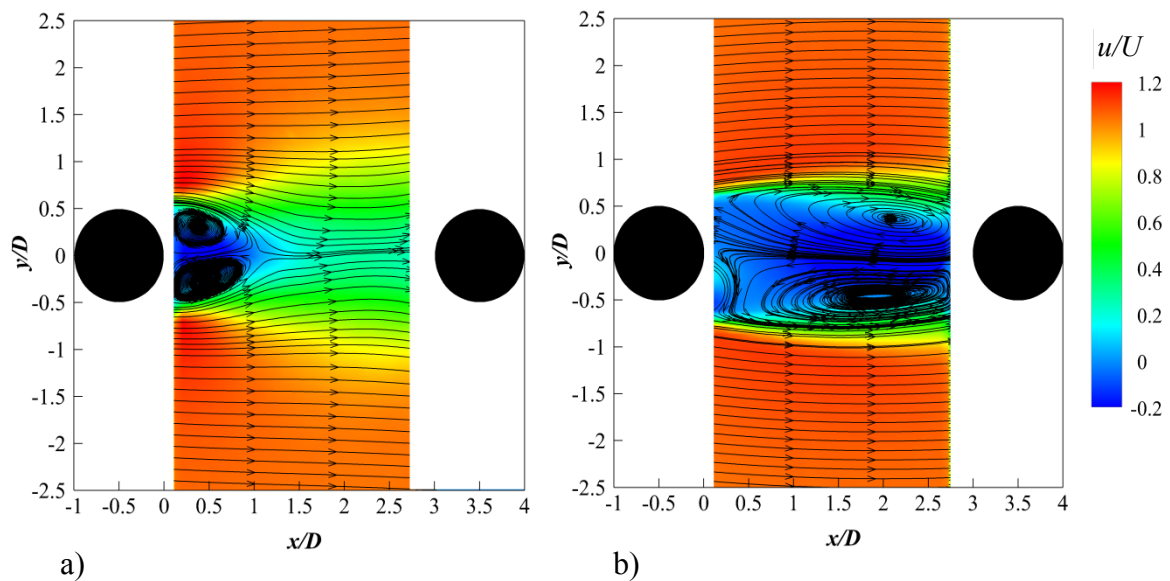
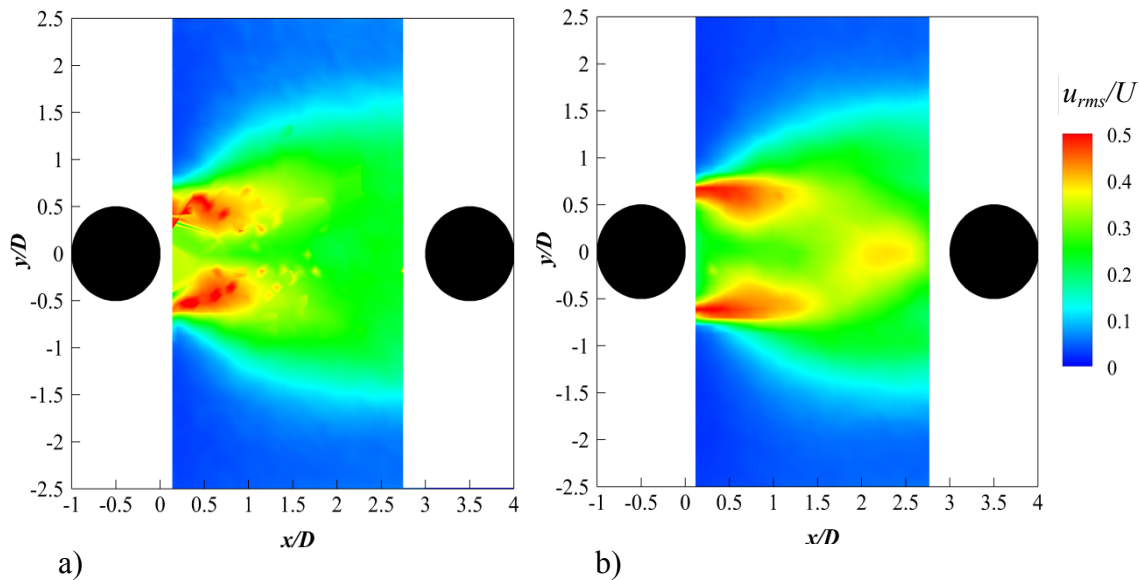*Figure 5.43 Time-averaged streamwise velocity contours for tandem cylinders with both cylinders are subjected to a) Plasma off and b) Plasma on case at free stream velocity $U = 10$ ms^{-1} at $V_{(input)}$ = 6 kV and $f_{(input)}$ = 8 kHz.*

Figure 5.44 shows a comparison of the wake half width between the baseline "plasma off" case, upstream cylinder actuation only, and the current simultaneous actuation of both upstream and downstream cylinders. When the plasma actuator is turned on, both the upstream cylinder activation only and the simultaneous activation of both the upstream and downstream cylinder lead to an increase in the thickness of the wake half at $0.5 \leq x/D \leq 1.5$. A reduction in the wake half width occurs at streamwise location $1.75 < x/D < 3$, with more reduction can be noticed when both the upstream and downstream cylinders are simultaneously activated. This reduction in the wake half width means that simultaneous actuation leads to better suppression of the vortex shedding near the front face of the downstream cylinder than the upstream cylinder

actuation only case. This reduction in the wake half width implies that the both downstream and upstream plasma induced jets leads to a better reduction in the vortex shedding, when compared to the plasma off case.
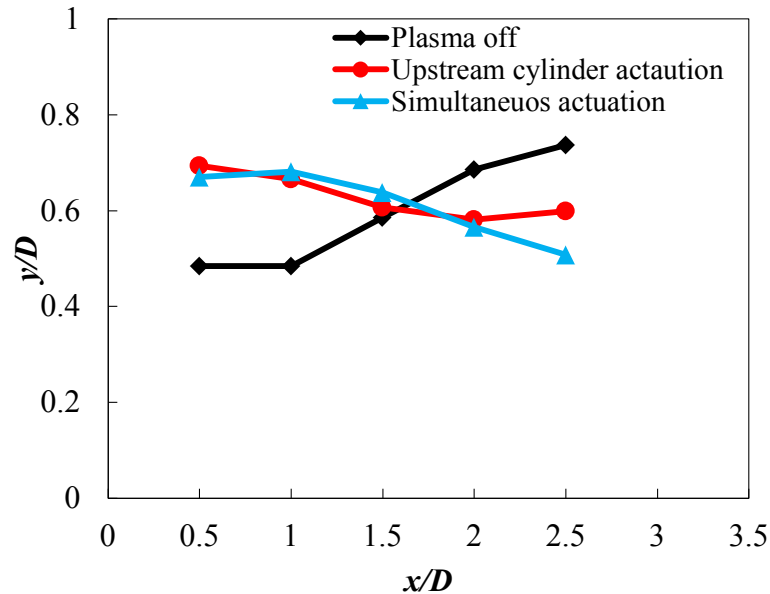
Figure 5.44 Comparison of plasma off and plasma on of streamwise evolution of the wake half width for both upstream and upstream and downstream cylinders simultaneous actuation at $U = 10 \ ms^{-1}$ at $V_{(input)} = 6 \ kV$ and $f_{(input)} = 8 \ kHz$.

Figure 5.45 shows the vertical velocity component for both the plasma off and plasma on cases. For the plasma on case the vertical velocity is significantly reduced in comparison with the baseline, plasma off case. It can also be seen that the mean flow pertaining to the upstream cylinder exhibits a "diverge" flow pattern, whilst the mean flow for the downstream cylinder shows a sign of converging towards the front portion of the downstream cylinder. This could be due the increase in the wake thickness close to the upstream cylinder base and the reduction close to downstream cylinder front face compared with the baseline case seen earlier in Fig.5.44.

Figure 5.46 shows the time-averaged spanwise vorticity for both plasma on and plasma off cases. The plasma actuators can extend the separating shear layer extensively in the downstream direction up to $x/D \approx 2$. This extension in the spanwise vorticity can be interpreted to an increase in the vortex formation length, which entails the delay formation of the vortex shedding and the reduced level of tonal noise increase (as the result of the vortex shedding) and the enhanced

broadband noise (as the result of less turbulence intensity level upon the downstream cylinder, this will be discussed in the next paragraph).

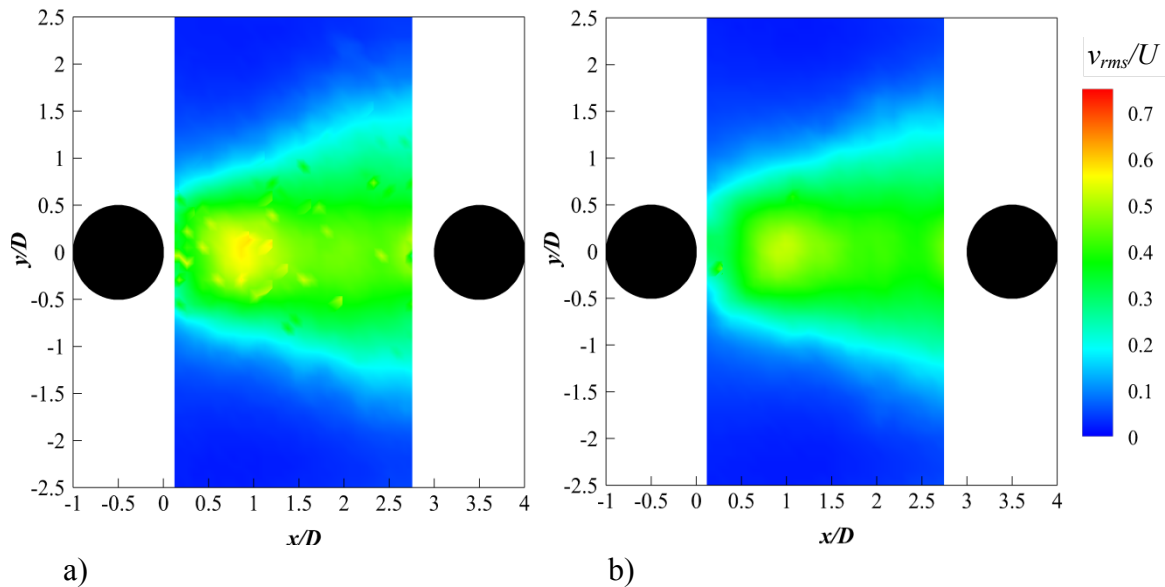a)   b)
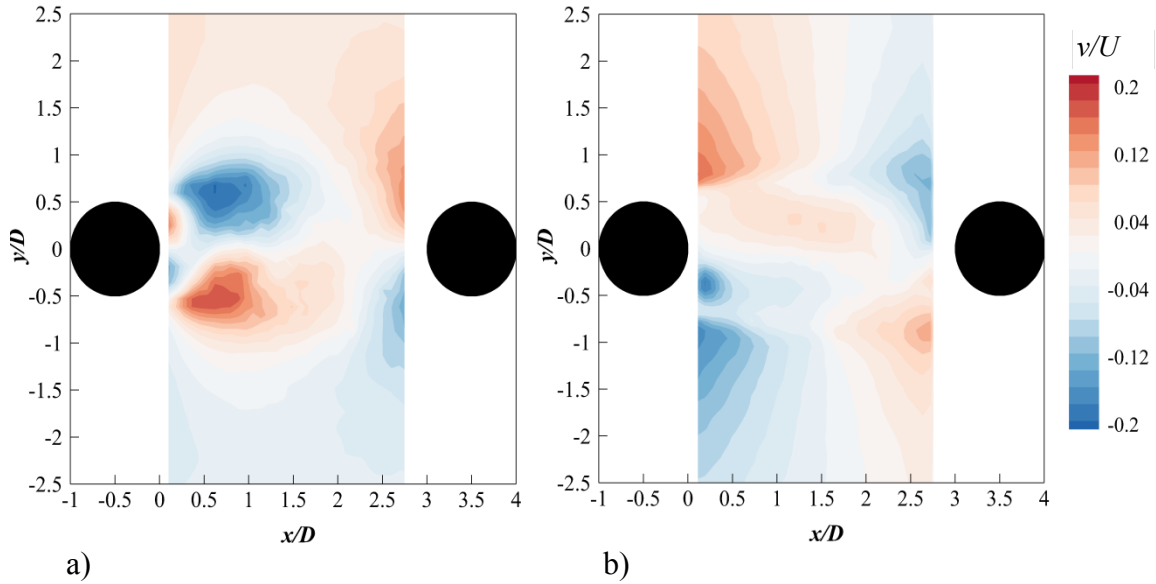
Figure 5.45 Time-averaged vertical velocity contours for tandem cylinders with both cylinders are subjected to a) Plasma off and b) Plasma on case at free stream velocity
$U = 10 \ ms^{-1}$ at $V_{(input)} = 6 \ kV$ and $f_{(input)} = 8 \ kHz$.

a)   b)
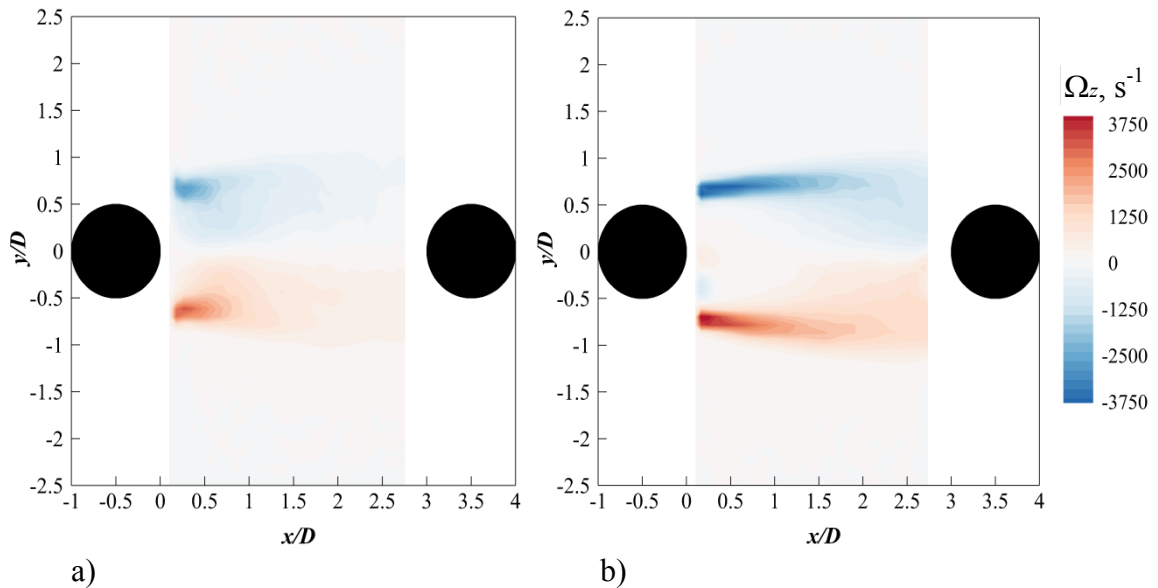
Figure 5.46 Time-averaged spanwise vorticity contours for the tandem cylinders with both cylinders are subjected to a) Plasma off and b) Plasma on case at free stream velocity
$U = 10 \ ms^{-1}$ at $V_{(input)} = 6 \ kV$ and $f_{(input)} = 8 \ kHz$.

The streamwise and vertical velocity fluctuations for both the plasma off and plasma on cases are shown in Fig. 5.47. The results clearly show a significant reduction in the streamwise velocity fluctuation when the plasma actuators on both cylinders are activated compared with the plasma off case. It can also be seen that having both cylinders been activated leads to more reduction in the streamwise velocity fluctuation compared with the case where only the upstream cylinder is actuated. The vertical velocity fluctuations in the wake region between the cylinders for both the plasma off and plasma on cases are also shown. For plasma on case, the results show that a significant reduction in the velocity fluctuation can be achieved.

Figure 5.48 and 5.49 shows the streamwise and vertical velocity fluctuations for the baseline "plasma off", upstream cylinder actuation, and the current upstream and downstream cylinders simultaneous actuation case at four different streamwise positions $0.5 \leq x/l_f \leq 2.5$. From figure 5.48, it can be seen that at $x/l_f \leq 2$ the simultaneous actuation of the both upstream and downstream cylinders leads to more reduction in the velocity fluctuation compared with the other cases (the baseline and the actuation of the upstream cylinder only). Because the streamwise velocity fluctuation is related to separating shear layer, which in turn leads to vortex shedding, it can be said that this increase in the velocity fluctuation reduction level for the simultaneous actuation case leads to the higher narrowband tonal noise reduction compared to other configurations.
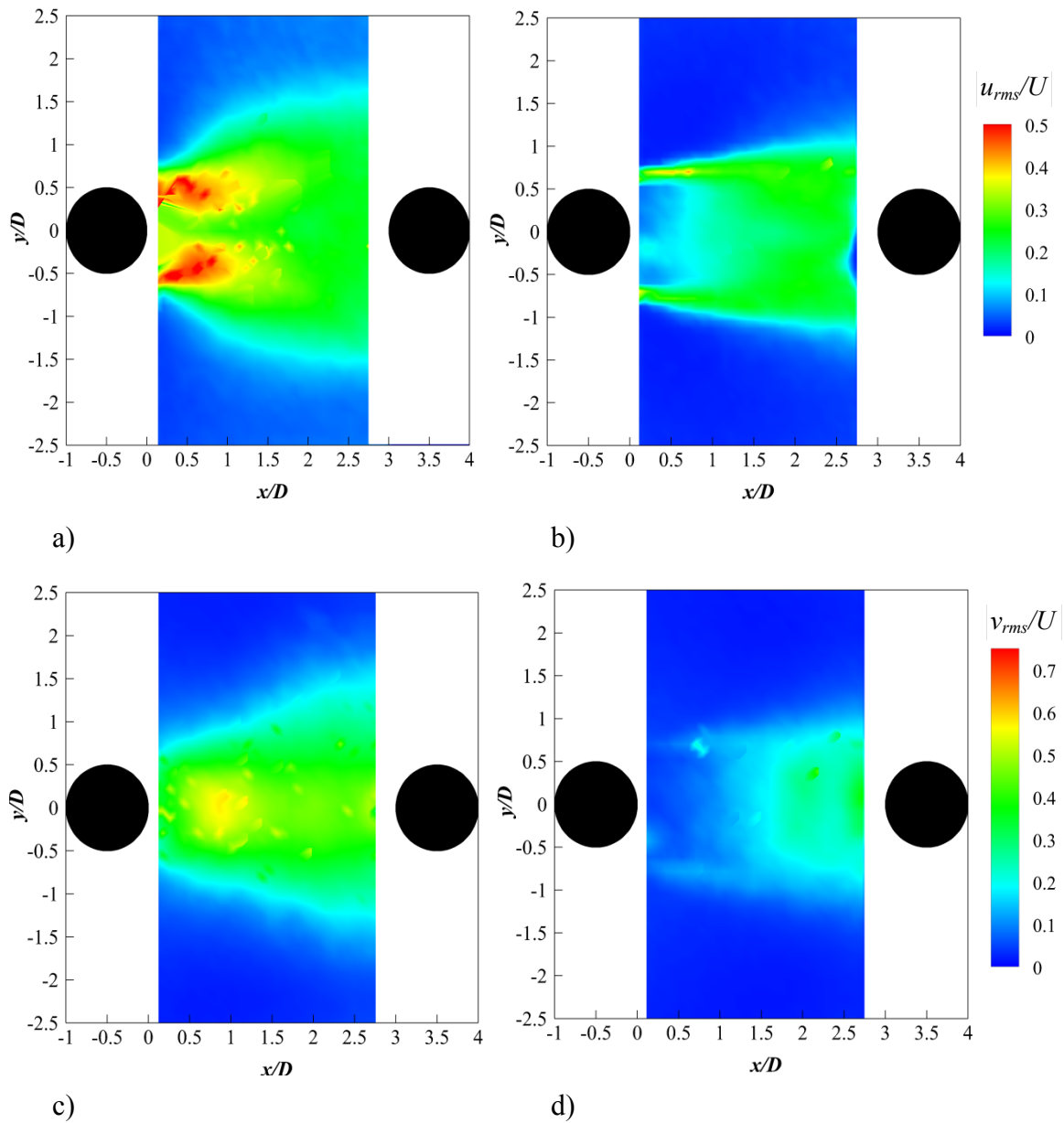
Figure 5.47 Time-averaged streamwise and vertical velocity fluctuation contours for the tandem cylinders with both cylinders subjected to (a,c) Plasma off and (b,d) Plasma on case at free stream velocity U = 10 ms⁻¹ at V(input) = 6 kV and f(input) = 8 kHz.
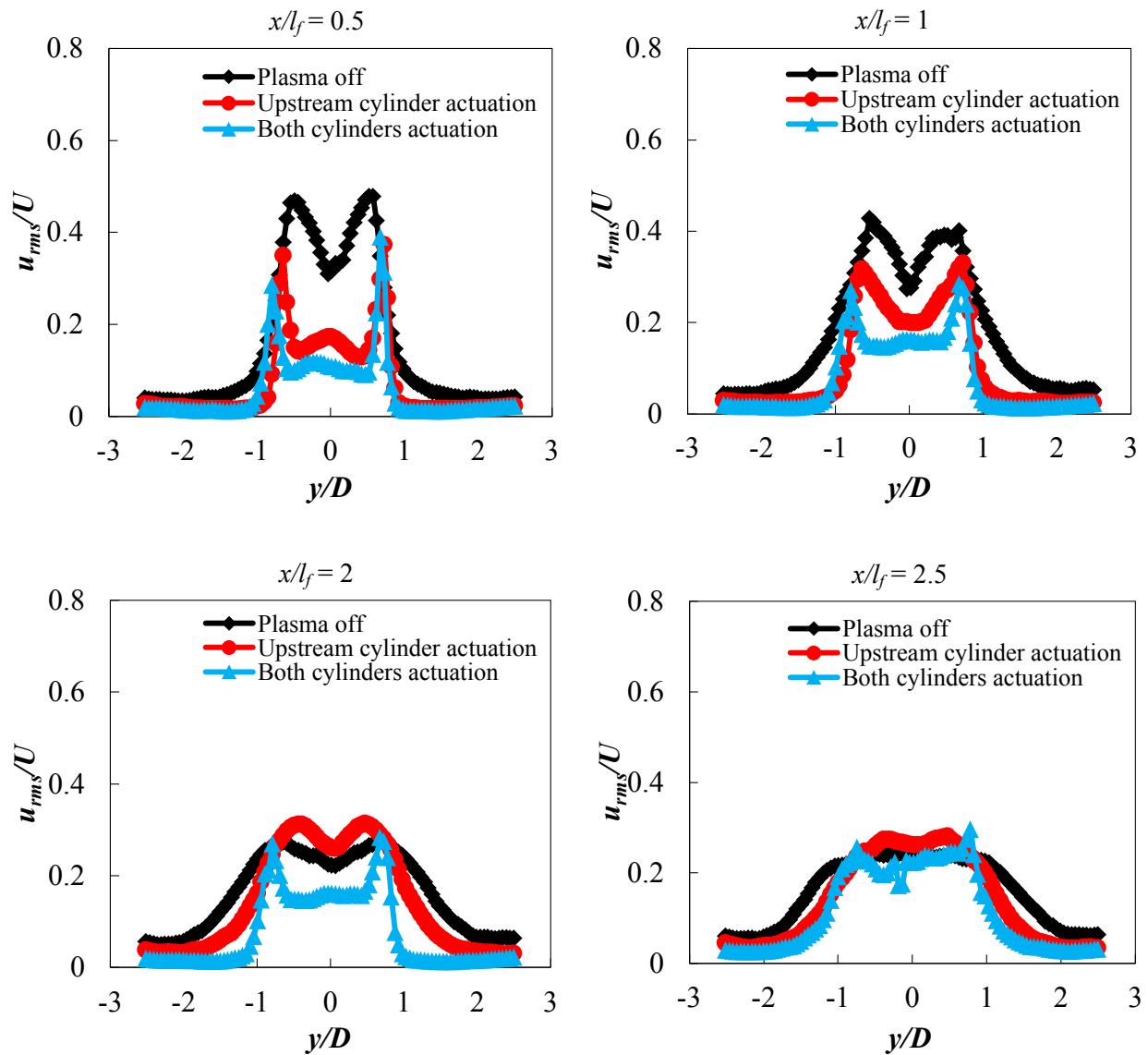
Figure 5.48 Comparison of the streamwise velocity fluctuation between plasma off, upstream cylinder actuation, and the simultaneous actuation of both upstream and downstream cylinders case at free stream velocity $U = 10\ ms^{-1}$ at $V_{(input)} = 6\ kV$ and $f_{(input)} = 8\ kHz$.

From Fig. 5.49, it can be seen that simultaneous actuation of both upstream and downstream cylinders outperforms the actuation of the upstream cylinder only in terms of the vertical velocity fluctuation reduction. Because vertical velocity fluctuation is associated with vortex shedding, this reduction in the fluctuation near the front face of the downstream cylinder results in a better tonal and broadband noise reduction in the case of simultaneous actuation of the upstream and downstream cylinders at $\theta_{UCj} = \pm125^{\circ}$ and $\theta_{DCj} = \pm55^{\circ}$ seen earlier in Fig. 5.22 .
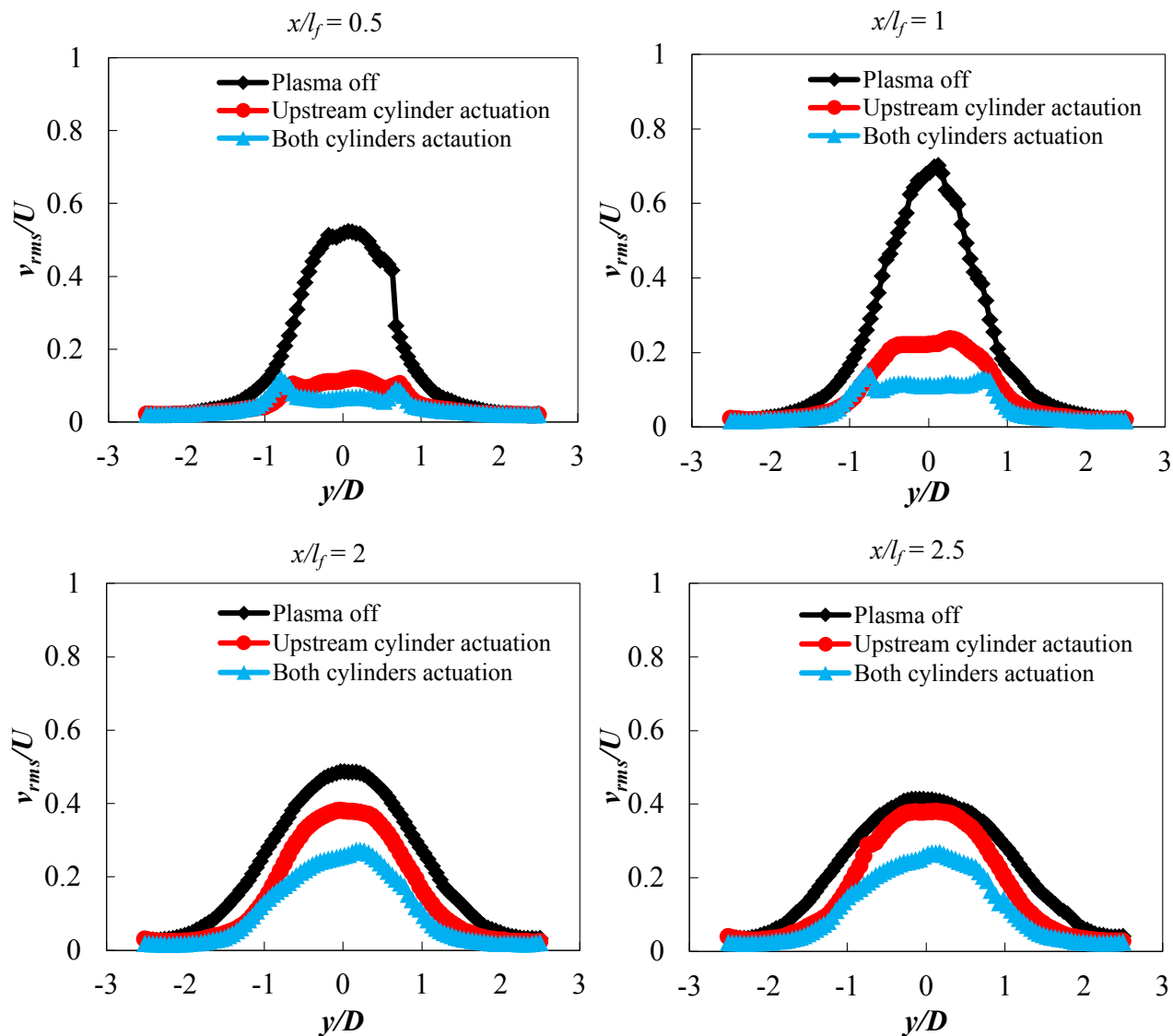
Figure 5.49 Comparison of the vertical velocity fluctuation between plasma off, upstream cylinder actuation, and the simultaneous actuation of both upstream and downstream cylinders case at free stream velocity $U = 10 \text{ ms}^{-1}$ at $V_{(input)} = 6 \text{ kV}$ and $f_{(input)} = 8 \text{ kHz}$.
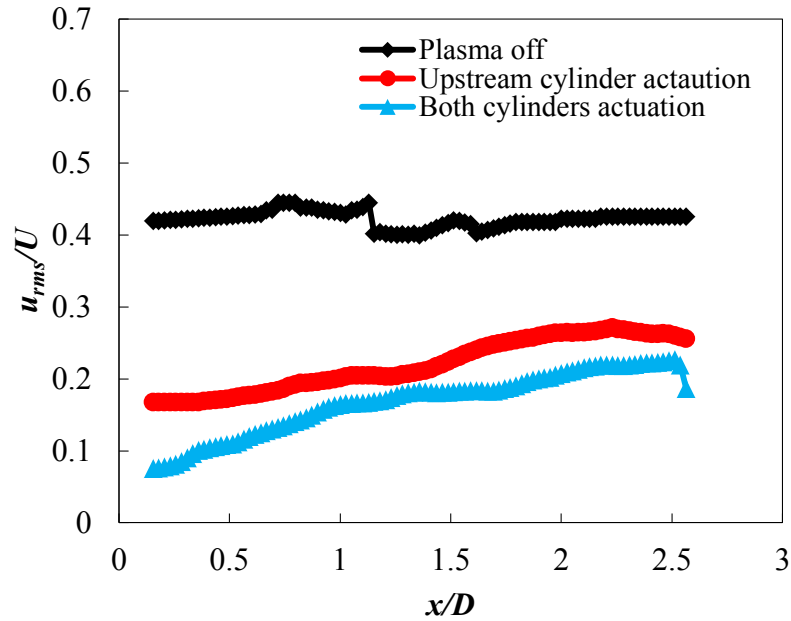
a) Streamwise velocity fluctuation
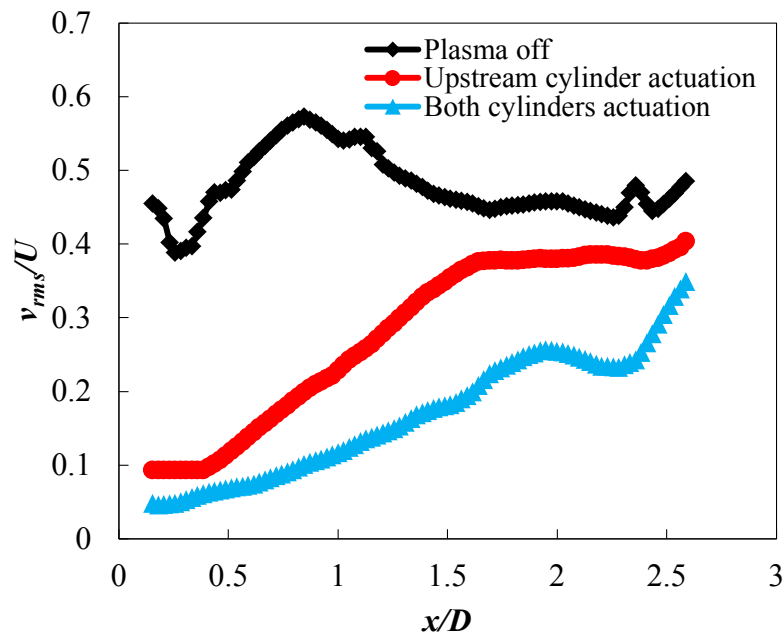
b) Vertical velocity Fluctuation

Figure 5.50 streamwise and vertical velocity fluctuations along the center of the wake region between the cylinders.

Figure 5.50 shows the distribution of the streamwise and vertical velocity fluctuation along the center of the wake region. It can be seen, that the simultaneous activation of the upstream and downstream cylinders leads to better reduction in the velocity fluctuations, when compared to the

plasma off case. This reduction in the wake energy corroborates the delay in vortex shedding (Fig. 5.46b), which are triggered at a more downstream location, when compared to plasma off and upstream cylinder activation only. As a result, the narrowband vortex tonal noise is further reduced when both the upstream and downstream cylinders are activated (Fig. 5.22).

Furthermore, POD analysis has been performed in order to capture the large scale vortex shedding structures in the wake region between the two cylinders with both cylinders are subjected to the plasma off and plasma on at free stream velocity $U = 10$ ms^{-1}. Figure 5.52 illustrates the spatial distribution of the first mode, the highest energy mode, in terms of the streamwise velocity components, u for both plasma off and plasma on cases. One can notice that high energy patterns concentrate in the near wake region, while further downstream; the intensity of these structures is reduced. For the plasma on case, the results show that two rows of anti-symmetrical velocity distribution patterns occur in the far wake region and alternately develop into the wake. Close to the downstream cylinder. There is no significant energy at the near wake region

a)

b)
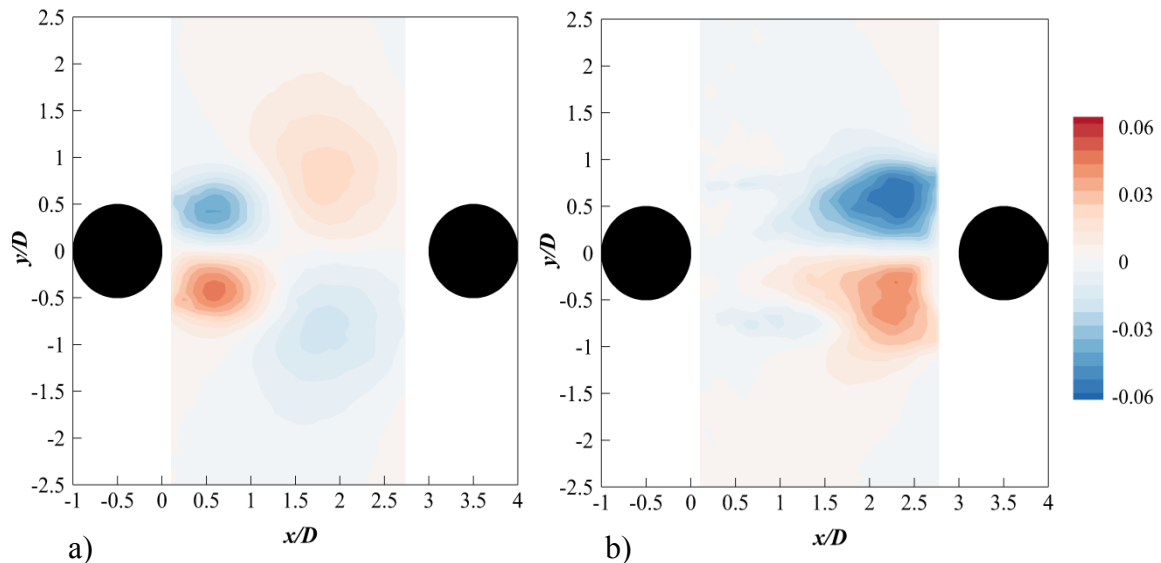
Figure 5.51 POD first mode in terms of the streamwise velocity for tandem cylinders with both cylinders are actuated a) Plasma off and b) Plasma on case at free stream velocity $U = 10$ ms^{-1} at $V_{(input)} = 6$ kV and $f_{(input)} = 8$ kHz.

Figure 5.52 shows the first mode spatial distribution contours in terms of the vertical velocity component for both the plasma off and plasma on cases. For plasma on case, it can be seen that a significant reduction in the energy of the large scale patterns in the near wake region can be

observed. However, this can also be interpreted that the original spatial distribution of the POD modes in the plasma off case has been "Pushed back" towards the more downstream location.

a)   b)
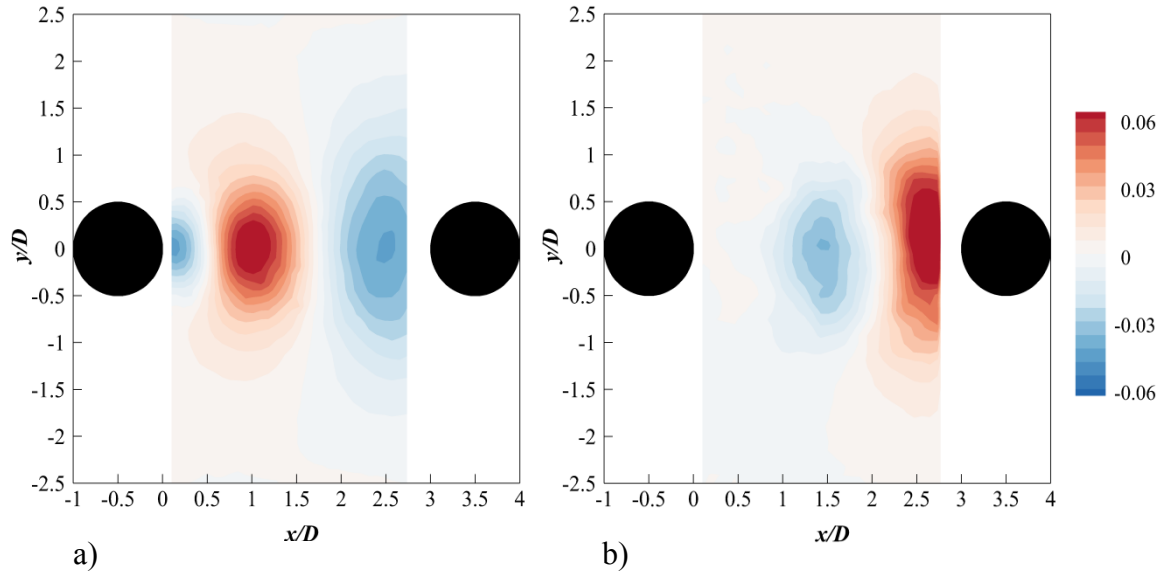
Figure 5.52 POD first mode in terms of the vertical velocity for tandem cylinders with both cylinders are actuated a) Plasma off and b) Plasma on case at free stream velocity U = 10 ms^{-1} at V$_{(input)}$ = 6 kV and f$_{(input)}$ = 8 kHz.

To summarize, the energy contributions of the first twenty modes for the three plasma configurations namely, (1) upstream cylinder actuation, (2) downstream cylinder actuation, and (3) double cylinder actuation are shown in Fig. 5.53. The results show that the first two modes contribute by 47% of the total energy with the other modes. It can be seen that having only the downstream cylinder activated by the plasma actuator, i.e. the jet is induced in the upstream direction, could only reduce the energy of the first mode by about 7. 25% compared with baseline case. Finally, having both the upstream and downstream cylinders activated by the plasma jet in the in the downstream and upstream direction can reduce the energy of the first and the second modes significantly by about 47% and 41%, respectively. These findings agree with acoustic results, which suggest that higher level of narrowband tonal noise reduction can be achieved when both the upstream and downstream cylinders are subjected to the plasma actuator. The reason that the interaction broadband noise is also reduced in this double cylinder actuation configuration can be explained by the turbulence intensity level, demonstrated in Fig. 5.48 and Fig. 5.49, which shows that under simultaneous actuation more rapid decay of turbulence

intensity towards the downstream cylinder compared with the actuation of the upstream cylinder only.
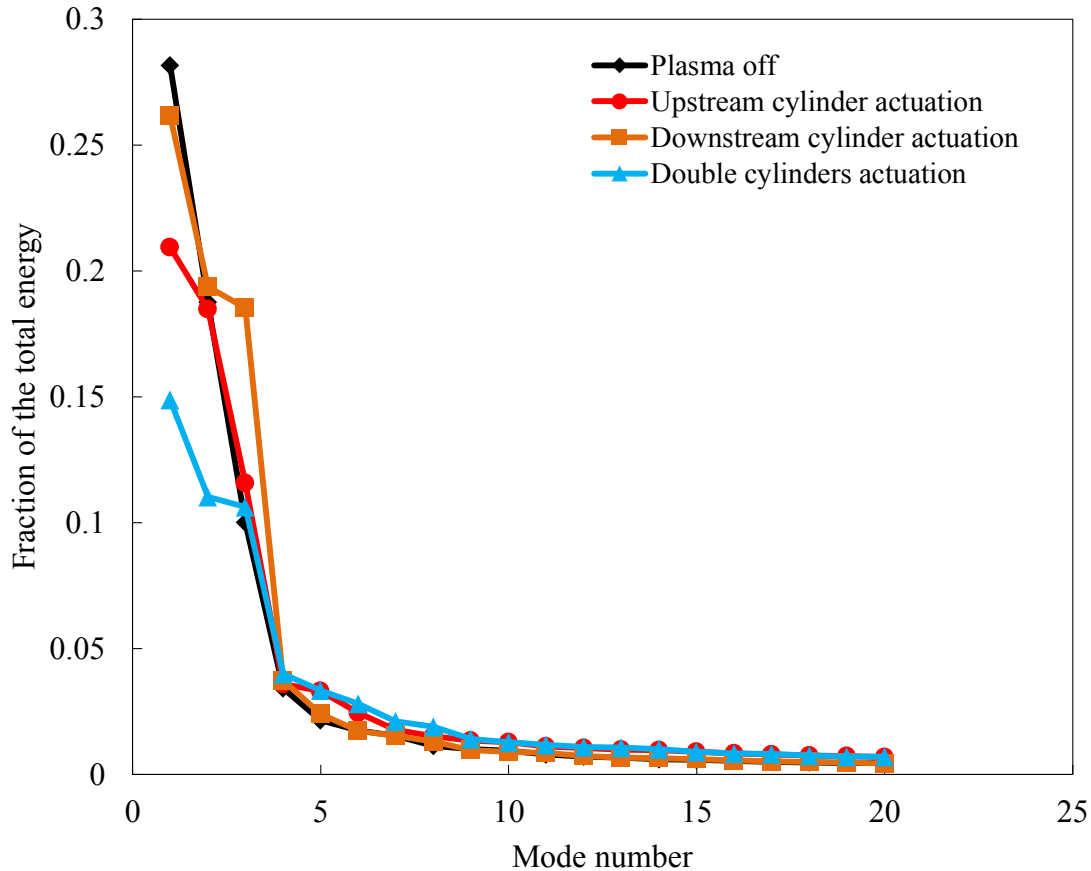
Figure 5.53 Energy contribution versus POD mode number for both plasma off and plasma on cases at free stream velocity U = 10 ms^{-1} at V$_{(input)}$ = 6 kV and f$_{(input)}$ = 8 kHz.

5.5 Summary

This chapter focused on the effect of using Surface Dielectric Barrier Discharge (DBD) plasma actuator on the narrowband tonal noise of single cylinder and the interaction broadband noise between two cylinders in tandem configuration. Both cases were tested at free stream velocity $U = 10$ ms^{-1} and the corresponding Reynolds number, $Re_D = 1.1$ x 10^4. Plasma actuators were positioned on both upper and lower sides of the cylinder at different azimuthal angles $\pm 27^o \leq \theta_j \leq \pm 153^o$. For the tandem cylinders, three cases were investigated based on the actuated cylinder namely, (1) upstream cylinder actuation, (2) downstream cylinder actuation, and (3) double cylinder actuation. The input voltage and frequency were kept the same for all the cases,

$V_{(input)}$ = 6 kV *and* $f_{(input)}$ = 8 kHz, respectively. These parameters are selected for being the best set up which gives the highest the most uniform plasma induced electrical wind.

For the single cylinder, the acoustic results showed that distinct peak and its harmonic occur in the Sound Pressures Level (SPL) spectra at a dimensionless frequencies fD/U = 0.185 and 0.545, respectively. Because the main narrowband tonal peak Strouhal number is very close to the bluff body, the main aerodynamic noise is generated as a result of the separation of the shear layer and the consequent vortex shedding into the wake region. The results showed that the highest reduction in the narrowband tonal noise level of 12 ±0.5dB is achieved when the plasma actuator is placed at θ_j = ±133°. The unsteady velocity power spectral density that is obtained from hot wire measurements showed that a primary peak occurs at fD/U = 0.188 which is very close to the frequency of the vortex shedding obtained from the acoustic measurement. Therefore, the narrowband tonal noise is produced due to the vortex shedding in the wake region of the cylinder. The activation of plasma actuator results in a reduction in the narrowband peak, by about 15 dB at x/D = 0.75. Although, the plasma actuator can produce a streamwise jet of 2 ms^{-1}, the results suggest that the plasma induced jet is not enough to suppress the vortex shedding. Therefore, the mechanism of the narrowband tonal noise reduction is not due to the direct momentum injection into the wake deficit, rather it is due to the delay in the vortex formation length. This is also confirmed through the significant decay of the velocity fluctuations in the near wake region. The elongation of wake region behind the cylinder base is similar to the effect that a splitter plate is attached to base of a bluff body (Blunt trailing edge flat plates and cylinders). This elongation is a clear sign of a separation delay and drag reduction.

For the tandem cylinders, three cases were investigated based on the activated plasma actuator namely, (1) upstream cylinder actuation, (2) downstream cylinder actuation, and (3) double cylinder actuation. The acoustic results showed that the noise radiated from the tandem is of narrowband and broadband nature. The flow results showed that the narrowband tonal noise is due to the vortex shedding from the upstream cylinder, while the broadband noise is due to the interaction of the turbulent wake of the upstream cylinder with downstream one. The activation of plasma actuator placed at θ_j = ±125° on the upstream cylinder leads to the highest narrowband and broadband noise reduction among the other angles. The flow results showed that the activation of the plasma actuator on the upstream cylinder leads to a reduction in the streamwise

and vertical velocity fluctuation and a delay of vortex shedding, which leads to the reduction in the broadband and narrowband noise. The effectiveness of the plasma actuator is reduced when the actuator placed on the downstream cylinder only with no significant noise reduction can be observed. This confirmed by the flow results which showed that the turbulence level is not affected by the activation of the plasma actuator. However, the simultaneous actuation of both the upstream and downstream cylinders with the plasma actuator is placed at $\theta_{UCj} = \pm125^{\circ}$ and $\theta_{DCj} = \pm55^{\circ}$ outperforms the upstream cylinder activation case with maximum narrowband and broadband noise reduction of about 16 ±0.5dB dB and 6 ±0.5dB, respectively. This narrowband tonal noise and broadband interaction noise reduction is corroborated by vortex shedding delay and the significant decay of the turbulence level toward the front face of the downstream cylinder. This is also manifested in the POD analysis results where the energy of the first twenty modes is more reduced when both the upstream and downstream cylinders simultaneously activated when compared to the other cases (plasma off, the upstream cylinder activation only, and downstream cylinder activation only)

Chapter 6

Conclusions and Future Work

6.1 Conclusions

Since 1990's when the atmospheric plasma actuators established themselves as one of the promising flow control technologies, the Dielectric Barrier Discharge DBD plasma actuators have been thoroughly investigated by many researchers. This type of flow control actuator offers a number of advantages over other flow control techniques. For example, it is simple, easy to design, highly adaptable to complicated geometry, and has a very fast time response. The DBD plasma actuators are proven to be effective in the boundary layer separation control and skin friction reduction of a turbulent boundary layer.

In the aeroacoustic field, a separated or turbulent flow on an aerodynamic body (e.g. airfoil) can radiate high level of aerodynamic noise. A logical concept to reduce the level of the aerodynamic noise is therefore to tackle these noise sources directly by the flow control techniques. Most of the current efforts focus on passive flow control, e.g. the trailing edge serrations, permeable surfaces, shape optimization and splitter plates on blunt body. However, there are relatively few studies focusing on the application of active flow control for the reduction of aerodynamic noise. Despite a promising technology, little attention has been paid to investigate the effect of DBD plasma actuators on the aerodynamic noise. This PhD work attempts to fill this gap and to conduct a combined aeroacoustic/fluid dynamic study into the effect DBD plasma actuators on the followings:

1. Narrowband tonal noise produced by the Karman vortex shedding pertaining to a flat plate with blunt trailing edge, and a symmetrical airfoil with cut-in type serrated trailing edge.
2. Turbulent broadband noise by the fluid-structure interaction between the tandem cylinders.

6.1.1 Bluntness-Induced Vortex Shedding Tonal Noise

In this study, a flat plate with a blunt trailing edge and an airfoil with cut-in type serrated trailing edge were investigated. Both models were subjected to a wind tunnel speed of $7.5 \leq U \leq 40$ ms^{-1}, which correspond to Reynolds numbers based on the chord length of 0.75 x $10^5 \leq Re_C \leq 4$ x 10^5. The models were examined at zero incidence with respect to the incoming flow. The boundary layers on both the upper and lower sides were artificially tripped to turbulent using rough sand paper.

Three plasma actuators configurations were investigated in the flat plate case. The first plasma actuator is referred to the PA1 plasma actuator. This actuator is designed to produce a tangential electric wind parallel to the flow direction on both sides of the flat plate. The second actuator is called the PA2 plasma actuator, which produces downward electric wind from both upper and lower sides, which merge into one streamwise jet towards the center of the wake. The last plasma actuator, PA3, composes of several spanwise-distributed plasma actuators. This configuration is designed to produce electric wind in the spanwise direction. The results of the flat plate with blunt trailing edge can be summarized as follows:

- The results of the electric and geometrical characteristics of the DBD plasma actuator showed that increasing the input voltage leads to a linear increase in the ΔOASPL up to a certain value of the input voltage. Beyond this critical value any increase in the input voltage does not have any effect on the radiated noise level. It is also found that the level of the aerodynamic noise reduction is a weak function of the input frequency. In terms of the geometrical parameters represented by the thickness of the dielectric material (Kapton tape), the pre-test results suggest that thin layer of dielectric material is preferred for a larger level of aerodynamic noise reduction. However, too thin the layer of the dielectric can cause a frequent breakdown of the plasma actuators. As a compromise, five layers of Kapton tape were used consistently throughout the experiments.

- The extensive acoustic measurements were mainly performed at $U = 7.5$ ms^{-1}. The Sound Pressure Level SPL spectra revealed that for the plasma off (baseline) case, a significant narrowband peak occurs at a frequency $f_{(acoustic)}$, which produces a Strouhal number of $f_{(acoustic)}H/U = 0.19$. The relationship between the narrowband tone peak in the acoustic

field and the vortex shedding in the wake region of the hydrodynamic field is confirmed by the presence of a distinct narrowband-hump of the fluctuating velocity power spectral density at $f_{(hydrodynamic)}$, which corresponds to $f_{(hydrodynamic)}H/U = 0.19$.

- From the SPL spectra, the plasma actuator is shown to produce a non-aerodynamic self-noise. It is important to point out that this extraneous noise only occurs at very high frequency, which does not interfere with the narrowband tonal noise that predominantly occurs at a much lower frequency. The actuator self-noise level reduces when the free stream velocity increases due to the masking effect from the background noise.

- The PA1 plasma actuator that produces a tangential electric wind parallel to the flow direction yields no significant aerodynamic noise reduction. The POD analysis showed that the large scale coherent structures in the wake region are more compact when compared with the plasma off, baseline case. This suggests that the application of the PA1 plasma actuator can slightly alter vortex shedding frequency downstream of the trailing edge of the flat plate.

- The second plasma actuator PA2 shows a significant reduction in the narrowband vortex shedding tone noise with a maximum noise reduction of about 14.5 ±0.5dB at U = 7.5 ms^{-1}. This noise reduction is supported by the POD analysis, which shows that a weak parallel jet induced at the blunt face of the trailing edge leads to a dramatic decrease in the energy of the large scale structures in the wake region. During the quiescent, no flow condition, the PA2 plasma actuator is shown to produce a maximum streamwise jet of 1.8 ms^{-1} over a considerably large downstream distance. However, this plasma-induced jet was diminished quite quickly when the mean flow is present. In the analysis of the time-averaged streamwise velocity, there is no evidence of direct momentum injection into the wake deficit, but rather there is a very quick decay of the plasma-induced jet. The non-convective, separating shear layers are extended in the downstream direction, and in the process increasing the vortex shedding formation length. It is concluded that the reduction of the narrowband vortex shedding noise is not exclusively related to the direct suppression of the vortex shedding, but rather it is mainly due to the delay mechanism for the cross-talk between the two separating shear layers at the blunt trailing edge.

- An important implication of the noise reduction mechanism described above is the facilitation of low-input voltage to the plasma actuator system for a successful suppression of the aerodynamic noise. This finding is a step further for the promotion of the plasma actuator technology.

- The PA2 plasma actuator leads to a considerable reduction in the mean and fluctuating drag coefficient of about 15% and 26%, respectively.

- The third configuration is related to the PA3 plasma actuator. The acoustic results indicate that this type of plasma actuator has a potential to outperform both the PA1 and PA2 plasma actuators under the same low-input voltages. For example, the PA3 plasma actuator can reduce the narrowband vortex shedding tonal noise by about 4 ±0.5dB at an input voltage of 2.4 kV, where no noise reduction can be achieved by the PA1 and PA2 at the same input voltage. The maximum reduction in the bluntness-induced tonal noise of about 12 ±0.5dB can be achieved when the PA3 actuator is operated at 3kV. This significant reduction in the narrowband tone noise is corroborated by the absence of the large scale coherent structures in the flow field between any two adjacent actuators. The mechanism responsible for the bluntness-induced noise reduction is found to be due the propagation of the streamwise vortices to eventually counteract or interrupt the otherwise dominant spanwise vorticity field in the wake.

The second model that also generates bluntness-induced vortex shedding in the wake is an airfoil with a cut-in type serrated trailing edge. Three different exposed electrode configurations were investigated: the *EE1*, *EE2*, and *EE3* plasma actuators.

- The first plasma configuration (*EE1*) results in a slight reduction of about 2 ±0.5dB in the narrowband tone noise generated as a result of the bluntness-induced vortex shedding. In addition, the narrowband tone is shifted towards a slightly high frequency in the same way as the flat plate case with the PA1 plasma actuator.

- The *EE2* plasma actuator, which has an exposed electrode with a spanwise spacing similar to the PA3 plasma actuator, leads to a 9 ±0.5dB reduction in the narrowband tonal noise.

- A 6 ±0.5dB reduction in the narrowband tonal noise can be achieved when the *EE3* plasma actuator is applied.

- The *EE2* plasma actuator is chosen for an airfoil with a truncated trailing edge because it leads to the highest level of noise reduction amongst all the plasma configurations. The results showed that the narrowband tonal noise can be completely suppressed at $U = 7.5$ ms^{-1}. However, the effectiveness of the *EE2* plasma actuator decreases as the free stream velocity increases.

6.1.2 Single and Tandem Cylinders

The second investigation is related to the acoustic and flow fields pertaining to a single cylinder, as well as two cylinders in a tandem configuration. For the single cylinder, it is known to produce Karman vortex shedding in the wake under a certain range of Reynolds number. The vortex shedding will also radiate narrowband tonal noise. For the tandem cylinders, the radiation of the vortex shedding tonal noise from the upstream cylinder is expected. In addition, the fluid-structure interaction between the wake from the upstream cylinder, and the stagnation part of the downstream cylinder, is expected to generate broadband turbulent interaction noise. The effect of the DBD plasma actuators on these noise sources was investigated. The two cases were investigated at $U = 10$ ms^{-1}, corresponding to a subcritical Reynolds number $Re_D = 1.1$ x 10^4. The actuator was placed on both upper and lower sides of the cylinder and at $\pm 27^o \leq \theta_j \leq \pm 153^o$, where θ_j is the polar angle. The results are summarized as follows:

- For the single cylinder case, where the separation bubbles occur at $\pm\ 75^o \leq \theta_j \leq \pm\ 90^o$, the maximum level of noise reduction of about 12 ±0.5dB is achieved when the plasma actuator is placed on both the upper and lower sides of the cylinder at $\theta_j = \pm\ 133^o$. This significant level of noise reduction is corroborated by the reduction in the energy of the most dominant POD modes (the first and the second mode). When the plasma actuators are activated under the quiescent flow condition, the result shows the generation of a streamwise plasma induced jet of maximum velocity of about 2 ms^{-1}. The activation of the plasma actuator results in an increase in the vortex shedding formation length. Therefore it can be assumed that the mechanism of the far field narrowband noise reduction is similar to the flat plate model in which the plasma-induced electric wind acts

as an isolator that prevents the near wake separating shear layers from interacting with each other.

- For the tandem cylinders, three plasma actuation cases were investigated. These are the (case 1) actuation on the upstream cylinder only, (case 2) actuation on the downstream cylinder only, and (case 3) actuation on both the cylinders.

- For the plasma off baseline case, the SPL spectra revealed that a significant narrowband tone occurs at a reduced frequency of $fD/U = 0.155$ (where D is the cylinder diameter). The noise level is higher than that of a single upstream /downstream cylinder placed in the same mean flow condition, respectively. A broadband hump at a reduced frequency $0.28 \leq fD/U \leq 1.6$ can also be observed in the SPL spectra, which is believed to be generated from the interaction between the turbulent wake of the upstream cylinder and the front face of the downstream cylinder. Fluctuating velocity power spectral density was obtained from the hot wire measurements at several streamwise locations between the two cylinders. The results show that a similar hydrodynamic broadband hump occurs at the same frequency range as the counterpart in the acoustic far field.

- The (case 1, actuation on the upstream cylinder only) results in a maximum noise reduction of about 15 ±0.5dB in the narrowband tone peak with plasma actuator placed at $\theta_j = \pm 125^\circ$ on the upper and lower sides of the upstream cylinder, respectively. This reduction in the tonal noise is corroborated by the decrease in the energy of the most dominant modes (the first and the second) obtained from the POD analysis. In addition, a reduction in the broadband hump of about 4 ±0.5dB can be achieved. Because the radiated broadband acoustic energy level is related to the turbulent wake interaction between the two cylinders, the noise reduction suggests that the turbulence level in the wake region has been reduced by the plasma actuator in case 1. This interpretation is confirmed through both the hot wire and PIV measurements, where the fluctuating velocity power spectral density measured by the hot wire demonstrate a consistent reduction in the broadband component for all the streamwise locations. This confirms the reduction in the turbulence level in the wake region between the cylinders by case 1. In addition, the two-dimensional flow field measurement by the PIV clearly shows the

reduction in the velocity fluctuations in the wake region for both the streamwise and vertical velocity components when the case 1 plasma actuator is activated.

- The (case 2) with the plasma-induced jet in the upstream direction (against the mean flow direction) from the downstream cylinder is not as effective when compared to the case 1. Noise reduction of only 2 ±0.5dB in the frequency region pertaining to the broadband hump can be achieved.

- The (case 3, simultaneous activation on both the upstream and downstream cylinders) leads to a better noise reduction when compared to the case 1 and case 2. The acoustic results showed that when plasma actuator is placed at $\theta_{UCj} = \pm\ 125^o$ on the upstream cylinder and $\theta_{DCj} = \pm\ 55^o$ on the downstream cylinder, the maximum narrowband and broadband noise reduction that can be achieved is about 16 ±0.5dB and 6 ±0.5dB, respectively. This noise reduction is correlated with the significant reduction in the energy contribution of the most dominant POD modes (the first and the second modes) related to the coherent structures in the wake. In addition, plasma actuators in case 3 lead to the best reduction in the streamwise and vertical velocity fluctuations in the near and far wake regions. Two control mechanisms are involved in the noise reduction in this double actuation case. The first is related to the delay mechanism by the plasma-induced jet from the upstream cylinder to the vortex shedding. The significantly weakened vortex shedding is also manifested in the lower turbulence intensity in the wake. The second is due to the upstream-directed plasma-induced jet from the downstream cylinder, which acts as a virtual fluidic shield that displaces the already weakened turbulent wake from the upstream cylinder away from the front face of the downstream cylinder.

6.2 Suggested Future Work

The entire PhD focuses on the DBD plasma actuator for the manipulation of the vortex shedding and the subsequent suppression of the tonal noise. Overall, the DBD plasma actuator can significantly reduce the bluntness-induced narrowband tone noise, and moderately reduce the broadband turbulent interaction noise. The followings are the suggested future works following this thesis:

- Developing the multi-plasma actuators has a potential to further increase the level of electric wind speed. These include the slide discharge plasma actuators, and the "three-electrode" configuration. This means that the plasma actuator can become more effective in the aerodynamic noise reduction at higher mean flow condition.

- The effectiveness of the spanwise plasma actuation (PA3) can be enhanced by reducing the width of the exposed electrode, which can result in a better coverage of the active flow control area. Another suggestion is to use two rows of staggered exposed electrodes. This will ensure that the inactive area of the downstream row can be covered by the upstream row.

- It has been shown that one of the problems associated with the DBD plasma actuators is the generation of the non-aerodynamic noise predominantly at the high frequency region. To overcome this it is suggested to operate the plasma actuator system at a much higher frequency outside the audible range.

- Recently, a new concept of the so-called Plasma Synthetic Jet (PSJ), which is a form of the thermal plasma actuator, can generate jet velocities order of magnitude higher than the conventional plasma actuators. It is envisaged that the future development is to place an array of the PSJ actuators in the strategic locations within the fluid body for the reduction of the aerodynamic noise.

References

Akbıyık, H., Akansu, Y. E., and Yavuz, H. (2017). Active control of flow around a circular cylinder by using intermittent DBD plasma actuators. *Flow Measurement and Instrumentation*, 53, 215-22

Amitay, M., Honohan, A., Trautman, M., Glezer, A., Amitay, M., Honohan, A., Trautman, M. and Glezer, A. (1997). Modification of the aerodynamic characteristics of bluff bodies using fluidic actuators. In *28th Fluid Dynamics Conference* (p. 2004).

Amitay, M., Smith, B. L., and Glezer, A. (1998). Aerodynamic flow control using synthetic jet technology. *AIAA paper*, *208*.

Angland, D., Zhang, X., and Goodyer, M. (2012). Use of Blowing Flow Control to Reduce Bluff Body Interaction Noise. *AIAA journal*, *50*(8), 1670-1684.

Apelt, C.J. and West, G.S. (1975). The effects of wake splitter plates on bluff-body flow in the range $10^4 < \text{Re} < 5\times 10^4$. Part 2. *Journal of Fluid Mechanics*, *71*(1), pp.145-160.

Apelt, C.J., West, G.S. and Szewczyk, A.A. (1973). The effects of wake splitter plates on the flow past a circular cylinder in the range $10^4 < \text{Re} < 5 \times 10^4$. *Journal of Fluid Mechanics*, *61*(1), pp.187-198.

Argüelles, P., Bischoff, M., Busquin, P., Droste, B. A. C., Evans, and S. R. (2001). European Aeronautics: A vision for 2020. *Advisory Council for Aeronautics Research in Europe, Report*.

Arie, M., Kiya, M., Moriya, M. and Mori, H. (1983). Pressure fluctuations on the surface of two circular cylinders in tandem arrangement. *Journal of fluids engineering*, *105*(2), pp.161-166.

Artana, G., D', J., Adamo, Lé, L., ger, Moreau, E., Gé and Touchard, R. (2002). Flow control with electrohydrodynamic actuators. *AIAA journal*, *40*(9), pp.1773-1779.

Bearman, P.W. (1965). Investigation of the flow behind a two-dimensional model with a blunt trailing edge and fitted with splitter plates. Journal of Fluid Mechanics, 21(2), pp.241-255.

Bearman, P. W. (1967). The effect of base bleed on the flow behind a two-dimensional model with a blunt trailing edge. *The Aeronautical Quarterly*, *18*(3), 207-224.

Belinger, A., Hardy, P., Barricau, P., Cambronne, J. P., and Caruana, D. (2011). Influence of the energy dissipation rate in the discharge of a plasma synthetic jet actuator. *Journal of Physics D: Applied Physics*, *44*(36), 365201.

Benard, N., and Moreau, E. (2012). Role of the electric waveform supplying a dielectric barrier discharge plasma actuator. *Applied Physics Letters*, *100*(19), 193503.

Blake, W.K. and Temkin, S. (1988). Mechanics of Flow-Induced Sound and Vibration. Vol. I: General Concepts and Elementary Sources by William K. Blake.

Brooks, T. F., Pope, D. S., and Marcolini, M. A. (1989). Airfoil self-noise and prediction.

Campos, L. M. B. C. (2014,). On the reduction of the engine and aerodynamics noise of aircraft. In *INTER-NOISE and NOISE-CON Congress and Conference Proceedings* (Vol. 249, No. 3, pp. 4715-4722). Institute of Noise Control Engineering.

Castro, I. P. (1971). perforated plates normal to an air-stream. *J. Fluid Mech*, *46*(part 3), 599-609.

Cattafesta III, L. N., and Sheplak, M. (2011). Actuators for active flow control. *Annual Review of Fluid Mechanics*, *43*, 247-272.

Che, X.K., Nie, W.S. and Hou, Z.Y. (2015). High altitude plasma flow control simulation through ground experiment. *Acta Aeronaut Astronaut Sin*, *36*(2), pp.441-8.

Chen, F. F. (2012). *Introduction to plasma physics*. Springer Science & Business Media.

Chen, P., Zhang, X., and Angland, D. (2011). Slat noise reduction using a leading edge strip. *AIAA Paper*, *2908*, 2011.

Choi, H., Jeon, W. P., and Kim, J. (2008). Control of flow over a bluff body. *Annu. Rev. Fluid Mech.*, *40*, 113-139.

Choi, K.S., Jukes, T.N., Whalley, R.D., Feng, L., Wang, J., Matsunuma, T. and Segawa, T. (2014). Plasma virtual actuators for flow control. *Journal of Flow Control, Measurement & Visualization*, *3*(01), p.22.

Chong, T. P., Vathylakis, A., Joseph, P. F., and Gruber, M. (2013). Self-noise produced by an airfoil with nonflat plate trailing-edge serrations. *AIAA journal*.

Choudhari, M. M., and Khorrami, M. R. (2006). Slat Cove Unsteadiness Effect of 3D Flow Structures.

Corke, T. C., Enloe, C. L., and Wilkinson, S. P. (2010). Dielectric barrier discharge plasma actuators for flow control. *Annual review of fluid mechanics*, *42*, 505-529.

Corke, T. C., Post, M. L., and Orlov, D. M. (2008). Single-dielectric barrier discharge plasma enhanced aerodynamics: concepts, optimization, and applications. *Journal of Propulsion and Power*, *24*(5), 935-945.

Corke, T. C., Post, M. L., and Orlov, D. M. (2009). Single dielectric barrier discharge plasma enhanced aerodynamics: physics, modeling and applications. *Experiments in Fluids*, *46*(1), 1-26.

Curle, N. (1955). The influence of solid boundaries upon aerodynamic sound. In *Proceedings of the Royal Society of London A: Mathematical, Physical and Engineering Sciences*(Vol. 231, No. 1187, pp. 505-514). The Royal Society.

Dareck, M., Edelstenn, C., Ender, T., Fernande, E., Hartman, P., Herteman, J., and Orsi, G. (2011). Flightpath 2050 Europes Vision for Aviation. *Off. Eur*.

Debien, A., Benard, N., and Moreau, E. (2011). Electric wind produced by sliding discharges. *Proceeding of 2nd ISNPEDADM new electrical technologies for environment, Nouméa*.

Deck, S., Gand, F., Brunet, V. and Khelil, S.B. (2014). High-fidelity simulations of unsteady civil aircraft aerodynamics: stakes and perspectives. Application of zonal detached eddy simulation. *Phil. Trans. R. Soc. A*, *372*(2022), p.20130325.

Dickson, N. (2014). Aircraft Noise Technology and International Noise Standards. *Environment Branch, ICAO Air Transport Bureau*.

Dobrzynski, W. (2010). Almost 40 years of airframe noise research: what did we achieve?. *Journal of aircraft*, *47*(2), 353-367.

Dobrzynski, W., Buchholz, H., Dobrzynski, W., and Buchholz, H. (1997). Full-scale noise testing on Airbus landing gears in the German Dutch wind tunnel. In *3rd AIAA/CEAS Aeroacoustics Conference* (1597).

Dobrzynski, W., Chow, L. C., Guion, P., and Shiells, D. (2002). Research into landing gear airframe noise reduction. *AIAA paper*, *2409*, 2002.

Dobrzynski, W., Gehlhar, B., and Buchholz, H. (2001). Model and full scale high-lift wing wind tunnel experiments dedicated to airframe noise reduction. *Aerospace science and technology*, *5*(1), 27-33.

Durscher, R.J. and Roy, S. (2012). Three-dimensional flow measurements induced from serpentine plasma actuators in quiescent air. *Journal of Physics D: Applied Physics*, *45*(3), p.035202.

El-Refaee, M. M. (1994). Boundary layer control of separated flow over circular cylinders—A BEM parametric study. *Engineering analysis with boundary elements*, *14*(3), 239-254.

Eltaweel, A., Wang, M., Kim, D., Thomas, F.O. and Kozlov, A.V. (2014). Numerical investigation of tandem-cylinder noise reduction using plasma-based flow control. *Journal of Fluid Mechanics*, *756* pp.422-451.

Enloe, C. L., McLaughlin, T. E., VanDyken, R. D., Kachner, K. D., Jumper, E. J., and Corke, T. C. (2004). Mechanisms and responses of a single dielectric barrier plasma actuator: plasma morphology. *AIAA journal*, *42*(3), 589-594.

Feng, L. H., Wang, J. J., and Pan, C. (2010). Effect of novel synthetic jet on wake vortex shedding modes of a circular cylinder. *Journal of Fluids and Structures*, *26*(6), 900-917.

Feng, L.H. and Wang, J.J. (2014). The virtual aeroshaping enhancement by synthetic jets with variable suction and blowing cycles. *Physics of Fluids*, *26*(1), p.014105.

Forte, M., Jolibois, J., Baudoin, F., Moreau, E. and Touchard, G. (2006). Optimization of a dielectric barrier discharge actuator and non-stationary measurements of the induced flow velocity-application to airflow control. In *Proc. 3rd AIAA Flow Control Conference, 10 pages, Paper 2006, San Fransisco USA, 5-8 Juin 2006.*

Forte, M., Leger, L., Pons, J., Moreau, E., and Touchard, G. (2005). Plasma actuators for airflow control: measurement of the non-stationary induced flow velocity. *Journal of Electrostatics*, *63*(6), 929-936.

Fransson, J.H., Talamelli, A., Brandt, L. and Cossu, C. (2006). Delaying transition to turbulence by a passive mechanism. *Physical review letters*, *96*(6), p.064501.

Gibson, J. S. (1972). The ultimate noise barrier-far field radiated aerodynamic noise. In *Inter-Noise and NOISE-CON congress and conference proceedings* (Vol. 1972, No. 1, pp. (332-337). Institute of Noise Control Engineering.

Grimwood, C. J., Skinner, C. J., and Raw, G. J. (2002). The UK national noise attitude survey 1999/2000. In *Proceedings of the Noise Forum Conference*.

Grossman, K. R., Cybyk, B. Z., and VanWie, D. M. (2003). Sparkjet actuators for flow control. *AIAA paper*, *57*, 2003.

Guo, S., Simon, T., Ernie, D., and Kortshagen, U. (2010). Separation control using DBD plasma actuators: thrust enhancement studies. In *48th AIAA Aerospace Sciences Meeting* (Vol. 1090)

Henning, L., and King, R. (2005). Drag reduction by closed-loop control of a separated flow over a bluff body with a blunt trailing edge. In *Decision and Control, 2005 and 2005 European Control Conference. CDC-ECC'05. 44th IEEE Conference on* (pp. 494-499). IEEE.

Hoskinson, A. R., and Hershkowitz, N. (2010). Differences between dielectric barrier discharge plasma actuators with cylindrical and rectangular exposed electrodes. *Journal of Physics D: Applied Physics*, *43*(6), 065205.

Hoskinson, A. R., Hershkowitz, N., and Ashpis, D. E. (2008). Force measurements of single and double barrier DBD plasma actuators in quiescent air. *Journal of Physics D: Applied Physics*, *41*(24), 245209.

Howe, M.S. (1991). Aerodynamic noise of a serrated trailing edge. *Journal of Fluids and Structures*, *5*(1), pp.33-45.

Huang, X., Zhang, X., and Li, Y. (2010). Broadband flow-induced sound control using plasma actuators. *Journal of Sound and Vibration*, *329*(13), 2477-2489.

Hwang, J.Y., Yang, K.S. and Sun, S.H. (2003). Reduction of flow-induced forces on a circular cylinder using a detached splitter plate. *Physics of Fluids*, *15*(8), pp.2433-2436.

Ingram, J. D. (1964). *A survey of aerodynamic noise*. GENERAL TECHNOLOGY CORP ELGIN IL.

Inoue, O. (1985). A new approach to flow problems past a porous plate. *AIAA journal*, *23*(12), 1916-1921.

Jacob, M. C., Boudet, J., Casalino, D., and Michard, M. (2005). A rod-airfoil experiment as a benchmark for broadband noise modeling. *Theoretical and Computational Fluid Dynamics*, *19*(3), 171-196.

Jukes, T. N. and Choi, K. S. (2009). Flow control around a circular cylinder using pulsed dielectric barrier discharge surface plasma. Physics of fluids, 21(8), 084103.

Jukes, T. N. and Choi, K. S. (2012). Dielectric-barrier-discharge vortex generators: characterisation and optimisation for flow separation control. *Experiments in fluids*, *52*(2), pp.329-345.

Jukes, T., Choi, K.S., Johnson, G. and Scott, S. (2006), June. Turbulent drag reduction by surface plasma through spanwise flow oscillation. In *3rd AIAA Flow Control Conference* (p. 3693).

Kawai, H. (1990). Discrete vortex simulation for flow around a circular cylinder with a splitter plate. Journal of Wind Engineering and Industrial Aerodynamics, 33(1-2), pp.153-160.

Ketcham, J., and Velkoff, H. R. (1968). Effect of an electrostatic field on boundary-layer transition. *AIAA Journal*, *6*(7), 1381-1383.

Khalighi, Y., Mani, A., Ham, F. and Moin, P. (2010). Prediction of sound generated by complex flows at low Mach numbers. *AIAA journal*, *48*(2), pp.306-316.

Kim, J., and Choi, H. (2005). Distributed forcing of flow over a circular cylinder. *Physics of Fluids*, *17*(3), 033103.

Kim, J., Hahn, S., Kim, J., Lee, D. K., Choi, J., Jeon, W. P., and Choi, H. (2004). Active control of turbulent flow over a model vehicle for drag reduction. *Journal of Turbulence*, *5*(019), 1-12.

Kogelschatz, U. (2003). Dielectric-barrier discharges: their history, discharge physics, and industrial applications. *Plasma chemistry and plasma processing*, *23*(1), 1-46.

Kozlov, A. and Thomas, F. (2009). Active noise control of bluff-body flows using dielectric barrier discharge plasma actuators. In 15th AIAA/CEAS Aeroacoustics Conference (30th AIAA Aeroacoustics Conference) (p. 3245).

Kozlov, A.V. and Thomas, F.O. (2011a). Bluff-body flow control via two types of dielectric barrier discharge plasma actuation. *AIAA journal*, *49*(9), pp.1919-1931.

Kozlov, A.V., and Thomas, F.O. (2011b). Plasma flow control of cylinders in a tandem configuration. *AIAA journal*, *49*(10), 2183-2193.

Labergue, A., Moreau, E. and Touchard, G. (2005), October. A parametric study of surface corona discharge along an insulating flat plate in atmospheric pressure. In *Electrical Insulation and Dielectric Phenomena, 2005. CEIDP'05. 2005 Annual Report Conference on* (pp. 490-494). IEEE.

Léger, L., Moreau, E., and Touchard, G. G. (2002). Effect of a DC corona electrical discharge on the airflow along a flat plate. *IEEE Transactions on Industry Applications*, *38*(6), 1478-1485.

Leylekian, L., Lebrun, M., and Lempereur, P. (2014). An overview of aircraft noise reduction technologies. *AerospaceLab*, (6),1.

Li, Y., Wang, X., and Zhang, D. (2013). Control strategies for aircraft airframe noise reduction. *Chinese Journal of Aeronautics*, *26*(2), 249-260.

Lighthill, M. J. (1952). On sound generated aerodynamically. I. General theory. In *Proceedings of the Royal Society of London A: Mathematical, Physical and Engineering Sciences* (Vol. 211, No. 1107, pp. 564-587). The Royal Society.

Lighthill, M. J. (1954). On sound generated aerodynamically. II. Turbulence as a source of sound. In *Proceedings of the Royal Society of London A: Mathematical, Physical and Engineering Sciences* (Vol. 222, No. 1148, pp. 1-32).

Louste, C., Artana, G., Moreau, E., and Touchard, G. (2005). Sliding discharge in air at atmospheric pressure: electrical properties. *Journal of Electrostatics*, *63*(6), 615-620.

Ma, L., and Feng, L. (2013). Experimental investigation on control of vortex shedding mode of a circular cylinder using synthetic jets placed at stagnation points. *Science China Technological Sciences*, 1-12.

Malik, M., Weinstein, L. and Hussaini, M. (1983), January. Ion wind drag reduction. In *21st Aerospace Sciences Meeting* (p. 231).

McLaughlin, T. E., Munska, M. D., Vaeth, J. P., Dauwalter, T. E., Goode, J. R., and Siegel, S. G. (2004). Plasma-based actuators for cylinder wake vortex control. *AIAA paper*, *2129*, 2004.

Milano, M., Koumoutsakos, P., Giannakopoulos, X. and Schmidhuber, J. (2000). Evolving strategies for active flow control. In Evolutionary Computation, 2000. Proceedings of the 2000 Congress on (Vol. 1, pp. 212-218). IEEE.

Moreau, E. (2007). Airflow control by non-thermal plasma actuators. *Journal of physics D: applied physics*, *40*(3), 605.

Moreau, E., Debien, A., Bénard, N., Jukes, T., Whalley, R., Choi, K. S., and Mizeraczyk, J. (2013). Surface dielectric barrier discharge plasma actuators. *ERCOFTAC Bull*, *94*(5).

Moreau, E., Labergue, A., and Touchard, G. (2005). DC and pulsed surface corona discharge along a dielectric flat plate in air: Electrical properties and discharge-induced ionic wind. *Journal of Advanced Oxidation Technologies*, *8*(2), 241-247.

Moreau, E., Léger, L., and Touchard, G. (2006). Effect of a DC surface-corona discharge on a flat plate boundary layer for air flow velocity up to 25m/s. *Journal of electrostatics*, *64*(3), 215-225.

Moreau, E., Louste, C., and Touchard, G. (2008). Electric wind induced by sliding discharge in air at atmospheric pressure. *Journal of Electrostatics*, *66*(1), 107-114.

Munska, M. D., and McLaughlin, T. E. (2005). Circular cylinder flow control using plasma actuators. In 43rd AIAA Aerospace Sciences Meeting and Exhibit (Vol. 141, pp. 2005-141).

Nakayama, A. and Noda, H. (2000). LES simulation of flow around a bluff body fitted with a splitter plate. Journal of Wind Engineering and Industrial Aerodynamics, 85(1), pp.85-96.

Nati, G., Kotsonis, M., Ghaemi, S., and Scarano, F. (2013). Control of vortex shedding from a blunt trailing edge using plasma actuators. *Experimental Thermal and fluid science*, *46*, 199-210.

Oerlemans, S. and Fuglsang, P. (2012). Low-noise wind turbine design. *Siemens AG*, 11.

Oerlemans, S., and Bruin, A. (2009). Reduction of landing gear noise using an air curtain. In *15th AIAA/CEAS Aeroacoustics Conference* (pp. 1-25).

Park, S., Cvelbar, U., Choe, W. and Moon, S.Y. (2018). The creation of electric wind due to the electrohydrodynamic force. *Nature communications*, *9*(1), p.371.

Paterson, R. W., Amiet, R. K., and Munch, C. L. (1975). Isolated airfoil-tip vortex interaction noise. *J. Aircraft*, *12*(1), 34-40.

Petrusma, M. S., and Gai, S. L. (1994). The effect of geometry on the base pressure recovery of segmented blunt trailing edges. *Aeronautical Journal*, *98*(977), 267-274.

Popkin, S. H., Taylor, T. M., and Cybyk, B. Z. (2013). Development and application of the spark jet actuator for high-speed flow control. *Johns Hopkins APL technical digest*, *32*(1), 404-418.

Post, M.L. and Corke, T.C. (2006). Separation control using plasma actuators: dynamic stall vortex control on oscillating airfoil. *AIAA journal*, *44*(12), pp.3125-3135.

Pott-Pollenske, M. (2010). *Splitter plate and deceleration plate noise test, report*. OPENAIR-DLR-D4. 1.6-D4. 1.7–R1. 0.

Riherd, M. and Roy, S. (2013). Serpentine geometry plasma actuators for flow control. *Journal of applied physics*, *114*(8), p.083303.

Roshko, A. (1954). On the drag and shedding frequency of two-dimensional bluff bodies. NACA Tech. Note 3169.

Roth, J. R., Sherman, D. M., and Wilkinson, S. P. (1998). *Boundary layer flow control with a one atmosphere uniform glow discharge surface plasma*. American Institute of Aeronautics and Astronautics.

Roth, J.R., Sherman, D.M. and Wilkinson, S.P. (2000). Electrohydrodynamic flow control with a glow-discharge surface plasma. *AIAA journal*, *38*(7), pp.1166-1172.

Roy, S. and Wang, C.C. (2008). Bulk flow modification with horseshoe and serpentine plasma actuators. *Journal of Physics D: Applied Physics*, *42*(3), p.032004.

Santhanakrishnan, A. and Jacob, J.D. (2007). Flow control with plasma synthetic jet actuators. *Journal of Physics D: Applied Physics*, *40*(3), p.637.

Sato, M., Okada, K., Nonomura, T., Aono, H., Yakeno, A., Asada, K., Abe, Y. and Fujii, K. (2013). Massive parametric study by LES on separated-flow control around airfoil using DBD plasma actuator at Reynolds number 63,000. In *43rd AIAA Fluid Dynamics Conference* (p. 2750).

Schlichting, H., Gersten, K., Krause, E., Oertel, H. and Mayes, K. (1955). *Boundary-layer theory* (Vol. 7). New York: McGraw-hill.

Schneck III, W. C., and O'Brien, W. F. (2012). Flow control over a circular cylinder using pulsed DBD actuators. In *ASME Turbo Expo 2012: Turbine Technical Conference and Exposition* (pp. 947-957). American Society of Mechanical Engineers.

Schutze, A., Jeong, J.Y., Babayan, S.E., Park, J., Selwyn, G.S. and Hicks, R.F. (1998). The atmospheric-pressure plasma jet: a review and comparison to other plasma sources. *IEEE transactions on plasma science*, *26*(6), pp.1685-1694.

Seyhan, M., Akansu, Y. E., Karakaya, F., Yesildag, C., and Akbıyık, H. (2016). Effect of the duty cycle on the spark-plug plasma synthetic jet actuator. In *EPJ Web of Conferences* (Vol. 114, p. 02104). EDP Sciences.

Shahinfar, S., Sattarzadeh, S.S. and Fransson, J.H. (2014). Passive boundary layer control of oblique disturbances by finite-amplitude streaks. *Journal of Fluid Mechanics*, *749*, pp.1-36.

Siller, H., Jacob, M., & Michel, U. (2005). Flow and noise modification by suction and blowing on a rod-airfoil configuration. *Theor Comput Fluid Dyn*, *19*, 171-196.

Standish, K. J., and Van Dam, C. P. (2003). Aerodynamic analysis of blunt trailing edge airfoils. *TRANSACTIONS-AMERICAN SOCIETY OF MECHANICAL ENGINEERS JOURNAL OF SOLAR ENERGY ENGINEERING*, *125*(4), 479-487.

Tensi, J., Boué, I., Paillé, F. and Dury, G. (2002). Modification of the wake behind a circular cylinder by using synthetic jets. *Journal of Visualization*, *5*(1), pp.37-44.

Thill, C. L., Etches, J., Bond, I., Potter, K., and Weaver, P. (2008). Morphing skins. *The aeronautical journal*, *112*(1129), 117-139.

Thomas, F. O., Corke, T. C., Iqbal, M., Kozlov, A., and Schatzman, D. (2009). Optimization of dielectric barrier discharge plasma actuators for active aerodynamic flow control. *AIAA journal*, *47*(9), 2169.

Thomas, F. O., Kozlov, A., and Corke, T. C. (2006). Plasma actuators for bluff body flow control. AIAA paper, 2845, 2006.

Thomas, F.O., Kozlov, A. and Corke, T.C. (2008). Plasma actuators for cylinder flow control and noise reduction. *AIAA journal*, *46*(8), pp.1921-1931

Tombazis, N., and Bearman, P. W. (1997). A study of three-dimensional aspects of vortex shedding from a bluff body with a mild geometric disturbance. *Journal of Fluid Mechanics*, *330*, 85-112.

Van Dam, C. P., Cooperman, A., McLennan, A., Chow, R., and Baker, J. (2010). Thick airfoils with blunt trailing edge for wind turbine blades. In *ASME Turbo Expo 2010: Power for Land, Sea, and Air* (pp. 923-931). American Society of Mechanical Engineers.

Vathylakis, A., Chong, T.P. and Joseph, P.F. (2015). Poro-serrated trailing-edge devices for airfoil self-noise reduction. AIAA Journal, 53(11), pp.3379-3394.

Ver, I. (1987). Noise of jet engine test cells. Jet Engine test cells meeting, noise of jet engine test cells.

Von Kármán, T. (2004). *Aerodynamics: selected topics in the light of their historical development*. Courier Corporation.

Wang, C.C., Durscher, R. and Roy, S. (2011). Three-dimensional effects of curved plasma actuators in quiescent air. *Journal of Applied Physics*, *109*(8), p.083305.

Wang, J., Feng, L. and Xu, C. (2007). Experimental investigations on separation control and flow structure around a circular cylinder with synthetic jet. *Science in China Series E: Technological Sciences*, *50*(5), pp.550-559.

Whitelegg, J. (2000). AVIATION: the social, economic and environmental impact of flying. *Ashden Trust, London*.

Williams, J. F., and Hawkings, D. L. (1969). Sound generation by turbulence and surfaces in arbitrary motion. *Philosophical Transactions of the Royal Society of London A: Mathematical, Physical and Engineering Sciences*, *264*(1151), 321-342.

Williamson, C. H. K. (1996). Vortex dynamics in the cylinder wake. *Annual review of fluid mechanics* 28.1 (1996): 477-539.

Wong, H. Y. (1985). Wake flow stabilization by the action of base bleed. *Journal of Fluids Engineering*, *107*(3), 378-384.

Wood, C. J. (1964). The effect of base bleed on a periodic wake. *The Aeronautical Journal*, *68*(643), 477-482.

Yabe, A., Mori, Y., and Hijikata, K. (1978). EHD study of the corona wind between wire and plate electrodes. *AIAA journal*, *16*(4), 340-345.

Yokoyama, H., Tanimoto, I. and Iida, A. (2017). Experimental Tests and Aeroacoustic Simulations of the Control of Cavity Tone by Plasma Actuators. *Applied Sciences*, *7*(8), p.790.

Zdravkovich, M. M. (1981). Review and classification of various aerodynamic and hydrodynamic means for suppressing vortex shedding. *Journal of Wind Engineering and Industrial Aerodynamics*, *7*(2), 145-189.

Zdravkovich, M. M. (1985). Flow induced oscillations of two interfering circular cylinders. *Journal of Sound and Vibration*, *101*(4), 511-521.

Zhang, Z., Wu, Y., Jia, M., Song, H., Sun, Z., Zong, H., and Li, Y. (2017). The multichannel discharge plasma synthetic jet actuator. *Sensors and Actuators A: Physical*, *253*, 112-117.

Yokuda, S. and Ramaprian, B.R. (1990). The dynamics of flow around a cylinder at subcritical Reynolds numbers. Physics of Fluids A: Fluid Dynamics, 2(5), pp.784-791.

Zong, H. H., Wu, Y., Jia, M., Song, H. M., Liang, H., Li, Y. H., and Zhang, Z. B. (2015). Influence of geometrical parameters on performance of plasma synthetic jet actuator. *Journal of Physics D: Applied Physics*, *49*(2), 025504.